Regularized Singularities and Spectral Deferred Correction Methods: A Mathematical Study of Numerically Modeling Stokes Fluid Flow

Elizabeth L. Bouzarth

A dissertation submitted to the faculty of the University of North Carolina at Chapel Hill in partial fulfillment of the requirements for the degree of Doctor of Philosophy in the Department of Mathematics.

Chapel Hill
2008

Approved by

Advisor: Michael L. Minion
Reader: Richard M. McLaughlin
Reader: Roberto Camassa
Reader: Peter J. Mucha
Reader: Richard Superfine

ABSTRACT

ELIZABETH L. BOUZARTH: Regularized Singularities and Spectral Deferred Correction Methods: A Mathematical Study of Numerically Modeling Stokes Fluid Flow

(Under the direction of Michael L. Minion)

Regularized Stokeslets and spectral deferred correction methods are used to model variations of a rigid body precessing in Stokes flow. Numerical solutions are compared to exact and asymptotic closed form solutions for a spheroid precessing about its center. This provides the opportunity to perform careful error analysis and identify different numerical errors in regard to the motion of both slender and non-slender precessing spheroids. The error has components relating to quadrature, asymptotics, regularization, and time integration. Often, the quadrature error and time integration error are small with respect to the other error contributions, all of which are discussed. The motion of both slender and non-slender spheroids is studied to find the parameter and boundary condition choices that minimize velocity error. A system of regularized image singularities is developed to create a no-slip plane that mimics the effect of a nearby wall in the experiment setup. A temporal integration strategy based on spectral deferred correction (SDC) methods using an explicit treatment with different time steps for different components of the physical system is discussed. Multi-explicit SDC (MESDC)

methods provide an increase in efficiency for stiff problems by allowing non-stiff parts of the physical setup to use a larger time step requiring fewer expensive computations. The numerical methods are used to study experimental fluid dynamics phenomena relating to precessing rods that are not described by an exact closed form solution. This work has biological motivations resulting from the study of pulmonary cilia in conjunction with cystic fibrosis research as well as the motion of primary nodal cilia in developing embryos whose motion plays a critical role in developing left-right asymmetry in mammals.

ACKNOWLEDGEMENTS

I would like to thank the numerous people who have supported me and challenged me personally, professionally, and intellectually throughout my time in graduate school and my life as a whole. I've had the privilege of working with a variety of researchers at UNC from undergraduates working in the fluids lab to tenured professors in a variety of fields of study. The opportunities afforded to me at UNC are invaluable. From the beginning stages of research with my advisor to getting involved in the Virtual Lung Project, the NSF Research Training Group, and the interdisciplinary team of the Rotational Mixing Experiment (RMX) research group, I've gotten to experience different aspects of research as both a participant and an observer. I appreciate the challenge of tackling complicated questions in a team of people with different expertise to bring to the situation. My dissertation is evidence of my various collaborations.

I would like to thank my advisor, Michael Minion, for being a supportive, guiding force through the process of completing my Ph.D. requirements and generating research. I am forever grateful for your patience, insight, and many rounds of proof reading. I would also like to thank my committee members, Rich McLaughlin, Roberto Camassa, Peter Mucha, and Rich Superfine, for taking the time to give me valuable feedback on my research in both formal and informal settings. I truly appreciate the constructive criticism and the opportunity to work with you all. I also would like to thank the University of North Carolina at Chapel Hill, the UNC-CH Math Department, the Carolina Center

for Interdisciplinary Applied Mathematics, and the following grants for institutional and financial support throughout my tenure at UNC: NSF RTG DMS-0502266 and DOE SciDac DE-FC02-01ER25471.

I would like to recognize the people involved with the RMX research group during my involvement with the project. This research group has given me the opportunity to become intimately involved with the process of incorporating results of laboratory experiments with those of mathematical and numerical models. While this can be challenging, frustrating, and overwhelming, there have been many lively discussions and interesting findings over the years that make it quite rewarding. I appreciate the contributions of each and every person with whom I've interacted through that group. Here is a listing of people involved with the RMX group, past and present: Rich McLaughlin, Roberto Camassa, Rich Superfine, Leandra Vicci, Terry Jo Leiterman, Hao Jing, Longhua Zhao, Ben Evans, Adam Shields, Jonathan Toledo, Ben LaRoque, David Marron, Pavel Chtcheprov, Brian Bouzarth, and anyone else I've accidentally omitted from this collaborative effort.

In addition to the RMX group, I would also like to recognize everyone involved with the Virtual Lung Project and the NSF RTG fluids group, both at UNC. While there are too many people to name specifically, I certainly appreciate learning about and being a part of the interdisciplinary research that goes on in these groups.

After Hurricane Katrina, Ricardo Cortez was in residence at UNC for a semester and I had the opportunity to work with him. While I had started learning about and working with regularized Stokeslets before his arrival, having him on campus was incredibly valuable. I would like to thank him for working with me in developing my research and I look forward to working with him again in the future.

In addition to the people I've met professionally in graduate school, I'd like to recognize the life-long friends that I've made while at UNC. Without good friends in Chapel Hill, graduate school would have been a less fun and less rewarding experience. My friends here have been a network of support who understand what it's like to navigate the ups and downs of graduate school since they have experience with it too.

The best friend I've made during graduate school is my fiancé, Steven. Your generosity, kindness, thoughtfulness, intelligence, humor, and respect are unparalleled. I am so grateful to have someone so supportive and caring by my side. I hope I can be as supportive of you when you're writing your dissertation as you were of me. Thank you from the bottom of my heart.

I'd also like to thank my good friend Amanda for being an amazing, inspiring, intelligent, supportive confidant over the years. I look forward to wearing our floppy hats together some day.

Lastly, the unconditional love and support of my family is a constant source of strength and stability. To have a family who loves and supports me in every endeavor is all I could ask for. I thank you for that and look forward to becoming the second Dr. Bouzarth.

I am grateful to everyone who's helped me in both big and small ways. The opportunities, guidance, support, love, and friendship I've experienced have gotten me where I am today. Thank you.

TABLE OF CONTENTS

LIST OF FIGURES x

CHAPTER

1. Introduction 1

    1.1. Biological Applications 8

    1.2. Fluid Experiments 13

    1.3. Exact and Asymptotic Solutions for Precessing Spheroids 16

        1.3.1. Exact Solution for a Prolate Spheroid 18

        1.3.2. Asymptotic Solution for a Slender Prolate Spheroid 20

        1.3.3. Blakeslet Solution for a Slender Prolate Spheroid in a Semi-Infinite Fluid 22

2. Method of Regularized Stokeslets 23

    2.1. Stokes Equations 24

    2.2. Stokeslets and Other Singularities 25

        2.2.1. Stokeslets 26

        2.2.2. Point-Source Dipoles and Quadrupoles 27

        2.2.3. Stokes Doublets, Stresslets, and Rotlets 28

    2.3. Image Singularities 30

    2.4. Method of Regularized Stokeslets 32

        2.4.1. Regularized Stokeslets 33

        2.4.2. Regularized Dipoles and Quadrupoles 35

        2.4.3. Regularized Stokes Doublets, Stresslets, and Rotlets 36

    2.5. Regularized Image Singularities 37

2.6. Implementation 39

3. Slender Prolate Spheroids 41

3.1. Physical Setup 42

3.2. Quantifying Error 44

3.3. Varying the Spreading Parameter 49

3.4. Varying the Location of Boundary Conditions 61

3.4.1. Projected Boundary Condition 64

3.4.2. Helical Boundary Condition 65

3.5. Condition Number 69

3.6. Summary 71

4. Non-Slender Prolate Spheroids 73

4.1. Dependence of Exact Solution on Radius 76

4.2. Regularized Stokeslets on the Surface 77

4.3. Inset Regularized Stokeslets 81

4.3.1. Boundary Condition at Regularized Stokeslets 82

4.3.2. Boundary Condition at Exact Solution Radius 89

4.4. Condition Number 92

4.5. Summary 96

5. A Multi-rate Numerical Integrator for Regularized Stokeslets 99

5.1. Spectral Deferred Correction Method 102

5.2. Multi-Explicit Spectral Deferred Correction Method 105

5.2.1. Rigid Sphere Implementation 106

5.2.2. Multi-Explicit Spectral Deferred Correction Method 109

5.3. Numerical Tests 117

5.4. Summary 124

6. Rotational Mixing Experiments 127

6.1. Tilted rod 128

6.2. Bent rod 134

7. Summary 152

APPENDIX A: Nondimensionalization of the Navier-Stokes Equations 156

APPENDIX B: Derivation of Image Singularities for a Stokeslet 159

APPENDIX C: Derivation of a Regularized Stokeslet 162

APPENDIX D: Derivation of a Regularized Dipole 167

APPENDIX E: Derivation of a Regularized Rotlet 169

APPENDIX F: Derivation of Regularized Image Singularities for a Regularized Stokeslet 171

APPENDIX G: Centroidal Voronoi Tessellations 175

BIBLIOGRAPHY 177

LIST OF FIGURES

1.1. Cross-section of the human lung above the epithelial cells (not shown). This sketch shows a few representative cilia, the periciliary liquid (PCL) layer, the mucus layer, and the airway. 10

1.2. Simplification of primary nodal cilia motion. The rectangle at the bottom of the figure represents a cell in the nodal region. The slender rigid body precesses about its base in an upright conical configuration. 12

1.3. (a) Sketch of a non-slender prolate spheroid used in the exact free space solution. (b) Sketch of a slender prolate spheroid used in the free space asymptotic solution. (c) Sketch of a slender prolate spheroid precessing about its tip near a no-slip plane used in the Blakeslet solution. 17

2.1. The image singularities are placed at $\mathbf{y}_0$ for a Stokeslet located at $\mathbf{x}_0$ to create a no-slip plane at $x_3 = w$. The blue region ($x_3 > w$) represents the fluid domain. 31

2.2. Normalized cutoff functions $\hat{\phi}_\epsilon(r) = \frac{\phi_\epsilon(r)}{\phi_\epsilon(0)}$ and $\hat{\varphi}_\epsilon(r) = \frac{\varphi_\epsilon(r)}{\varphi_\epsilon(0)}$ used to create regularized singularities. 33

3.1. A slender spheroid precessing about its center in an infinite fluid. 42

3.2. Velocity error between the exact and slender asymptotic solutions averaged over the marker locations shown in Figure 3.3. The error is calculated with respect to a reference solution of the exact solution computed with many singularities. 47

3.3. Initial position of regularized Stokeslets and fluid markers where velocity is calculated. 50

3.4. Velocity error between the exact and regularized Stokeslet solutions ($|u(\mathbf{x}, \sigma) - \tilde{u}(\mathbf{x}, \epsilon, N)|$) averaged over the marker locations shown in Figure 3.3. The spreading parameter varies along the length of the body according to (3.17). Notice that the error is minimized for ϵ such that $\epsilon \approx 4.3\sigma$. 51

3.5. Alternate view of the velocity error between the exact and regularized Stokeslet solutions shown in Figure 3.4. 52

3.6. Spreading parameter versus singularity spacing that generate the local minima in velocity error from Figure 3.4 for a slender spheroid with tapered spreading parameters. 53

3.7. Velocity error between the exact and regularized Stokeslet solutions ($|u(\mathbf{x}, \sigma) - \tilde{u}(\mathbf{x}, \epsilon, N)|$) averaged over the marker locations shown in Figure 3.3. The spreading parameter is the same for each regularized Stokeslet comprising the spheroid, as in (3.18). 53

3.8. Spreading parameter versus singularity spacing that generate the local minima in velocity error from Figure 3.7 for a slender spheroid with constant spreading parameters. 55

3.9. Computed regularized Stokeslet strengths versus position along rod for the tapered and constant spreading parameter scenarios with $N = 50$ regularized Stokeslets, slenderness $\sigma = 0.01$, and spreading parameter $\epsilon = 0.01$. The dashed line represents the Stokeslet strengths from (1.12) used in the slender asymptotic solution. 56

3.10. Computed regularized Stokeslet strengths versus position along rod for (a) tapered and (b) constant spreading parameter scenarios with $N = 50$ regularized Stokeslets and slenderness $\sigma = 0.01$ for a variety of spreading parameters. The dashed line represents the Stokeslet strengths from (1.12) used in the slender asymptotic solution. 57

3.11. Error in initial velocity as a function of regularized Stokeslet spacing, h, for fixed slenderness $\sigma = 0.01$ when the boundary condition is imposed at the location of the regularized Stokeslets along the centerline. Each subplot has a fixed $q = \frac{h}{\epsilon}$ value and each data series has a fixed ζ value (defined in (3.19)). The dashed line represents the error from the solution with the singularity strength from the slender asymptotic solution ($\boldsymbol{\alpha}$) imposed on the regularized Stokeslets. 60

3.12. Error in initial velocity as a function of regularized Stokeslet spacing, h, for fixed $\zeta = 1$ when the boundary condition is evaluated at the location of the regularized Stokeslets. Each subplot has a fixed $q = \frac{h}{\epsilon}$ for a variety of slenderness parameters. 61

3.13. Three different methods for implementing the velocity boundary condition for a slender spheroid. The blue dots along the centerline represent the location of the regularized Stokeslets and the black ellipse represents the surface of the spheroid used in the exact solution. The red circles denote where the boundary condition is imposed in each of the three cases: (a) on the centerline, (b) on a projection of the centerline onto the surface, and (c) on curve that wraps around the surface of the spheroid in a helical fashion. 63

3.14. Error in initial velocity as a function of regularized Stokeslet spacing, h, for fixed slenderness $\sigma = 0.01$ when the boundary condition is imposed at the projection of the regularized Stokeslets onto the surface of the spheroid. Each subplot has a fixed $q = \frac{h}{\epsilon}$ value and each data series has a fixed ζ value (defined in (3.19)). The dashed line represents the error from the solution with the singularity strength from the slender asymptotic solution ($\boldsymbol{\alpha}$) imposed on the regularized Stokeslets. 65

3.15. Error in initial velocity as a function of regularized Stokeslet spacing, h, for fixed $\zeta = 1$ when the boundary condition is evaluated at the projection of

the regularized Stokeslets onto the surface of the spheroid. Each subplot has a fixed $q = \frac{h}{\epsilon}$ for a variety of slenderness parameters. 66

3.16. Error in initial velocity as a function of regularized Stokeslet spacing, h, for fixed slenderness $\sigma = 0.01$ when the boundary condition is imposed in a helical fashion on the surface of the spheroid. Each subplot has a fixed $q = \frac{h}{\epsilon}$ value and each data series has a fixed ζ value (defined in (3.19)). The dashed line represents the error from the solution with the singularity strength from the slender asymptotic solution ($\boldsymbol{\alpha}$) imposed on the regularized Stokeslets. 68

3.17. Error in initial velocity as a function of regularized Stokeslet spacing, h, for fixed $\zeta = 1$ when the boundary condition is evaluated in a helical fashion on the surface of the spheroid. Each subplot has a fixed $q = \frac{h}{\epsilon}$ for a variety of slenderness parameters. 69

3.18. Error in initial velocity as a function of regularized Stokeslet spacing, h, for fixed $\zeta = 1$ and $\sigma = 0.01$ with the boundary condition implemented three different ways (described at the beginning of Section 3.4). The dashed line represents the error from the solution with the singularity strength from the slender asymptotic solution ($\boldsymbol{\alpha}$) imposed on the regularized Stokeslets. 70

3.19. Condition number versus $\frac{\epsilon}{h}$ for $\sigma = 0.01$ with varying ϵ and N for the data shown in Figures 3.4 and 3.7. 71

4.1. A non-slender spheroid precessing about its center in an infinite fluid. 75

4.2. Initial position of tracer locations where velocity is calculated and an example of initial regularized Stokeslet placement. 77

4.3. Difference in velocity between the exact solution computed with a spheroid of radius $r = 0.8 + \gamma$ compared to the exact solution calculated with a spheroid of radius $r = 0.8$. 78

4.4. Initial velocity error between exact and regularized Stokeslet solutions versus singularity spacing for fixed $q = \frac{h}{\epsilon}$. The regularized Stokeslets are located at $r = 1$, the boundary condition is imposed at $r_{bc} = 1$, and the spheroid in the exact solution has $r_{exact} = 1$. Notice the convergence is linear suggesting the presence of an effective radius varying linearly with spreading parameter ϵ. 79

4.5. Initial velocity error between exact and regularized Stokeslet solutions versus singularity spacing for fixed spreading parameter. The regularized Stokeslets are located at $r = 1$, the boundary condition is imposed at $r_{bc} = 1$, and the spheroid in the exact solution has $r_{exact} = 1$. 80

4.6. Velocity error between exact and regularized Stokeslet solutions versus $q = \frac{h}{\epsilon}$ for fixed N. The regularized Stokeslets are located at $r = 1$, the boundary

condition is imposed at $r_{bc} = 1$, and the spheroid in the exact solution has $r_{exact} = 1$. 81

4.7. Velocity error between exact and regularized Stokeslet solutions versus h for fixed $q = 2.7$. The regularized Stokeslets are located at $r = 1$, the boundary condition is imposed at $r_{bc} = 1$, and the spheroid in the exact solution has $r_{exact} = 1$. 82

4.8. Visualization of regularized Stokeslets placed (a) on the surface of and (b) inset from the surface of the spheroid. The shading demonstrates how that the net effect of an arrangement of regularized Stokeslets may have a larger effective radius than that of their placement at r. The radius of the spheroid used in the exact solution is denoted r_{exact} and the radius of the spheroid where the regularized Stokeslets are placed is r. The slenderness parameter remains fixed. 83

4.9. Velocity error averaged over 14 fluid locations away from the precessing body generated by $N = 100$ regularized Stokeslets placed on a spheroid of radius r. 84

4.10. Velocity error averaged over 14 fluid locations away from the precessing body generated by $N = 400$ regularized Stokeslets placed on a spheroid of radius r. 85

4.11. Velocity error averaged over 14 fluid locations away from the precessing body generated by $N = 1000$ regularized Stokeslets placed on a spheroid of radius r. 85

4.12. Optimal radius as a function of the ratio of spreading parameter to singularity spacing for various values of N. The plotted lines $r_{opt} = a\frac{\epsilon}{h} + b$ are linear least squares fits of the data for each N. 86

4.13. Coefficients (a) a and (b) b plotted as a function of h from the linear fits in Figure 4.12. 86

4.14. Optimal radius as a function of regularized Stokeslet spacing for a non-slender spheroid. The regularized Stokeslets are inset at the optimal radius, $r_{opt} < r_{exact}$, as described in (4.4). 88

4.15. Velocity error averaged over 14 fluid locations away from the precessing body generated by 300 regularized Stokeslets placed on a spheroid of radius r for $r_{bc} = r_{exact} = 1$. 89

4.16. Velocity error at projected regularized Stokeslet locations on surface ($\mathbf{x}_{0,bc}$) versus radius of regularized Stokeslet placement r for $N = 300$. 91

4.17. Velocity error between neighboring projected regularized Stokeslet locations on surface ($\hat{\mathbf{x}}$) versus radius of regularized Stokeslet placement r for $N = 300$. 92

4.18. Condition number versus q for varying ϵ and r. 93

4.19. Condition number versus $q = \frac{h}{\epsilon}$ for N=300 regularized Stokeslets with (a) $r_{bc} = r$ and (b) $r_{bc} = r_{exact}$. 94

4.20. Condition number versus r for various ϵ with $r_{bc} = r_{exact}$. 95

4.21. Mean surface velocity error at $\mathbf{x}_{0,bc}$ versus r for various ϵ with $r_{bc} = r$. 96

4.22. Mean surface velocity error at $\hat{\mathbf{x}}$ versus r for various ϵ with $r_{bc} = r$. 97

4.23. Condition number versus r for N=300 regularized Stokeslets with (a) $r_{bc} = r$ and (b) $r_{bc} = r_{exact}$. 98

5.1. The ith time step $[t_i, t_{i+1}]$ is split into N_m substeps $[t_{i,m}, t_{i,m} + \Delta t_m]$, $m = 0, 1, \ldots, N_m - 1$ for use with the SDC Method. 104

5.2. A rigid rod precessing with a prescribed angular velocity generates fluid flow moving a rigid sphere that also interacts with the fluid. 106

5.3. Time step $[t_i, t_{i+1}]$ is split into substeps for the explicit rod piece $[t_{i,m}, t_{i,m} + \Delta t_m]$ and smaller substeps for the explicit sphere contribution $[t_{i,m,p}, t_{i,m,p} + \Delta t_p]$, where $\Delta t_p \leq \Delta t_m \leq \Delta t$. 112

5.4. Error in position versus time step using SDC and MESDC for a variety of n_{iter} values (number of correction iterations). Notice that the convergence rate increases as n_{iter} increases. Here $k = 8$ and $k_c = 0.8$. 119

5.5. Error in position versus time step using SDC and MESDC for a variety of n_{iter} values (number of correction iterations). Notice that the convergence rate increases as n_{iter} increases. Here $k = k_c = 0$. 121

5.6. Error in position versus time step using SDC and MESDC for a variety of spring constants with $n_{iter} = 5$. 122

5.7. Error in position versus effective time step using SDC and MESDC for a variety of spring constants with $n_{iter} = 5$. 123

5.8. Mean normalized displacement (η) of points on the sphere as a function of time. The horizontal lines represent the time averaged mean normalized displacement ($\bar{\eta}$). 125

5.9. Time averaged mean normalized displacement versus time step and spring constant. 125

6.1. Sketch of a slender rod precessing about an axis tilted off vertical by a tilt angle, τ, above a no-slip plane. 129

6.2. Side view of trajectories of nine initial conditions, fixed with respect to the cone that the rod sweeps through. The tilt angle varies from (a) $\tau = 0$ to (b) $\tau = \frac{\pi}{10}$ to (c) $\tau = \frac{\pi}{5}$. The initial positions are marked by green circles. Each trajectory is shown for 1000 rod rotations. Image produced in conjunction with Bouzarth *et. al.* (RMX group work in preparation) [**9**]. 131

6.3. Top view of trajectories of nine initial conditions, fixed with respect to the cone that the rod sweeps through. The tilt angle varies from (a) $\tau = 0$ to (b) $\tau = \frac{\pi}{10}$ to (c) $\tau = \frac{\pi}{5}$. The initial positions are marked by green circles. Each trajectory is shown for 1000 rod rotations. Image produced in conjunction with Bouzarth *et. al.* (RMX group work in preparation) [**9**]. . 132

6.4. A zoomed in top view of a portion of two trajectories from the $\tau = 0$ top view shown in Figure 6.3(a). This demonstrates the fine scale structure that is lost in the way the data is displayed in Figures 6.2 and 6.3. Image produced in conjunction with Bouzarth *et. al.* (RMX group work in preparation) [**9**]. 133

6.5. Radial position versus time measured in rod rotations for the nine markers depicted in Figures 6.2 and 6.3. The tilt angle varies from (a) $\tau = 0$ to (b) $\tau = \frac{\pi}{10}$ to (c) $\tau = \frac{\pi}{5}$. Image produced in conjunction with Bouzarth *et. al.* (RMX group work in preparation) [**9**]. 135

6.6. Vertical position versus time measured in rod rotations for the nine markers depicted in Figures 6.2 and 6.3. The tilt angle varies from (a) $\tau = 0$ to (b) $\tau = \frac{\pi}{10}$ to (c) $\tau = \frac{\pi}{5}$. Image produced in conjunction with Bouzarth *et. al.* (RMX group work in preparation) [**9**]. 136

6.7. Vertical position versus time measured in rod rotations for the nine markers depicted in Figures 6.2 and 6.3 over shorter time scales to show the epicycle structure. The tilt angle varies from (a) $\tau = 0$ to (b) $\tau = \frac{\pi}{10}$ to (c) $\tau = \frac{\pi}{5}$. Image produced in conjunction with Bouzarth *et. al.* (RMX group work in preparation) [**9**]. 137

6.8. Profile view of a bent pin used in RMX experiments. Image courtesy of Bouzarth *et. al.* (RMX group work in preparation) [**9**]. 139

6.9. Top and side views of representative time snapshots of a bent rod in the belly out configuration with scooping angle $\rho = 0$. Image produced in conjunction with Bouzarth *et. al.* (RMX group work in preparation) [**9**]. . 140

6.10. Top and side views of representative time snapshots of a bent rod in the scooping configuration with scooping angle $\rho = \frac{\pi}{2}$. The rod moves counterclockwise in the top view. Image produced in conjunction with Bouzarth *et. al.* (RMX group work in preparation) [**9**]. 140

6.11. Top and side views of representative time snapshots of a bent rod in the belly in configuration with scooping angle $\rho = \pi$. Image produced in conjunction with Bouzarth *et. al.* (RMX group work in preparation) [**9**]. 141

6.12. Top and side views of representative time snapshots of a bent rod in the slicing configuration with scooping angle $\rho = \frac{3\pi}{2}$. The rod moves counterclockwise in the top view. Image produced in conjunction with Bouzarth *et. al.* (RMX group work in preparation) [**9**]. 141

6.13. Side views of trajectories resulting from a scooping rod in (a) an experiment and (b) a regularized singularity simulation. The green circle denotes the starting position of the fluid particle and the red square denotes its final position some time later. The parameters are not exactly matched, so slight discrepancies exist, but the general structure is the same. The bottom of the each figure coincides with the no-slip plane. The contact point of the pin with the fluid tank floor is in the center of the bottom edge of each plot. In the simulation plot, the blue dots denote locations of the tip of the rod at different instances in time. Notice the vertical descent and radial fluctuation trends in both cases, which are not present for an analogous straight rod. Image produced in conjunction with Bouzarth *et. al.* (RMX group work in preparation) [**9**]. 142

6.14. Radial position versus time for a variety of scooping angles and a straight rod. Image produced in conjunction with Bouzarth *et. al.* (RMX group work in preparation) [**9**]. 144

6.15. Vertical position versus time for a variety of scooping angles and a straight rod. Image produced in conjunction with Bouzarth *et. al.* (RMX group work in preparation) [**9**]. 144

6.16. (a) A trajectory generated by a straight rod in 100 rotations. (b) A trajectory generated by a scooping bent rod in 100 rotations. (c) Same trajectory as (b) except for 1000 rod rotations. (d) Trajectory from (a) shown from the side in the body frame. (e) Trajectory from (c) shown from the side in the body frame. The initial and final positions are marked with a green circle and red square. In all plots, the initial positions are $(x, y, z) = (-0.25, 0, 1)$. Image produced in conjunction with Bouzarth *et. al.* (RMX group work in preparation) [**9**]. 146

6.17. (a) Three dimensional and (b) side views of a trajectory generated by a bent rod in the lab frame. (c) Three dimensional and (d) side views of the same trajectory viewed in the body frame. The initial and final positions are marked with a green circle and red square, respectively. In all plots, the initial position is $(x, y, z) = (-1, 0, 1)$. Image produced in conjunction with Bouzarth *et. al.* (RMX group work in preparation) [**9**]. 148

6.18. A slice through $y = 0$ in the body frame for 45 initial positions, marked by black squares. The blue regions of the plot denote where the tips of the bent

rod penetrate the plane. In this scooping configuration, the bend of the rod comes out of the page. Image produced in conjunction with Bouzarth *et. al.* (RMX group work in preparation) [**9**]. 149

6.19. A slice through $y = 0$ in the body frame for 45 initial positions, marked by black squares. The blue region of the plot denotes where the straight lies in the plane. Image produced in conjunction with Bouzarth *et. al.* (RMX group work in preparation) [**9**]. 149

6.20. A slice through $y = 0$ in the body frame for 45 initial positions, marked by black squares. The black curve denotes where the belly in bent rod lies in the plane for the $\rho = \pi$ case. Data is shown for four scooping angles, $\rho = \frac{\pi}{2}$, $\rho = \frac{3\pi}{4}$, $\rho = \frac{11\pi}{12}$ and $\rho = \pi$. Image produced in conjunction with Bouzarth *et. al.* (RMX group work in preparation) [**9**]. 150

0.1. Results of using Burkhardt's CCVT routine [**35**] to distribute 200 regularized Stokeslets on the surface of (a) a sphere and (b) a non-slender spheroid. 176

CHAPTER 1

Introduction

Fluid flow generated on small spatial scales is a topic of current computational, mathematical, and experimental research that extends beyond mathematics into many biological applications. Areas of active research include microorganism locomotion [**3, 19, 23, 24**] and feeding [**55**], pulmonary mucociliary transport [**32, 44, 47**], and left-right asymmetry development of internal organs in mammals [**14, 15, 34, 49, 50**]. The Virtual Lung Project at the University of North Carolina at Chapel Hill is an interdisciplinary research effort aimed at investigating many aspects of the human lung to develop an integrative model that can aid in the development and testing of treatments and cures of pulmonary diseases like cystic fibrosis [**5**]. One research focus within the Virtual Lung Project is the study of hydrodynamics of cilia, which is a fluid-structure interaction on a small spatial scale. This effort incorporates mathematical models [**10, 11, 42**], low Reynolds number fluid dynamics experiments on the micro- and macro-scales [**7, 37**], and the numerical solutions constructed in this dissertation along with the numerical simulation work of Mitran [**47**].

Incompressible fluid flow on small scales is governed by the Stokes equations, a simplification of the Navier-Stokes equations in the low Reynolds number regime. The Reynolds number is a dimensionless quantity that compares inertial and viscous forces. The small length scales of the biological flows in question contribute to the low Reynolds number

resulting in the fluid regime where viscous forces dominate inertial forces. The Stokes equations are a desirable simplification of the Navier-Stokes equations for many reasons. First, the Stokes equations are linear in fluid velocity, allowing for the construction of solutions by superimposing fundamental solutions. Second, solutions of the three dimensional Stokes equations can be found analytically. Third, the Stokes equations are easier to solve numerically than the full Navier-Stokes equations. These facts will be utilized frequently throughout this discussion to build numerical solutions to the Stokes equations that will be compared to analogous closed form exact solutions.

In general, the modeling of arbitrary fluid-structure interactions is difficult. However, Camassa *et. al.* and Leiterman [**10, 11, 42**] constructed closed form exact and asymptotic solutions for a useful simplified geometry: a precessing spheroid. The fluid flow generated by slender precessing spheroids in Stokes flow provides common ground for the mathematical models of Camassa *et. al.*, the fluid dynamics experiments of the Rotational Mixing Experiment (RMX) group, Bouzarth *et. al.* [**7, 8**], and the numerical solutions presented in this dissertation to coalesce. While these research findings developed out of the Virtual Lung Project, the physical scenario to which they are more closely related is that of primary nodal cilia rather than pulmonary cilia. Primary nodal cilia are more rigid than the whip-like motile cilia in the lung; primary nodal cilia beat in a conical fashion [**34**]. The motion of primary nodal cilia has been linked to the breaking of left-right symmetry in developing mammalian embryos [**34, 49, 50**]. Both pulmonary and primary nodal cilia are discussed in more detail in Section 1.1.

A common method to study cilia, flagella, or other immersed slender objects is to use singularity theory to relate forces and resulting fluid velocities [**16, 56, 57**]. Camassa *et. al.* and Leiterman developed exact and asymptotic closed form mathematical solutions

using singularity theory and slender body theory that describe the fluid flow generated by a precessing prolate spheroid in both infinite and semi-infinite fluids [**10, 11, 42**]. While these closed form representations of exact and asymptotic solutions are valuable to this research, they also have limitations. For instance, the exact closed form solution only applies to a prolate spheroid in free-space. However, as experiments develop and new questions arise, the need to model more complicated features increases. The study of the exact solution in relation to the numerical solution for the prolate spheroid provides the foundation for using the numerical solutions to develop asymptotic solutions and to model the experimental data.

The numerical solutions developed in this dissertation utilize the method of regularized Stokeslets, developed by Cortez [**18, 19**], and other regularized singularities to calculate the fluid flow due to a collection of nonsingular regularized forces. A collection of such forces can be used to represent a structure interacting with the fluid (*e.g.* a spirochete [**19**] or a spheroid). When using singular Stokeslets to model fluid flow, the Stokeslets must be placed outside of the fluid domain (*e.g.* along the centerline of a spheroid) to avoid infinite velocities at the locations of the imposed point forces. However, when nonsingular regularized forces are implemented with the method of regularized Stokeslets, this restriction no longer exists. The regularization process creates finite velocities at the location of the regularized forces. As such, the regularized Stokeslets may be placed anywhere within the fluid domain. This allows for more flexibility in the physical scenarios for which regularized singularities can be used but singularities cannot.

To model a cilium using regularized Stokeslets, there are choices regarding where to distribute the Stokeslets. For example, placing them on the surface of a slender rigid body as well as only along its centerline will be investigated in this work, showing how

these choices affect numerical error. Choosing to distribute the regularized Stokeslets along a curve rather than a surface in the slender body case provides a way to reduce the size of the system. Chapter 3 explores the case where a one dimensional line of regularized singularities is used to model a thin three dimensional structure. The effectiveness of different parameter and boundary condition choices with the method of regularized Stokeslets in relation to the exact mathematical solution of Camassa *et. al.* are discussed.

The exact mathematical solution of Camassa *et. al.* for the flow generated by a prolate spheroid precessing about its center in free space serves as a nontrivial exact solution to which the results of the numerical solutions discussed in this dissertation utilizing regularized singularities can be scrutinized. This provides the rare and desirable opportunity to study a current numerical method (the method of regularized Stokeslets) against a nontrivial exact solution. As such, careful error analysis is performed in Chapters 3 and 4 that reveals components of the error due to regularization, quadrature, body slenderness, and time integration. It is shown that the quadrature and time integration errors are negligible with respect to the regularization and slenderness errors. Hence, the regularization and slenderness errors will be a focus of the discussion in Chapters 3 and 4. Another benefit of having a nontrivial exact solution with which to compare the numerical solutions is that a careful study of the effects that parameter choice has on velocity error in the case of precessing rigid spheroids is possible. Again, this careful analysis is desired in a numerical method, but is often lacking due to the complexity of many of the systems modeled with current numerical methods such as the immersed boundary method [**24, 51**], the immersed interface method [**41, 43**], or the method of regularized Stokeslets before this study [**19**].

While studying slender spheroids is useful in biological applications involving cilia and flagella, studying non-slender spheroids numerically with regularized Stokeslets in comparison with the exact solution of Camassa *et. al.* is also beneficial. In the slender case discussed in Chapter 3, to reduce the number of regularized Stokeslets needed, regularized Stokeslets are placed only along the centerline of a slender spheroid to model the fluid velocity resulting from the spheroid's precessing motion. In contrast, when modeling a non-slender spheroid in Chapter 4, the regularized Stokeslets are initially placed on the surface of the spheroid, rather than its centerline. Placing regularized Stokeslets on the surface of the body is a somewhat intuitive and traditional step [**19**]. In fact, when regularized Stokeslets are placed distributed on the surface of a body, the method of regularized Stokeslets can be considered a discretized boundary integral method, or similarly a boundary element method [**19, 56**]. However, unlike with the boundary integral method, the method of regularized Stokeslets is still viable when the regularized forces are not distributed over a closed surface (*e.g.* distributing regularized Stokeslets along a line to model a slender spheroid). Thus, the method of regularized Stokeslets has an additional realm of physical scenarios that standard boundary integral methods can not accommodate.

Since regularized Stokeslets represent the exertion of regularized forces on a fluid, it seems like a natural beginning to exert the forces where the body contacts the fluid. However, further analysis of the numerical solution in contrast to the exact solution reveals that placing the regularized Stokeslets along a spheroidal surface slightly smaller and inset from the original spheroid produces smaller error. The effect of where the boundary conditions are enforced is also studied in both the slender and non-slender cases. It is shown in Chapters 3 and 4 that there are parameter and boundary condition

choices that minimize the velocity error in both the slender and non-slender cases. While these choices are somewhat sensitive to the specific geometry of a prolate spheroid, these findings can still be used as guidelines for parameter and boundary condition implementation in applications that are not as idealized as that used to compare the numerical and exact solutions in this work. Hence, the result of these studies generates guidelines for choosing numerical parameters in other situations.

One application where modeling a sphere with regularized Stokeslets is helpful is in determining what physically significant effects spherical tracer beads used in some RMX fluid dynamics experiments have on both the micro- and macro-scale results. This physical configuration is implemented in the numerical solution with an additional collection of regularized Stokeslets connected pairwise with virtual springs. Incorporating springs is a common technique utilized in modeling elastic and flexible structures immersed in fluid [**19, 22, 47**]. The error analysis of parameter and boundary condition choices for the non-slender spheroid discussed in Chapter 4 is used to choose parameters for the rigid sphere implementation. The introduction of spring forces into the numerical solution creates stiffness in the system of differential equations. Thus, in this work and other applications involving the temporal integration of localized stiff systems, an effective numerical integration technique is needed. A novel variation of spectral deferred correction methods [**27**], termed the *multi-explicit* spectral deferred correction (MESDC) method, is developed here and discussed in Chapter 5. This method integrates the fluid velocity in a stable, accurate, and efficient manner treating different parts of the physical system with different time steps. Specifically, the MESDC method uses a small time step for the stiff portion of the system pertaining to the spring forces of the sphere, and a larger time step for the remainder of the fluid calculations. One benefit of using the MESDC

method is that expensive linear solves can be executed less frequently than when using standard time integration techniques. The MESDC method is applicable to other classes of fluid-structure interactions, *e.g.* solving the Navier-Stokes equations with the Blob Projection Method [**20**].

While much attention is given to the comparison of the numerical solutions with the exact mathematical solution of Camassa *et. al.*, Chapter 6 discusses the results of two classes of RMX experiments in conjunction with the numerical results. The numerical solutions developed and tested in this dissertation are used to model and predict experimental results for which exact mathematical solutions do not exist. The two physical scenarios are a straight rod precessing about a tilted axis (rather than a vertical axis) and a bent rod precessing in different configurations. The tilted rod scenario more closely matches the biological application of the primary nodal cilia as they sweep out tilted cones, as discussed in Section 1.1. The numerical solution plays a critical role in both analyzing and predicting the results of the RMX experiment when a bent rod is used in place of a straight one. The results of modeling tilted and bent rods with regularized singularities are also used to help develop closed form asymptotic solutions that continue to incorporate more advanced features of the experimental design [**8**].

With the study of cilia in the context of the Virtual Lung Project as initial motivation, a collection of mathematical models, numerical solutions, and experimental results emerges that has a common ground in modeling a physical scenario of a slender rigid rod precessing in a conical fashion that mimics the motion of primary nodal cilia. This common ground provides a valuable benchmarking opportunity where closed form solutions, numerical simulations, and experimental results support, predict, and verify

each other. Developing numerical solutions that utilize regularized Stokeslets and multi-explicit spectral deferred correction methods in this environment provides the unique opportunity for careful error analysis and parameter studies for nontrivial fluid flows with an exact solution. The intuition and tools developed in the benchmarking process between the mathematical models, numerical solutions, and experiments greatly aid in adapting these methods to study more complicated physical systems that incorporate increasingly more features of the motivating biological problems.

This manuscript will discuss the aforementioned exact and asymptotic mathematical solutions, fluid dynamics experiments, and numerical solutions in the context of a precessing rigid body and the fluid flow it generates. The remainder of this chapter further introduces the motivating biological applications, the fluid dynamics experiments on both the micro- and macro-scales, and the closed form exact and asymptotic mathematical models. Chapter 2 discusses the fundamental fluid dynamics associated with this problem, specifically Stokeslets, regularized Stokeslets, and systems of image singularities (singular and regularized) that produce a no-slip plane. Chapters 3 and 4 discuss the numerical errors and parameter choices when modeling slender and non-slender spheroids, respectively, with regularized Stokeslets in reference to the exact solution. The multi-explicit spectral deferred correction method is developed in Chapter 5. Chapter 6 contains a discussion of the numerical solution in comparison with RMX experimental results and Chapter 7 presents conclusions and topics for future work.

1.1. Biological Applications

This section contains a brief introduction to two biological examples of cilia that are of particular interest in the current context; conventional motile cilia are discussed in the

context of mucus transport mechanisms in the human lung, followed by a discussion of primary nodal cilia in mammalian embryos. These examples provide motivating questions and applications of the closed form solution discussed in Section 1.3 and the numerical method discussed throughout the remaining chapters of this manuscript.

As mentioned above, one motivation for this research originates from the Virtual Lung Project at the University of North Carolina at Chapel Hill [**36**]. This is an interdisciplinary effort to study different components of the human lung that incorporates researchers from applied mathematics, physics, computer science, chemistry, biochemistry, biophysics, and the medical school's Cystic Fibrosis Center. The ultimate goal is to develop an integrated computational model to aid in developing and testing cures and treatments for cystic fibrosis. The research discussed here falls under one goal of the Virtual Lung Project: to understand the hydrodynamics of cilia.

Cilia are slender protrusions from cells that are ubiquitous in nature. Cilia can be classified into two main categories: conventional motile cilia and primary cilia. Conventional motile cilia are flexible, whip-like protrusions whereas primary cilia are more rigid and in most cases immotile. Cilia in the lung belong to the conventional motile cilia category. See [**30**] for a review of fluid mechanics research involving cilia and flagella.

The structure of the lung immediately surrounding the cilia can be described as follows. Cilia protrude from the epithelial cells that line the lung. Immediately above the epithelial cells, there is a liquid layer referred to as the periciliary liquid (PCL) layer that surrounds the cilia and supports a mucus layer resting atop the PCL layer. The PCL layer is more watery than the mucus layer, which is in contact with the air [**44**]. The mucus layer is responsible for trapping contaminants in the lung while the cilia try to expel the contaminant-ridden mucus from the lung to prevent infection. Figure 1.1

shows a simplification of the structure of the lung. The bottom of the figure corresponds to the top of the epithelial cells.

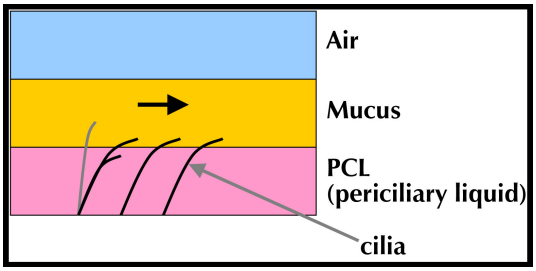

FIGURE 1.1. Cross-section of the human lung above the epithelial cells (not shown). This sketch shows a few representative cilia, the periciliary liquid (PCL) layer, the mucus layer, and the airway.

The cilia use a whip-like motion to agitate the surrounding fluid in the PCL layer and ultimately transport the mucus out of the lung (see *e.g.* [**44**]). The cycle is broken up into two strokes, the recovery stroke and the power stroke. The cilium moves quickly during the power stroke in an effort to propel the PCL and mucus layers and returns to its original position during the recovery stroke. It is not fully understood how neighboring cilia coordinate their beat to collectively move mucus. In recent work, Mitran presents a three dimensional numerical study of cilia which suggests the coordination develops when cilia interact only with the surrounding fluid. The beat patterns are coordinated in such a way that a metachronal wave is created at the top of the cilia layer. Mitran presents a three dimensional numerical model of the formation of metachronal waves [**47**]. Modeling the hydrodynamics of this situation will give researchers insight into how the cilia coordinate their beat and create this metachronal wave.

Investigating the hydrodynamics of pulmonary cilia and other biological factors will help researchers learn more about cystic fibrosis and other pulmonary and cilia-related

diseases. One cause of infection occurs when mucus and contaminants cannot be transported out of the lung in a timely manner. The failure of timely contaminant clearance could be due to a number of factors, such as defective or absent pulmonary cilia, a change of the viscoelastic properties of the mucus layer, or a reduction in the volume of the PCL layer. Cystic fibrosis depletes the PCL layer and changes the properties of the mucus layer making the mucus thicker and more viscous than in the healthy case [**5**]. These changes increase the likelihood of serious infections in cystic fibrosis patients due to the reduced contaminant clearance out of the lung. It is not completely known how the mechanisms regulating mucus clearance relate. As such, current research investigating regulation of the PCL volume, mucus properties, and cilia interactions in a variety of experiments, mathematical models, and numerical simulations is a central focus of the Virtual Lung Project and the pulmonary health community at large.

Besides pulmonary diseases like cystic fibrosis, where cilia are involved in a breakdown of pulmonary function, other health problems can manifest as a result of dysfunctional cilia. For instance, Kartagener's syndrome bears the symptoms of chronic sinusitis, bronchiectasis, and *situs inversus* [**60**]. While these symptoms can all be explained by immotile cilia, Afzelius discovered the connection between immotile cilia and *situs inversus* [**1**]. *Situs inversus* refers to the condition where one's internal organs are located on the opposite side of his or her body, *e.g.* the heart is on the right side rather than the left. Nonaka *et. al.* found evidence that the motion of primary nodal cilia is the first point where left-right symmetry is broken in mammalian embryonic development [**34, 49, 50**].

In contrast to conventional motile cilia, primary cilia are more rigid, more sparsely packed, and move differently. Where primary cilia are present, there is only one cilium

per cell. Many researchers believed that primary cilia are immotile and either serve no function or act as mechanical sensors [**60**]. However, Nonaka *et. al.* discovered primary cilia that were motile in the nodal region of developing embryos [**49**]. The nodal region is a ciliated pit on an embryo. Each cell in this pit has a single cilium on it that precesses in a conical fashion. That is, each cilium is affixed to the cell at its base but its tip is sweeping out a circle. Figure 1.2 displays a simplified version of this motion for one cilium (see [**34**] for additional visual descriptions of this motion in the nodal region).

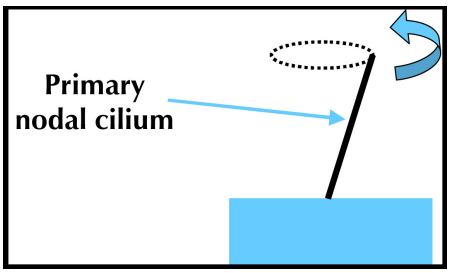

FIGURE 1.2. Simplification of primary nodal cilia motion. The rectangle at the bottom of the figure represents a cell in the nodal region. The slender rigid body precesses about its base in an upright conical configuration.

As Hirokawa *et. al.* suggest, the primary nodal cilia do not precess about a vertical axis, rather an axis that tilts toward the posterior. This is due to the fact that they are not attached at the center of each curved cell, rather their base is located on the posterior side. As such, the curvature of the cell generates a posterior tilt and a leftward flow is generated in the nodal region. This flow is believed to be the earliest point where the development of the left-right asymmetry in mammals [**34**]. Modeling the hydrodynamics of primary nodal cilia will begin with the simplification shown in Figure 1.2. This represents a slender rigid body sweeping out a vertical in the Stokes regime. One tip of the rod is in contact with a plane and the other tip sweeps out a circle. In the mathematical and numerical solutions the plane is an infinite no-slip plane whereas

in the RMX fluid experiments, the plane represents the bottom surface of the fluid tank. The discussion in Section 6.1 incorporates a tilted axis of precession in the numerical solution to more closely represent the motion of primary nodal cilia.

Gaining insight into the two cilia applications mentioned here, beating whip-like conventional motile cilia in the lung and conically precessing primary nodal cilia in developing embryos, serves as a motivating factor in studying the motion of precessing rods with experiments, mathematical models, as well as numerical simulation.

1.2. Fluid Experiments

This section will introduce the fluid dynamics laboratory experiments that are used in conjunction with the closed form asymptotic solutions of Camassa *et. al.* [**10, 42**] and numerical solutions described in this work as both motivation for and validation of different aspects of this research. The experiments that are discussed here mimic the motion of primary nodal cilia. Two classes of experiments are discussed; both have the common element of a slender rigid body precessing about its tip, which is affixed to a no-slip plane. The first class of experiments discussed studies this motion on the micro-scale. The second looks at variations of this motion on a larger spatial scale, keeping the same Reynolds number[1] and hydrodynamic characteristics.

Research collaborators at the University of North Carolina at Chapel Hill are involved in a variety of experiments that serve as a link between mathematical modeling and biological applications. In one study of hydrodynamics on the cilia, Jing [**37**] fabricates magnetic rods that measure approximately $10\mu m$ in length and $200nm$ in diameter. He uses a three dimensional force microscope (3DFM) developed by Fisher *et. al.* [**31**]

[1]See Section 2.1 for a discussion of Reynolds number.

to manipulate the small rods so that they precess in a conical fashion, mimicking the motion of primary nodal cilia. The resulting fluid motion is tracked by following the location of micron-sized tracer beads from digitized movies. This work is compared with the mathematical models of Camassa *et. al.* and Leiterman in an effort to determine if macro-scale boundary conditions are appropriate to consider on this small length scale. The experimental results show evidence of an epicyclic orbit whose period is roughly commensurate with that of the precessing rod as well as a larger orbit about the rod on a longer time scale. Bouzarth *et. al.* compare micro-scale trajectories with predictions of the model of Camassa *et. al.* and Leiterman [**7, 11, 42**]. While the model captures some characteristics of the experimental trajectory, like the epicyclic period and radial amplitude, there is some discrepancy between the model and experiment and motivation for further study.

While the microfluidic research of Jing accomplishes many things, its shortcomings in comparison with the mathematical theory contributed to the development of another laboratory research project, the Rotational Mixing Experiment (RMX). Due to the fact that Jing's experiments are performed on the micro-scale, it is difficult to determine if discrepancies between the mathematical models of Camassa *et. al.* and the experimental trajectories are due to confounding experimental factors or limitations of the model. Since the experiment is performed on such a small scale, the effects from thermal fluctuations and Brownian motion are noticeable. Secondly, since the diameter of the rod is smaller than the wavelength of visible light, it is difficult to obtain a clear image depicting the rod's geometry with the cameras used to visualize the experimental results. Finally, due to the experimental design using the 3DFM, images are only collected from the top of the experiment. As such, vertical position information cannot be extracted from the

experimental data. These three limitations can be eliminated by considering experiments on a larger spatial scale.

To try to eliminate these concerns with the micro-scale experiment, dynamic similarity is used as an argument for scaling up the experiment to a size where the design eliminates the three aforementioned concerns. The idea behind dynamic similarity is that the hydrodynamic behavior will be similar for situations with similar flow geometry. That is, flows with the same Reynolds numbers will exhibit the same behavior. Jing's experiments are run in a low Reynolds number regime. By keeping a similar low Reynolds number in the larger scale RMX experiments, they capture the same hydrodynamic effects and gain better insight into the agreement of the experiment and mathematical theory by eliminated the concerns of noticeable thermal fluctuations, visualization problems, and limited view points for data collection.

The first RMX experiments started with a magnetic rod in Karo corn syrup driven by a motor-mounted magnet. With this setup, the rod undergoes the same motion as in Jing's experiment, a conical precession about a vertical axis, but the pin and fluid environment are larger (the pin length does not exceed $1cm$). In both the micro- and macro-scale experiments the Reynolds number does not exceed 10^{-3}. The macro-scale RMX experiments provide cleaner data sets than the micro-scale experiment with which the mathematical theory can be compared. Bouzarth *et. al.* demonstrate that the mathematical solutions of Camassa *et. al.* and Leiterman capture the characteristics of the RMX experimental trajectories [**7**]. In an interdisciplinary effort, the research of the RMX group shows that the asymptotic models of Camassa *et. al.* and Leiterman agree well with both the micro- and macro-scale experiments [**7**]. However, questions arise that extend beyond the realm of the analytical solution, making a numerical simulation

of the experiment that can be applied to a more general physical configuration desirable. For instance, how do the trajectories change when the geometry of the rod changes to something other than a spheroid or straight rod precessing about a vertical axis? The introduction of a tilted axis of precession and a bent rod will be discussed as two examples for which an exact solution does not exist, but the numerical solutions discussed in this dissertation provide valuable insight. The experiments and results of the RMX project in conjunction with the numerical results discussed in this work will be explored further in Chapter 6.

1.3. Exact and Asymptotic Solutions for Precessing Spheroids

As mentioned above, the mathematical solutions by Camassa *et. al.* and Leiterman [**10, 11, 42**], play an important role in the development of the numerical solution that utilizes regularized singularities. In terms of the larger picture of trying to gain some global understanding of biologically motivated fluid dynamics phenomena, the closed form solutions of Camassa *et. al.* provide exact and asymptotic mathematical models. In terms of this study of numerical methods, certain incantations of the mathematical models will provide a non-trivial exact solution with which the numerical results can be compared.

The work of Camassa *et. al.* and Leiterman uses singularity theory and slender body theory to construct solutions to the Stokes equations for the flow generated by a precessing spheroid. There are three different solutions that will be referred to throughout this manuscript:

(1) An exact solution for a prolate spheroid

(2) An asymptotic solution for a slender prolate spheroid

(3) An asymptotic solution for a slender prolate spheroid in the presence of a no-slip plane (referred to as the Blakeslet solution).

Figure 1.3 depicts the three spheroid scenarios used in the exact and asymptotic closed form theoretical solutions. In Figures 1.3(a) and 1.3(b), the spheroid precesses about its center and in Figure 1.3(c) the spheroid precesses about its tip. The first two solutions are constructed in an infinite fluid in free space, so the only boundary conditions imposed are on the surface of the spheroidal body. In the third case, there is an additional no-slip boundary condition imposed on the plane perpendicular to the axis of precession at the base of the rod. In all three cases, the spheroid is precessing about a vertical axis with a constant angular velocity.

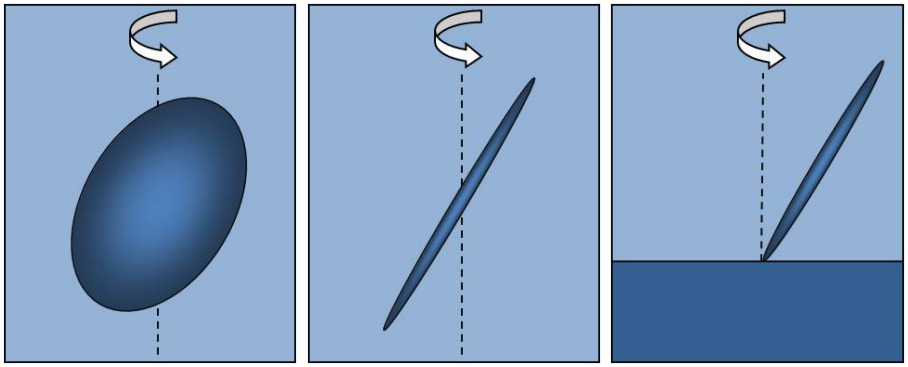

(a) (b) (c)

FIGURE 1.3. (a) Sketch of a non-slender prolate spheroid used in the exact free space solution. (b) Sketch of a slender prolate spheroid used in the free space asymptotic solution. (c) Sketch of a slender prolate spheroid precessing about its tip near a no-slip plane used in the Blakeslet solution.

Each of these solutions is useful in different ways. The exact solution is beneficial because it is an exact closed-form solution to the Stokes equations for an arbitrary prolate spheroid precessing about its center. Comparing the numerical results against this

solution provides a two-fold benefit. First, it allows the method of regularized Stokeslets to be tested against a non-trivial exact solution. Second, it provides insight pertaining to the construction of physical objects within the numerical model that are spherical or non-slender in nature. While this deviates from the slender body focus of the cilia application, there are benefits in the experimental and numerical comparisons to studying non-slender bodies that will be discussed further in Section 5.2.1.

The asymptotic solution is beneficial to study because its slender body more closely resembles that of a cilium or the rods used in the micro- and macro-scale fluid dynamics experiments introduced in Section 1.2. The slender asymptotic solution also has the added benefit that the solution is simpler; it only utilizes Stokeslets while the exact solution contains a collection of singularities. Cortez's method of regularized Stokeslets [**18, 19**] similarly builds solutions only using regularized Stokeslets and will be invoked frequently. Stokeslets and regularized Stokeslets are introduced in Sections 2.2 and 2.4, respectively.

The third solution, referred to as the Blakeslet solution in [**11, 42**], is the most useful when comparing with experimental results. This is due to the presence of the no-slip plane in the asymptotic solution that represents the floor of the fluid tank where the experiments are conducted.

1.3.1. Exact Solution for a Prolate Spheroid. This section explores the details of the exact closed form solution of Camassa *et. al.* and Leiterman [**11, 42**] for a prolate spheroid precessing about its center in free space (see Figure 1.3(a)). The exact solution for a prolate spheroid precessing about its center in Stokes flow is an integral of three types of singularities placed along the centerline of the spheroid between its foci.

Throughout this discussion, the *centerline* refers to the major axis of the spheroid. The singularities in the exact solution include stresslets, rotlets, and point-source dipoles, which are introduced in Section 2.2. Consider the equation of a prolate spheroid:

$$\frac{x^2}{a^2} + \frac{y^2 + z^2}{b^2} = 1 \tag{1.1}$$

for $a > b$. Recall the equation to determine the distance from the center to either focus: $c = \sqrt{a^2 - b^2}$. The eccentricity is then defined as

$$e = \frac{c}{a}. \tag{1.2}$$

While c and e appear in the equations for the solutions discussed in this section, a parameter that will be more widely used throughout this manuscript will be the slenderness parameter, σ. Define the slenderness parameter as the ratio of the spheroid's diameter to its length, which can also be expressed in terms of the semi-major and semi-minor axes of the spheroid, a and b:

$$\sigma = \frac{b}{a}. \tag{1.3}$$

In the body frame, where the rod is fixed and the fluid rotates around it, Camassa *et. al.* show the velocity at a point $\mathbf{x}$ is given by:

$$\begin{aligned} \mathbf{u}(\mathbf{x}) \;=\; & R_\kappa^T \mathbf{U}(R_\kappa \mathbf{x}) + \\ & \dot{\omega}\sin(\kappa)\int_{-c}^{c}(c^2 - s^2)\left[\alpha \mathbf{u}_{SS}(\mathbf{x} - s;\mathbf{e}_x,\mathbf{e}_y) + \tilde{\gamma}_1 \mathbf{u}_R(\mathbf{x} - s;\mathbf{e}_z)\right] ds + \\ & \dot{\omega}\beta\sin(\kappa)\int_{-c}^{c}(c^2 - s^2)^2 \frac{\partial}{\partial y}\mathbf{u}_D(\mathbf{x} - s;\mathbf{e}_x) ds + \\ & \dot{\omega}\tilde{\gamma}_2\cos(\kappa)\int_{-c}^{c}(c^2 - s^2)\mathbf{u}_R(\mathbf{x} - s;\mathbf{e}_x) ds, \end{aligned} \tag{1.4}$$

where $\mathbf{u}_{SS}$, $\mathbf{u}_R$, and $\mathbf{u}_D$ are the velocities due to a stresslet, rotlet, and point-source dipole, respectively, and

$$\tilde{\gamma}_1 = \frac{2-e^2}{-2e+(1+e^2)\ln\left(\frac{1+e}{1-e}\right)} \tag{1.5}$$

$$\tilde{\gamma}_2 = \frac{1-e^2}{2e-(1-e^2)\ln\left(\frac{1+e}{1-e}\right)} \tag{1.6}$$

$$\alpha = \frac{e^2}{-2e+(1+e^2)\ln\left(\frac{1+e}{1-e}\right)} \tag{1.7}$$

$$\beta = \frac{1-e^2}{4\left(-2e+(1+e^2)\ln\left(\frac{1+e}{1-e}\right)\right)} \tag{1.8}$$

are constants where e is the spheroid's eccentricity, as given in (1.2) [**11, 42**]. Expressions for $\mathbf{u}_{SS}$, $\mathbf{u}_D$, and $\mathbf{u}_R$ are given in Section 2.2. Notationally in (1.4), the singularities are located at s with strengths given by the unit vectors denoted after the semicolon in each velocity function argument. To obtain the velocity in the lab frame, one must change variables from $\mathbf{x}$ in the body frame to $\mathbf{x}^*$ in the lab frame, where $\mathbf{x}^* = R_\omega R_\kappa \mathbf{x}$:

$$\mathbf{u}^*(\mathbf{x}^*) = -\mathbf{U}(\mathbf{x}^*) + R_\omega R_\kappa \mathbf{u}(R_\kappa^T R_\omega^T \mathbf{x}^*) \tag{1.9}$$

R_κ and R_ω are rotation matrices about the y and z axes, respectively, that adjust for the tilt of the rod and its rotation in time. The integrals in (1.4) all have closed form solutions, as shown in [**42**].

The exact solution for a prolate spheroid precessing about its center in free space is used in comparison with numerical results to study the behavior of the velocity error in Chapters 3 and 4.

1.3.2. Asymptotic Solution for a Slender Prolate Spheroid. This section discusses the details of the solution of Camassa *et. al.* that uses singularity theory and slender body theory to model a slender spheroid precessing about its center in free space.

The slender asymptotic free space solution only utilizes Stokeslets rather than a collection of singularities as in the exact solution discussed in the previous section. Leiterman finds the velocity at $\mathbf{x}$ due to a distribution of Stokeslets along the centerline of the rod of length $2L$ is

$$\mathbf{u}(\mathbf{x}) = \int_{-L}^{L} \mathbf{u}_S(\mathbf{x} - \mathbf{x}_S(s); \boldsymbol{\alpha}) ds. \tag{1.10}$$

where $\mathbf{x}_S(s) = (s\sin(\kappa), 0, s\cos(\kappa))$, $s \in [-L, L]$, κ represents the cone angle, and $\mathbf{u}_S$ represents a Stokeslet of strength $\boldsymbol{\alpha}$ that will be introduced in Section 2.2 [**42**]. Here the cone angle κ is the acute angle measured from the z-axis to the centerline of the spheroid. Throughout this manuscript, the complement of κ may also be referred to as the cone angle. When this occurs, it will be labeled as θ, such that $\kappa + \theta = \frac{\pi}{2}$ and θ represents the angle from the xy-plane to the centerline of the spheroid. The asymptotic slender free space solution prescribes the singularity strength as

$$\boldsymbol{\alpha}(s) = (0, \alpha s, 0), \tag{1.11}$$

where s parameterizes the length of the body and

$$\alpha = \frac{\omega\beta\sin(\kappa)}{2}. \tag{1.12}$$

By choosing $\boldsymbol{\alpha}$ from (1.12), the velocity solution has errors of order $\beta = \left[\log\left(\frac{2}{\sigma}\right)\right]^{-1}$. Provided that $\sigma \ll 1$ and $L \pm s \gg r$

$$\mathbf{u}_{exact} = \mathbf{u} + O(\beta), \tag{1.13}$$

where $\mathbf{u}_{exact}$ denotes the exact solution from Section 1.3.1 and $\mathbf{u}$ represents the velocity due to the distribution of Stokeslets in (1.10). This demonstrates the magnitude of the error that arises from representing a slender body with only Stokeslets in the slender

asymptotic solution rather than stresslets, quadrupoles, and rotlets, as in the exact solution. This error will be discussed further in Section 3.2, where the numerical error is dissected into its different error components, one of which is the slenderness error discussed here.

1.3.3. Blakeslet Solution for a Slender Prolate Spheroid in a Semi-Infinite Fluid. The Blakeslet solution uses the slender asymptotic solution discussed in Section 1.3.2 as well as a system of image singularities to construct a Stokes flow solution which matches a no-slip boundary condition on the surface of the spheroid as well as a plane. The Blakeslet solution models a slender rod precessing about its tip rather than its center, as shown in Figure 1.3(c). This solution includes a no-slip plane that models the floor of a fluid tank, making this solution useful when comparing mathematical results with laboratory results. Besides Stokeslets, the system of image singularities includes point-source dipoles and Stokes doublets. These singularities are introduced in Section 2.2 and the construction of the image singularities are discussed in Section 2.3 in more detail. In [**42**], Leiterman compares an RMX experimental trajectory with both the exact free space solution (from Section 1.3.1) and the Blakeslet solution described in this section and finds that the Blakeslet solution is more accurate than the exact free space solution in capturing the trajectory characteristics of the experiment.

CHAPTER 2

Method of Regularized Stokeslets

While the study of fluids is a robust area of mathematical and experimental research, there are areas where recent developments contribute to the knowledge base in fundamental ways. The study of Newtonian fluids at low Reynolds numbers is an established field dating back decades. The singularity theory invoked in the mathematical models of Camassa *et. al.* and Leiterman [**10, 11, 42**], discussed in Section 1.3, has also been in circulation for quite some time with many works in the 1970's using singularity methods [**4, 16**]. However, newer methods like the method of regularized Stokeslets, developed in the past decade by Cortez [**18, 19**], provide new tools to construct solutions to the Stokes equations. This dissertation also develops other regularized singularities in addition to those implemented in the method of regularized Stokeslets.

This chapter discusses how concepts of fluid dynamics are utilized in the singularity theory of the closed form solutions of Section 1.3. It also shows how to regularize the singularities and use the method of regularized Stokeslets to build solutions to the Stokes equations. In both the singular and regularized cases, the image singularities required to satisfy a no-slip boundary condition on a plane bounding a semi-infinite fluid are introduced. A section is devoted to exploring how regularized singularities are implemented to model precessing rod problems and beyond. Sections 2.2 and 2.3 present fundamental

solutions based on singularities; Sections 2.4 and 2.5 present the same concepts, but the derived quantities rely on regularized singularities rather than singular expressions.

2.1. Stokes Equations

This section discusses the governing equations of Newtonian fluid dynamics and the assumptions necessary to study the quasi-steady Stokes regime. The equations governing incompressible Newtonian fluid motion are the incompressible Navier-Stokes equations:

$$\rho\frac{\partial \mathbf{u}}{\partial t} + \rho\mathbf{u}\cdot\nabla\mathbf{u} = -\nabla p + \mathbf{F} + \mu\nabla^2\mathbf{u} \tag{2.1}$$

$$\nabla\cdot\mathbf{u} = 0, \tag{2.2}$$

where $\mathbf{u}$ is the fluid velocity, ρ is the fluid density, μ is the dynamic viscosity, p is the pressure, and $\mathbf{F} = \rho\mathbf{g}$ is the body force. It is assumed throughout this manuscript that the density and viscosity remain constant and uniform throughout the fluid. By considering dimensionless variables, one can nondimensionalize (2.1). Let

$$\hat{\mathbf{u}} = \frac{\mathbf{u}}{\mathcal{U}}, \quad \hat{\mathbf{x}} = \frac{\mathbf{x}}{\mathcal{L}}, \quad \hat{t} = \frac{t}{\mathcal{T}}, \quad \hat{p} = \frac{p\mathcal{L}}{\mu\mathcal{U}}, \quad \hat{\mathbf{g}} = \frac{\mathbf{g}}{g}, \tag{2.3}$$

where $\mathcal{U}$ represents a characteristic velocity, $\mathcal{L}$ a characteristic length, $\mathcal{T}$ a characteristic time scale, and g is the gravitational constant [**57**]. The details of the nondimensionalization are shown in Appendix A. The nondimensionalized Navier-Stokes equations become

$$\beta\frac{\partial \hat{\mathbf{u}}}{\partial \hat{t}} + Re\hat{\mathbf{u}}\cdot\hat{\nabla}\hat{\mathbf{u}} = -\hat{\nabla}\hat{p} + \hat{\nabla}^2\hat{\mathbf{u}} + \frac{Re}{Fr^2}\hat{\mathbf{g}}, \tag{2.4}$$

where $\beta = \frac{\mathcal{L}^2}{\nu \mathcal{T}}$ is the unsteadiness parameter,[1] $Re = \frac{\mathcal{U}\mathcal{L}}{\nu}$ is the Reynolds number, $Fr = \frac{\mathcal{U}}{\sqrt{g\mathcal{L}}}$ is the Froude number, and $\nu = \frac{\mu}{\rho}$ is the kinematic viscosity. When $\beta \ll 1$ and $Re \ll 1$, the time derivative and the nonlinear velocity term become negligible with respect to the terms on the right hand side of (2.4). As shown in Appendix A, in this limit, the Navier-Stokes equations become the quasi-steady incompressible Stokes equations:

$$\mu \nabla^2 \mathbf{u} = \nabla p - \mathbf{F} \tag{2.5}$$

$$\nabla \cdot \mathbf{u} = 0. \tag{2.6}$$

Under these assumptions, viscous forces dominate inertial forces. The absence of the time derivative in the Stokes equations does not necessarily imply that the velocity is constant with respect to time, rather the forces applied to the fluid, which may vary in time, are in a state of dynamic equilibrium.

2.2. Stokeslets and Other Singularities

The numerical comparisons discussed in this work rely heavily on the exact and asymptotic solutions of Camassa *et. al.* and Leiterman [**10, 11, 42**] as a basis for careful numerical error analysis. This section reviews the singularities that contribute to the exact, asymptotic, and Blakeslet solutions discussed in Section 1.3. This section will define singularities that produce fundamental solutions of the Stokes equations. Specifically, Stokeslets will be introduced in addition to the other singularities used in the exact and Blakeslet solutions discussed in Sections 1.3.1 and 1.3.3.

[1] In [**57**], β is used as the coefficient of the time derivative. This quantity can also be expressed as the product of the Reynolds and Strouhal numbers. The Strouhal number $St = \frac{\omega \mathcal{L}}{\nu}$ is a measure of the oscillatory nature of the flow, where ω is the frequency associated with the flow.

2.2.1. Stokeslets. The linearity of the Stokes equations allows solutions of (2.5) and (2.6) to be constructed by a linear combination of fundamental solutions. Consider applying a point force to the fluid at some location $\mathbf{x}_0$. That is, $\mathbf{F} = \mathbf{f}\delta(\mathbf{x} - \mathbf{x}_0)$, where δ represents the Dirac delta function and $\mathbf{f}$ describes the direction and magnitude of the force. The Stokeslet[2] is a fundamental solution to the singularly forced Stokes equations:

$$\mu\Delta\mathbf{u} = \nabla p - \mathbf{f}\delta(\hat{\mathbf{x}}) \tag{2.7}$$

$$\nabla \cdot \mathbf{u} = 0. \tag{2.8}$$

The velocity at $\mathbf{x}$ due to a Stokeslet of strength $\mathbf{f}$ located at $\mathbf{x}_0$ is

$$\mathbf{u}^S(\mathbf{x}) = \frac{\mathbf{f}}{r} + \frac{\hat{\mathbf{x}}(\hat{\mathbf{x}} \cdot \mathbf{f})}{r^3}, \tag{2.9}$$

where $\hat{\mathbf{x}} = \mathbf{x} - \mathbf{x}_0$ and $r = |\hat{\mathbf{x}}|$. Using Einstein summation notation,[3] the Stokeslet can be represented as

$$S_{ij} = \frac{\delta_{ij}}{r} + \frac{\hat{x}_i \hat{x}_j}{r^3}, \tag{2.10}$$

and the velocity at $\mathbf{x}$ due to a singular force $\mathbf{f}$ located at $\mathbf{x}_0$ can be represented as [**56, 57**]

$$u_i^S = \frac{1}{8\pi\mu} S_{ij} f_j. \tag{2.11}$$

This form of the velocity will be used frequently throughout the remainder of this discussion.

Other solutions to the Stokes equations can be formulated from derivatives of fundamental solutions. As mentioned in Section 1.3.1, the exact free space solution for a

[2]The Stokeslet is also referred to as the Oseen-Burgers tensor [**56**].

[3]Depending on the circumstances, either (x_1, x_2, x_3) or (x, y, z) may be used to refer to the components of a position vector $\mathbf{x}$.

prolate spheroid precessing about its center requires point-source dipoles, stresslets, and rotlets, which are introduced in Sections 2.2.2 and 2.2.3.

2.2.2. Point-Source Dipoles and Quadrupoles. A point source is an fundamental solution for irrotational incompressible flow, derived as a solution of the singularly forced Laplace equation:

$$\nabla^2\Phi = m\delta(\hat{\mathbf{x}}), \tag{2.12}$$

where Φ is a scalar velocity potential and m is the strength of the point source. In three dimensions,

$$\Phi = -\frac{m}{4\pi r}, \tag{2.13}$$

and the fluid velocity due to a point source is [**57**]

$$u_i = \frac{\partial\Phi}{\partial x_i} \tag{2.14}$$

$$= \frac{m\hat{x}_i}{4\pi r^3}. \tag{2.15}$$

A point-source dipole[4] results from differentiating a point source with respect to its singular point:

$$D_{ij} = \frac{\partial S_i}{\partial x_{0,j}} = \frac{\partial}{\partial x_{0,j}}\left(\frac{\hat{x}_i}{r^3}\right) = -\frac{\delta_{ij}}{r^3} + 3\frac{\hat{x}_i\hat{x}_j}{r^5}, \tag{2.16}$$

where S_i is a point source. The velocity due to a point-source dipole is

$$u_i^D = \frac{1}{4\pi}D_{ij}d_j, \tag{2.17}$$

[4]Also referred to as a potential dipole in [**57**].

where $\mathbf{d} = (d_1, d_2, d_3)$ is the point-source dipole strength [**56**]. Upon inspection of (1.4), one may notice that the point-source dipole appears within a spatial derivative. As such, consider a derivative of the point-source dipole, which will be referred to as a quadrupole.

The quadrupole is the derivative of a point-source dipole with respect to $\mathbf{x}_0$:

$$Q_{ijk} = \frac{\partial D_{ij}}{\partial x_{0,k}} \tag{2.18}$$

$$= \frac{\partial}{\partial x_{0,k}} \left(-\frac{\delta_{ij}}{r^3} + 3\frac{\hat{x}_i \hat{x}_j}{r^5} \right) \tag{2.19}$$

$$= \frac{-3(\delta_{ij}\hat{x}_k + \delta_{ik}\hat{x}_j + \delta_{jk}\hat{x}_i)}{r^5} + \frac{15\hat{x}_i\hat{x}_j\hat{x}_k}{r^7}. \tag{2.20}$$

As such, the velocity induced by a quadrupole is:

$$u_i^Q = \frac{1}{4\pi} Q_{ijk} \alpha_j \beta_k, \tag{2.21}$$

where $\boldsymbol{\alpha}$ is the strength of the dipole and $\boldsymbol{\beta}$ is a constant [**56**]. The remaining singularities used in the exact solution are derived from the Stokes doublet.

2.2.3. Stokes Doublets, Stresslets, and Rotlets. The Stokes doublet[5] is found by differentiating a Stokeslet with respect to its location $\mathbf{x}_0$:

$$SD_{ijk} = \frac{\partial S_{ij}}{\partial x_{0,k}} \tag{2.22}$$

$$= \frac{\partial}{\partial x_{0,k}} \left(\frac{\delta_{ij}}{r} + \frac{\hat{x}_i \hat{x}_j}{r^3} \right) \tag{2.23}$$

$$= \frac{\delta_{ij}\hat{x}_k - \delta_{ik}\hat{x}_j - \delta_{jk}\hat{x}_i}{r^3} + 3\frac{\hat{x}_i\hat{x}_j\hat{x}_k}{r^5}. \tag{2.24}$$

The velocity due to a Stokes doublet is

$$u_i^{SD} = \frac{1}{8\pi\mu} SD_{ijk} \alpha_j \beta_k, \tag{2.25}$$

[5] Also referred to as a point-force dipole in [**57**].

where $\boldsymbol{\alpha}$ and $\boldsymbol{\beta}$ are singularity strength coefficients, with $\boldsymbol{\alpha}$ being the strength of the Stokeslet [**56**].

The stresslet and rotlet are derived as the symmetric and anti-symmetric parts of the Stokes doublet, respectively. A rotlet is the rotational analog to a Stokeslet. That is, a rotlet calculates the fluid velocity resulting from a point torque exerted on the fluid. Define the stresslet[6] SS_{ijk}, and the rotlet, R_{ijk} as

$$SS_{ijk} = \frac{1}{2}\left(SD_{ijk} + SD_{ikj}\right) \tag{2.26}$$

$$= \frac{-\delta_{jk}\hat{x}_i}{r^3} + \frac{3\hat{x}_i\hat{x}_j\hat{x}_k}{r^5} \tag{2.27}$$

$$R_{ijk} = \frac{1}{2}\left(SD_{ijk} - SD_{ikj}\right) \tag{2.28}$$

$$= \frac{\delta_{ij}\hat{x}_k - \delta_{ik}\hat{x}_j}{r^3}. \tag{2.29}$$

Then, the velocity due to the stresslet and rotlet, respectively, are [**42, 56**]:

$$u_i^{SS} = \frac{1}{8\pi\mu} SS_{ijk}\alpha_j\beta_k \tag{2.30}$$

$$u_i^{R} = \frac{1}{8\pi\mu} R_{ijk}\alpha_j\beta_k. \tag{2.31}$$

Since the Stokes equations are linear, the superposition of fundamental solutions also represents a solution. This fact is exploited in building the solutions discussed here. The quadrupole, stresslet, and rotlet singularities discussed in this section are used to build an exact solution, but the slender asymptotic solution only uses the Stokeslets that were introduced in Section 2.2.1. This solution is the starting point for building the system of image singularities used in the Blakeslet solution discussed in Section 1.3.3.

[6] In [**57**], the stresslet is defined as the symmetric part of the Stokes doublet without the point source term. In [**42**] (which cites [**16**]), the stresslet is defined as the symmetric part of the Stokes doublet. In this discussion, the latter definition will be used to remain analogous to the derivation of the theoretical solution.

2.3. Image Singularities

This section discusses constructing solutions to the Stokes equations for a semi-infinite fluid. That is, it will be shown how singularities are strategically placed outside of a semi-infinite fluid domain to create a no-slip boundary condition on the plane bounding the fluid.

Models incorporating the no-slip plane more closely match experimental results than free space solutions due to the proximity of the fluid tank floor to the rod. In [**42**], Leiterman demonstrates that the Blakeslet solution captures the behavior of the fluid better than the exact free space solution with respect to an RMX experiment with a straight slender rod.

Singularities will be placed outside of the fluid domain that will analytically satisfy the no-slip boundary condition on the plane. For each Stokeslet in the fluid domain, a Stokeslet, Stokes doublet, and point-source dipole will be placed at the image location to create the desired boundary conditions [**4, 42**]. This system is duplicated for each Stokeslet placed in the fluid.

Let $\mathbf{x}_0$ be the location of the Stokeslet located in the flow domain, and let $\mathbf{y}_0$ be the location of the image singularities outside of the fluid domain, as shown in figure 2.1. If the location of the wall is at $x_3 = w$, then $\mathbf{y}_0 = (x_{0,1}, x_{0,2}, 2w - x_{0,3})$ for $\mathbf{x}_0 = (x_{0,1}, x_{0,2}, x_{0,3})$. Consider $\mathbf{x}$ on the wall, such that $\mathbf{x} = (x_1, x_2, w)$. Let $r = |\mathbf{x} - \mathbf{x}_0| = |\mathbf{x} - \mathbf{y}_0|$. The goal is to come up with a combination of singularities whose net velocity evaluates to zero for $\mathbf{x} = (x_1, x_2, w)$. As calculated in Appendix B, the combination of velocities that satisfies the desired boundary condition is:

$$u_i = u_i^S - u_i^{S*} + 2h(2\delta_{i3} - 1)\left(u_i^{SD*} - \frac{h}{2}u_i^{D*}\right), \tag{2.32}$$

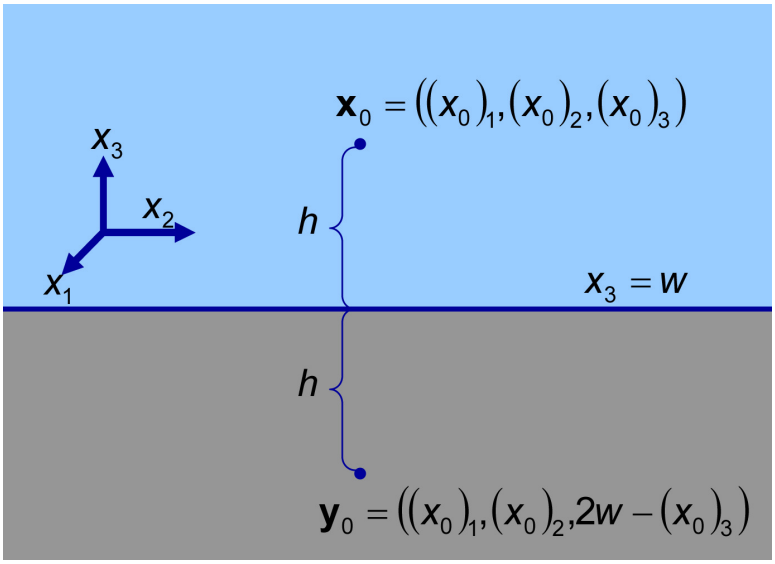

FIGURE 2.1. The image singularities are placed at $\mathbf{y}_0$ for a Stokeslet located at $\mathbf{x}_0$ to create a no-slip plane at $x_3 = w$. The blue region ($x_3 > w$) represents the fluid domain.

where u_i^S is the original Stokeslet placed in the fluid at $\mathbf{x}_0$ and the remaining singularities are placed at $\mathbf{y}_0$ outside of the fluid domain (denoted by asterisks) and $h = x_{0,3} - w$. Equations (2.11), (2.17), and (2.25) give the velocities due to the Stokeslet, point-source dipole, and Stokes doublet, respectively, that are used in (2.32).

The singularities discussed in this section are singular expressions, so the fluid velocity cannot be evaluated at the location of any of these singularities. In addition, dealing with singularities numerically is undesirable in the implementation of the numerical solution because the singular nature of the velocity fields can lead to ill-conditioned matrices. Cortez proposed the method of regularized Stokeslets, a numerical method that uses regularized forces rather than singular forces to find the fluid velocity [**18, 19**]. This concept will be used extensively in building numerical models of precessing rods in this dissertation.

2.4. Method of Regularized Stokeslets

The method of regularized Stokeslets, developed by Cortez [**18, 19**], calculates the fluid velocity in Stokes flow due to a collection of regularized forces. Cutoff functions are introduced as a way to regularize a point force. Since the regularization removes the singular nature from the velocity field, the velocity can be evaluated at the location of a regularized Stokeslet. That is, $\mathbf{u}(\mathbf{x}_0)$ is finite, whereas $\mathbf{u}(\mathbf{x}_0)$ is infinite for a Stokeslet or other singularities, as discussed in Section 2.2. This small difference between the velocity generated by a regularized Stokeslet versus a Stokeslet is fundamental to the method of regularized Stokeslets. Now there is a linear relationship between a force anywhere in space and a velocity anywhere in space. By utilizing the linearity of Stokes flow, one can superimpose the regularized Stokeslets solutions to build more complicated solutions.

Instead of representing the point force with a delta function, consider regularizing the forces using a radially symmetric cutoff function, ϕ_ϵ. It is assumed that the cutoff function is a smooth approximation to the delta function that satisfies

$$\int \phi_\epsilon(\mathbf{x}) d\mathbf{x} = 1 \tag{2.33}$$

$$lim_{\epsilon \to 0} \phi_\epsilon(\mathbf{x}) = \delta(\mathbf{x}), \tag{2.34}$$

where ϵ is the spreading parameter that controls the extent of the distribution. This discussion will primarily use the cutoff function

$$\phi_\epsilon(r) = \frac{15\epsilon^4}{8\pi(r^2+\epsilon^2)^{7/2}}, \tag{2.35}$$

where $r = |\mathbf{x} - \mathbf{x}_0|$ [**18**]. Depending on the demands of a particular application, it may be advantageous to choose a different cutoff function that satisfies the aforementioned

properties listed in (2.33) – (2.34). For instance, the calculation of the system of regularized image singularities to create a no-slip plane presented in Section 2.5 will require regularized singularities that are derived from a second cutoff function, φ_ϵ [**17**]:

$$\varphi_\epsilon(r) = \frac{6\epsilon^2}{8\pi(r^2+\epsilon^2)^{5/2}}. \tag{2.36}$$

Figure 2.2 displays the normalized cutoff functions $\hat{\phi}_\epsilon(r) = \frac{\phi_\epsilon(r)}{\phi_\epsilon(0)}$ and $\hat{\varphi}_\epsilon(r) = \frac{\varphi_\epsilon(r)}{\varphi_\epsilon(0)}$.

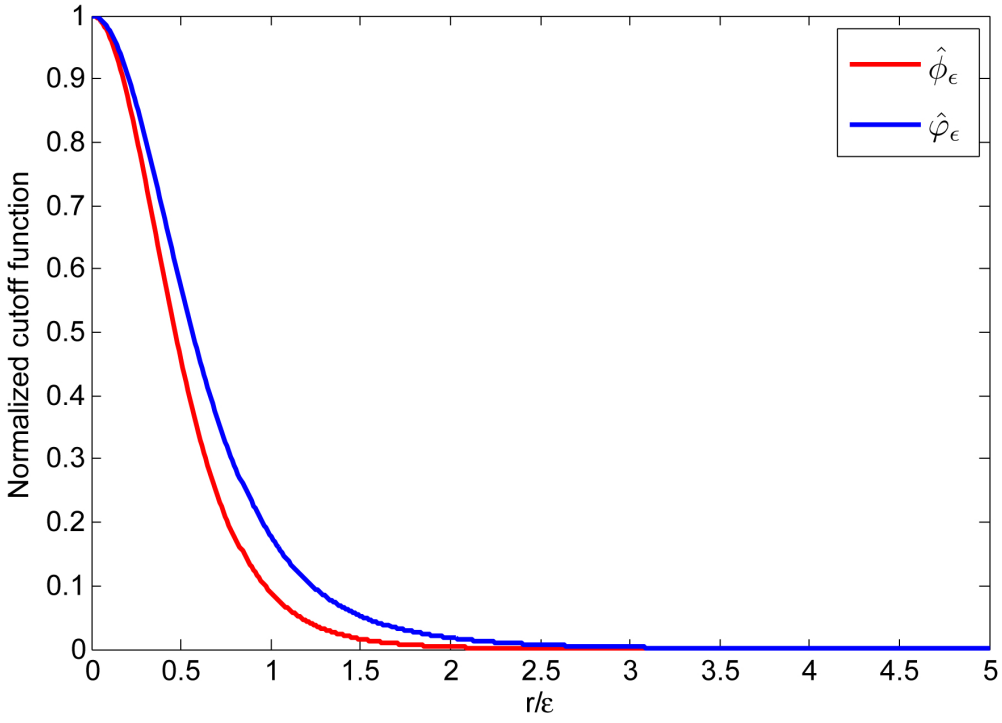

FIGURE 2.2. Normalized cutoff functions $\hat{\phi}_\epsilon(r) = \frac{\phi_\epsilon(r)}{\phi_\epsilon(0)}$ and $\hat{\varphi}_\epsilon(r) = \frac{\varphi_\epsilon(r)}{\varphi_\epsilon(0)}$ used to create regularized singularities.

2.4.1. Regularized Stokeslets. Rather than solving the singularly forced Stokes equations as in previous sections, consider solving the Stokes equations with a regularized

forcing term at $\mathbf{x}_0$, again with $\hat{\mathbf{x}} = \mathbf{x} - \mathbf{x}_0$:

$$\mu\Delta\mathbf{u} = \nabla p - \mathbf{f}\phi_\epsilon(\hat{\mathbf{x}}) \tag{2.37}$$

$$\nabla \cdot \mathbf{u} = 0. \tag{2.38}$$

In an analogous manner to previous sections, one can represent a solution to (2.37) – (2.38) with a regularized Stokeslet constructed from the cutoff function ϕ_ϵ [**19**]:

$$S_{ij}^{\phi_\epsilon} = \delta_{ij}\frac{r^2 + 2\epsilon^2}{(r^2+\epsilon^2)^{3/2}} + \frac{\hat{x}_i\hat{x}_j}{(r^2+\epsilon^2)^{3/2}}. \tag{2.39}$$

Notice that in the limit as $\epsilon \to 0$, one recovers the expression for the Stokeslet, given in (2.10):

$$\lim_{\epsilon\to 0} S_{ij}^{\phi_\epsilon} = \frac{\delta_{ij}}{r} + \frac{\hat{x}_i\hat{x}_j}{r^3} = S_{ij}. \tag{2.40}$$

The velocity due to a regularized point force can be represented as

$$u_i^{S,\phi_\epsilon}(\mathbf{x}) = \frac{1}{8\pi\mu} S_{ij}^{\phi_\epsilon} f_j, \tag{2.41}$$

where $S_{ij}^{\phi_\epsilon}$ is the regularized Stokeslet derived from the cutoff function ϕ_ϵ. Appendix C contains a detailed derivation of the regularized Stokeslet.

Equation (2.41) provides a way to calculate the velocity at a location $\mathbf{x}$ due to a regularized point force located at $\mathbf{x}_0$. Now, consider calculating the velocity at a point $\mathbf{x}$ due to a collection of N regularized Stokeslets located at $\mathbf{x}_n$:

$$u_i^{S,\phi_\epsilon}(\mathbf{x}) = \frac{1}{8\pi\mu}\sum_{n=1}^{N} S_{ij}^{\phi_\epsilon}(\mathbf{x}-\mathbf{x}_n) f_{j,n}. \tag{2.42}$$

To calculate the fluid velocity at M locations due to N regularized Stokeslets, this relationship can be expressed in matrix form:

$$\mathbf{u}(\mathbf{x}) = S^{\phi_\epsilon}(\mathbf{x}, \mathbf{x}_0)\mathbf{f}, \tag{2.43}$$

where $\mathbf{u}$ is a $3M \times 1$ vector containing the velocity components at the locations $\mathbf{x}$ ($3M \times 1$), $\mathbf{x}_0$ is a $3N \times 1$ vector of regularized Stokeslet locations, $\mathbf{f}$ is a $3N \times 1$ vector of force coefficients, and S^{ϕ_ϵ} is a $3M \times 3N$ matrix incorporating the regularized Stokeslet information. When $M = N$, the matrix S^{ϕ_ϵ} can be inverted to compute the forces necessary to satisfy a given velocity boundary condition. This is the basis of the method of regularized Stokeslets. Besides regularized Stokeslets, one can also develop analogous regularized singularities to those discussed in Section 2.2 to be used in the system of regularized image singularities and also in a an effort to regularize the exact solution.

2.4.2. Regularized Dipoles and Quadrupoles. The details of the regularized dipole derivation are shown in Appendix F. A regularized point-source dipole using the cutoff function φ_ϵ is

$$D_{ij}^{\varphi_\epsilon} = -\frac{\delta_{ij}}{(r^2+\epsilon^2)^{3/2}} + \frac{3\epsilon^2\delta_{ij}}{(r^2+\epsilon^2)^{5/2}} + \frac{3\hat{x}_i\hat{x}_j}{(r^2+\epsilon^2)^{5/2}}. \tag{2.44}$$

The velocity resulting from such a regularized dipole is

$$u_i^{D,\varphi_\epsilon} = \frac{1}{4\pi\mu} D_{ij}^{\varphi_\epsilon} d_j, \tag{2.45}$$

where $\mathbf{d} = (d_1, d_2, d_3)$ is the dipole strength [**17**]. Again, as in the singular case, the regularized quadrupole is obtained by differentiating the regularized dipole with respect

to its location:

$$Q_{ijk}^{\varphi_\epsilon} = \frac{\partial D_{ij}^{\varphi_\epsilon}}{\partial x_{0,k}} \tag{2.46}$$

$$= \frac{\partial}{\partial x_{0,k}}\left(-\frac{\delta_{ij}}{(r^2+\epsilon^2)^{3/2}} + \frac{3\epsilon^2\delta_{ij}}{(r^2+\epsilon^2)^{5/2}} + \frac{3\hat{x}_i\hat{x}_j}{(r^2+\epsilon^2)^{5/2}}\right) \tag{2.47}$$

$$= -\frac{3\hat{x}_k\delta_{ij}}{(r^2+\epsilon^2)^{5/2}} - \frac{3\hat{x}_i\delta_{jk}}{(r^2+\epsilon^2)^{5/2}} - \frac{3\hat{x}_j\delta_{ik}}{(r^2+\epsilon^2)^{5/2}} + \frac{15\epsilon^2\hat{x}_h\delta_{ij}}{(r^2+\epsilon^2)^{7/2}}$$

$$+\frac{15\hat{x}_i\hat{x}_j\hat{x}_k}{(r^2+\epsilon^2)^{7/2}}. \tag{2.48}$$

The velocity produced by a regularized quadrupole is given by

$$u_i^{Q,\varphi_\epsilon} = \frac{1}{4\pi\mu}Q_{ijk}^{\varphi_\epsilon}\alpha_j\beta_k. \tag{2.49}$$

The remaining regularized singularities necessary to construct regularized versions of the exact and Blakeslet solutions, regularized stresslets and rotlets, are derived from a regularized Stokes doublet, as discussed in Section 2.4.3.

2.4.3. Regularized Stokes Doublets, Stresslets, and Rotlets. To find the expression for the regularized Stokes doublet, differentiate a regularized Stokeslet with respect to its location. The regularized Stokes doublet will utilize ϕ_ϵ as its cutoff function:

$$SD_{ijk}^{\phi_\epsilon} = \frac{\partial S_{ij}^{\phi_\epsilon}}{\partial x_{0,k}} \tag{2.50}$$

$$= \frac{\partial}{\partial x_{0,k}}\left(\delta_{ij}\frac{r^2+2\epsilon^2}{(r^2+\epsilon^2)^{3/2}} + \frac{\hat{x}_i\hat{x}_j}{(r^2+\epsilon^2)^{3/2}}\right) \tag{2.51}$$

$$= \frac{\hat{x}_k\delta_{ij}}{(r^2+\epsilon^2)^{3/2}} - \frac{\hat{x}_i\delta_{jk}}{(r^2+\epsilon^2)^{3/2}} - \frac{\hat{x}_j\delta_{ik}}{(r^2+\epsilon^2)^{3/2}} + \frac{3\epsilon^2\hat{x}_k\delta_{ij}}{(r^2+\epsilon^2)^{5/2}}$$

$$+\frac{3\hat{x}_i\hat{x}_j\hat{x}_k}{(r^2+\epsilon^2)^{5/2}}. \tag{2.52}$$

The velocity produced by a regularized Stokes doublet is

$$u_i^{SD,\phi_\epsilon} = \frac{1}{8\pi\mu}SD_{ij}^{\phi_\epsilon}\alpha_j\beta_k, \tag{2.53}$$

where $\boldsymbol{\alpha}$ and $\boldsymbol{\beta}$ are strength coefficients [**17**]. Again, the regularized stresslet and the regularized rotlet are derived from the symmetric and anti-symmetric parts, respectively, of the regularized doublet:

$$SS_{ijk}^{\phi_\epsilon} = \frac{1}{2}\left(SD_{ijk}^{\phi_\epsilon} + SD_{ikj}^{\phi_\epsilon}\right) \tag{2.54}$$

$$= -\frac{\hat{x}_i\delta_{jk}}{(r^2+\epsilon^2)^{3/2}} + \frac{3\epsilon^2\hat{x}_k\delta_{ij}}{2(r^2+\epsilon^2)^{5/2}} + \frac{3\epsilon^2\hat{x}_j\delta ik}{2(r^2+\epsilon^2)^{5/2}} + \frac{3\hat{x}_i\hat{x}_j\hat{x}_k}{(r^2+\epsilon^2)^{5/2}} \tag{2.55}$$

$$R_{ijk}^{\phi_\epsilon} = \frac{1}{2}\left(SD_{ijk}^{\phi_\epsilon} - SD_{ikj}^{\phi_\epsilon}\right) \tag{2.56}$$

$$= \frac{\hat{x}_i\delta_{ij}}{(r^2+\epsilon^2)^{3/2}} - \frac{\hat{x}_j\delta_{ik}}{(r^2+\epsilon^2)^{3/2}} + \frac{3\epsilon^2\hat{x}_k\delta_{ij}}{2(r^2+\epsilon^2)^{5/2}} - \frac{3\epsilon^2\hat{x}_j\delta_{ik}}{2(r^2+\epsilon^2)^{5/2}}. \tag{2.57}$$

The velocity due to a regularized stresslet is

$$u_i^{SS,\phi_\epsilon} = \frac{1}{8\pi\mu} SS_{ijk}^{\phi_\epsilon}\alpha_j\beta_k, \tag{2.58}$$

and the velocity due to a regularized point torque (rotlet) is given by [**17**]

$$u_i^{R,\phi_\epsilon} = \frac{1}{8\pi\mu} R_{ijk}^{\phi_\epsilon}\alpha_j\beta_k. \tag{2.59}$$

The calculation in Section 2.5 will also require a regularized rotlet derived from φ_ϵ, which is derived in Appendix E.

Now that the framework is set to find the velocity due to a variety of regularized singularities, Section 2.5 will discuss how to implement a no-slip plane using a system of regularized image singularities.

2.5. Regularized Image Singularities

Analogous to developing the image singularities used in the Blakeslet solution in Section 2.3, this section will discuss how to implement a system of regularized image singularities, first formulated by Cortez [**18**]. Again, the goal is to create a no-slip

boundary condition on a plane at $x_3 = w$. The setup is similar to that described in Section 2.3. Consider a regularized Stokeslet in the flow domain at $\mathbf{x}_0 = (x_{0,1}, x_{0,2}, x_{0,3})$. The image singularities will be placed at $\mathbf{y}_0 = (x_{0,1}, x_{0,2}, 2w - x_{0,3})$, which is outside of the physical fluid domain of interest (see Figure 2.1). Let $\mathbf{x} = (x_1, x_2, w)$ be an arbitrary point on the no-slip plane and let r represent the distance from that point to the locations of the regularized Stokeslet and the images, $r = |\mathbf{x} - \mathbf{x}_0| = |\mathbf{x} - \mathbf{y}_0|$. Notationally, let $\hat{\mathbf{x}} = \mathbf{x} - \mathbf{y}_0$.

As done previously in Section 2.3, start the collection of regularized image singularities with a regularized Stokeslet at $\mathbf{x}_0$ and a regularize Stokeslet, dipole, and doublet at $\mathbf{y}_0$ (denoted by asterisks):

$$u_{net} = u^{S,\phi_\epsilon} - u^{S,\phi_\epsilon *} + 2h\left(u^{SD,\varphi_\epsilon *} - \frac{h}{2}u^{D,\phi_\epsilon *}\right)(2\delta_{i3} - 1) \tag{2.60}$$

$$= \frac{1}{8\pi\mu}\left[\frac{6\epsilon^2 x_j h \delta_{i3}}{(r^2+\varepsilon^2)^{5/2}} - \frac{6\epsilon^2 h^2 \delta_{ij}}{(r^2+\varepsilon^2)^{5/2}}\right] f_j, \tag{2.61}$$

where $h = x_{0,3} - w$. The calculation details of the system of regularized image singularities are shown in Appendix F. As shown in (2.61), there are two non-zero terms remaining. Thus, the system of regularized singularities requires more components than the system built in Section 2.3. Specifically, including rotlets produced from both ϕ_ϵ and φ_ϵ will eliminate the extra terms in (2.61). Appendix F contains the details involved with calculating the desired combination of regularized image singularities.

The appropriate combination of regularized image singularities to create a no-slip plane at $z = w$ is [**17**]:

$$\begin{aligned} u_i = {} & u_i^{S,\phi_\epsilon} - u_i^{S,\phi_\epsilon *} - 2h\,(1 - 2\delta_{i3})\left(u_i^{SD,\phi_\epsilon *} - \frac{h}{2}u_i^{D,\varphi_\epsilon *}\right) \\ & + (1 - 2\delta_{i3})\left(u_i^{R,\phi_\epsilon *} - u_i^{R,\varphi_\epsilon *}\right). \end{aligned} \tag{2.62}$$

The velocity due to this collection of regularized singularities can be expressed in a linear fashion, similar to (2.41):

$$u_i(\mathbf{x}) = \frac{1}{8\pi\mu} M_{ij}(\mathbf{x}, \mathbf{x}_0) f_j. \tag{2.63}$$

Here M_{ij} contains the collective singularity information for the entire system of image singularities. This will provide for the same implementation as the solution using only regularized Stokeslets in free space, but with a different matrix.

2.6. Implementation

The mathematical relationship between forces and velocity in (2.43) and (2.63) is used extensively in the models discussed in this manuscript. Consider using regularized Stokeslets to model a rigid rod precessing with a prescribed angular velocity. Regularized Stokeslets will be placed in the fluid to mimic the precessing rod. The manner of distributing the regularized Stokeslets to represent a rod varies depending on whether one is trying to model a slender or non-slender spheroid. This will be discussed further in Chapters 3 and 4. Regardless, since the velocity is known at any point on the rod, the linear relationship can be used to solve for the forces required to satisfy the velocity at the specified locations on the rod. Consider $\mathbf{u}(\mathbf{x}) = A(\mathbf{x}, \mathbf{x}_0)\mathbf{f}$, where A is a matrix containing regularized singularity information. For example, $A = S_{ij}^{\phi_\epsilon}$ from (2.43) when modeling a rod in free space or $A = M_{ij}$ from (2.63) when implementing a no-slip plane. The force is:

$$\mathbf{f} = \left[S^{\phi_\epsilon}(\mathbf{x}_{rod}, \mathbf{x}_{rod})\right]^{-1} \mathbf{u}(\mathbf{x}_{rod}), \tag{2.64}$$

where $\mathbf{x}_{rod}$ is a $3N \times 1$ vector containing the locations of N regularized Stokeslets on the rod. This matrix is not always invertible, as Cortez discusses in [**19**]. The condition

number of this matrix will be discussed further in Sections 3.5 and 4.4. In the models discussed in the coming chapters, the general minimal residual method (GMRES) [**21, 58**] is used to solve for $\mathbf{f}$ in (2.64).

Once the forces for the regularized Stokeslets on the rod to satisfy the rod boundary condition are known, they can be used to calculate the fluid velocity anywhere in the fluid:

$$\mathbf{u}(\mathbf{x}) = S^{\phi_\epsilon}(\mathbf{x}, \mathbf{x}_0)\mathbf{f}. \tag{2.65}$$

Thus, the regularized singularity information is used to solve for both the forces on the rod to satisfy the desired boundary condition and the fluid velocity anywhere in the fluid domain. The calculation in (2.65) to evaluate the fluid velocity at M locations due to N regularized forces is $O(NM)$ at each time step, as S^{ϕ_ϵ} is dense. As such, when the system becomes large, the inversion of the matrix becomes expensive. Similarly, implementing an efficient temporal integration method such as the multi-explicit spectral deferred correction method discussed in Chapter 5 is advantageous because it reduces the number of expensive dense linear system solves without a significant reduction in temporal accuracy. It may be desirable to implement fast summation techniques, e.g. the Fast Mulitpole Method [**33**] which is $O(N + M)$, because this calculation is done in each iteration of the GMRES method. Exploring this calculation in a more efficient manner is a topic of future consideration.

CHAPTER 3

Slender Prolate Spheroids

This chapter discusses the accuracy of using regularized singularities to model the velocity generated by a slender spheroid precessing about its center. The different components of the velocity error relating to regularization, quadrature, and slenderness will be emphasized throughout this chapter. A consideration of the condition number of the matrix relating fluid velocity with imposed regularized forces is also included. One benefit of studying the numerical simulation built with regularized singularities with respect to the exact closed form mathematical solution of Camassa *et. al.* and Leiterman [**11, 42**] is to carefully study how the parameters of the computational model affect the error between the two solutions.

With any numerical model, a complete picture of parameter choices and their relation to numerical error with respect to an exact solution is desired. However, with many current numerical methods, exact mathematical models are lacking for nontrivial problems. As such, the work presented in this dissertation utilizes the exact mathematical solution of Camassa *et. al.* in comparison with the numerical model built with the method of regularized Stokeslets to perform careful error analysis on a nontrivial flow problem. Conducting a careful study of the relationship between the model parameters and the error develops a sense of the best way to model a given situation. In other words, given a physical situation one wants to model using regularized singularities, what is a good

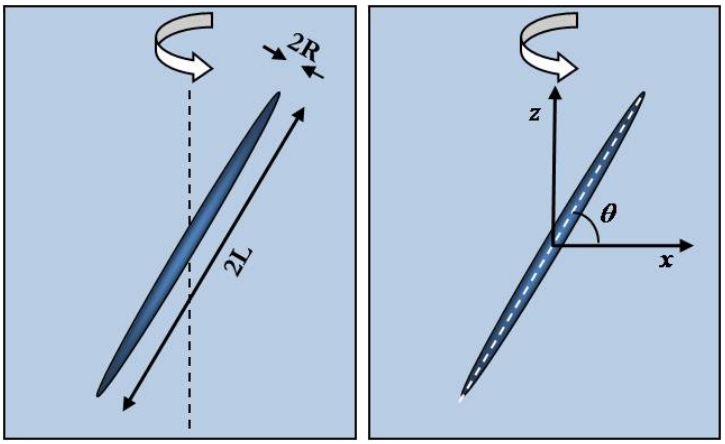

(a) (b)

FIGURE 3.1. A slender spheroid precessing about its center in an infinite fluid.

distribution of singularities? Where should they be placed? How should the singularity strengths be chosen? Where should boundary conditions be imposed? This chapter explores these questions in the context of modeling a slender three dimensional spheroid. Regularized Stokeslets are placed along a one dimensional curve to represent the spheroid. In Chapter 4, regularized Stokeslets are placed on a two dimensional surface to model a non-slender spheroid.

3.1. Physical Setup

Consider the task of modeling a slender prolate spheroid of length $2L$ and radius R with cone angle θ (measured from the horizontal to the centerline of the spheroid). Figure 3.1 depicts the variables used to describe a slender spheroid precessing about its center in free space. Define a slenderness parameter, σ, as the ratio of the spheroid's diameter to its length:

$$\sigma = \frac{R}{L}. \tag{3.1}$$

The assumption that the spheroid is slender implies $\sigma \ll 1$. Although this is a three dimensional object, it is desirable to represent the spheroid with a one dimensional line of regularized Stokeslets to reduce computational cost. Consider spacing the regularized Stokeslets evenly along the major axis of the spheroid. If all regularized Stokeslets have the same spreading parameter, the effective shape of the collection of singularities is cylindrical. However, one can also consider varying the spreading parameter along the length of the rod in an ellipsoidal fashion, for example, to more closely mimic a prolate spheroid. The numerical explorations in Section 3.3 include results where the spreading parameter both remains constant and varies ellipsoidally along the length of the body.

This chapter addresses how to choose the number of regularized Stokeslets and the spreading parameters to model a slender spheroid of a given slenderness so as to minimize the velocity error with respect to the exact solution that is discussed in Section 1.3.1. First, the effect of varying the spreading parameter proportionally to the radius of the spheroid will be compared to keeping the spreading parameter constant will be discussed. Second, the component of the regularization error due to the discrepancy between the Stokeslet strengths imposed in the slender asymptotic solution of Section 1.3.2 and the regularized Stokeslet strengths solved for in the numerical solution will be discussed. Third, the difference between evaluating the boundary condition at the location of the regularized Stokeslets and the surface of the slender spheroid will be investigated. Lastly, the condition number of the matrix relating regularized forces to fluid velocities will be discussed. The results of this chapter show that there are choices one can make in the numerical solution that provide more accurate results than the slender asymptotic solution and provide guidance on how to minimize the velocity error.

3.2. Quantifying Error

This section identifies different components of the velocity error between the numerical solution for a slender spheroid precessing about its center in free space and the exact solution of Camassa *et. al.* and Leiterman [**11, 42**] that is discussed in Section 1.3.1. The error has contributions due to quadrature, regularization, slenderness, and time integration. The slenderness error arises because the numerical solution only utilizes regularized Stokeslets, but the exact solution uses stresslets, quadrupoles, and rotlets. This error depends on slenderness, as was shown in the case of the slender asymptotic solution in Section 1.3.2. The temporal integration error will be discussed separately in Chapter 5. It will be shown that the quadrature error is often smaller than the regularization and slenderness error. In Chapters 3 and 4, the error analysis is always conducted at the initial time step to eliminate the temporal integration error from the present discussion.

Chapters 3 and 4 focus on the numerical results for modeling two different classes of spheroids: slender and non-slender. The numerical velocity results will often be compared to the exact analytical solution that was discussed in Section 1.3.1. While the error will be plotted as $|\mathbf{u}^{exact} - \mathbf{u}^{S,\phi_\epsilon}|$, where $\mathbf{u}^{S,\phi_\epsilon}$ represents the velocity calculated with regularized Stokeslets, it is important to recognize that there are multiple components of the error, as will be discussed here.

Consider starting with the velocity error represented by the exact solution in (1.4) and working towards the velocity calculated with a collection of regularized Stokeslets, referred to as the numerical solution. A compressed representation of the ith component

of the exact velocity generated by a prolate spheroid is

$$u_i^{exact} = \int_{-c}^{c} \left[K_1 u_i^{SS} + K_2 u_i^{Q} + K_3 u_i^{R_1} + K_4 u_i^{R_2} \right] ds, \tag{3.2}$$

where K_1, K_2, K_3 and K_4 are functions of s and represent the velocity coefficients from (1.4). The velocity due to a collection of N regularized Stokeslets can be represented as

$$u_i^{S,\phi_\epsilon} = \sum_{n=1}^{N} u_{i,n}^{S,\phi_\epsilon} q_n, \tag{3.3}$$

where $u_{i,n}^{S,\phi_\epsilon}$ is the velocity due to the nth regularized Stokeslet, as given in (2.41), and q_n is a quadrature weight. Note that u_i^{S,ϕ_ϵ} can also be represented without the sum as $u_i^{S,\phi_\epsilon} = \frac{1}{8\pi\mu} S_{ij}^{\phi_\epsilon} f_j$, where $\mathbf{f}$ has dimensions $3M \times 1$, S^{ϕ_ϵ} is $3M \times 3N$, and M is the number of places where the velocity is calculated. The first representation will be used for the purposes of this discussion, but the second is how the velocity is implemented, as discussed in Section 2.6.

The error between the exact solution and the numerical solution can be expressed as:

$$\begin{aligned} \left| u_i^{exact} - u_i^{S,\phi_\epsilon} \right| &= \left| \int_{-c}^{c} \left[K_1 u_i^{SS} + K_2 u_i^{Q} + K_3 u_i^{R_1} + K_4 u_i^{R_2} \right] ds - \sum_{n=1}^{N} u_{i,n}^{S,\phi_\epsilon} q_n \right| \\ &= \left| \int_{-c}^{c} \left[K_1 u_i^{SS} + K_2 u_i^{Q} + K_3 u_i^{R_1} + K_4 u_i^{R_2} \right] ds - \int_{-L}^{L} u_i^{S} ds \right. \\ &\quad \left. + \int_{-L}^{L} u_i^{S} ds - \sum_{n=1}^{N} u_{i,n}^{S} q_n + \sum_{n=1}^{N} u_{i,n}^{S} q_n - \sum_{n=1}^{N} u_{i,n}^{S,\phi_\epsilon} q_n \right|. \end{aligned} \tag{3.4, 3.5}$$

Using the triangle inequality, one obtains

$$\begin{aligned} \left| u_i^{exact} - u_i^{S,\phi_\epsilon} \right| &\leq \left| \int_{-c}^{c} \left[K_1 u_i^{SS} + K_2 u_i^{Q} + K_3 u_i^{R_1} + K_4 u_i^{R_2} \right] ds - \int_{-L}^{L} u_i^{S} ds \right| \\ &\quad + \left| \int_{-L}^{L} u_i^{S} ds - \sum_{n=1}^{N} u_{i,n}^{S} q_n \right| + \left| \sum_{n=1}^{N} u_{i,n}^{S} q_n - \sum_{n=1}^{N} u_{i,n}^{S,\phi_\epsilon} q_n \right|. \end{aligned} \tag{3.6}$$

For discussion purposes, define

$$\xi_1 = \left| \int_{-c}^{c} \left[K_1 u_i^{SS} + K_2 u_i^{Q} + K_3 u_i^{R_1} + K_4 u_i^{R_2} \right] ds - \int_{-L}^{L} u_i^{S} ds \right| \tag{3.7}$$

$$\xi_2 = \left| \int_{-L}^{L} u_i^{S} ds - \sum_{n=1}^{N} u_{i,n}^{S} q_n \right| \tag{3.8}$$

$$\xi_3 = \left| \sum_{n=1}^{N} u_{i,n}^{S} q_n - \sum_{n=1}^{N} u_{i,n}^{S,\phi_\epsilon} q_n \right|. \tag{3.9}$$

As mentioned in Section 1.3, the slender asymptotic solution is represented by an integral of Stokeslets (see (1.10)). Thus, ξ_1 represents the error between the exact solution for a prolate spheroid and the asymptotic solution for a slender prolate spheroid discussed in Sections 1.3.1 and 1.3.2, respectively. As Camassa *et. al.* and Leiterman report in [**11, 42**], the asymptotic solution is asymptotic in slenderness with order $\beta = \left[\ln\left(\frac{2}{\sigma}\right)\right]^{-1}$, where σ is the slenderness of the spheroid defined in (3.1).

The second error term, ξ_2, represents quadrature error. Using either the midpoint rule or trapezoid rule, ξ_2 is second order in h, where h represents the regularized Stokeslet spacing. Consider studying the quadrature error with respect to a reference solution for both the exact solution that utilizes stresslets, quadrupoles, and rotlets (Section 1.3.1) and the asymptotic solution that only invokes Stokeslets (Section 1.3.2). Figure 3.2 shows the velocity error as a function of singularity spacing h. For both solutions, the reference solution is computed with the exact solution. To simplify notation, let $\chi_i^{exact} = K_1 u_i^{SS} + K_2 u_i^{Q} + K_3 u_i^{R_1} + K_4 u_i^{R_2}$. Then, the velocity error for the exact solution is

$$\left| \sum_{n=1}^{N} \chi_n^{exact} q_n - \sum_{n=1}^{1000} \chi_n^{exact} q_n \right|. \tag{3.10}$$

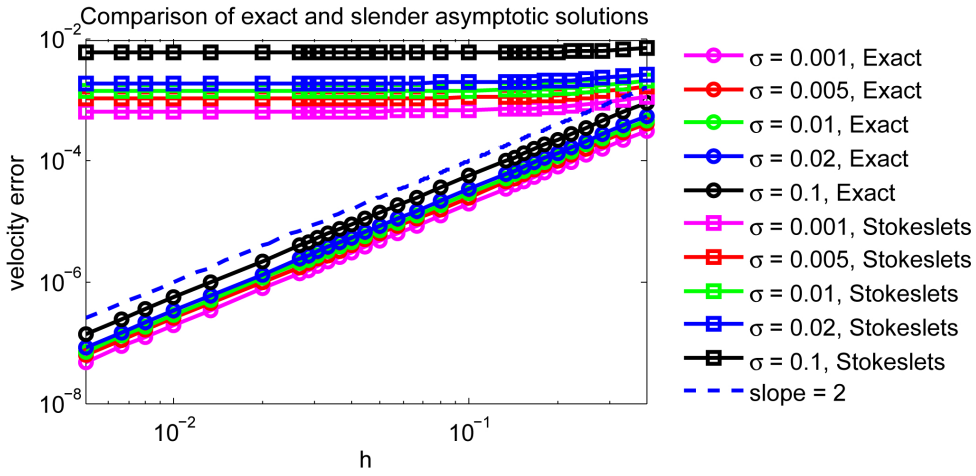

FIGURE 3.2. Velocity error between the exact and slender asymptotic solutions averaged over the marker locations shown in Figure 3.3. The error is calculated with respect to a reference solution of the exact solution computed with many singularities.

Similarly, define the velocity error for the slender asymptotic solution as

$$\left| \sum_{n=1}^{N} u_i^S q_n - \sum_{n=1}^{1000} \chi_n^{exact} q_n \right|. \tag{3.11}$$

Again, notice that in both cases, the reference solution for the exact solution is being used to compare the results of the Stokeslet solution as well. As such, one would expect to see second order convergence in the exact solution as a result of visualizing the quadrature error. In studying the velocity error in (3.11) for the slender asymptotic solution, one might anticipate that the error will depend on slenderness with the initial convergence rate due to quadrature, but then the error will stabilize and decrease with σ. Figure 3.2 demonstrates second-order behavior in the exact solution. This figure also shows that the error decreases for the slender asymptotic solution as the slenderness parameter decreases, which justifies the earlier claim that the quadrature error is small with respect to the other errors discussed here.

The third error term, ξ_3, represents the regularization error created by replacing singular Stokeslets with regularized Stokeslets. Cortez reports that the regularization error is $O(\epsilon)$ in the near field and $O(\epsilon^2)$ in the far field [**19**]. Replacing u_i^S and u_i^{S,φ_ϵ} with their definitions from (2.11) and (2.41), the regularization error can be further divided as follows:

$$\xi_3 = \left| \sum_{n=1}^{N} S_{ij}\alpha_{j,n}q_n - \sum_{n=1}^{N} S_{ij}^{\phi_\epsilon} f_{j,n}q_n \right| \tag{3.12}$$

$$= \left| \sum_{n=1}^{N} S_{ij}\alpha_{j,n}q_n - \sum_{n=1}^{N} S_{ij}^{\phi_\epsilon}\alpha_{j,n}q_n + \sum_{n=1}^{N} S_{ij}^{\phi_\epsilon}\alpha_{j,n}q_n - \sum_{n=1}^{N} S_{ij}^{\phi_\epsilon} f_{j,n}q_n \right| \tag{3.13}$$

$$\leq \left| \sum_{n=1}^{N} S_{ij}\alpha_{j,n}q_n - \sum_{n=1}^{N} S_{ij}^{\phi_\epsilon}\alpha_{j,n}q_n \right| + \left| \sum_{n=1}^{N} S_{ij}^{\phi_\epsilon}\alpha_{j,n}q_n - \sum_{n=1}^{N} S_{ij}^{\phi_\epsilon} f_{j,n}q_n \right|. \tag{3.14}$$

Define

$$\xi_{3a} = \left| \sum_{n=1}^{N} S_{ij}\alpha_{j,n}q_n - \sum_{n=1}^{N} S_{ij}^{\phi_\epsilon}\alpha_{j,n}q_n \right| \tag{3.15}$$

$$\xi_{3b} = \left| \sum_{n=1}^{N} S_{ij}^{\phi_\epsilon}\alpha_{j,n}q_n - \sum_{n=1}^{N} S_{ij}^{\phi_\epsilon} f_{j,n}q_n \right|. \tag{3.16}$$

The error in ξ_{3a} is only due to the fact that a regularized Stokeslet is used in place of a Stokeslet while the strengths are prescribed by the asymptotic solution. As shown in (2.40), $S^{\phi_\epsilon} \to S$ as $\epsilon \to 0$. This error will be negligible away from the spheroid. The error in ξ_{3b} is the dominant component of ξ_3. This is due to the discrepancy between the prescribed Stokeslet strengths in the closed form asymptotic solution $\boldsymbol{\alpha}$ and the forces solved for to match the boundary condition in the numerical solution, $\mathbf{f}$. This will be studied further in Section 3.3, specifically discussing the convergence of $\mathbf{f}_n(\epsilon, N)$ to $\boldsymbol{\alpha}_n$. All three components of the velocity error, ξ_1, ξ_2, and ξ_3, are present in the numerical studies in the remainder of this discussion, but it is often the case that some of these

errors are subdominant to others. Most often, the quadrature error ξ_2 will be smaller than the other errors.

In addition to the aforementioned types of error, for time dependent problems there is also time integration error to take into account, which will be discussed further in Chapter 5. Spectral deferred correction methods provide an efficient time integrator so that time integration error is kept small. In the error discussions in this chapter and Chapter 4, the velocity error is computed at the initial position of the fluid particle. Small time integration errors are not introduced into the solution until the position of the fluid particle is updated.

3.3. Varying the Spreading Parameter

A natural question that might arise is: How should the spreading parameter vary based on the geometry of a slender three dimensional object? Alternatively, what is the best way to distribute regularized Stokeslets and choose the spreading parameter to best model a spheroid of a given slenderness? First consider placing regularized Stokeslets along the centerline of the spheroid and varying the spreading parameter, ϵ, ellipsoidally along the length of the body. To gauge how well this models a spheroid of a given slenderness, consider comparing the velocity calculated with regularized Stokeslets for a range of spreading parameters and spacing against the velocity from the exact solution generated by a spheroid of slenderness $\sigma = 0.01$. The velocity will be calculated at 14 locations away from the rod, as shown in Figure 3.3. The rod, shown in blue, initially lies in the xz-plane as do the 14 initial marker positions, shown in red. Figure 3.4 shows the velocity error as a function of spreading parameter, where the velocity error is measured as $|u(\mathbf{x}, \sigma) - \tilde{u}(\mathbf{x}, \epsilon, N)|$. $u(\mathbf{x}, \sigma)$ represents the initial velocity calculated at $\mathbf{x}$ with the

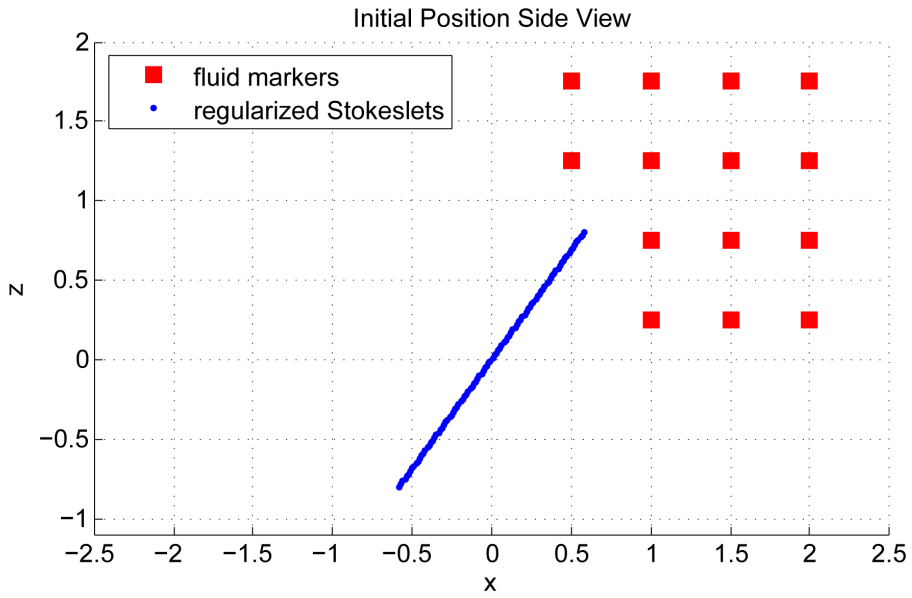

FIGURE 3.3. Initial position of regularized Stokeslets and fluid markers where velocity is calculated.

exact solution for a spheroid of radius σ, and $\tilde{u}(\mathbf{x}, \epsilon, N)$ is the initial velocity calculated at $\mathbf{x}$ with N regularized Stokeslets and spreading parameter ϵ. While the spreading parameter actually varies as

$$\varepsilon(s) = \epsilon\sqrt{1 - \frac{s^2}{L^2}}, \tag{3.17}$$

where $s \in [-L, L]$ parameterizes the rod length, the reported value of spreading parameter in plots and discussions is the ϵ coefficient from (3.17)[1]. The cone angle is $\theta = \frac{3\pi}{10}$ and the rod length in both the exact and numerical cases is 2 ($L = 1$). For the data shown in Figure 3.4, one would expect the error to approach that of the slender asymptotic solution as $\epsilon \to 0$ and $N \to \infty$. As shown later in this section, that indeed is the case, but the minimum in the error for moderate spreading parameters shows that another choice

[1]It should be noted that the spreading parameter need not vary with rod geometry as in (3.17). This is a particular case, not an exhaustive description. Other variations of distributing ϵ along the length of the spheroid are discussed later in this section.

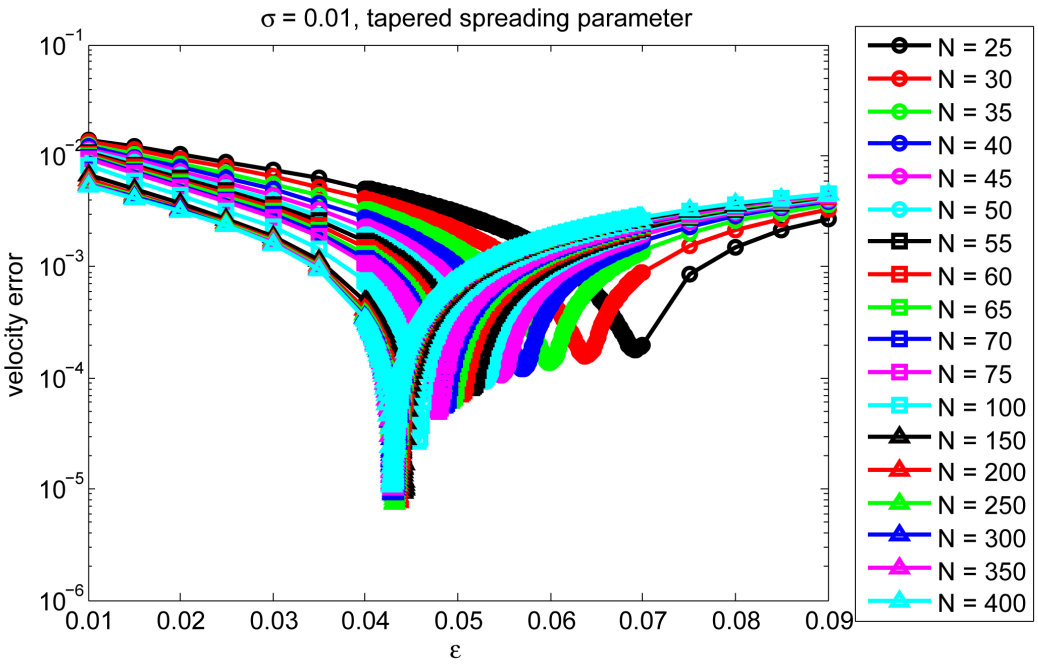

FIGURE 3.4. Velocity error between the exact and regularized Stokeslet solutions ($|u(\mathbf{x},\sigma) - \tilde{u}(\mathbf{x},\epsilon,N)|$) averaged over the marker locations shown in Figure 3.3. The spreading parameter varies along the length of the body according to (3.17). Notice that the error is minimized for ϵ such that $\epsilon \approx 4.3\sigma$.

of ϵ can further reduce the error beyond the slenderness error mentioned in Section 3.2. Figure 3.5 shows a zoomed in view of the local minima in Figure 3.4. Notice that the error is minimized for $\epsilon \approx 0.043$, $N = 250$, and $\sigma \approx 0.233\epsilon$. This provides evidence that there are scenarios where modeling the spheroid with regularized Stokeslets is more accurate than the slender asymptotic solution with respect to the exact solution. Recall from Figure 3.2 that the error in the slender asymptotic solution of Camassa *et. al.* is on the order of 10^{-3}, while the error resulting from the numerical model using regularized Stokeslets can reach 10^{-5}, as shown in Figure 3.5. Thus, it is possible to decrease

the velocity error by a few orders of magnitude in the numerical solution depending on parameter choice.

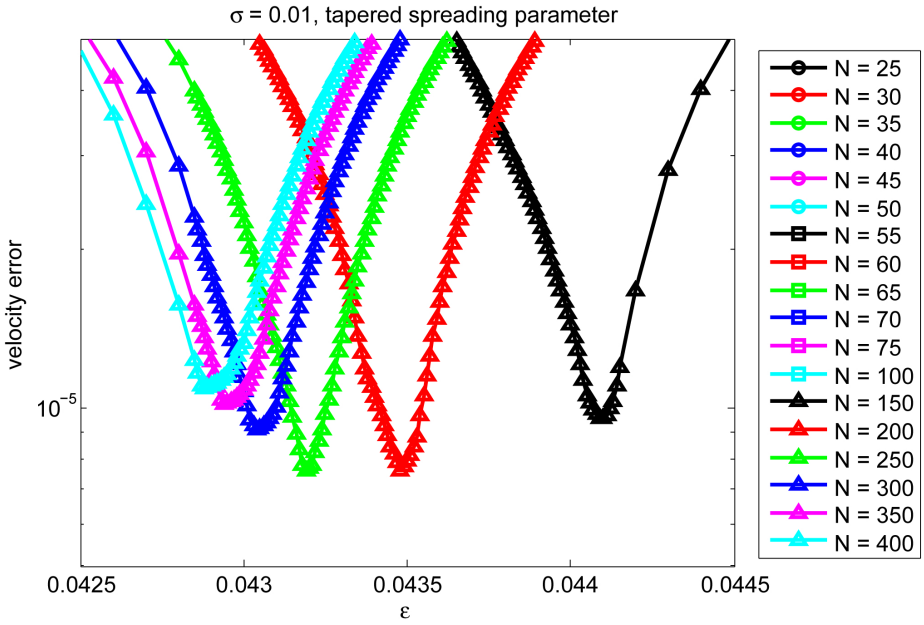

FIGURE 3.5. Alternate view of the velocity error between the exact and regularized Stokeslet solutions shown in Figure 3.4.

The relationship between the spreading parameter that produces a local minima in the velocity error and the number of regularized Stokeslets is summarized in Figure 3.6. The data is fit with a fourth degree polynomial relating ϵ and h. Notice that as $h \to 0$, $\epsilon \to 0.042758$ according to the equation reproduced from the legend in Figure 3.6.

Now consider looking at the velocity error resulting from a slender rod precessing about its center with spreading parameters that do not vary along the body length. That is, let

$$\varepsilon(s) = \epsilon. \tag{3.18}$$

Figure 3.7 shows the velocity error again, but with constant spreading parameter for each regularized Stokeslet as in (3.18). The axes are scaled the same as in Figure 3.4, but a

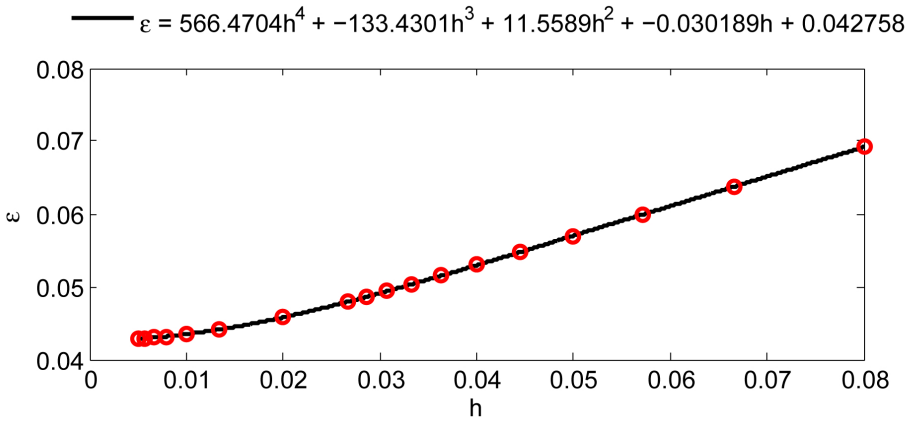

FIGURE 3.6. Spreading parameter versus singularity spacing that generate the local minima in velocity error from Figure 3.4 for a slender spheroid with tapered spreading parameters.

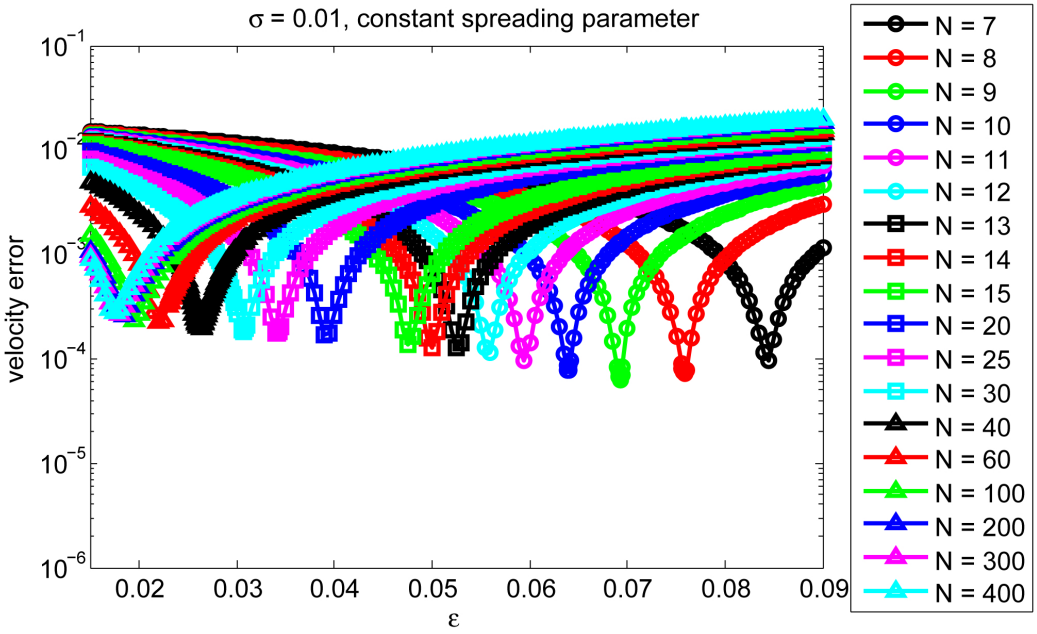

FIGURE 3.7. Velocity error between the exact and regularized Stokeslet solutions ($|u(\mathbf{x}, \sigma) - \tilde{u}(\mathbf{x}, \epsilon, N)|$) averaged over the marker locations shown in Figure 3.3. The spreading parameter is the same for each regularized Stokeslet comprising the spheroid, as in (3.18).

larger range of spreading parameters are shown in Figure 3.7. Notice that the minimum velocity error is not as small as when the spreading parameters are tapered in Figure 3.4. This suggests that incorporating tapered spreading parameters with appropriately chosen parameters can be more accurate than either using regularized Stokeslets with the same spreading parameters or the slender asymptotic closed form solution of Section 1.3.2, as will be shown in Section 3.4. Also, the minima do not converge as nicely as N increases in the constant spreading parameter case (Figure 3.7) as in the tapered spreading parameter case (Figure 3.4). This makes it more difficult to suggest a spreading parameter to model a general physical configuration. Figure 3.8 shows the spreading parameter versus singularity spacing for the local minima in the constant spreading parameter case in Figure 3.7. Notice as $h \to 0$, $\epsilon \to 0.016659$, which is approximately $\sigma = 0.01$. This suggests that to model a spheroid of a given slenderness, when one uses tapered singularity strengths, the ϵ that minimizes velocity error is approximately four times larger than σ, but when the spreading parameter is constant, ϵ should be chosen only slightly larger than the actual slenderness of the rod. When ϵ is chosen properly, the initial velocity error is smaller for the tapered case than the constant case, suggesting that tapering the spreading parameter is a desirable choice.

Now consider the form of the singularity strengths for each of the cases where the spreading parameter is tapered or constant, as in 3.17 and 3.18, respectively. As mentioned in Section 3.2, there is a component of the velocity error that is due to the fact that the strength of the regularized Stokeslets solved for in (2.64) may not match the Stokeslet strengths prescribed by (1.12) in the slender asymptotic solution discussed in Section 1.3.2. This error component is labeled ξ_{3b} in Section 3.2. As shown in Figure 3.3, the centerline of the spheroid lies in the xz-plane. Its initial velocity is in the y-direction

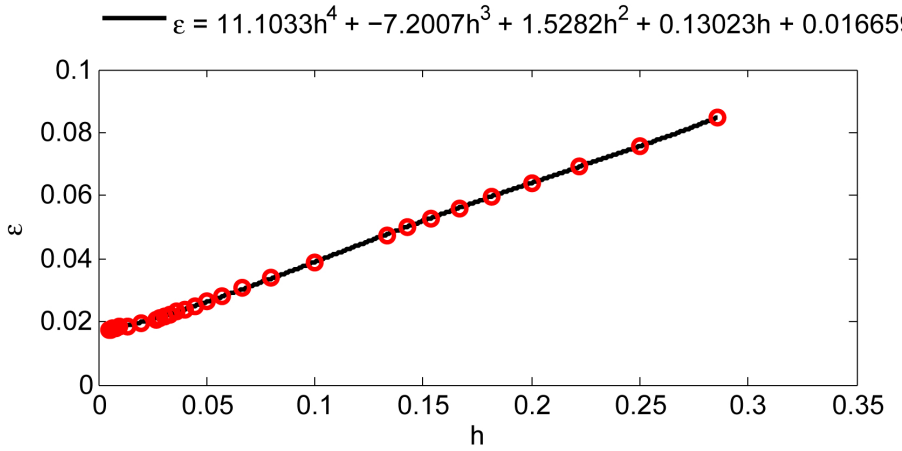

FIGURE 3.8. Spreading parameter versus singularity spacing that generate the local minima in velocity error from Figure 3.7 for a slender spheroid with constant spreading parameters.

in this configuration. As such, the x- and z-components of the singularity strengths will intuitively be zero since the strength correlates to the magnitude of the force exerted on the fluid. In other words, since the velocity of the rod is initially in the y-direction, it only exerts a force on the fluid in the y-direction at that time. As such, only the y-component of the singularity strength is plotted in Figure 3.9 as a function of s, which parameterizes the length of the spheroid. This figure shows the imposed Stokeslet strength from (1.12) for the slender asymptotic solution as well as the regularized Stokeslet strengths that are computed to satisfy the no-slip boundary condition at the centerline of the spheroid. The strengths are shown for both aforementioned cases where the spreading parameters vary along the body length and as well as remain constant ((3.17) and (3.18), respectively). Observe that the behavior near the tips of the spheroid differs for the tapered and constant spreading parameter cases.

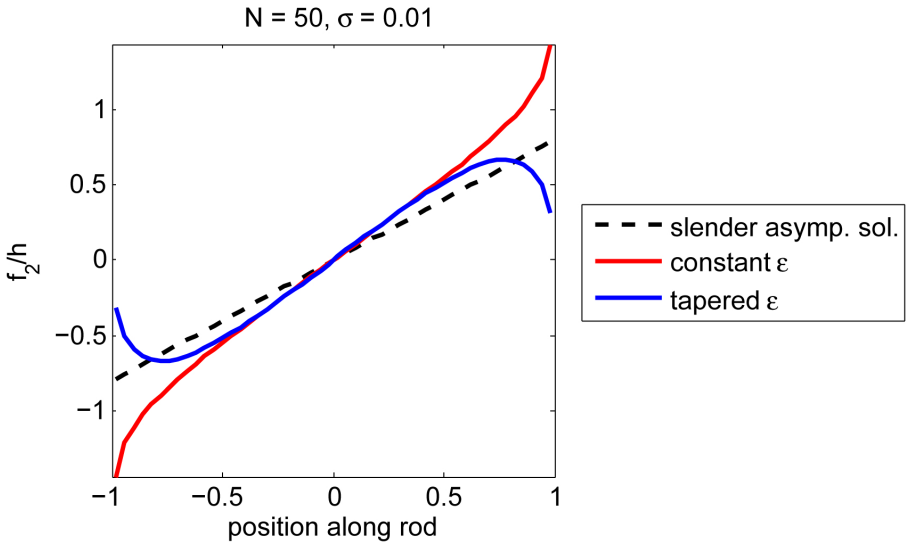

FIGURE 3.9. Computed regularized Stokeslet strengths versus position along rod for the tapered and constant spreading parameter scenarios with $N = 50$ regularized Stokeslets, slenderness $\sigma = 0.01$, and spreading parameter $\epsilon = 0.01$. The dashed line represents the Stokeslet strengths from (1.12) used in the slender asymptotic solution.

Figure 3.10 shows the regularized Stokeslet strengths for the tapered (Figure 3.10(a)) and constant (Figure 3.10(b)) cases for a variety of spreading parameters with fixed number of regularized Stokeslets $N = 50$ and slenderness $\sigma = 0.01$. Notice that for these figures where the singularity spacing h is fixed, as the spreading parameter decreases the regularized Stokeslet strength approaches the Stokeslet strength for the slender asymptotic solution. Alternatively, as ϵ increases for fixed h, oscillations appear in the strength, particularly in the constant spreading parameter case compared to the tapered ϵ case. For plots of this nature made with more regularized Stokeslets (smaller h), the oscillations become more pronounced in both the tapered and constant cases and appear for smaller ϵ values. This behavior may be related to the condition number of the matrix

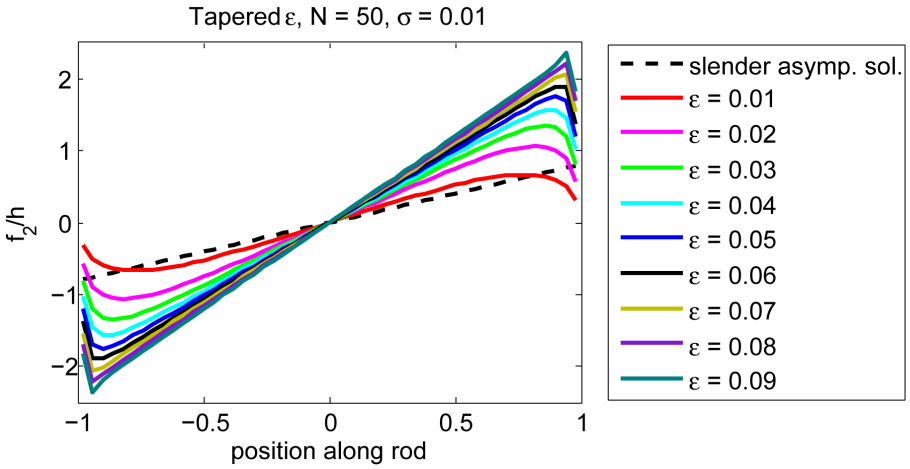

(a)

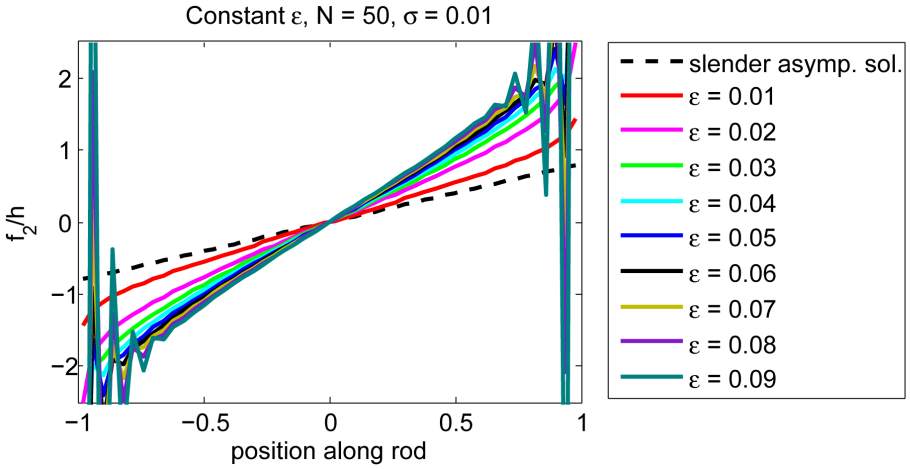

(b)

FIGURE 3.10. Computed regularized Stokeslet strengths versus position along rod for (a) tapered and (b) constant spreading parameter scenarios with $N = 50$ regularized Stokeslets and slenderness $\sigma = 0.01$ for a variety of spreading parameters. The dashed line represents the Stokeslet strengths from (1.12) used in the slender asymptotic solution.

that is inverted in solving for the regularized Stokeslet strength. As will be discussed in Section 3.5, the condition number of the matrix increases as $\frac{h}{\epsilon}$ decreases.

Consider varying the spreading parameter, ϵ, along the length of the spheroid as follows:

$$\epsilon = R\left(\sqrt{1-\frac{s^2}{L^2}}\right)^{\zeta}, \tag{3.19}$$

where $s \in [-L, L]$ parameterizes the length of the body and ζ is a parameter that controls the tapering of the spreading parameters. When $\zeta = 0$, the spreading parameters will be constant along the length of the rod and when $\zeta = 1$, ϵ will vary with the radius of the spheroid itself. The two cases when $\zeta = 0$ and $\zeta = 1$ correspond to the constant and tapered spreading parameters discussed in Section 3.3. The discussion in this section samples for a wider range of ζ values.

The asymptotic analytical solution for a slender prolate spheroid rotating about its center in free-space only uses Stokeslets to calculate the fluid velocity. This solution, asymptotic in σ, derives Stokeslet strengths that vary linearly with position along the body. Thus, in addition to solving for the regularized Stokeslet strengths that satisfy a given boundary condition, the calculated Stokeslet strengths will be imposed on the regularized Stokeslets to gain insight into the different components of error.

In the error plots shown in Figure 3.11, the results of the regularized Stokeslet solution for a sampling of $\zeta \in [0, 1]$ are compared with the results of the regularized Stokeslet solution imposed with the asymptotic singularity strengths. The error plotted for the regularized Stokeslet solution with computed singularity strengths is $\eta_C = \frac{1}{N_t}\sum_{i=1}^{N_t} |\mathbf{u}_e(\mathbf{x}_i) - \mathbf{u}_{RS}(\mathbf{x}_i; q, \zeta, \mathbf{f})|$, while the error for the imposed singularity strength from the slender asymptotic solution is $\eta_I = \frac{1}{N_t}\sum_{i=1}^{N_t} |\mathbf{u}_e(\mathbf{x}_i) - \mathbf{u}_{RS}(\mathbf{x}_i; q, \zeta, \boldsymbol{\alpha})|$. Notice the difference between η_C and η_I is the singularity strength. $\mathbf{f}$ represents the

regularized Stokeslet strengths that are computed by the numerical method and $\boldsymbol{\alpha}$ represents the imposed Stokeslet strengths given in the slender asymptotic solution. Within each subplot, each data series has a different value of ζ, from (3.19). Each subplot has a different fixed value of q increasing from top left to bottom right, where q is defined as the ratio of singularity spacing to spreading parameter:

$$q = \frac{h}{\epsilon}. \tag{3.20}$$

For small values of q, the error of the regularized Stokeslet solution becomes more than an order of magnitude smaller than the error of the regularized Stokeslet solution with imposed analytical Stokeslet strengths. This behavior occurs regardless of the ζ value, allowing one to conclude that independent of the choice of spreading parameter ϵ, the regularized Stokeslets can provide a more accurate solution than the analogous asymptotic solution. It should be noted that while this occurs for the range of ζ values shown here, the h (and consequently ϵ) values that minimize the error do depend on ζ. However, as q increases, the discrepancy becomes less noticeable to the point that the error in the regularized Stokeslet solution increases beyond the level of the regularized Stokeslet solution with imposed strengths as h decreases. When the spreading parameter ϵ is small, the exponent ζ does not effect the error much. However, for larger spreading parameters, ζ has a more significant effect.

Figure 3.12 displays the velocity error as a function of spreading parameter for the largest and smallest q values sampled: $q = 0.6$ and $q = 5$, each shown in a different subplot with $\zeta = 1$. The data series within each subplot have fixed slenderness parameters. Notice that for small h, the error decreases as the slenderness parameter σ decreases. This is consistent with the idea that imposing the velocity boundary condition along the

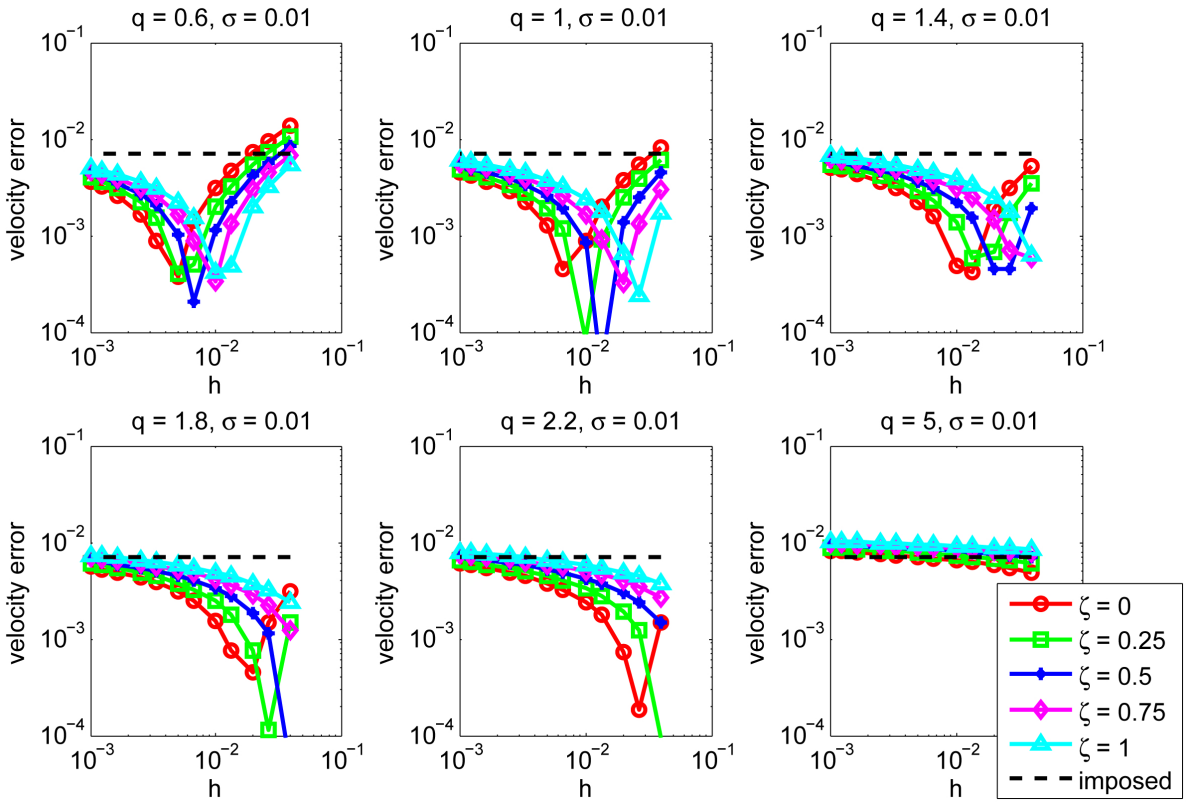

FIGURE 3.11. Error in initial velocity as a function of regularized Stokeslet spacing, h, for fixed slenderness $\sigma = 0.01$ when the boundary condition is imposed at the location of the regularized Stokeslets along the centerline. Each subplot has a fixed $q = \frac{h}{\epsilon}$ value and each data series has a fixed ζ value (defined in (3.19)). The dashed line represents the error from the solution with the singularity strength from the slender asymptotic solution ($\boldsymbol{\alpha}$) imposed on the regularized Stokeslets.

centerline of the spheroid will become less accurate as slenderness parameter increases as discussed earlier in this section. In the large q case, ϵ is small when compared to h. As $h \to 0$, $\epsilon \to 0$ as well, which creates a regime where the regularized solution should approach the singular solution. Thus, it is not surprising that the error in the

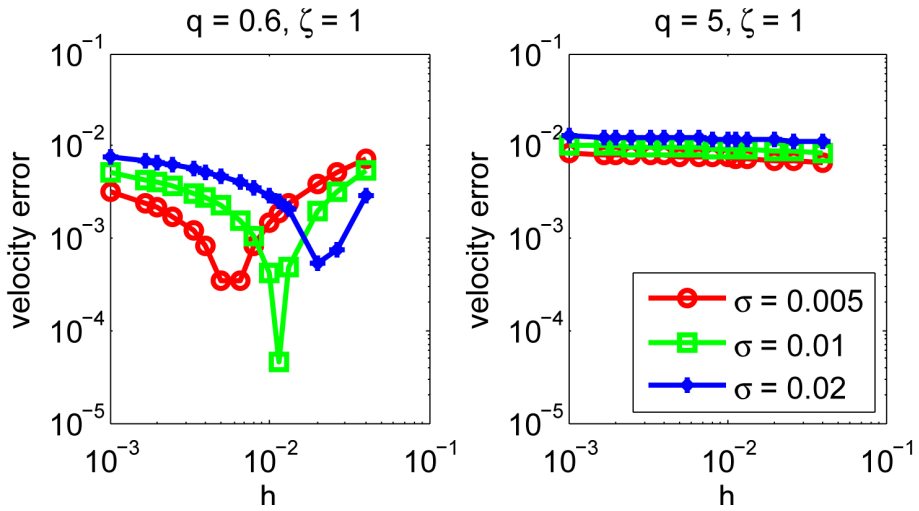

FIGURE 3.12. Error in initial velocity as a function of regularized Stokeslet spacing, h, for fixed $\zeta = 1$ when the boundary condition is evaluated at the location of the regularized Stokeslets. Each subplot has a fixed $q = \frac{h}{\epsilon}$ for a variety of slenderness parameters.

regularized Stokeslet solution approaches the error in the regularized Stokeslet solution with the singular forces imposed.

3.4. Varying the Location of Boundary Conditions

This section will explore how imposing the no-slip boundary condition at different locations affects the velocity error. The exact solution is derived by analytically evaluating the no-slip boundary condition on the surface of a spheroid where the solid body is in direct contact with the fluid. When using regularized Stokeslets to model the spheroid, consider three different ways of imposing the boundary condition, the first of which is the traditional approach:

(1) Match the fluid velocity with the velocity along the centerline (major axis) of the spheroid (Figure 3.13(a))

(2) Match the fluid velocity with the velocity along a projection of the spheroid's centerline onto its surface (Figure 3.13(b))

(3) Match the fluid velocity with the velocity along a curve that lies on the surface of the spheroid, but is not a projection of the centerline (Figure 3.13(c)).

The first method is the traditional approach often taken in applications of the method of regularized Stokeslets in the sense that the velocity boundary conditions are imposed at the locations of the regularized Stokeslets [**19**]. The second and third methods differ from the first in the fact that the boundary conditions are imposed away from the regularized Stokeslets. The effectiveness of each of these methods depends on σ. If σ is small, then the rod is slender and the velocity at the centerline will not differ much from the velocity at the surface. However, as σ increases, the discrepancy between the centerline and surface velocities increases as the surface moves further away from the extent of the regularized forces being exerted at the centerline. When the slenderness parameter increases to the point when it is no longer reasonable to approximate the spheroid with a line of regularized Stokeslets, one can transition to distributing the regularized Stokeslets along the surface rather than on a curve. This will be discussed in further detail in Chapter 4.

The numerical explorations discussed in the remainder of this section have the following in common: the initial velocity of the numerical regularized Stokeslet solution is compared with the initial velocity calculated with the exact, free-space analytical solution. The error plotted in the figures is calculated by averaging the difference in velocity over multiple locations in the fluid. That is, if $\mathbf{u}_e(\mathbf{x})$ represents the exact solution and $\mathbf{u}_{RS}(\mathbf{x})$ represents the regularized Stokeslet solution for the velocity at some location in the fluid $\mathbf{x}$, then the error, η, is calculated as $\eta = \frac{1}{N_t}\sum_{i=1}^{N_t} |\mathbf{u}_e(\mathbf{x}_i) - \mathbf{u}_{RS}(\mathbf{x}_i)|$, where N_t

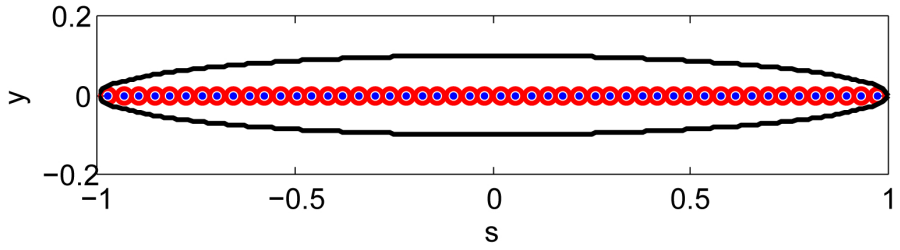

(a) Method (1)

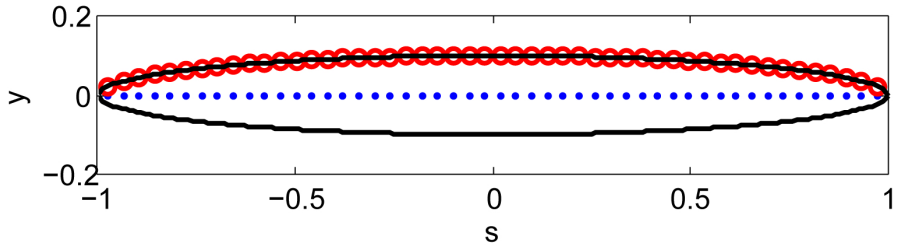

(b) Method (2)

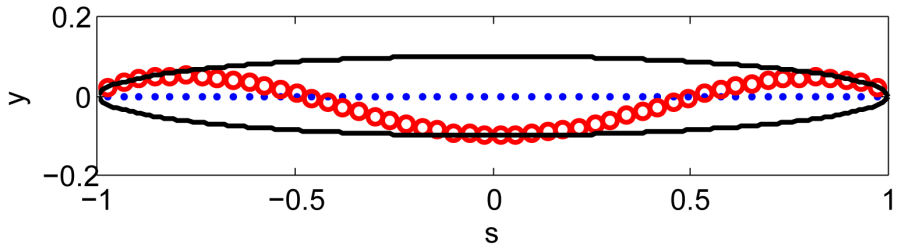

(c) Method (3)

FIGURE 3.13. Three different methods for implementing the velocity boundary condition for a slender spheroid. The blue dots along the centerline represent the location of the regularized Stokeslets and the black ellipse represents the surface of the spheroid used in the exact solution. The red circles denote where the boundary condition is imposed in each of the three cases: (a) on the centerline, (b) on a projection of the centerline onto the surface, and (c) on curve that wraps around the surface of the spheroid in a helical fashion.

is the number of tracer locations in the fluid where the velocity is calculated and $|\cdot|$ represents the Euclidean norm.

3.4.1. Projected Boundary Condition. Now consider implementing the boundary condition using the second method mentioned above, namely matching the fluid velocity with the velocity along a projection of the spheroid's centerline onto its surface. In this study, the centerline is projected orthogonally with respect to the xz-plane into the positive y-direction. Thus, since the motion of the rod is counterclockwise when looking down onto the xy-plane, this is the leading part of the spheroid as it rotates about the z-axis. The locations to evaluate the boundary condition are given by:

$$\mathbf{x}_{bc} = (s\cos\theta, r(s), s\sin\theta), \tag{3.21}$$

where

$$r(s) = \sigma\sqrt{1 - \left(\frac{s}{L}\right)^2} \tag{3.22}$$

is the radius of the spheroid at a position s along the length of the body and θ describes the tilt of the rod. θ is measured from the positive x-axis to the centerline of the spheroid, as shown in Figure 3.1(b). Figure 3.14 shows the velocity error versus singularity spacing for this scenario where the boundary condition is evaluated at the projection of the centerline onto the surface of the spheroid. Each subplot has a fixed q value increasing from top left to bottom right. Within each subplot, the data series correspond to fixed ζ values, as described in (3.19). Notice that as $h \to 0$, the error no longer approaches that of the asymptotic solution, rather it levels off almost an order of magnitude less. This is evidence again of a way to choose the spreading parameters and implement the boundary conditions to get a more accurate solution than the slender asymptotic solution discussed

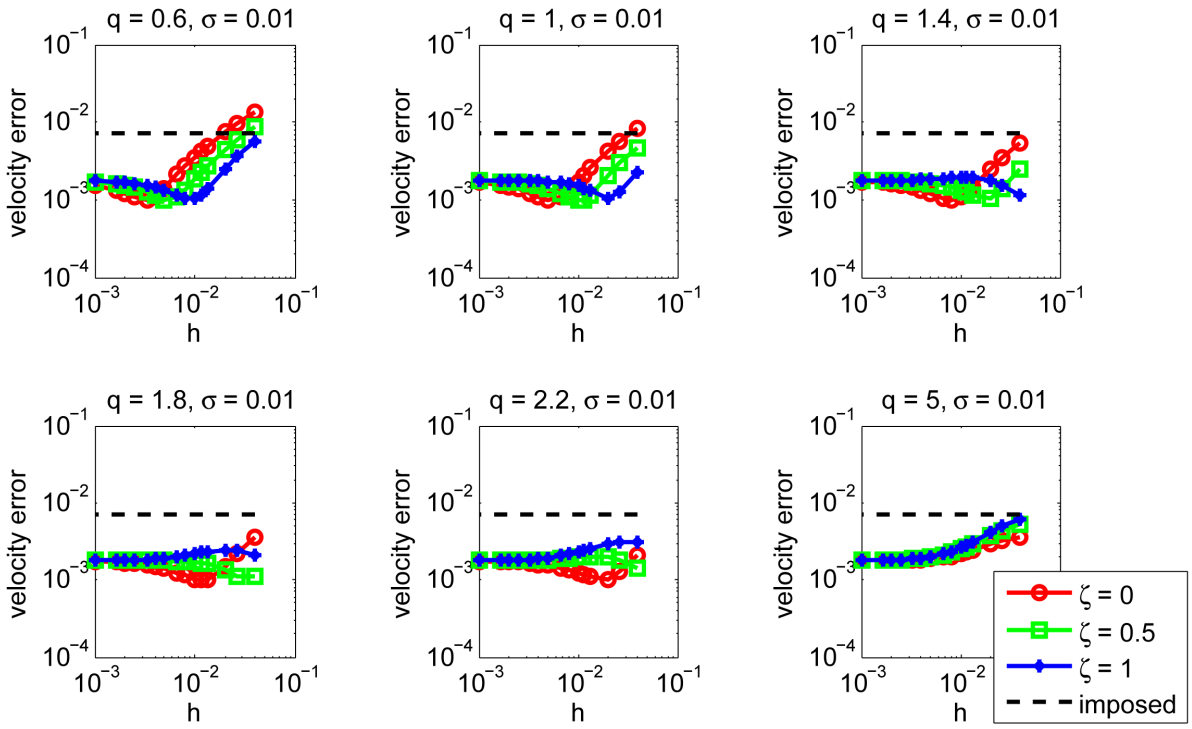

FIGURE 3.14. Error in initial velocity as a function of regularized Stokeslet spacing, h, for fixed slenderness $\sigma = 0.01$ when the boundary condition is imposed at the projection of the regularized Stokeslets onto the surface of the spheroid. Each subplot has a fixed $q = \frac{h}{\epsilon}$ value and each data series has a fixed ζ value (defined in (3.19)). The dashed line represents the error from the solution with the singularity strength from the slender asymptotic solution ($\boldsymbol{\alpha}$) imposed on the regularized Stokeslets.

in Section 1.3.2. Figure 3.15 again shows the velocity error as a function of h for $\zeta = 1$, but only for two q values, each shown in different subplots. Each data series represents a different slenderness. Notice again that the velocity error decreases as the slenderness parameter decreases.

3.4.2. Helical Boundary Condition. Now consider the third method to implement the boundary condition: match the fluid velocity with the rod velocity on the surface,

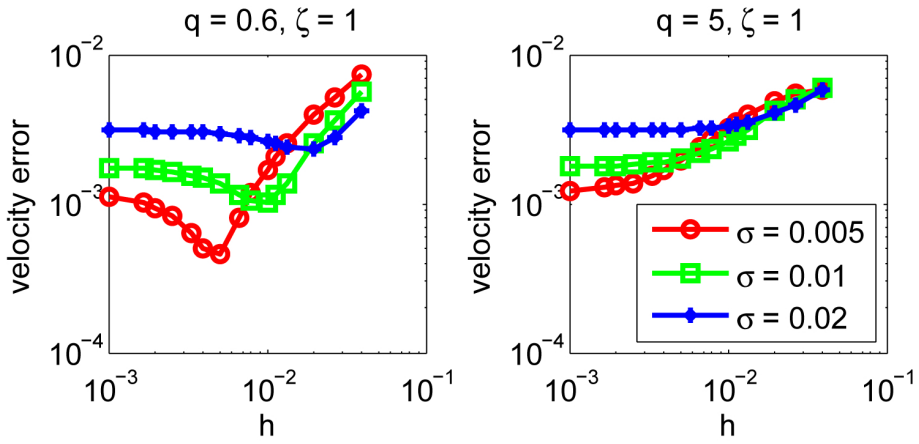

FIGURE 3.15. Error in initial velocity as a function of regularized Stokeslet spacing, h, for fixed $\zeta = 1$ when the boundary condition is evaluated at the projection of the regularized Stokeslets onto the surface of the spheroid. Each subplot has a fixed $q = \frac{h}{\epsilon}$ for a variety of slenderness parameters.

but not along a simple projection of the centerline. In this case, the points to evaluate the boundary condition, $\mathbf{x}_{bc}$, are given by

$$\mathbf{x}_{bc} = (s\cos\theta, r(s)\cos\phi, r(s)\sin\phi\sin\theta), \tag{3.23}$$

where

$$\begin{aligned} \phi &= 0, d\phi, 2d\phi, 3d\phi, \ldots, 2\pi - d\phi, \\ d\phi &= \frac{2\pi}{N}, \end{aligned}$$

$r(s)$ is given by (3.22), θ measures the tilt of the spheroid, and N is the number of regularized Stokeslets along the centerline of the spheroid. These points wrap around the surface of the spheroid in a helical fashion. Figure 3.16 shows the velocity error as a function of h for $\sigma = 0.01$ when the boundary condition is evaluated in a helical fashion on the surface of the spheroid. Each subplot has a fixed q value, with q increasing from

the top left subplot to the bottom right subplot. The data series within each subplot have fixed ζ values. Again, the most striking feature of these plots is that for small h, the error lies below the error from the imposed solution regardless of the value of q. This leads to the conclusion that evaluating the velocity boundary condition on the surface of the spheroid produces smaller errors for small h than prescribing the regularized Stokeslet strengths from the closed form slender asymptotic solution presented in Section 1.3.1. Figure 3.17 shows the velocity error as a function of singularity spacing with $\zeta = 1$ for $q = 0.6$ and $q = 5$, each shown in a different subplot. Each data series represents a different spheroid slenderness. Notice again that for small h, the velocity error decreases as the slenderness parameter decreases.

When evaluating the boundary condition along the centerline, there are choices of h, ϵ, and ξ that can produce even smaller errors than when the boundary condition is evaluated at the surface. Unfortunately, it is not obvious how to choose these values *a priori* and they are somewhat sensitive. However, in the worst case scenario where the parameters are not chosen to precisely minimize the velocity error, the accuracy of the numerical method still matches that of the slender asymptotic solution.

Figure 3.18 summarizes the information discussed in this section. Again, this figure shows the velocity error as a function of h for small and large $q = \frac{h}{\epsilon}$ values with $\zeta = 1$ and $\sigma = 0.01$. Each data series represents a different method of imposing the boundary conditions, as discussed above. For $q = 0.6$, all three methods of imposing the boundary condition with the numerical solution produce smaller error as $h \to 0$ than the solution with the singularity strengths imposed according to the slender asymptotic solution, as given by (1.12). However, for some moderately larger h (and ϵ) values, the accuracy improves for the case where the boundary condition is evaluated at the centerline (method

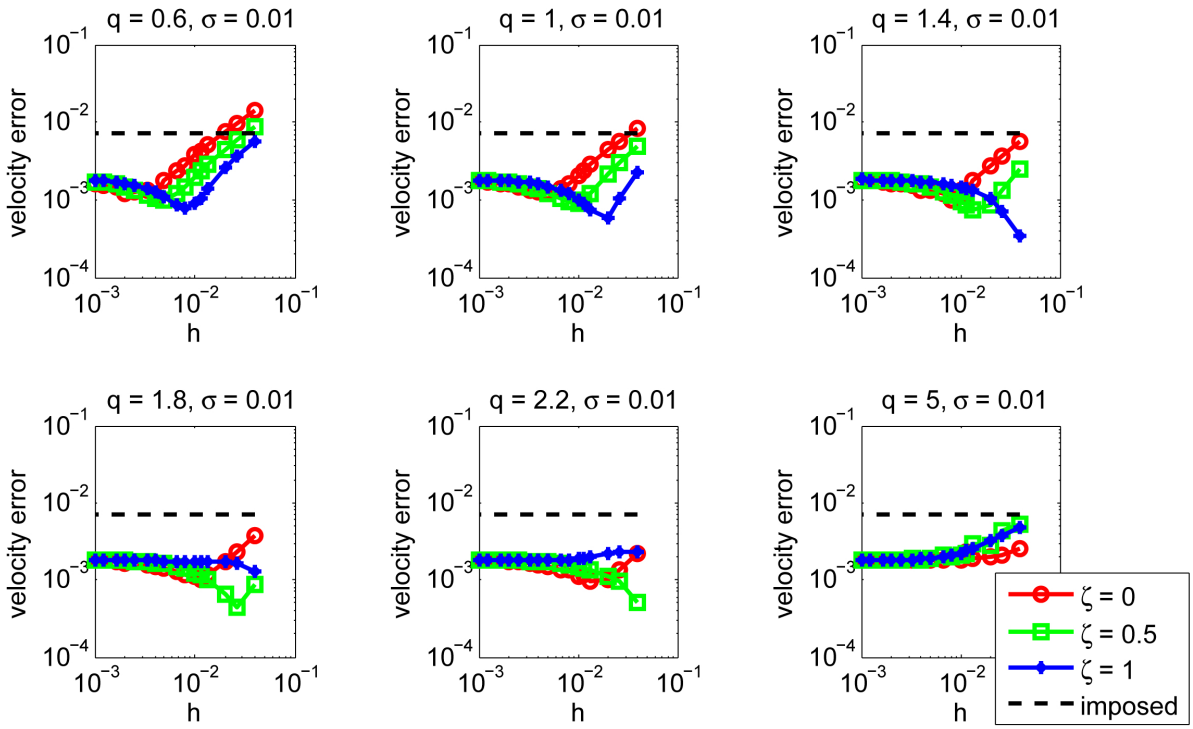

FIGURE 3.16. Error in initial velocity as a function of regularized Stokeslet spacing, h, for fixed slenderness $\sigma = 0.01$ when the boundary condition is imposed in a helical fashion on the surface of the spheroid. Each subplot has a fixed $q = \frac{h}{\epsilon}$ value and each data series has a fixed ζ value (defined in (3.19)). The dashed line represents the error from the solution with the singularity strength from the slender asymptotic solution ($\boldsymbol{\alpha}$) imposed on the regularized Stokeslets.

(1)), but not as much for the other two methods of imposing the boundary conditions. When you evaluate the boundary conditions on the centerline, an effective radius appears whereas this is not the case when the boundary conditions are evaluated at the surface. This feature is not noticeable for the larger $q = 5$ case. One common feature that appears to be independent of q is the fact that the velocity error decreases as the slenderness

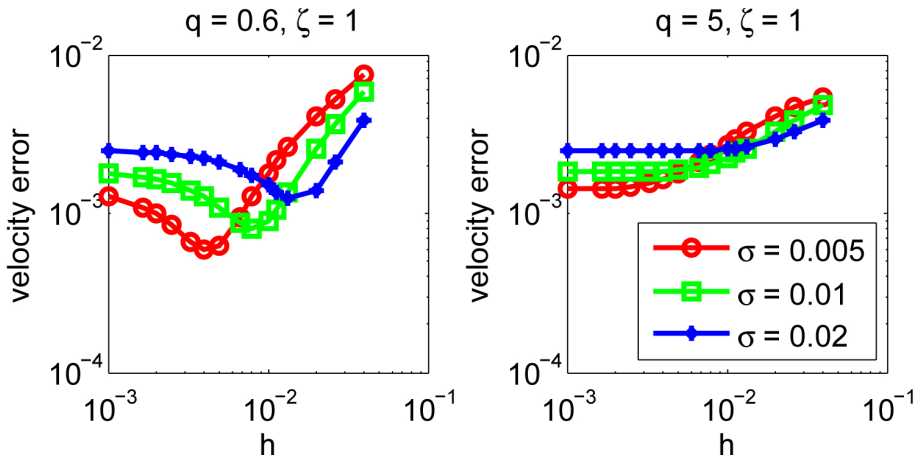

FIGURE 3.17. Error in initial velocity as a function of regularized Stokeslet spacing, h, for fixed $\zeta = 1$ when the boundary condition is evaluated in a helical fashion on the surface of the spheroid. Each subplot has a fixed $q = \frac{h}{\epsilon}$ for a variety of slenderness parameters.

parameter decreases. That is, modeling a spheroid with regularized Stokeslets along its centerline gains accuracy as the spheroid becomes more slender.

The data presented in this section suggests that there are options for choosing the spreading parameter and where to impose the no-slip boundary conditions when using regularized Stokeslets that produce smaller velocity error than the slender asymptotic solution. The singularity strengths discussed in Section 3.3 along with the data shown in this section may suggest more accurate methods of distributing regularized Stokeslet strengths than (1.12) of the slender asymptotic solution.

3.5. Condition Number

Consider investigating the condition number of the matrix, $A = \frac{1}{8\pi\mu} S_{ij}^{\phi_\epsilon}$ (from (2.39)), relating the singularity strength, $\mathbf{f}$, with the velocity computed at the collection of regularized Stokeslets, $\mathbf{u}$, by $\mathbf{u} = A\mathbf{f}$. There is a relationship between condition number and

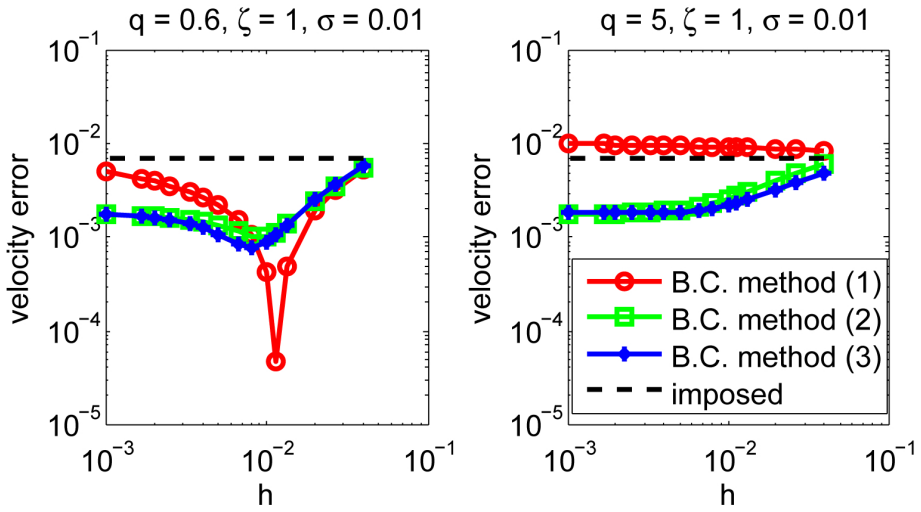

FIGURE 3.18. Error in initial velocity as a function of regularized Stokeslet spacing, h, for fixed $\zeta = 1$ and $\sigma = 0.01$ with the boundary condition implemented three different ways (described at the beginning of Section 3.4). The dashed line represents the error from the solution with the singularity strength from the slender asymptotic solution ($\boldsymbol{\alpha}$) imposed on the regularized Stokeslets.

$q = \frac{h}{\epsilon}$ as evidenced by Figure 3.19. This figure shows the condition number of A as a function of $\frac{1}{q} = \frac{\epsilon}{h}$ for both the tapered and constant spreading parameter cases shown in Figures 3.4 and 3.7, respectively.

To avoid potentially losing numerous significant digits in the accuracy of the computed singularity strengths, one should consider $\frac{h}{\epsilon} > c$. The constant c can be chosen appropriately to keep condition numbers within a desired range. A reasonable choice of c is 0.5. This restriction makes computing reference solutions difficult for large values of ϵ while remaining in the desired range of condition numbers. Despite the fact that efforts are made to avoid choices of $\frac{h}{\epsilon}$ that lead to ill-conditioned matrices, one can check the extent to which the condition number indeed is affecting the accuracy of the singularity

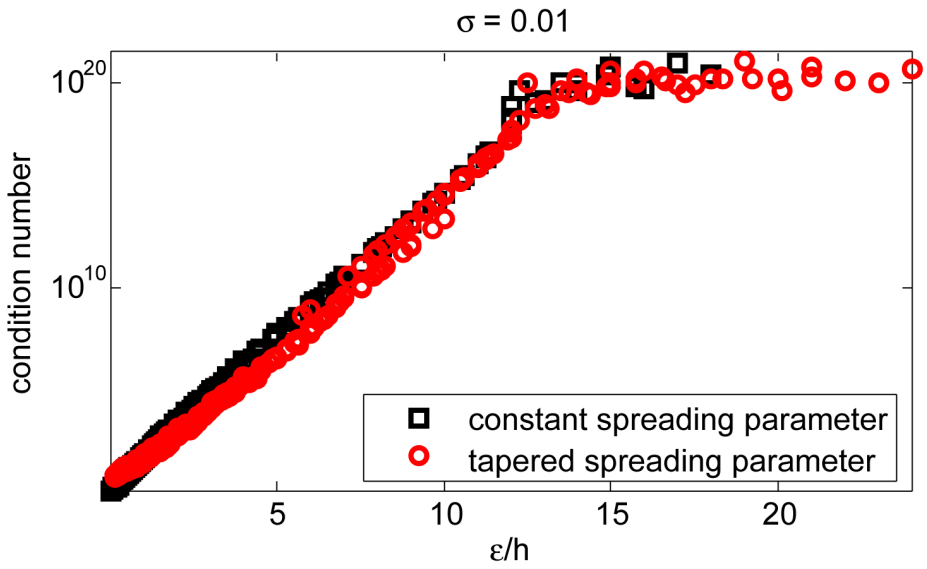

FIGURE 3.19. Condition number versus $\frac{\epsilon}{h}$ for $\sigma = 0.01$ with varying ϵ and N for the data shown in Figures 3.4 and 3.7.

strengths. Since $\mathbf{u}$ is prescribed, $\mathbf{f}$ is the remaining unknown quantity. Once the linear system has been solved for $\mathbf{f}$, consider the quantity $\mathbf{u} - A\mathbf{f}$ as a measure of the effect of the condition number.

3.6. Summary

The results of this chapter suggest how to choose the parameters of the numerical solution to minimize the initial velocity error. Here are some observations discussed in this chapter:

- The quadrature error is small with respect to the slenderness and regularization errors.
- The dominant component of the regularization error comes from the discrepancy between the imposed Stokeslet strengths $\boldsymbol{\alpha}$ in the slender asymptotic solution of Camassa *et. al.* in Section 1.3.2 (see (1.12)) and the regularized Stokeslet

strength $\mathbf{f}$ solved for with the numerical method to satisfy the desired velocity boundary condition.

- When the boundary condition is imposed at the centerline and the spreading parameters are tapered according to the radius of the spheroid, the smallest velocity error is produced. To achieve this, one should choose the spreading parameter at the center of the spheroid, ϵ, to be roughly four times the slenderness, σ.
- Other choices of how to impose the boundary condition and choose the spreading parameter and singularity strengths also show desirable error results. That is, the velocity error from the numerical solution remains smaller than the velocity error from the slender asymptotic solution.

The next chapter discusses the parameter choices that minimize the velocity errors associated with modeling a non-slender spheroid with regularized Stokeslets.

CHAPTER 4

Non-Slender Prolate Spheroids

This chapter discusses how to choose parameters to best model a non-slender spheroid with regularized Stokeslets to minimize error. As was the case in Chapter 3, time integration error will not play a role in the discussion in this chapter since the instantaneous velocity error is calculated at the initial time. The temporal error will be discussed in Chapter 5. It will be shown that a change in the radius of the spheroid results in linear convergence in the exact solution. Similarly, when regularized Stokeslets are placed on the surface of a spheroid with $q = \frac{h}{\epsilon}$ fixed, the error decreases linearly with ϵ. This is indicative of an effective radius, *i.e.* the collection of regularized Stokeslets models a spheroid of a slightly larger size than intended. However, to use this fact as an advantage, Section 4.3 discusses placing the regularized Stokeslets on a slightly inset surface so that the size of the effective spheroid matches the desired spheroid. When placing regularized Stokeslets inside the spheroid, two choices of boundary condition implementation will be discussed: evaluating the velocity at the regularized Stokeslet location and evaluating the velocity at the effective surface. It will be shown how to choose the number and location of inset regularized Stokeslets and their spreading parameters to minimize the velocity error.

Parallels will be drawn between the slender and non-slender cases discussed in Chapters 3 and 4 , respectively. The slender case provides information that not only relates

closely to the experimental data motivated by the biological applications concerning cilia, but also allows for comparison with the slender asymptotic solution of Camassa *et. al.* The non-slender spheroids are useful to concentrate on the exact solution as well as learn proper parameter choices that minimize velocity error when looking at a sphere, for instance, which may be acting as a fluid tracer. This chapter concludes with a discussion of the condition number for the matrix relating regularized forces and the resulting fluid velocities.

Consider using the exact free space solution for a prolate spheroid which is not slender, unlike in Chapter 3. In some numerical methods that involve a choice of where to impose forces to represent an object, like the immersed boundary method and the method of regularized Stokeslets [**19, 22, 51**], it is conventional to exert the forces on the desired surface. Recall from Chapter 3 that regularized Stokeslets placed along the centerline of a spheroid create an effective radius that varies with the spreading parameter. Thus, in the specific context of regularized Stokeslets, one might imagine the regularization process can alter the effective location of the surface. As such, one may want to reconsider how to distribute the regularized Stokeslets to minimize error.

A question of general interest is how the numerical solution converges to the exact solution as parameters of interest vary, namely the number of regularized Stokeslets, N, and the regularization parameter, ϵ. Again let the slenderness parameter, σ, from (3.1) describe the spheroid's proportions. Now σ no longer remains small, but remains strictly bounded by 1 for the spheroid to remain prolate. The exact solution described in Section 1.3.1 is only valid for $0 < \sigma < 1$, so studies involving the exact solution will be restricted to this range. However, the information obtained in this chapter will be advantageous

in building spheres with regularized Stokeslets where $\sigma = 1$ in Section 5.2.1. Figure 4.1 shows the general spheroid setup for the scenarios discussed in this section.

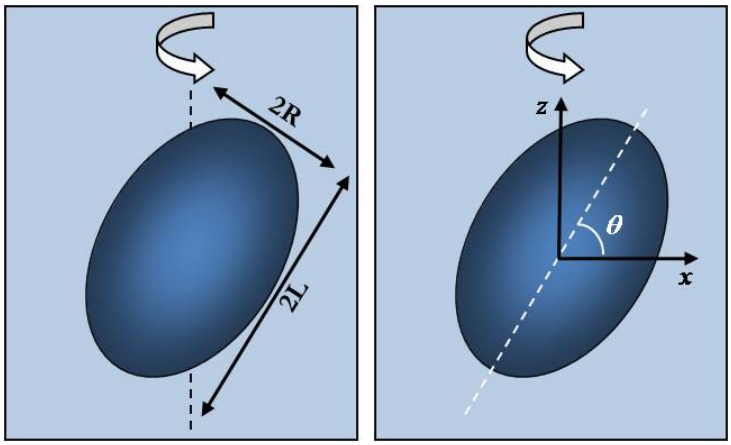

(a) (b)

FIGURE 4.1. A non-slender spheroid precessing about its center in an infinite fluid.

Let $\tilde{\mathbf{u}}(\mathbf{x}, r, \epsilon, N)$ be the velocity at $\mathbf{x}$ computed with the numerical solution using N regularized Stokeslets and spreading parameter ϵ on the surface of a spheroid of semi-minor axis r. Unless stated otherwise, the slenderness parameter will remain constant $\sigma = 0.75$ throughout this chapter. Consider studying the velocity error $|\tilde{\mathbf{u}}(\mathbf{x}, r, \epsilon, N) - \mathbf{u}(\mathbf{x}, r)|$ for a variety of parameters, where $\mathbf{u}(\mathbf{x}, r)$ represents the velocity calculated with the exact solution discussed in Section 1.3.1. Let h denote the singularity spacing on the surface of a spheroid. In computing h, it is assumed that the spheroid is sufficiently spherical so that the surface area of a sphere of radius r is a reasonable approximation to the surface area of a spheroid of semi-minor radius r and slenderness σ:

$$h \approx \sqrt{\frac{4\pi r^2}{N}}. \tag{4.1}$$

The following labeling conventions will be used throughout the remainder of this chapter:

- r: the radius (semi-minor axis) of the spheroid on the surface of which the regularized Stokeslets are placed
- r_{exact}: the radius of the spheroid used in the exact solution
- r_{bc}: the radius of the spheroid where the no-slip boundary condition is imposed.

It is worth noting that these quantities are not radii referring to a sphere, rather they are the length of the semi-minor axis of a spheroid. The radius/semi-minor axis is used along with slenderness as a way to identify the size of the spheroid. Recall that the equation of the spheroid whose centerline lies along the x-axis can be expressed in terms of r (or r_{exact}, or r_{bc}) and σ as:

$$\frac{x^2}{\left(\frac{r}{\sigma}\right)^2} + \frac{y^2+z^2}{r^2} = 1. \tag{4.2}$$

Centroidal Voronoi tessellations are used in the numerical model to evenly distribute regularized Stokeslets on the surface of a spheroid. Appendix G contains more information on this aspect of the model [**25, 26**].

4.1. Dependence of Exact Solution on Radius

This section explores the dependence of the exact solution on spheroid radius when compared to a reference solution also computed with the exact solution of Camassa *et. al.* The numerical solution is not used in this section. Let $\mathbf{u}(\mathbf{x}, r)$ be the velocity at a location $\mathbf{x}$ generated by a spheroid rotating about an axis other than its axes of symmetry, with semi-minor axis r and slenderness σ using the exact solution. Using $r = 0.8$, $\sigma = 0.75$, and $\theta = \frac{2\pi}{5}$ (see Figure 4.1(b) for the definition of θ), consider the difference in velocity

$|\mathbf{u}(\mathbf{x}, r+\gamma) - \mathbf{u}(\mathbf{x}, r)|$ at the 14 locations noted in Figure 4.2. Figure 4.3 shows that the velocity difference decreases linearly as γ decreases to 0.

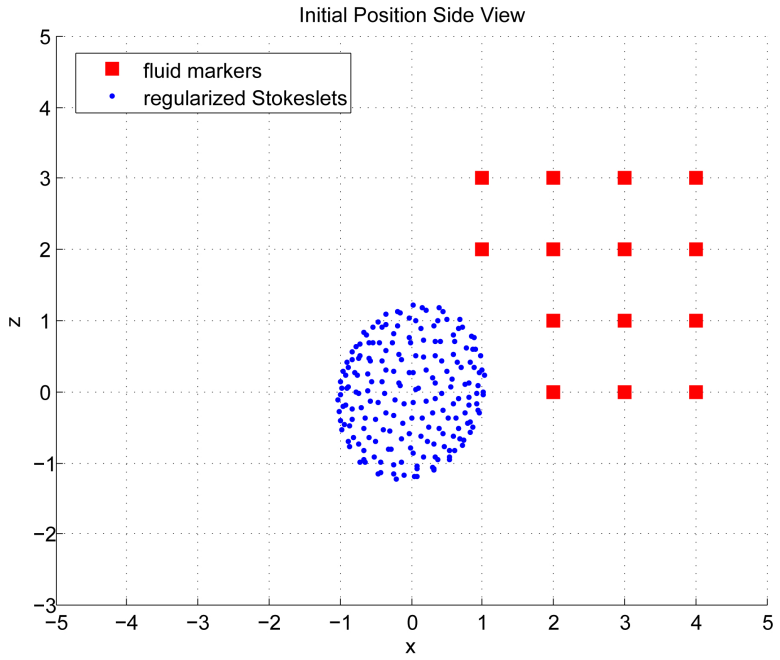

FIGURE 4.2. Initial position of tracer locations where velocity is calculated and an example of initial regularized Stokeslet placement.

This observation does not involve regularized Stokeslets, only the exact solution, but it is helpful in identifying an error dependence on the spreading parameter. This dependence on ϵ corresponds to an effective radius and is discussed in the remainder of this chapter in the context of using regularized Stokeslets.

4.2. Regularized Stokeslets on the Surface

This section will discuss the numerical error in modeling a non-slender spheroid with regularized Stokeslets located on the surface of the spheroid. It will be shown that this results in linear convergence with respect to the spreading parameter, suggesting the presence of an effective radius, as discussed in the slender case in Chapter 3.

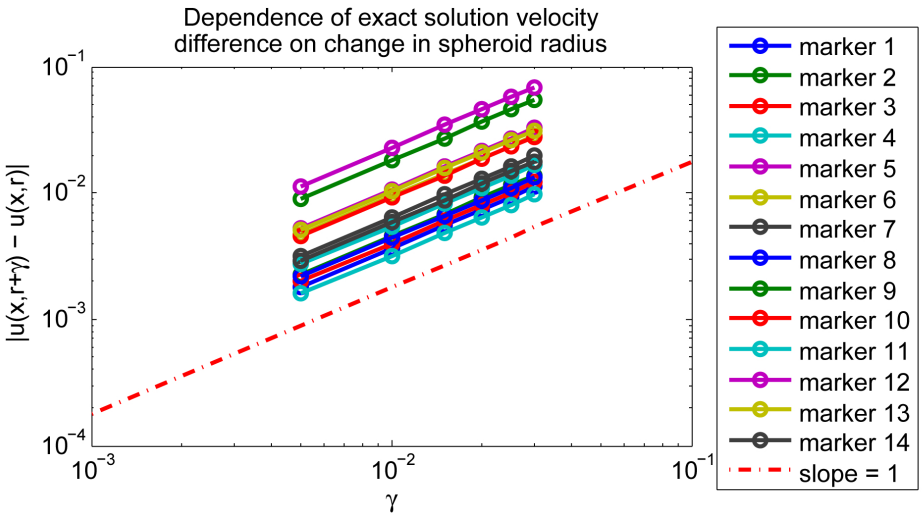

FIGURE 4.3. Difference in velocity between the exact solution computed with a spheroid of radius $r = 0.8 + \gamma$ compared to the exact solution calculated with a spheroid of radius $r = 0.8$.

Consider using regularized Stokeslets placed on the surface of the spheroid keeping the ratio of singularity spacing to spreading parameter, $\frac{h}{\epsilon}$, fixed. Define this ratio as

$$q = \frac{h}{\epsilon}. \tag{4.3}$$

Here $r = r_{bc} = 1$, which corresponds to the standard practice of placing regularized Stokeslets on the surface and enforcing the boundary conditions at the same locations. The velocity will be compared to the exact solution for $r_{exact} = 1$. Figure 4.4 shows the velocity error $|\tilde{\mathbf{u}}(\mathbf{x}, r, \epsilon, N) - \mathbf{u}(\mathbf{x}, r_{exact})|$ averaged over 14 fluid markers for $q = 0.5, 0.6, \ldots, 1.9, 2$. Notice that the convergence is linear as h decreases. Since q is fixed, as h decreases, ϵ also decreases. The linear convergence in Figure 4.4 along with the linear convergence of the exact solution in Figure 4.3 supports the idea that regularization creates an effective radius. That is, when ϵ changes, the effective radius of the spheroid itself changes, despite r remaining fixed.

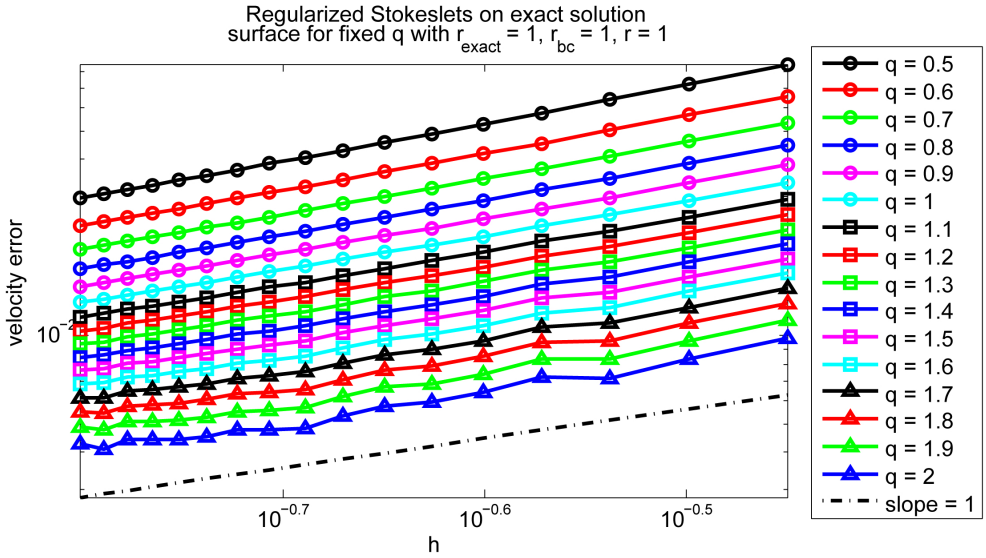

FIGURE 4.4. Initial velocity error between exact and regularized Stokeslet solutions versus singularity spacing for fixed $q = \frac{h}{\epsilon}$. The regularized Stokeslets are located at $r = 1$, the boundary condition is imposed at $r_{bc} = 1$, and the spheroid in the exact solution has $r_{exact} = 1$. Notice the convergence is linear suggesting the presence of an effective radius varying linearly with spreading parameter ϵ.

Figure 4.5 again shows velocity error as a function of singularity spacing, but from a slightly different view point than Figure 4.4. Now each curve corresponds to a fixed $\epsilon = 0.1, 0.2, \ldots, 0.9, 1$. It should be noted that all of the parameters are the same between the data in Figures 4.4 and 4.5 except the choice of spreading parameter. The behavior is not linear because of the choice of ϵ with respect to h. The spreading parameter is fixed along each curve in Figure 4.5, so as h decreases, ϵ remains constant. As such, the effective radius is not changing, since it is related to ϵ. Notice that as was the case in Chapter 3, there are local minima in the velocity error that do not equate to small h. That is, there is a combination of singularity spacing h and spreading parameter ϵ that

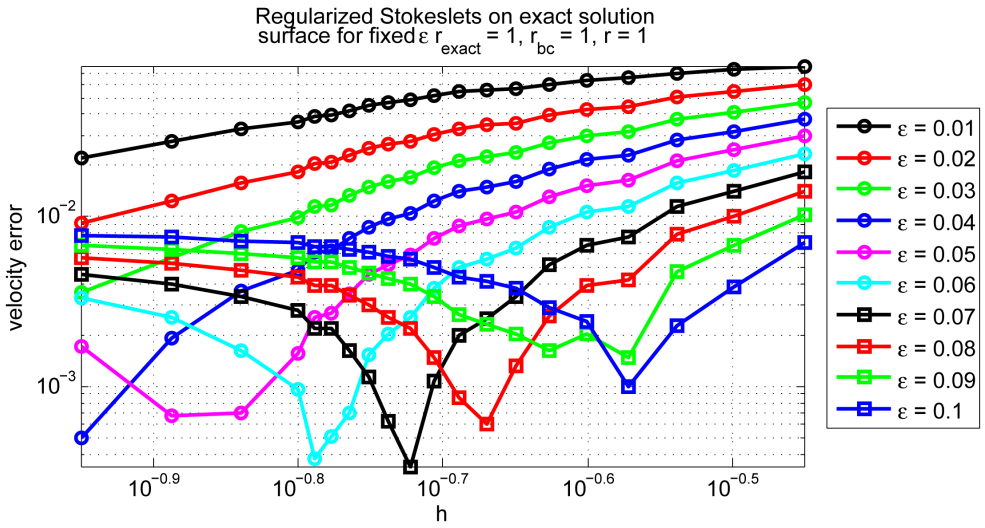

FIGURE 4.5. Initial velocity error between exact and regularized Stokeslet solutions versus singularity spacing for fixed spreading parameter. The regularized Stokeslets are located at $r = 1$, the boundary condition is imposed at $r_{bc} = 1$, and the spheroid in the exact solution has $r_{exact} = 1$.

minimizes the velocity error. This will be explored in more detail in the remainder of this chapter.

An important question that can now be addressed is how best to choose q when the regularized Stokeslets are placed on the surface. Figure 4.6 shows the error in velocity versus q for many h values. Note that the data shown in Figure 4.4 is for $q \leq 2$, which only comprises a portion of the graph in Figure 4.6. From this figure, the error appears to be minimized for $q \in (2.5, 3)$. Thus, the results of Figure 4.6 suggest that to model a non-slender spheroid when the regularized Stokeslets are placed on the surface, a choice of $q \in (2.5, 3)$ will provide the best results, which differs from some values used in the literature [**19**]. The velocity error as a function of singularity spacing h is shown in Figure 4.7 for fixed $q = 2.7$, which is in the interval of q values that minimizes the velocity error in Figure 4.6. For smaller q, Figure 4.4 shows that the error decreases linearly with h,

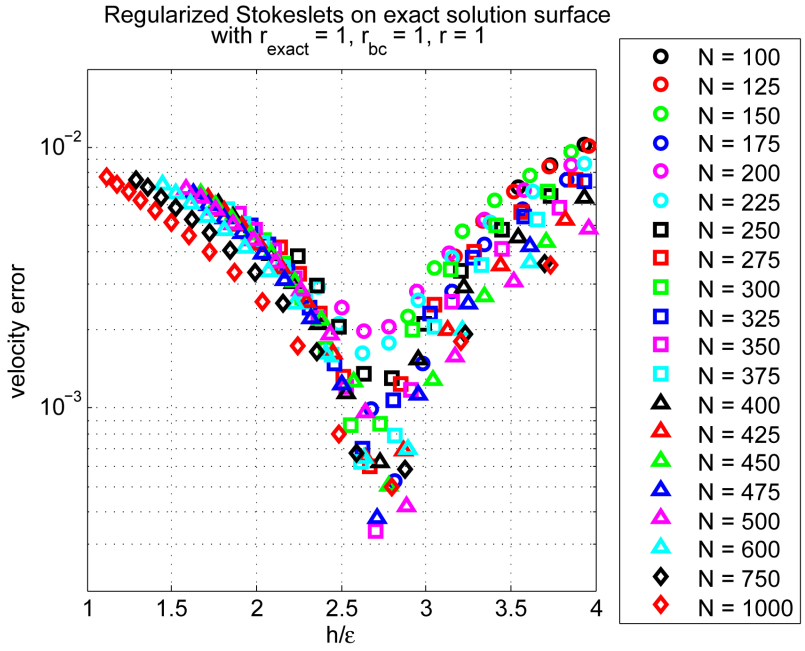

FIGURE 4.6. Velocity error between exact and regularized Stokeslet solutions versus $q = \frac{h}{\epsilon}$ for fixed N. The regularized Stokeslets are located at $r = 1$, the boundary condition is imposed at $r_{bc} = 1$, and the spheroid in the exact solution has $r_{exact} = 1$.

but as q increases, the error becomes noisier, although it still follows the general first order trend. One should note that the choice of q discussed here may be sensitive to the cutoff function used as well as the geometry of the problem.

4.3. Inset Regularized Stokeslets

Section 4.1 shows that the velocity difference for the exact solution decreases linearly with radius. Section 4.2 demonstrates linear convergence of the numerical solution to the exact solution, suggesting an effective spheroid radius due to regularization. In this section, the effective radius will be taken into account with the goal of establishing a connection between the location of the regularized Stokeslets and the effective radius, which depends on the spreading parameter. These findings motivate the investigation

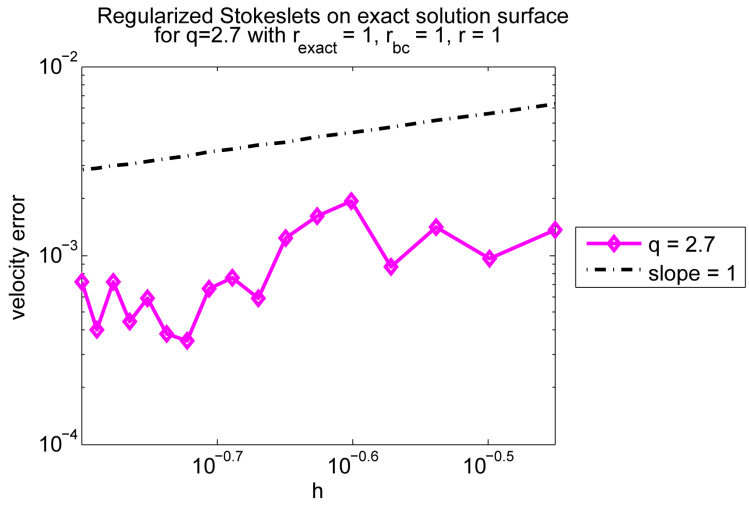

FIGURE 4.7. Velocity error between exact and regularized Stokeslet solutions versus h for fixed $q = 2.7$. The regularized Stokeslets are located at $r = 1$, the boundary condition is imposed at $r_{bc} = 1$, and the spheroid in the exact solution has $r_{exact} = 1$.

of the error when the regularized Stokeslets are no longer placed on the surface of the spheroid, rather on a spheroid of a smaller radius inside the desired spheroid, both of which are illustrated in Figure 4.8. The discussion in this section will provide quantitative information about effective radius, as discussed in Section 4.2. Two different methods of choosing where to impose the no-slip boundary condition will be discussed. Section 4.3.1 will explore evaluating the boundary condition at the location of the regularized Stokeslets ($r_{bc} = r$) and Section 4.3.2 will look at evaluating the velocity at the projection of the regularized Stokeslet locations onto the surface of the spheroid in the exact solution ($r_{bc} = r_{exact}$).

4.3.1. Boundary Condition at Regularized Stokeslets. First consider the $r_{bc} = r$ case with $r_{exact} = 1$ for varying r. Figures 4.9 – 4.11 show the velocity error versus r for three different values of N. These figures show that for each value of the spreading

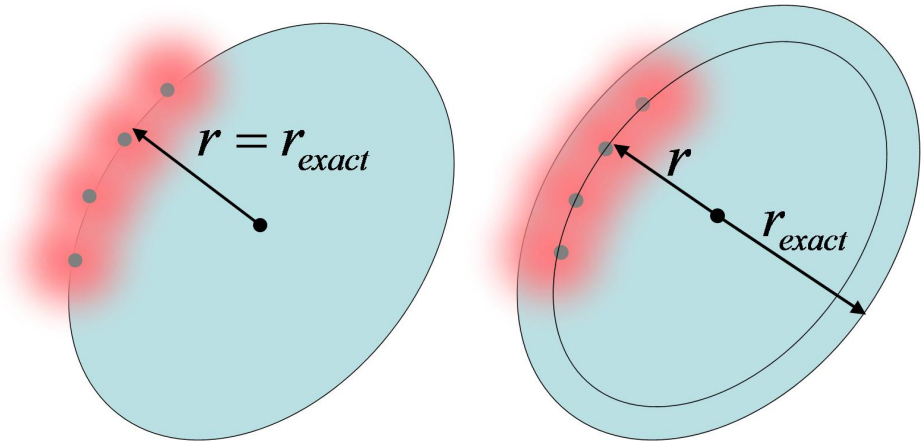

(a) (b)

FIGURE 4.8. Visualization of regularized Stokeslets placed (a) on the surface of and (b) inset from the surface of the spheroid. The shading demonstrates how that the net effect of an arrangement of regularized Stokeslets may have a larger effective radius than that of their placement at r. The radius of the spheroid used in the exact solution is denoted r_{exact} and the radius of the spheroid where the regularized Stokeslets are placed is r. The slenderness parameter remains fixed.

parameter, ϵ, there is a distinct radius, r, where the error is minimized. Define the optimal radius r_{opt} as:

$$r_{opt}(\epsilon, h) \quad = \quad \{R : |\mathbf{u}(\mathbf{x}, r_{exact}) - \tilde{\mathbf{u}}(\mathbf{x}, R, \epsilon, h)| = \min_{r} |\mathbf{u}(\mathbf{x}, r_{exact}) - \tilde{\mathbf{u}}(\mathbf{x}, r, \epsilon, h)|\}, \tag{4.4}$$

where $\mathbf{u}(\mathbf{x}, r_{exact})$ is the velocity at $\mathbf{x}$ calculated with the exact solution for a spheroid of radius r_{exact} and $\tilde{\mathbf{u}}(\mathbf{x}, r, \epsilon, h)$ is the velocity computed at $\mathbf{x}$ with N regularized Stokeslets spaced approximately h apart (see (4.1)) with spreading parameter ϵ that are placed on a the surface of a spheroid of radius r. That is, the error is minimized when the regularized

Stokeslets are placed on a surface of radius r_{opt}. In Figures 4.9 – 4.11, this equates to finding the r value of each local error minimum.

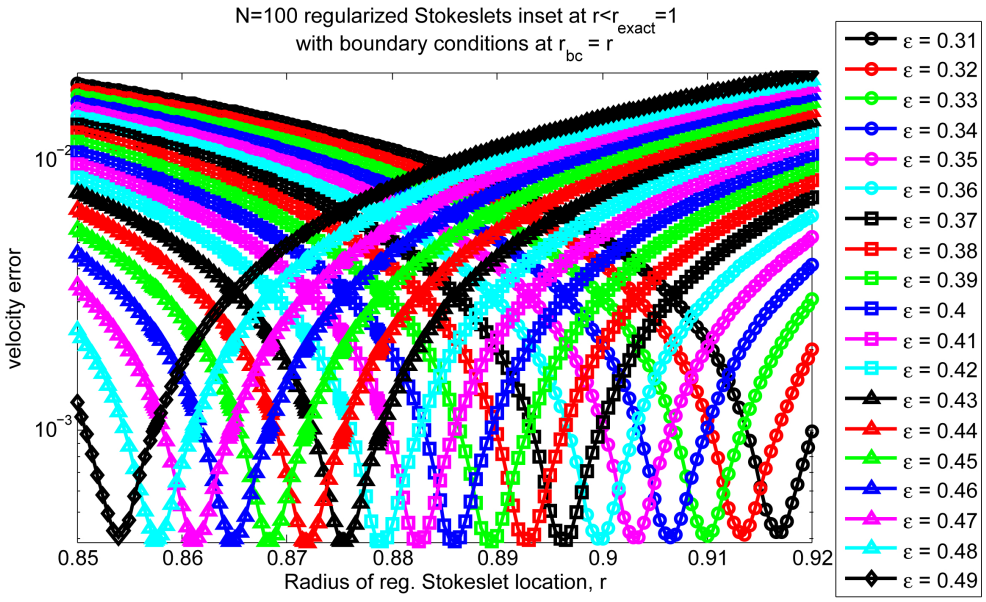

FIGURE 4.9. Velocity error averaged over 14 fluid locations away from the precessing body generated by $N = 100$ regularized Stokeslets placed on a spheroid of radius r.

One can derive a relationship between the optimal radius, the spreading parameter, and the number of regularized Stokeslets by plotting r_{opt} versus $\frac{1}{q} = \frac{\epsilon}{h}$, as shown in Figure 4.12. There is a linear relationship between r_{opt} and $\frac{1}{q} = \frac{\epsilon}{h}$, the parameters of which depend on h. This relationship provides an analogous result to that of Chapter 3 for non-slender spheroids expressing the difference of the actual and effective spheroid radii in terms of the spreading parameter. The discrepancy between the actual and effective radii caused by regularization is the focus of the remainder of this section.

Consider a linear least squares fit of the data that has the form

$$r_{opt} = a(h)\frac{\epsilon}{h} + b(h). \tag{4.5}$$

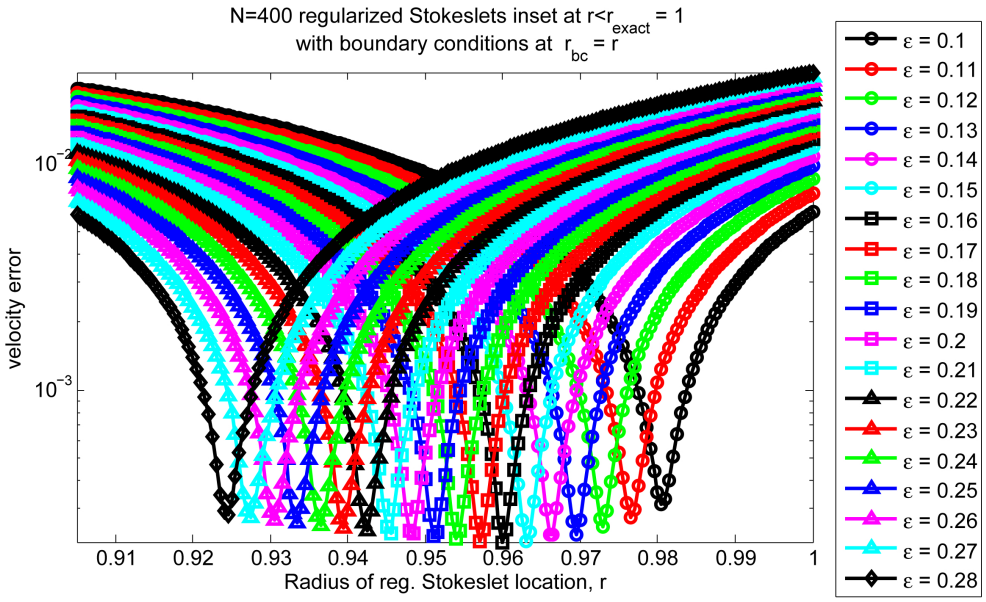

FIGURE 4.10. Velocity error averaged over 14 fluid locations away from the precessing body generated by $N = 400$ regularized Stokeslets placed on a spheroid of radius r.

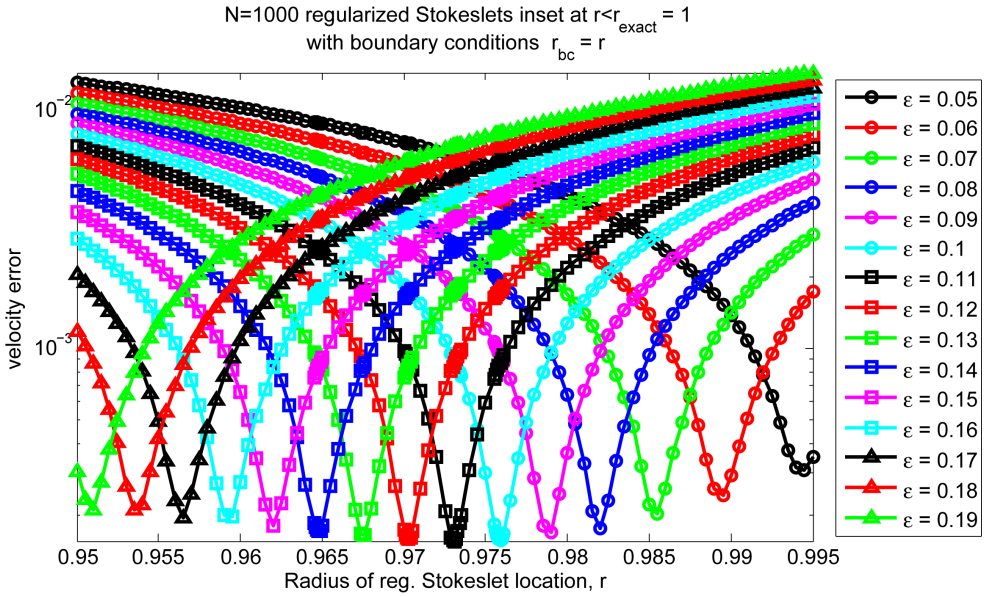

FIGURE 4.11. Velocity error averaged over 14 fluid locations away from the precessing body generated by $N = 1000$ regularized Stokeslets placed on a spheroid of radius r.

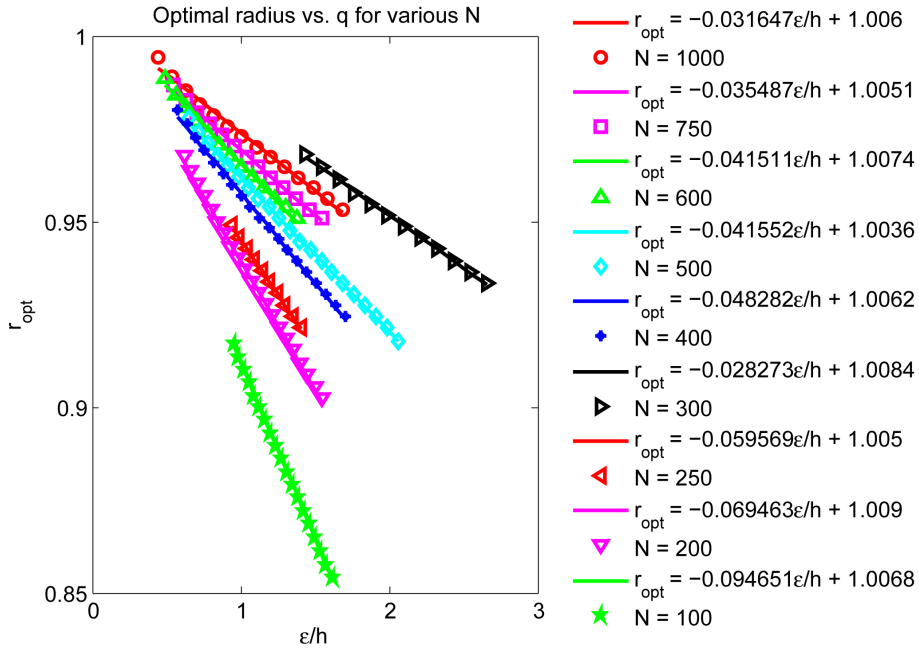

FIGURE 4.12. Optimal radius as a function of the ratio of spreading parameter to singularity spacing for various values of N. The plotted lines $r_{opt} = a\frac{\epsilon}{h} + b$ are linear least squares fits of the data for each N.

The quantities $a(h)$ and $b(h)$ are shown in Figure 4.13. A linear fit of these coefficients

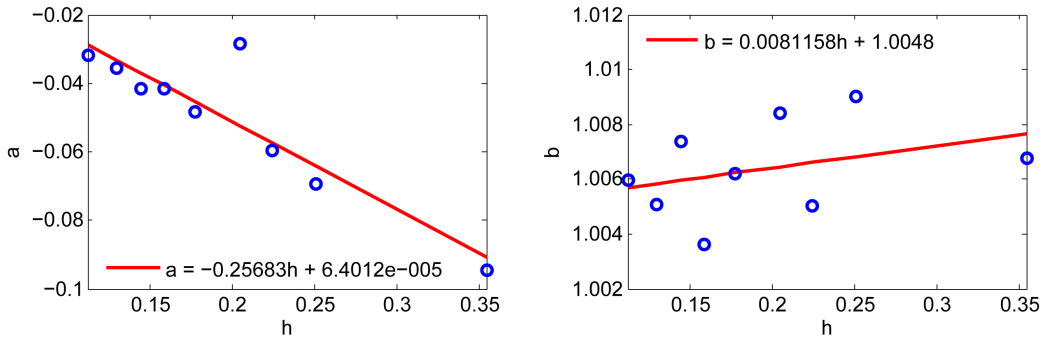

(a) (b)

FIGURE 4.13. Coefficients (a) a and (b) b plotted as a function of h from the linear fits in Figure 4.12.

leads to the following relationships:

$$a(h) = -0.25683h + 0.000064012 \tag{4.6}$$

$$b(h) = 0.0081158h + 1.0048 \tag{4.7}$$

$$= 0.0081158h + r_{exact} + 0.0048. \tag{4.8}$$

(4.5) along with $a(h)$ and $b(h)$ from (4.6) and (4.7) combine to produce a relationship between r_{opt}, ϵ, and h:

$$r_{opt}(\epsilon, h) = (-0.25683h + 0.000064012)\frac{\epsilon}{h} + (0.0081158h + 1.0048) \tag{4.9}$$

$$= -0.25683\epsilon + 0.000064012\frac{\epsilon}{h} + 0.0081158h + 1.0048 \tag{4.10}$$

or

$$r_{diff}(\epsilon, h) = r_{exact} - r_{opt}(\epsilon, h) \tag{4.11}$$

$$= 0.25683\epsilon - 0.000064012\frac{\epsilon}{h} - 0.0081158h - 0.0048, \tag{4.12}$$

when incorporating (4.8) and (4.10). Notice the dominant term on the right hand side of (4.12) scales like ϵ. The remaining terms provide fine tuning in calculating r_{diff}, but the relationship between ϵ and r_{diff} can be roughly approximated by

$$r_{diff}(\epsilon, h) \approx 0.257\epsilon. \tag{4.13}$$

That is, the distance one should inset the regularized Stokeslets is about one quarter of the spreading parameter. To investigate and refine the relationship a bit further, consider how r_{opt} relates to h, as shown in Figure 4.14.

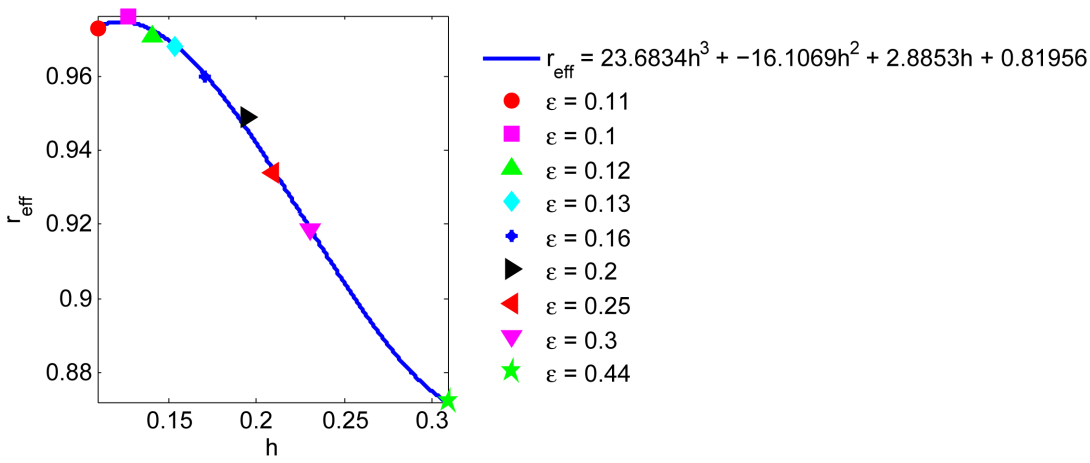

FIGURE 4.14. Optimal radius as a function of regularized Stokeslet spacing for a non-slender spheroid. The regularized Stokeslets are inset at the optimal radius, $r_{opt} < r_{exact}$, as described in (4.4).

One can also define a different optimal radius by taking the minimum of r_{opt} or the global minimum for each N:

$$r^*_{opt}(h) = \min_{\epsilon} r_{opt}(\epsilon, h). \tag{4.14}$$

Notice in Figures 4.9 – 4.11 that choosing r to be $r_{opt}(\epsilon, h)$ is quite sensitive for a given ϵ since a small variation in r can lead to a jump in error that could be an order of magnitude or more. However, choosing r near r^*_{opt} is of secondary importance because for a small variation in r, the error does not increase as dramatically as when choosing r with respect to r_{opt}. To summarize, while a detailed relationship was found between the optimal r that minimizes velocity error, spreading parameter, and the number of regularized Stokeslets used, a leading order relationship $r_{diff} = r_{exact} - r_{opt} \approx 0.257\epsilon$. As discussed in Chapter 3, when modeling a slender body with regularized Stokeslets distributed along a curve, the effective radius of the spheroid is approximately one quarter of the spreading parameter. Thus, the results of Chapters 3 and 4 reveal that regardless

of whether a spheroid is modeled with regularized Stokeslets distributed along a line or a surface, the regularization creates a larger effective geometry by a factor of one quarter of the spreading parameter for the particular cutoff function used in this study.

4.3.2. Boundary Condition at Exact Solution Radius. Consider the scenario where the velocity boundary condition is evaluated at the radius of the spheroid used in the exact solution. That is, $r_{bc} = r_{exact}$ and $r < r_{exact}$. As shown in Figure 4.15, the velocity error has a different character than those presented in Section 4.3.1. This data suggests

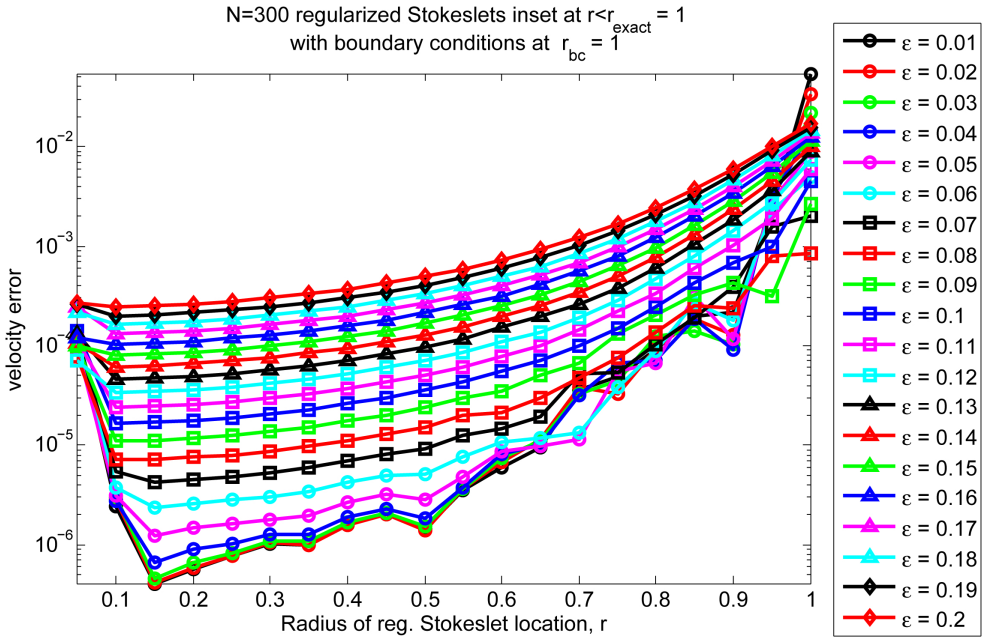

FIGURE 4.15. Velocity error averaged over 14 fluid locations away from the precessing body generated by 300 regularized Stokeslets placed on a spheroid of radius r for $r_{bc} = r_{exact} = 1$.

that to model a non-slender spheroid, the velocity error will decrease as you inset the regularized Stokeslets farther within the surface of the spheroid in the exact solution. At first this seems counterintuitive that for fixed ϵ and N, as r decreases, so does the velocity error.

Consider the velocity error on the surface of the spheroid used in the exact solution with radius r_{exact}. Let $\mathbf{x}_{0,bc}$ represent the location of the boundary condition evaluation for a regularized Stokeslet at $\mathbf{x}_0$ that is projected onto the surface of the spheroid. The surface velocity error will be calculated at both $\mathbf{x}_{0,bc}$ as well as locations between the boundary condition evaluation points. Let $\hat{\mathbf{x}}$ represent the points that approximately bisect the distance between neighboring $\mathbf{x}_{0,bc}$. These points are calculated by projecting the midpoint between neighboring $\mathbf{x}_{0,bc}$ points onto the surface of the spheroid. Figure 4.16 shows the velocity error on the surface at $\mathbf{x}_{0,bc}$ as a function of r for various values of ϵ. Notice that for r near $r_{exact} = 1$, the error at $\mathbf{x}_{0,bc}$ is small, but as r decreases, the error jumps to approximately 10^{-4}. This is not fully understood at this point, but seems to be related to the convergence (or lack thereof) of GMRES.

Notice that the velocity error jumps dramatically when $r \approx 0.9$. This is due to the fact that GMRES did not converge in solving for the force exerted at the spheroid. It is expected that the velocity error at $\mathbf{x}_{0,bc}$ is small by definition, since the velocity boundary conditions are imposed there. However, the value of the velocity error at $\hat{\mathbf{x}}$ is not necessarily small since $\hat{\mathbf{x}}$ lies away from $\mathbf{x}_{0,bc}$ where the velocity is imposed.

Figure 4.17 shows the velocity error on the surface at $\hat{\mathbf{x}}$ between boundary condition locations. Notice that when the regularized Stokeslets are placed near r_{exact}, the velocity error is larger than when the regularized Stokeslets are set further in from the spheroid's surface. As the points where the velocity is evaluated on the surface move further away from the regularized Stokeslets, the regularization effect diminishes on the surface, as discussed in Section 3.2. Notice as $r \to 0$, the velocity error at $\hat{\mathbf{x}}$ levels off around 10^{-4}, which is the same order of magnitude as the velocity error at $\mathbf{x}_{0,bc}$ when GMRES fails to converge. Again, it is not completely understood why GMRES fails to converge in

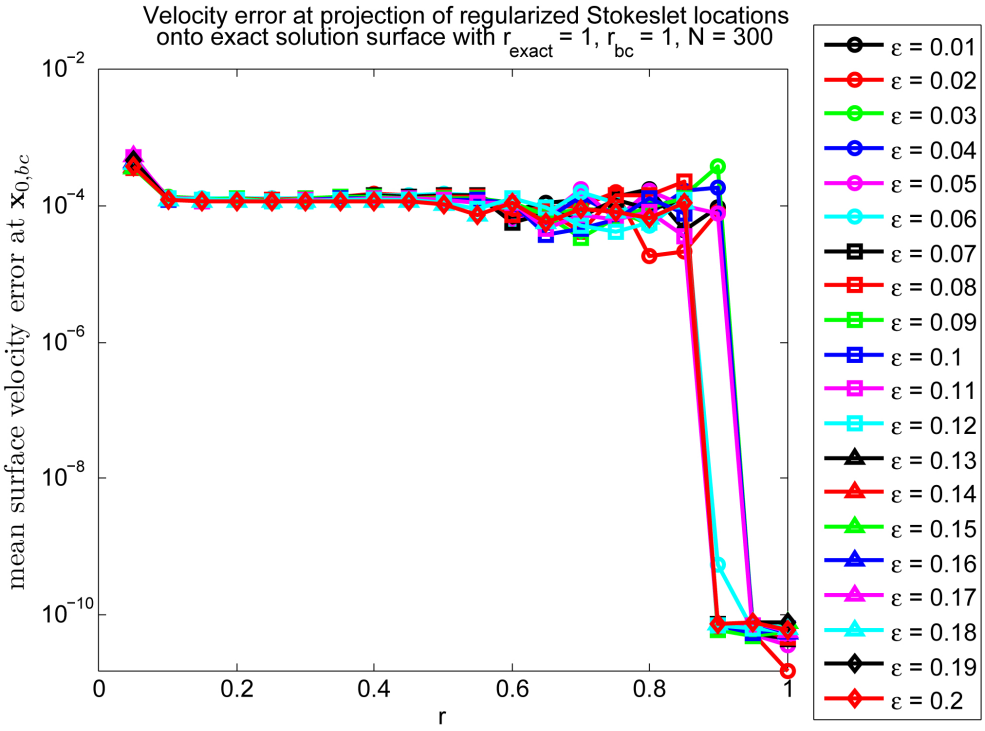

FIGURE 4.16. Velocity error at projected regularized Stokeslet locations on surface ($\mathbf{x}_{0,bc}$) versus radius of regularized Stokeslet placement r for $N = 300$.

these cases. This is a topic of future investigation. The intriguing behavior in these plots, particularly the sudden change in the convergence of GMRES, leads one to investigate the condition number of the matrix in question, which will be discussed in Section 4.4. Before discussing the condition number, it should be noted that while it appears advantageous to inset the regularized Stokeslets within the spheroid in the exact solution and evaluate the velocity boundary condition at the surface of the exact solution, this may not be practical or logical when modeling a different geometry.

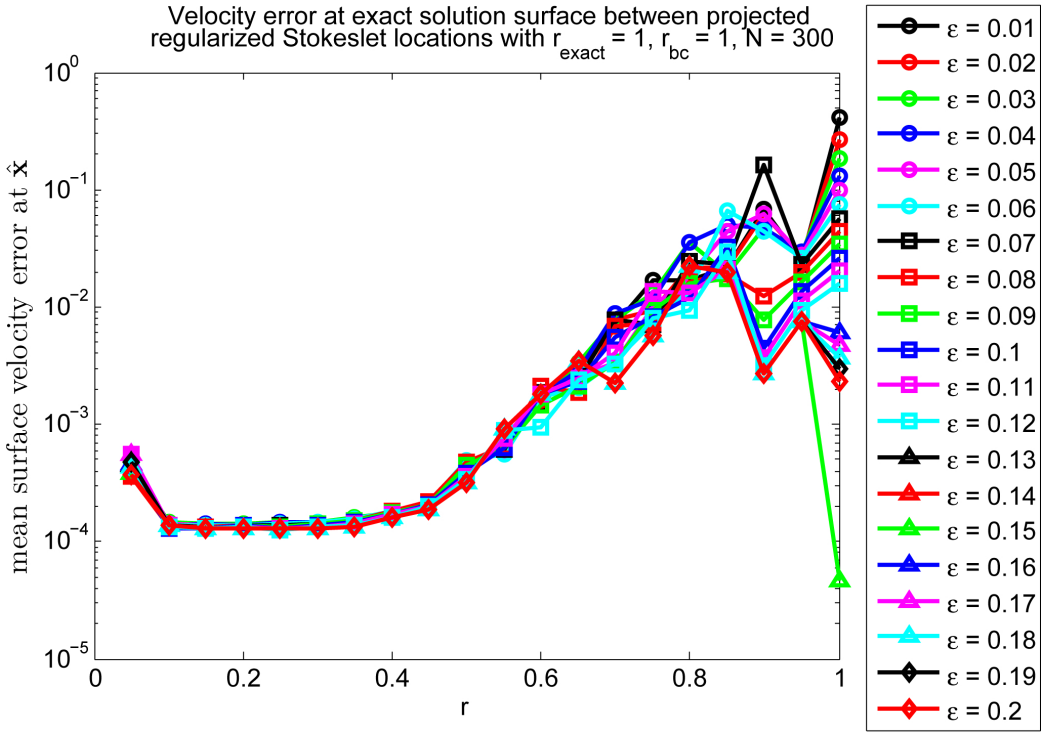

FIGURE 4.17. Velocity error between neighboring projected regularized Stokeslet locations on surface ($\hat{\mathbf{x}}$) versus radius of regularized Stokeslet placement r for $N = 300$.

4.4. Condition Number

Consider investigating the condition number of the matrix, $A = \frac{1}{8\pi\mu} S_{ij}^{\phi_\epsilon}$ (from (2.39)), relating the singularity strength, $\mathbf{f}$, with the velocity computed at the collection of regularized Stokeslets, $\mathbf{u}$, by $\mathbf{u} = A\mathbf{f}$. Both scenarios that were discussed in sections 4.3.1 and 4.3.2 are discussed in this section. Regularized Stokeslets are placed on an inset surface and the boundary condition is evaluated either at the location of the regularized Stokeslets ($r_{bc} = r$) or the projected location on the surface of the spheroid used in the exact solution ($r_{bc} = r_{exact}$). When $r_{bc} = r$, the condition number increases as $\frac{h}{\epsilon}$ decreases, as shown in Figure 4.18 for $N = 1000$.

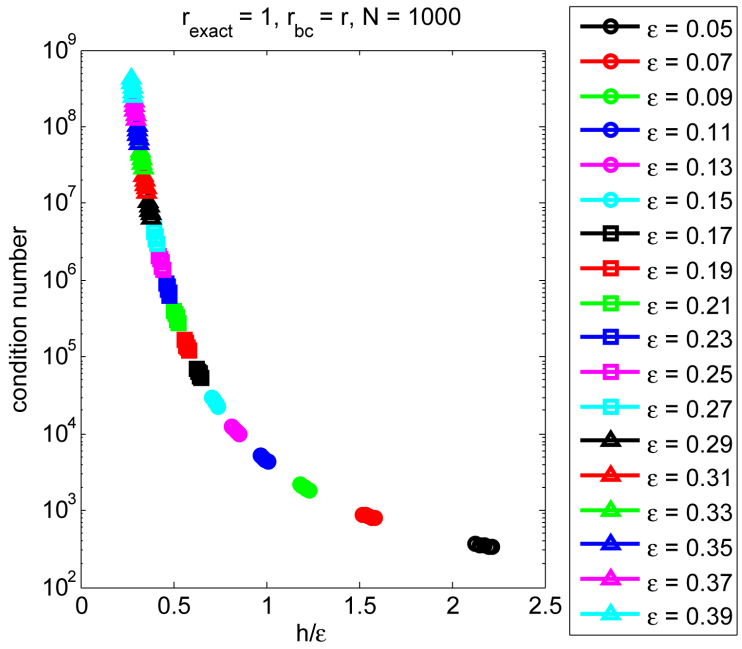

FIGURE 4.18. Condition number versus q for varying ϵ and r.

To avoid potentially losing numerous significant digits in the accuracy of the computed singularity strengths, one can consider $q = \frac{h}{\epsilon} > c$ and eliminate concerns about the condition number. Recall from Section 4.2 that the optimal choice of fixed q is approximately 2.75, as shown in Figure 4.6. As mentioned in Section 3.5, keeping $q > 0.5$ helps avoid ill-conditioned matrices. Thus, when $q \approx 2.75$ is used when regularized Stokeslets are placed on the surface, the system is well-conditioned.

Figure 4.19 shows the condition number versus q for $N = 300$ with $r_{bc} = r$ (Figure 4.19(a)) and $r_{bc} = r_{exact}$ (Figure 4.19(b)) when the regularized Stokeslets are inset from the surface used in the exact solution. Notice in Figure 4.19(a) when the boundary condition is evaluated at the location of the regularized Stokeslets, the condition number decreases as q decreases and remains somewhat manageable in magnitude. However, as shown in Figure 4.19(b), the decreasing trend is still somewhat visible, but the magnitude of the condition number is significantly larger in this case where the boundary condition

is imposed at the radius of the exact solution. Notice that for each value of ϵ there is a consistent trend that the condition number varies dramatically within the ranges sampled. For instance, when $\epsilon = 0.01$ in the $r_{bc} = 1$ case, the condition number changes by six orders of magnitude, whereas the range of condition numbers for the same spreading parameter value in the $r_{bc} = r$ case varies less than one order of magnitude. To compare

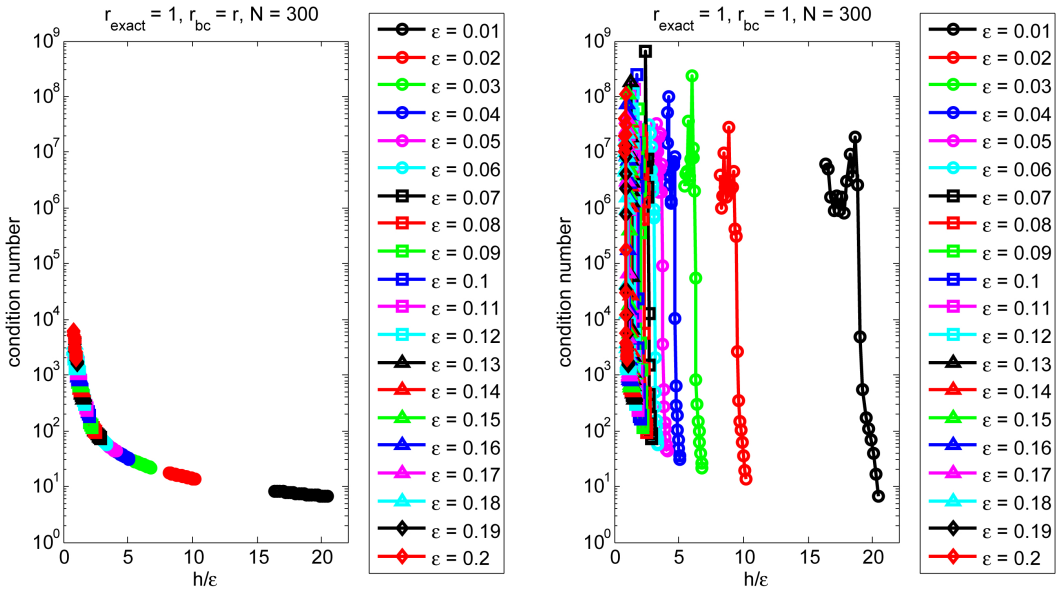

(a) (b)

FIGURE 4.19. Condition number versus $q = \frac{h}{\epsilon}$ for N=300 regularized Stokeslets with (a) $r_{bc} = r$ and (b) $r_{bc} = r_{exact}$.

the condition number of the matrix A with the velocity error on the surface of the spheroid at $\mathbf{x}_{0,bc}$ and $\hat{\mathbf{x}}$, consider the condition number as a function of regularized Stokeslet placement, r. Figure 4.20 shows the condition number versus r for $N = 300$, $r_{exact} = 1$, and $r_{bc} = r_{exact}$. Notice that the condition number increases as r decreases, but there is a small jump around $r = 0.9$. This corresponds to the region of Figure 4.16 where the surface velocity error jumps to approximately 10^{-4}, due to the fact that GMRES does

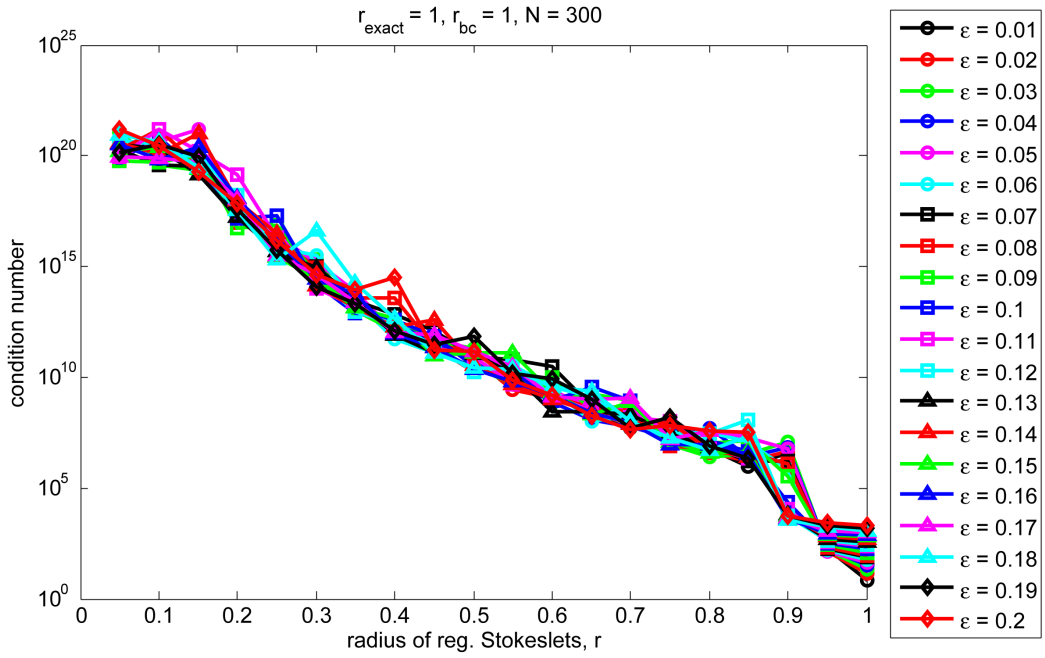

FIGURE 4.20. Condition number versus r for various ϵ with $r_{bc} = r_{exact}$.

not converge for these parameters. It is not fully understood why the condition number behaves as it does and why GMRES fails to converge in this instance.

For comparison, the surface velocity error at $\mathbf{x}_{0,bc}$ and $\hat{\mathbf{x}}$ are shown in figures 4.21 and 4.22, respectively. These plots show that as the radius where the regularized Stokeslets are placed decreases, the velocity error on the surface of the spheroid used in the exact solution decreases despite a large condition number. This suggests that as you inset the regularized Stokeslets by a larger distance, the error at the surface decreases. One possible explanation for this is that the nuances of the choices of spreading parameter and singularity spacing, for instance, are less noticeable at locations that are further away from their locations. In some sense, this corresponds with the idea used in the exact solution of Camassa *et. al.* discussed in Section 1.3.1. In these solutions, the singularities are placed on the centerline of the spheroid to impose boundary conditions on the surface of a prolate spheroid. The trend suggested in Figures 4.21 and 4.22 is

that the regularized Stokeslets should be concentrated near the center of the spheroid to minimize the velocity error on the surface of the spheroid. However, this analysis should be taken lightly due to the GMRES convergence issues that are not completely understood. Figure 4.23 shows the condition number versus r for both $r_{bc} = r$ and

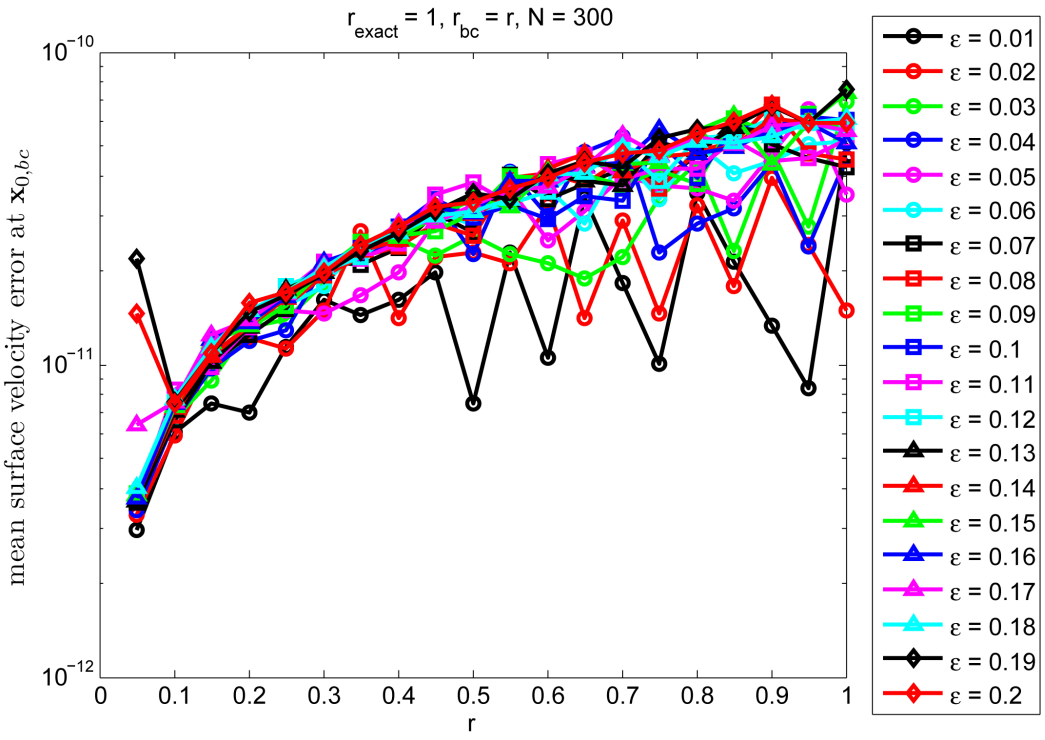

FIGURE 4.21. Mean surface velocity error at $\mathbf{x}_{0,bc}$ versus r for various ϵ with $r_{bc} = r$.

$r_{bc} = r_{exact}$ cases, but with a smaller r range on the horizontal axis than in Figure 4.20.

4.5. Summary

This chapter presents information on how to distribute regularized Stokeslets and choose parameters to effectively model the fluid velocity resulting from a non-slender spheroid precessing about its center in free space. The following observations are made throughout the discussion:

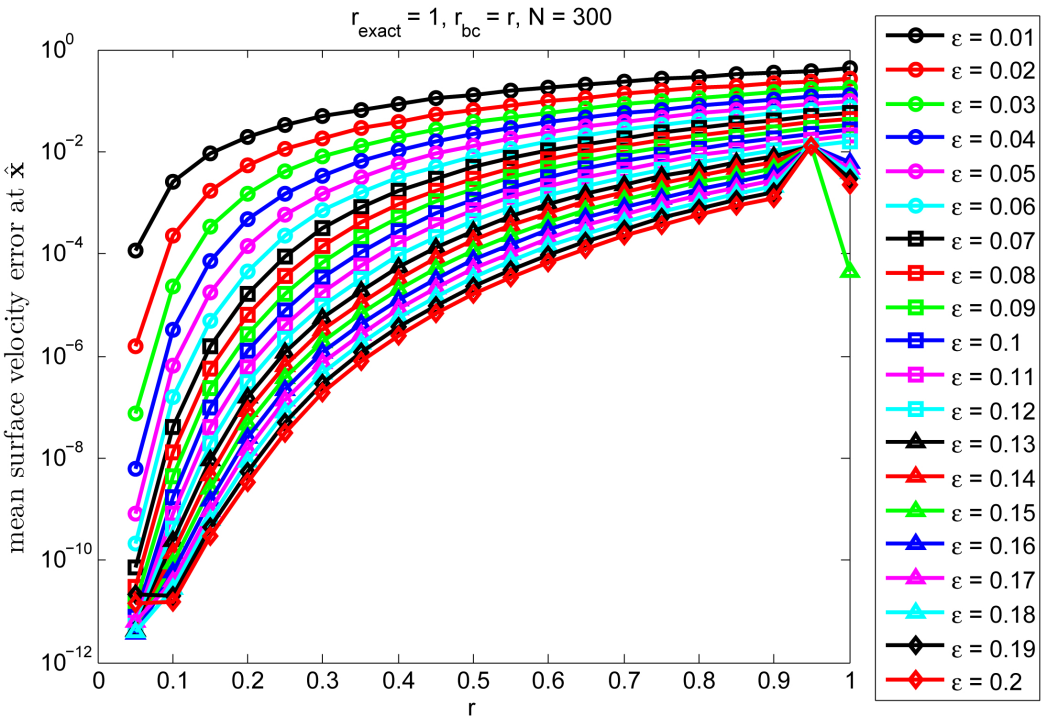

FIGURE 4.22. Mean surface velocity error at $\hat{\mathbf{x}}$ versus r for various ϵ with $r_{bc} = r$.

- When regularized Stokeslets are placed on the surface of a spheroid with fixed $q = \frac{h}{\epsilon}$, linear convergence in ϵ results, suggesting the presence of an effective radius related to the spreading parameter. Taking this into account, placing the regularized Stokeslets on a surface slightly smaller than the desired spheroid was studied to determine the parameter relationships that create an effective spheroid that matches the size of the desired spheroid in the exact solution.
- It was found that the discrepancy between the radius of the spheroid in the exact solution and the radius where the regularized Stokeslets should be placed to minimize initial velocity error is approximately one quarter of the spreading parameter. This is for the case when the boundary condition is evaluated at the location of the regularized Stokeslets, but evaluating the boundary condition at

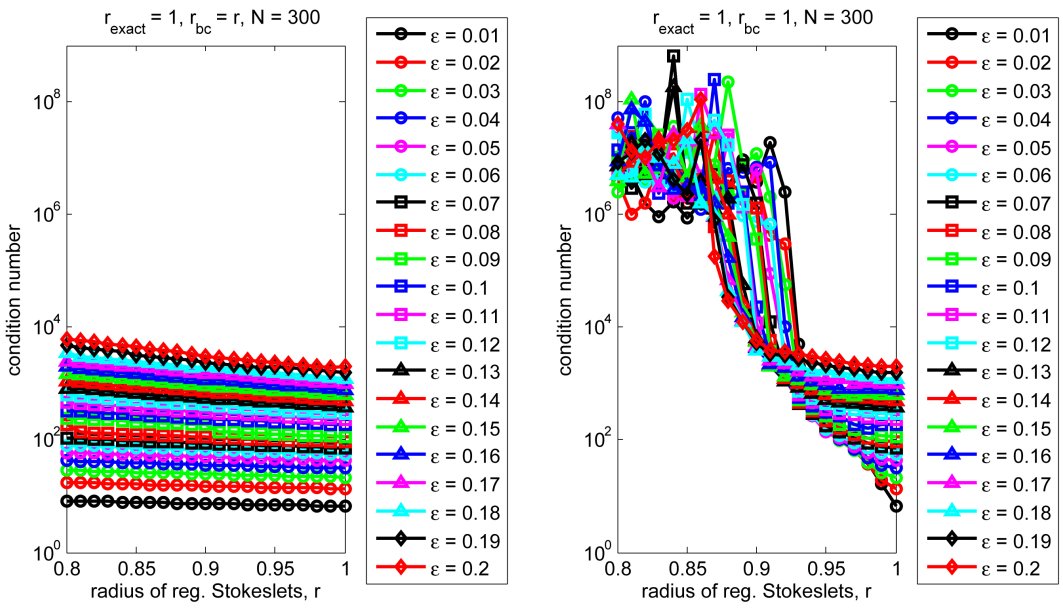

(a) (b)

FIGURE 4.23. Condition number versus r for N=300 regularized Stokeslets with (a) $r_{bc} = r$ and (b) $r_{bc} = r_{exact}$.

the projection of the inset regularized Stokeslets onto the larger surface of the spheroid in the exact solution was also studied.

- The scenario where the regularized Stokeslets are inset and the boundary condition is evaluated away from their location ($r_{bc} = r_{exact}$) is less desirable than the two aforementioned scenarios due to condition number concerns that are not fully understood.

In Chapter 3, the relationship between parameter choices and boundary conditions that minimize the initial velocity error was determined for slender spheroids precessing about their center in free space. This chapter achieved the same goal, except for non-slender spheroids. In both cases, the effective radius of the slender and non-slender spheroids increases by approximately one quarter of the spreading parameter used, as a result of regularization.

CHAPTER 5

A Multi-rate Numerical Integrator for Regularized Stokeslets

This chapter presents a new strategy for the temporal integration of regularized Stokeslets velocities which can increase the efficiency of problems with stiff boundaries. The use of a system of regularized singularities connected by virtual springs to model flexible structures interacting with a surrounding fluid was popularized by the seminal work of Peskin and Peskin and McQueen [**51, 52, 53, 54**]. In these works, the immersed boundary method is used to model the dynamics of simplified models of the human heart. The physical membranes of the heart are modeled by a collection of discrete delta functions which transfer force to the surrounding incompressible fluid (that is discretized with a standard projection method). To mimic the stiffness of the membranes, forces are generated at the singularity positions through a linear spring law applied to pairs of neighboring singularities. When the membranes are stiff, the underlying ODE governing the discretized fluid/structure dynamics is also stiff. In many immersed boundary applications, this stiffness restricts the size of the maximum stable time step to be much smaller than the CFL limit of the associated projection method.

The immersed boundary technique has since been widely applied in diverse applications ranging from the motion of molecular motors [**2**] to the unfolding of parachutes [**38**]. The ease of implementation of the immersed boundary method has also led to the use of stiff immersed boundaries to model rigid boundaries in incompressible fluids. The

advantage of this technique is that arbitrarily complex boundaries can be easily superimposed over a uniform computational grid on which the Navier-Stokes equations are solved. The drawback is that in order to make a boundary virtually rigid, the spring forces connecting the boundary points that enforce the rigidity must be made very stiff.

Although one could use the immersed boundary method for Stokes flow, the method of Regularized Stokeslets is more attractive for many problems since it avoids the necessity of solving the full fluid equations on an underlying numerical grid. However, the use of spring forces to model stiff and rigid bodies interacting with the flow still introduces (at times severe) stiffness into the underlying temporal ODE. Due to the nonlinear and nonlocal coupling of the fluid velocity and singularity position in both the immersed boundary and regularized Stokeslets methods, constructing efficient implicit temporal integration methods for immersed boundary problems is a challenging task (see *e.g.* [**45, 48, 59**]). Therefore, a different approach to mitigate the time step constraint for stiff systems based on an explicit multi-rate approach is considered here. This method will be tested on a target application involving a rigid sphere moving in Stokes flow, although the general idea is applicable to stiff flexible boundaries in both Stokes and Navier-Stokes flows.

The multi-explicit spectral deferred correction (MESDC) method is a variation of standard spectral deferred correction methods, developed by Dutt *et. al.* [**27**], that treats different components of the physical system with a different time step. Section 5.2.1 discusses the physical context used in this work in more detail, but the general idea is that a collection of regularized Stokeslets are implemented to model an object that moves with the fluid in addition to the regularized Stokeslets that comprise the conically precessing rigid rod discussed in previous sections.

A rigid sphere is the object added to the flow in this discussion, but the framework developed can be utilized to study other immersed objects, both rigid and flexible. A dense linear system must be solved to impose the velocity boundary conditions on the spheroid/rod, and the rigidity of the sphere is enforced by a collection of stiff springs. This requires a smaller time step due to an increase in stiffness of the underlying ODE. This means that the aforementioned linear solves (which are computationally expensive for a large system of many regularized Stokeslets) need to be computed more frequently in the stiff system compared to the original system. Thus, one goal in implementing the MESDC method is to use a coarse time step for the non-stiff component which requires expensive linear solves and a smaller time step to accommodate the stiff components of the system. While implementing an implicit method may seem like a logical choice since it allows for large time steps with stiff systems, implementing an implicit method in the current context is undesirable due to the structure of the numerical method, so only an explicit treatment is considered. It will be shown in the remainder of this chapter that the MESDC method is an accurate, stable explicit method utilizing two different time steps to accommodate the needs of different components of the physical system.

The MESDC method developed here is used to integrate the fluid velocity to update a fluid particle's position. After implementing regularized Stokeslets to find fluid velocities, one must solve an ordinary differential equation to update the position of fluid particles:

$$\frac{d\mathbf{x}}{dt} = \mathbf{u}(\mathbf{x}, t). \tag{5.1}$$

While (5.1) is a vector differential equation, in the remainder of this chapter the scalar ODE $\frac{dx}{dt} = u(x, t)$ will be considered in place of (5.1). The resulting discussions in sections 5.1 and 5.2 apply to each component of the vector differential equation individually.

For certain physical scenarios, like implementing a rigid sphere interacting with a fluid, the system is stiff due to a collection of springs exerting forces on the fluid. Thus, using standard explicit ODE solvers becomes undesirable because of the time step restriction. Generally, when stiffness enters a system of differential equations, an implicit treatment is used instead of an explicit method to reduce stability concerns. However, in this implementation using regularized singularities, it is not efficient to solve for the required position and velocity information needed to implement an implicit method due to the nonlinear dependence of the regularized singularities at the location where the velocity is evaluated.

5.1. Spectral Deferred Correction Method

The basic strategy of spectral deferred correction (SDC) methods developed by Dutt *et. al.* [**27**] is to use a simple numerical scheme to compute a provisional solution for a time step and then to solve correction equations during the time step to improve the accuracy of the provisional solution. One advantage of using SDC methods is that one can compute a solution to an arbitrarily high order of accuracy using a simple numerical method.

For a general overview of the SDC method, consider this governing ordinary differential equation:

$$\begin{aligned} x'(t) &= u(t, x(t)) \\ x(a) &= x_a \end{aligned}$$

for $t \in [a,b]$ where it is assumed x_a, $x(t) \in \mathcal{C}^n$, $u : \mathbb{R} \times \mathcal{C}^n \to \mathcal{C}^n$, and u is sufficiently smooth. Consider the Picard integral equation for the solution:

$$x(t) = x_a + \int_a^t u(\tau, x(\tau))d\tau. \tag{5.2}$$

Let $\tilde{x}(t)$ represent a provisional solution to the integral (5.2) and define the residual, $E(t,\tilde{x})$, as

$$E(t,\tilde{x}) = x_a + \int_a^t u(\tau, \tilde{x}(\tau))d\tau - \tilde{x}(t). \tag{5.3}$$

Also define the error, $\delta(t)$, as the difference between the solution and the provisional solution:

$$\delta(t) = x(t) - \tilde{x}(t). \tag{5.4}$$

Substitute the error from 5.4 into the equation for the solution (5.2) to obtain

$$\delta(t) + \tilde{x}(t) = x_a + \int_a^t u(\tau, \tilde{x}(\tau) + \delta(\tau))d\tau. \tag{5.5}$$

Combining (5.5) with the residual (5.3) produces another form of the correction equation:

$$\delta(t) = \int_a^t \left[u(\tau, \tilde{x}(\tau) + \delta(\tau)) - u(\tau, \tilde{x}(\tau))\right] d\tau + E(t,\tilde{x}). \tag{5.6}$$

This form of the correction equation will be used in conjunction with the provisional solution to update the solution. The following discussion demonstrates using SDC methods with forward Euler.

The goal of SDC is to compute a solution in the ith time step, $[t_i, t_{i+1}]$. First split the time step into N_m substeps such that $t_i = t_{i,0} < t_{i,1} < \ldots < t_{i,m} < \ldots < t_{i,N_m} = t_{i+1}$, as shown in Figure 5.1. Since a spectral deferred correction method is being used, one chooses the nodes of the substeps to correspond Gaussian quadrature rules. For the

discussion and examples presented here, Lobatto nodes are used. Layton and Minion explore other choices of quadrature nodes in detail in [**40**]. Thus, the size of each substep, Δt_m, is not uniform, but is naturally defined as $\Delta t_m = t_{i,m+1} - t_{i,m}$. Now compute the

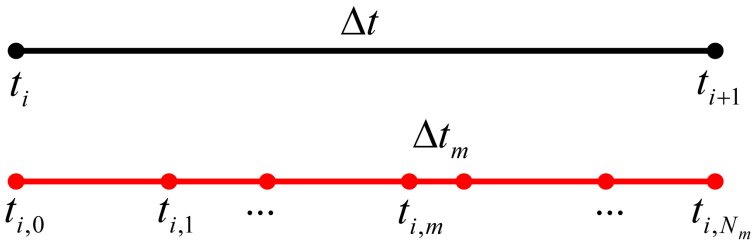

FIGURE 5.1. The ith time step $[t_i, t_{i+1}]$ is split into N_m substeps $[t_{i,m}, t_{i,m} + \Delta t_m]$, $m = 0, 1, \ldots, N_m - 1$ for use with the SDC Method.

provisional solution within the ith time step at each node of the substep level, $\tilde{x}^k(t_{i,m})$, which will be simplified notationally as $\tilde{x}^k_m$ (the superscript k denotes the iteration number that will be discussed shortly). In addition, to help simplify notation, the i subscript will be dropped when it is implied, so that $t_m = t_{i,m}$. Next, approximate the error $\delta^k_m = \delta^k(t_m)$ using the correction (5.6) and forward Euler:

$$\delta^k_{m+1} = \delta^k_m + \Delta t_m \left[u(t_m, \tilde{x}^k_m + \delta^k_m) - u(t_m, \tilde{x}^k_m)\right] + E_{m+1}(\tilde{x}^k) - E_m(\tilde{x}^k). \tag{5.7}$$

Use the residual (5.3) to compute $E_{m+1}(\tilde{x}^k) - E_m(\tilde{x}^k)$:

$$E_{m+1}(\tilde{x}^k) - E_m(\tilde{x}^k) = \int_{t_m}^{t_{m+1}} u(\tau, \tilde{x}^k(\tau))d\tau - \tilde{x}^k_{m+1} + \tilde{x}^k_m. \tag{5.8}$$

Since the solution and time values are discrete, consider replacing u in the integral in (5.8) with an interpolating polynomial

$$\hat{u}(t) = \sum_{j=0}^{N_m} u(t_j) l_j(t), \tag{5.9}$$

where $l_j(t)$ represents the jth basis polynomial that satisfies $l_j(t_i) = \delta_{ij}$. Let $I_m^{m+1}(\tilde{x}^k)$ approximate the integral in (5.8):

$$I_m^{m+1}(\tilde{x}^k) \approx \int_{t_m}^{t_{m+1}} u(\tau, \tilde{x}^k(\tau))d\tau. \tag{5.10}$$

The choice of quadrature in $I_m^{m+1}(\tilde{x}^k)$ corresponds to the choice of t_m. (5.7) can now be written as:

$$\delta_{m+1}^k = \delta_m^k + \Delta t_m \left[u(t_m, \tilde{x}_m^k + \delta_m^k) - u(t_m, \tilde{x}_m^k)\right] + I_m^{m+1}(\tilde{x}^k) - \tilde{x}_{m+1}^k + \tilde{x}_m^k. \tag{5.11}$$

Use (5.11) and $\tilde{x}^{k+1} = \tilde{x}^k + \delta^k$ to update the provisional solution:

$$\tilde{x}_{m+1}^{k+1} = \tilde{x}_m^{k+1} + \Delta t_m \left[u(t_m, \tilde{x}_m^k + \delta_m^k) - u(t_m, \tilde{x}_m^k)\right] + I_m^{m+1}(\tilde{x}^k). \tag{5.12}$$

Each iteration of the correction equation increases the order of accuracy by one, provided the quadrature in (5.10) is accurate enough.

5.2. Multi-Explicit Spectral Deferred Correction Method

This section introduces the motivating application for developing the multi-explicit spectral deferred correction method in Section 5.2.1 and develops the MESDC method in Section 5.2.2. The motivating application for developing the MESDC method is modeling a rigid sphere consisting of a network of stiff springs. In this case, as will be discussed in Section 5.2.1, the regularized Stokeslets comprising the sphere exert forces on the fluid to account for the fact that the sphere should remain rigid. The MESDC method attempts to alleviate the time step restriction by exploiting the fact that the spring forces are introducing stiffness into a localized region of the system of differential equations. The stiff and non-stiff components will be treated with different time steps to optimize

efficiency while maintaining accuracy. Section 5.2.2 discusses the MESDC method in detail.

5.2.1. Rigid Sphere Implementation. Consider the case of a rigid rod precessing about its center in free space with a prescribed angular velocity and a rigid sphere moving and interacting with the fluid, as shown in Figure 5.2. The rigid sphere is constructed

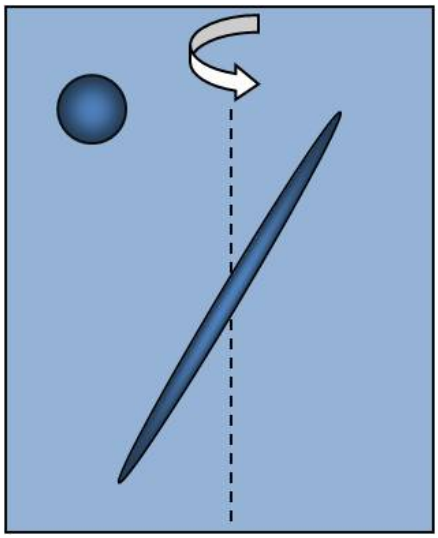

FIGURE 5.2. A rigid rod precessing with a prescribed angular velocity generates fluid flow moving a rigid sphere that also interacts with the fluid.

by regularized Stokeslets strategically placed within the fluid domain and connected by springs to neighboring regularized Stokeslets. Regularized Stokeslets connected by springs have been implemented in other works. For example, Cortez *et. al.* use regularized Stokeslets connected by springs to model motile spirochetes [**19**]. The findings of Chapter 4 can be used as a guide to choosing parameters for the regularized Stokeslets. Specifically, the regularized Stokeslets are inset so that the effective radius matches that of the desired rigid sphere and minimizes the velocity error, as discussed in Section 4.3.1. The spring forces are responsible for adding stiffness to the system, requiring a reduction in time step for an increase in the spring constant. Requiring the entire system to take

small time steps is inefficient, motivating the development of a multi-explicit spectral deferred correction method (MESDC). This method will separate the system into two parts, one for the velocity due to points on the rod and one for the velocity due to points on the sphere. Then, the rod and sphere can be treated with separate time steps using the MESDC method, with the sphere having a smaller time step and the rod having a larger time step.

Recall that the fluid velocity at $\mathbf{x}$ due to a regularized Stokeslet at $\mathbf{x}_0$ is given by $\mathbf{u}(\mathbf{x}, \mathbf{x}_0) = S^{\phi_\epsilon}(\mathbf{x}, \mathbf{x}_0)\mathbf{f}(\mathbf{x}_0)$, where S^{ϕ_ϵ} represents a regularized Stokeslet from (2.39). Let $\mathbf{x}_s$ represent a location on the sphere and let $\mathbf{x}_r$ be a location on the rod. Similarly, let $\mathbf{f}_s$ and $\mathbf{f}_r$ be forces located at $\mathbf{x}_s$ and $\mathbf{x}_r$, respectively. For the sake of completeness in notation, define the following:

- $\mathbf{u}_s = \mathbf{u}(\mathbf{x}_s, \cdot)$: velocity at points on the sphere due to forces at any fluid location
- $\mathbf{u}_r = \mathbf{u}(\mathbf{x}_r, \cdot)$: velocity at points on the rod due to forces at any fluid location
- $\mathbf{u}_{s,s} = \mathbf{u}(\mathbf{x}_s, \mathbf{x}_s) = {S^{\phi_\epsilon}}_{ss}\mathbf{f}_s$: velocity at points on the sphere due to forces at the collective points on the sphere
- $\mathbf{u}_{s,r} = \mathbf{u}(\mathbf{x}_s, \mathbf{x}_r) = {S^{\phi_\epsilon}}_{sr}\mathbf{f}_r$: velocity at points on the sphere due to forces at the points on the rod
- $\mathbf{u}_{r,r} = \mathbf{u}(\mathbf{x}_r, \mathbf{x}_r) = {S^{\phi_\epsilon}}_{rr}\mathbf{f}_r$: velocity at points on the rod due to forces at the collective points on the rod
- $\mathbf{u}_{r,s} = \mathbf{u}(\mathbf{x}_r, \mathbf{x}_s) = {S^{\phi_\epsilon}}_{rs}\mathbf{f}_s$: velocity at points on the rod due to forces at the points on the sphere.

Consider the following steps as an overview of the framework used to motivate the MESDC method, discussed in Section 5.2. A central idea here is that the fluid velocity

at an arbitrary location can be decomposed into two components, the velocity due to regularized forces exerted at points on the rod and the velocity due to regularized forces exerted at points on the sphere:

$$\mathbf{u}(\mathbf{x}) = \mathbf{u}(\mathbf{x}, \mathbf{x}_r) + \mathbf{u}(\mathbf{x}, \mathbf{x}_s). \tag{5.13}$$

Step 1: Prescribe the velocity of the rod at time t_i: $\mathbf{u}_{r,i} = \mathbf{u}_r(t_i)$.

Step 2: The rod and the sphere both exert forces on the fluid, so they will both contribute to the velocity on the rod at time t_i:

$$\mathbf{u}_{r,i} = \mathbf{u}_{r,r,i} + \mathbf{u}_{r,s,i} \tag{5.14}$$

$$= S^{\phi_\epsilon}{}_{rr,i}\mathbf{f}_{r,i} + S^{\phi_\epsilon}{}_{rs,i}\mathbf{f}_{s,i}. \tag{5.15}$$

Step 3: By assuming the sphere's initial position dictates the resting length of its springs, one concludes that $\mathbf{f}_{s,0} = 0$.

Step 4: Solve (5.15) for the forces exerted at the rod, $\mathbf{f}_{r,i}$, using GMRES:

$$\mathbf{f}_{r,i} = (S^{\phi_\epsilon}{}_{rr,i})^{-1}(\mathbf{u}_{r,i} - \mathbf{S}^{\phi_\epsilon}{}_{rs,i}\mathbf{f}_{s,i}). \tag{5.16}$$

Note that $\mathbf{f}_{r,i}$ is the only unknown quantity.

Step 5: Use the forces at the rod to calculate the fluid velocity at each location of interest on the sphere:

$$\mathbf{u}_{s,i} = \mathbf{u}_{s,r,i} + \mathbf{u}_{s,s,i} \tag{5.17}$$

$$= S^{\phi_\epsilon}{}_{sr,i}\mathbf{f}_{r,i} + S^{\phi_\epsilon}{}_{ss,i}\mathbf{f}_{s,i}. \tag{5.18}$$

Step 6: Find $\mathbf{x}_{s,i+1}$ according to $\frac{d\mathbf{x}_s}{dt} = \mathbf{u}_{s,i}$ using MESDC.

Step 7: Use Hooke's Law to calculate the spring forces generated by the new sphere locations. Let d_{i+1}^j be the new length of the jth spring and d_0^j be its resting length. For an arbitrary regularized Stokeslet location on the sphere, $\mathbf{x}_s$, let m be the number of springs attached to $\mathbf{x}_s$ and let $\hat{\mathbf{e}}_j$ be a unit vector directed along the jth spring. Then the net force on the regularized Stokeslet located at $\mathbf{x}_s$ is given by:

$$\mathbf{f}_{s,i+1} = \sum_{j=1}^{m} -k(d_{i+1}^j - d_0^j)\hat{\mathbf{e}}_j. \tag{5.19}$$

Step 8: Use $\mathbf{f}_{s,i+1}$ again in (5.15) to repeat the process for a new time interval.

This overview provides a glimpse into the interplay between solving for forces and calculating velocities at various locations of interest in the fluid. When MESDC is used in step 6 above for (5.18), notice the decomposition of the velocity evaluated at the sphere into terms that are generated by regularized forces on both the rod and the sphere. This decomposition becomes (5.20) in the discussion of the MESDC method in Section 5.2.2.

5.2.2. Multi-Explicit Spectral Deferred Correction Method. As mentioned in the Section 5.2.1, the multi-explicit spectral deferred correction method is intended to integrate a stiff ODE explicitly using different levels of time discretization. There are other variations of SDC methods that treat components of an ODE with different substeps and a mix of implicit and explicit treatments. Some of these methods are developed in the context of advection-diffusion-reaction equations in gas dynamics where there are three time scales present. In [**46**], Minion develops a semi-implicit SDC method allowing the advective component of the advection-diffusion equations to be treated explicitly while the diffusive component is treated implicitly. This idea is taken a step further in the work

of Bourlioux *et. al.* and Layton *et. al.* [**6, 39**], where the advective term of the advection-diffusion-reaction equations is still treated explicitly and the diffusive and reactive terms are treated implicitly, but now each component has different time discretizations that best accommodate the respective time scales.

In the case of the rigid sphere moving with the fluid flow created by a rod moving in a prescribed motion, as introduced in Section 5.2.1, the implementation of the sphere comprised of spring-connected regularized Stokeslets introduces stiffness into the system. As such, it is advantageous to use a small time step for the velocity due to the forces exerted by the sphere and a larger time step for the rest of the calculation that includes forces exerted away from the sphere. The decomposition of the velocity evaluated at the sphere into contributions from regularized forces exerted by both the rod and the sphere (as in (5.18)) is the starting point to consider when discussing the details of the MESDC method. Now focus on the components of the velocity at the sphere, from (5.17). To simplify the notation introduced in Section 5.2.1, define $\mathbf{u}_R = \mathbf{u}_{sr} = S_{sr}\mathbf{f}_r$ to be the velocity on the sphere due to the rod and $\mathbf{u}_S = \mathbf{u}_{ss} = S_{ss}\mathbf{f}_s$ to be the velocity on the sphere due to the forces at points on the the sphere. For locations on the sphere ($\mathbf{x}_s$) and velocities on the sphere ($\mathbf{u}_s = \mathbf{u}(\mathbf{x}_s)$), the s subscript and vector notation will often be suppressed to avoid clutter.

Now to repeat the general framework discussed in terms of the SDC method in Section 5.1, use the decomposed velocity from (5.18) to explore the MESDC method. Consider

$$x_s'(t) = u_s(t, x_s(t)) = u_R(t, x_s(t)) + u_S(t, x_s(t)) \tag{5.20}$$

$$x_s(a) = x_{s,a} \tag{5.21}$$

for $t \in [a,b]$, assuming $x_{s,a}$, $x_s(t) \in \mathcal{C}^n$, $u : \mathbb{R} \times \mathcal{C}^n \to \mathcal{C}^n$, and u is sufficiently smooth. Then the Picard integral equation for the solution (dropping the s subscripts) is

$$x(t) = x_a + \int_a^t u(\tau, x(\tau))d\tau \tag{5.22}$$

$$= x_a + \int_a^t [u_R(\tau, x(\tau)) + u_S(\tau, x(\tau))]\, d\tau. \tag{5.23}$$

Given a provisional solution to the integral equation for the ith time step, $t \in [t_i, t_{i+1}] \in [a,b]$, $\tilde{x}(t)$, define the residual $E(t,\tilde{x})$ by

$$E(t,\tilde{x}) = x(t_i) + \int_{t_i}^t [u_R(\tau, \tilde{x}(\tau)) + u_S(\tau, \tilde{x}(\tau))]\, d\tau - \tilde{x}(t). \tag{5.24}$$

Next define the error, $\delta(t)$:

$$\delta(t) = x(t) - \tilde{x}(t). \tag{5.25}$$

Combining (5.23) and (5.25) generates

$$\delta(t) + \tilde{x}(t) = x(t_i) + \int_{t_i}^t [u_R(\tau, \tilde{x}(\tau) + \delta(\tau)) + u_S(\tau, \tilde{x}(\tau) + \delta(\tau))]\, d\tau. \tag{5.26}$$

Moreover, incorporating the residual from (5.24) produces the correction equation:

$$\delta(t) = \int_{t_i}^t [u_R(\tau, \tilde{x}(\tau) + \delta(\tau)) - u_R(\tau, \tilde{x}(\tau)) + u_S(\tau, \tilde{x}(\tau) + \delta(\tau))$$

$$-u_S(\tau, \tilde{x}(\tau))]\, d\tau + E(t, \tilde{x}t). \tag{5.27}$$

Now rewrite the integral (5.27) as a weakly coupled system of integral equations:

$$\delta_R(t) = \int_{t_i}^t [u_R(\tau, \tilde{x}(\tau) + \delta_R(\tau)) - u_R(\tau, \tilde{x}(\tau))]\, d\tau + E(t, \tilde{x}) \tag{5.28}$$

$$\delta(t) = \int_{t_i}^t [u_R(\tau, \tilde{x}(\tau) + \delta_R(\tau)) - u_R(\tau, \tilde{x}(\tau)) + u_S(\tau, \tilde{x}(\tau) + \delta(\tau))$$

$$-u_S(\tau, \tilde{x}(\tau))]\, d\tau + E(t, \tilde{x}). \tag{5.29}$$

The expression for δ_R only contains terms relating to the rod, eliminating stiffness from this portion of the system. Thus, a larger time step can be used to calculate δ_R. However, δ in (5.29) incorporates velocity and error from both the rod and the sphere, so it must be treated with a smaller time step. As such, each integral in (5.28) and (5.29) can be treated with a different time step when discretized, as demonstrated in the following example.

As in the discussion of SDC methods in Section 5.1, an example using MESDC with forward Euler will be discussed here. Again, the goal is to find a solution on the ith time step $[t_i, t_{i+1}]$, which is split into N_m substeps: $t_i = t_{i,0} < t_{i,1} < \ldots < t_{i,m} < \ldots < t_{i,N_m} = t_{i+1}$. Now further split each substep into N_p substeps: $t_{i,m} = t_{i,m,0} < t_{i,m,1} < \ldots < t_{i,m,p} < \ldots < t_{i,m,N_p} = t_{i,m+1}$. Figure 5.3 shows the relationship between the time step and both levels of substeps. As discussed in Section 5.1 with regard to SDC,

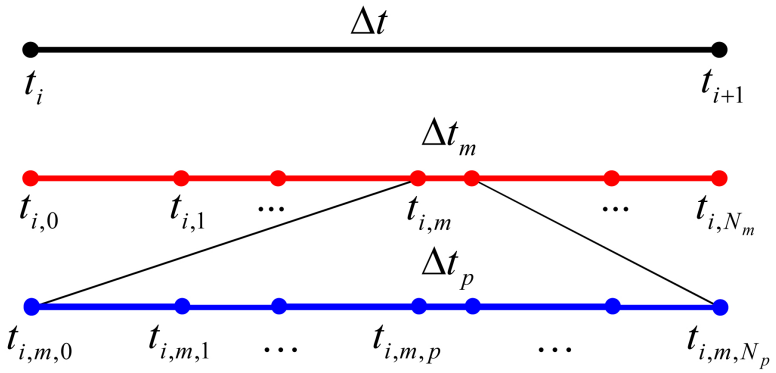

FIGURE 5.3. Time step $[t_i, t_{i+1}]$ is split into substeps for the explicit rod piece $[t_{i,m}, t_{i,m} + \Delta t_m]$ and smaller substeps for the explicit sphere contribution $[t_{i,m,p}, t_{i,m,p} + \Delta t_p]$, where $\Delta t_p \leq \Delta t_m \leq \Delta t$.

the size of each substep can vary depending on the quadrature method chosen. Again, $\Delta t_m = t_{i,m+1} - t_{i,m}$ and $\Delta t_p = t_{i,m,p+1} - t_{i,m,p}$. To simplify notation, let $t_m = t_{i,m}$ and $t_p = t_{i,m,p}$ when the deleted subscripts are understood. Now compute a provisional

solution, $\tilde{x}_{p+1}$, as follows:

$$\tilde{x}_{p+1} = \tilde{x}_p + \Delta t_p \left[u_{R,m}(\tilde{x}_m) + u_{S,p}(\tilde{x}_p) \right]. \tag{5.30}$$

Note that this solution is computed on the fine substep level (indexed by p) but it uses the velocity values due to the rod from the coarse substep (indexed by m) and velocities due to the sphere on the fine substep. That is, u_R is constant within each coarse substep. Now approximate $\delta^k_{R,m+1}$ and δ^k_{P+1} from the correction equations (5.28) and (5.29), respectively, with forward Euler:

$$\begin{aligned} \delta^k_{R,m+1} &= \delta^k_{R,m} + \Delta t_m \left[u_R(t_m, \tilde{x}^k_m + \delta^k_{R,m}) - u_R(t_m, \tilde{x}^k_m) \right] \\ &\quad + E_{m+1}(\tilde{x}^k) - E_m(\tilde{x}^k) \end{aligned} \tag{5.31}$$

$$\begin{aligned} \delta^k_{p+1} &= \delta^k_p + \Delta t_p \left[u_R(t_m, \tilde{x}^k_m + \delta^k_{R,m}) - u_R(t_m, \tilde{x}^k_m) + u_S(t_p, \tilde{x}^k_p + \delta^k_p) \right. \\ &\quad \left. - u_S(t_p, \tilde{x}^k_p) \right] + E_{p+1}(\tilde{x}^k) - E_p(\tilde{x}^k), \end{aligned} \tag{5.32}$$

where $E_{m+1}(\tilde{x}^k) - E_m(\tilde{x}^k)$ and $E_{p+1}(\tilde{x}^k) - E_p(\tilde{x}^k)$ are computed by approximating the residual (5.24):

$$E_{m+1}(\tilde{x}^k) - E_m(\tilde{x}^k) = \int_{t_m}^{t_{m+1}} \left[u_R(\tau, \tilde{x}^k(\tau)) + u_S(\tau, \tilde{x}^k(\tau)) \right] d\tau - \tilde{x}^k_{m+1} + \tilde{x}^k_m \tag{5.33}$$

$$E_{p+1}(\tilde{x}^k) - E_p(\tilde{x}^k) = \int_{t_p}^{t_{p+1}} \left[u_R(\tau, \tilde{x}^k(\tau)) + u_S(\tau, \tilde{x}^k(\tau)) \right] d\tau - \tilde{x}^k_{p+1} + \tilde{x}^k_p. \tag{5.34}$$

First consider approximating the integral from (5.33):

$$I_m^{m+1}(u_R + u_S) \approx \int_{t_m}^{t_{m+1}} \left[u_R(\tau, \tilde{x}^k(\tau)) + u_S(\tau, \tilde{x}^k(\tau)) \right] d\tau. \tag{5.35}$$

The form of $I_m^{m+1}(u_R + u_S)$ will be developed as follows, starting with the integral in (5.35) :

$$\int_{t_m}^{t_{m+1}} \left[u_R(\tau, \tilde{x}^k(\tau)) + u_S(\tau, \tilde{x}^k(\tau))\right] d\tau$$

$$= \int_{t_m}^{t_{m+1}} u_R(\tau, \tilde{x}^k(\tau)) d\tau + \int_{t_m}^{t_m} u_S(\tau, \tilde{x}^k(\tau)) d\tau \tag{5.36}$$

$$= \int_{t_m}^{t_{m+1}} u_R(\tau, \tilde{x}^k(\tau)) d\tau + \sum_{p=0}^{N_p-1} \int_{t_{m,p}}^{t_{m,p+1}} u_S(\tau, \tilde{x}^k(\tau)) d\tau. \tag{5.37}$$

Since u_R is only known at the coarse substeps (t_m's) and the integration occurs from t_m to t_{m+1}, use an interpolating polynomial to approximate the function values at all $N_m + 1$ points on the coarse substep level. Integrating u_S from t_p to t_{p+1} also requires an interpolating polynomial that matches the velocity value at each of the N_p+1 nodes of the mth fine substep. Use the known velocity values values to find interpolating polynomials $\hat{u}_R \approx u_R$ and $\hat{u}_S \approx u_S$ that will be used shortly in quadrature:

$$\hat{u}_R(t) = \sum_{m'=0}^{N_m} u_{R,m'} l_{m'}(t) \tag{5.38}$$

$$\hat{u}_S(t) = \sum_{p'=0}^{N_p} u_{S,p'} l_{p'}(t), \tag{5.39}$$

where $l_j(t)$ represents basis polynomials that satisfy $l_j(t_i) = \delta_{ij}$ for $j = m', p'$. Continuing from (5.37):

$$\int_{t_m}^{t_{m+1}} \left[u_R(\tau, \tilde{x}^k(\tau)) + u_S(\tau, \tilde{x}^k(\tau))\right] d\tau$$

$$\approx \int_{t_m}^{t_{m+1}} \sum_{m'=0}^{N_m} u_{R,m'} l_{m'}(\tau) d\tau + \sum_{p=0}^{N_p-1} \int_{t_{m,p}}^{t_{m,p+1}} \sum_{p'=0}^{N_p} u_{S,p'} l_{p'}(\tau) d\tau \tag{5.40}$$

$$\approx \sum_{m'=0}^{N_m} \int_{t_m}^{t_{m+1}} u_{R,m'} l_{m'}(\tau) d\tau + \sum_{p=0}^{N_p-1} \sum_{p'=0}^{N_p} \int_{t_{m,p}}^{t_{m,p+1}} u_{S,p'} l_{p'}(\tau) d\tau \tag{5.41}$$

$$\approx \sum_{m'=0}^{N_m} u_{R,m'} \int_{t_m}^{t_{m+1}} l_{m'}(\tau) d\tau + \sum_{p=0}^{N_p-1} \sum_{p'=0}^{N_p} u_{S,p'} \int_{t_{m,p}}^{t_{m,p+1}} l_{p'}(\tau) d\tau. \tag{5.42}$$

Defining the following

$$q_m^{m'} = \int_{t_m}^{t_{m+1}} l_{m'}(\tau) d\tau \tag{5.43}$$

$$q_p^{p'} = \int_{t_{m,p}}^{t_{m,p+1}} l_{p'}(\tau) d\tau. \tag{5.44}$$

allows (5.42) to become

$$\int_{t_m}^{t_{m+1}} \left[u_R(\tau, \tilde{x}^k(\tau)) + u_S(\tau, \tilde{x}^k(\tau))\right] d\tau$$

$$\approx \sum_{m'=0}^{N_m} u_{R,m'} q_m^{m'} + \sum_{p=0}^{N_p-1} \sum_{p'=0}^{N_p} u_{S,p'} q_p^{p'} \tag{5.45}$$

$$\approx \sum_{m'=0}^{N_m} u_{R,m'} q_m^{m'} + \sum_{p'=0}^{N_p} \sum_{p=0}^{N_p-1} u_{S,p'} q_p^{p'} \tag{5.46}$$

$$\approx \sum_{m'=0}^{N_m} u_{R,m'} q_m^{m'} + \sum_{p'=0}^{N_p} u_{S,p'} \sum_{p=0}^{N_p-1} q_p^{p'} \tag{5.47}$$

$$\approx \sum_{m'=0}^{N_m} u_{R,m'} q_m^{m'} + \sum_{p'=0}^{N_p} u_{S,p'} q^{p'}, \tag{5.48}$$

where

$$q^{p'} = \sum_{p=0}^{N_p-1} q_p^{p'}. \tag{5.49}$$

Now the form of I_m^{m+1} is defined as (5.48):

$$I_m^{m+1}(u_R + u_S) = \sum_{m'=0}^{N_m} u_{R,m'} q_m^{m'} + \sum_{p'=0}^{N_p} u_{S,p'} q^{p'}. \tag{5.50}$$

The choice of substep nodes t_m and t_p relate to the quadrature used in I_m^{m+1}.

Similarly, consider approximating the integral from (5.34):

$$I_p^{p+1}(u_R + u_S) \approx \int_{t_{m,p}}^{t_{m,p+1}} \left[u_R(\tau, \tilde{x}^k(\tau)) + u_S(\tau, \tilde{x}^k(\tau))\right] d\tau. \tag{5.51}$$

Again, to develop the form of I_p^{p+1}, begin with the integral in question and utilize interpolating polynomials:

$$\int_{t_{m,p}}^{t_{m,p+1}} \left[u_R(\tau, \tilde{x}^k(\tau)) + u_S(\tau, \tilde{x}^k(\tau))\right] d\tau$$

$$\approx \int_{t_{m,p}}^{t_{m,p+1}} \sum_{m'=0}^{N_m} u_{R,m'} l_{m'}(\tau) d\tau + \int_{t_{m,p}}^{t_{m,p+1}} \sum_{p'=0}^{N_p} u_{S,p'} l_{p'}(\tau) d\tau \tag{5.52}$$

$$\approx \sum_{m'=0}^{N_m} \int_{t_{m,p}}^{t_{m,p+1}} u_{R,m'} l_{m'}(\tau) d\tau + \sum_{p'=0}^{N_p} \int_{t_{m,p}}^{t_{m,p+1}} u_{S,p'} l_{p'}(\tau) d\tau \tag{5.53}$$

$$\approx \sum_{m'=0}^{N_m} u_{R,m'} \int_{t_{m,p}}^{t_{m,p+1}} l_{m'}(\tau) d\tau + \sum_{p'=0}^{N_p} u_{S,p'} \int_{t_{m,p}}^{t_{m,p+1}} l_{p'}(\tau) d\tau \tag{5.54}$$

$$\approx \sum_{m'=0}^{N_m} u_{R,m'} q_{m,p}^{m'} + \sum_{p'=0}^{N_p} u_{S,p'} q_p^{p'}, \tag{5.55}$$

where

$$q_{m,p}^{m'} = \int_{t_{m,p}}^{t_{m,p+1}} l_{m'}(\tau) d\tau \tag{5.56}$$

$$q_p^{p'} = \int_{t_{m,p}}^{t_{m,p+1}} l_{p'}(\tau) d\tau. \tag{5.57}$$

(5.55) produces

$$I_p^{p+1}(u_R + u_S) = \sum_{m'=0}^{N_m} u_{R,m'} q_{m,p}^{m'} + \sum_{p'=0}^{N_p} u_{S,p'} q_p^{p'}. \tag{5.58}$$

Now that (5.50) and (5.58) define I_m^{m+1} and I_p^{p+1}, respectively, all of the components of the correction equations are known. Combining (5.33), (5.34), (5.50), and (5.58) into (5.31) and (5.32) produces a new form of the correction equations:

$$\begin{aligned} \delta_{R,m+1}^k &= \delta_{R,m}^k + \Delta t_m \left[u_R(t_m, \tilde{x}_m^k + \delta_{R,m}^k) - u_R(t_m, \tilde{x}_m^k) \right] \\ &\quad + I_m^{m+1}(u_R(\tilde{x}^k) + u_S(\tilde{x}^k)) - \tilde{x}_{m+1}^k + \tilde{x}_m^k \end{aligned} \tag{5.59}$$

$$\begin{aligned} \delta_{p+1}^k &= \delta_p^k + \Delta t_p \left[u_R(t_m, \tilde{x}_m^k + \delta_{R,m}^k) - u_R(t_m, \tilde{x}_m^k) + u_S(t_p, \tilde{x}_p^k + \delta_p^k) \right. \\ &\quad \left. - u_S(t_p, \tilde{x}_p^k) \right] + I_p^{p+1}(u_R(\tilde{x}^k) + u_S(\tilde{x}^k)) - \tilde{x}_{p+1}^k + \tilde{x}_p^k. \end{aligned} \tag{5.60}$$

Finally, $\tilde{x}^{k+1} = \tilde{x}^k + \delta^k$ is used in addition to (5.59) and (5.60) to update the provisional solution:

$$\begin{aligned} \tilde{x}_{p+1}^{k+1} &= \tilde{x}_p^{k+1} + \Delta t_p \left[u_R(t_m, \tilde{x}_m^k + \delta_{R,m}^k) - u_R(t_m, \tilde{x}_m^k) + u_S(t_p, \tilde{x}_p^k + \delta_p^k) \right] \\ &\quad \Delta t_p \left[-u_S(t_p, \tilde{x}_p^k) \right] + I_p^{p+1}(u_R(\tilde{x}^k) + u_S(\tilde{x}^k)) \end{aligned} \tag{5.61}$$

Each iteration (in k) of the correction equation increases the order of accuracy by one, provided the quadrature used to calculate I_p^{p+1} is accurate enough.

5.3. Numerical Tests

The goal in implementing an MESDC method in place of a standard SDC method is to be able to handle stiff systems with a larger time step for the non-stiff components of the system than previously used with the SDC method. The stiff components will have similar small time steps in both MESDC and SDC treatments. Specifically, in

the stiff regularized singularity system outlined in Section 5.2.1, a dense linear system must be solved to recompute the singularity strengths at each time step. Since the size of the matrix involved in this linear system is $3N \times 3N$, where N is the number of regularized Stokeslets placed in the fluid, for systems whose geometry requires large N, solving the linear system becomes increasingly expensive. Thus, by implementing an MESDC method, the possibility of being able to compute this linear solve less often while maintaining accuracy will be studied. Another benefit of using MESDC instead of SDC is an increase in the stability region. Hence, the manner in which the stability of this system changes between MESDC and SDC implementations will also be investigated in this section.

To study the convergence and stability of the MESDC method in comparison to the SDC method, consider the previously mentioned system of a slender rigid rod precessing about its center in free space moving a fluid that contains a rigid sphere, as shown in Figure 5.2. To clarify, the rigid sphere is comprised of a collection of regularized Stokeslets that are connected with a network of springs. Each regularized Stokeslet is connected to its nearest neighbors by springs of spring constant k as well as the center of the sphere (with spring constant k_c). As the fluid moves these regularized Stokeslets, the displacement of the springs generates a spring force that the singularities transfer back to the fluid. This additional collection of forces then creates an additional velocity at the rod, which no longer satisfies the no-slip boundary condition we are trying to maintain on the rod. As such, the aforementioned linear system needs to be solved at each time step to account for the additional velocity created on the rod by the sphere.

First consider studying the convergence rate. With both MESDC and SDC, Sections 5.1 and 5.2 claim that the order of the error relates to the number of correction iterations

used, provided the quadrature choices are accurate enough. When $k = 0$, the correction loop of the algorithms are not used, so the SDC and MESDC algorithms simplify to forward Euler. As such, one would expect the error to decrease linearly with Δt. As claimed, each iteration will increase the order by one. Figure 5.4 shows the error versus time step (Δt) for various numbers of iterations, $n_{iter} = 0, 2, 3, 4, 5$, for both SDC and MESDC. Notationally, the iteration count n_{iter} begins with $n_{iter} = 2$ so that the order

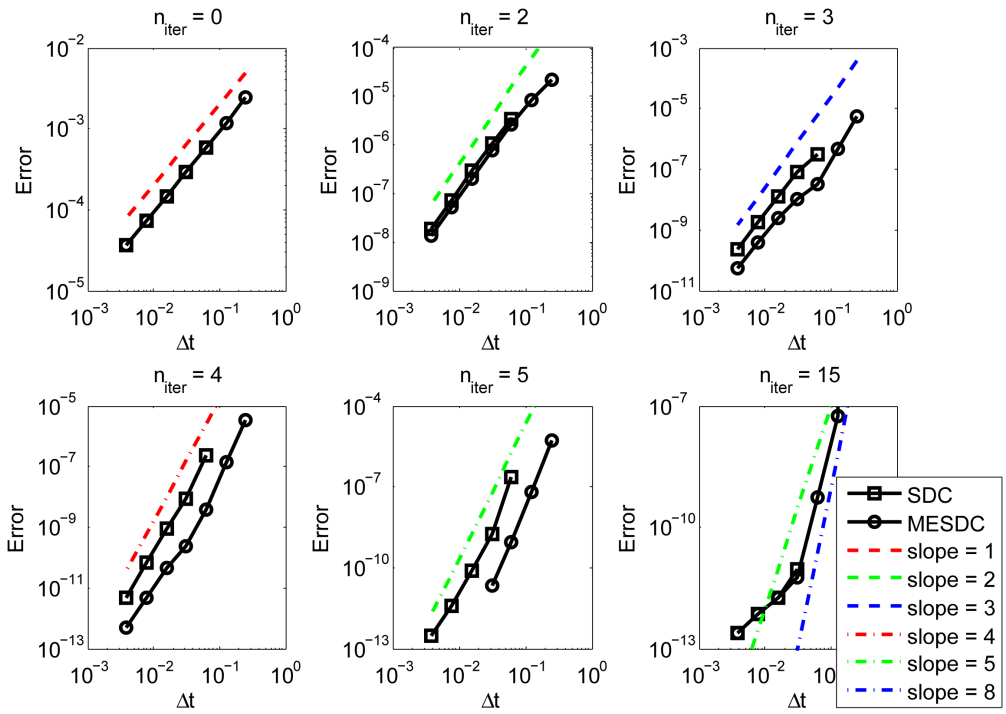

FIGURE 5.4. Error in position versus time step using SDC and MESDC for a variety of n_{iter} values (number of correction iterations). Notice that the convergence rate increases as n_{iter} increases. Here $k = 8$ and $k_c = 0.8$.

of the method will correspond with the n_{iter} value. For the data displayed in Figure 5.4, the spring constants for the sphere are $k = 8$, $k_c = 0.8$. The error here is the Euclidean norm of the error in position at a fixed time[1]. Notice that for $n_{iter} = 15$, the convergence

[1]It should be noted that the error is not being compared to a system with an actual rigid sphere, rather the numerical solution with a given set of stiffness parameters.

rate seems to approach 8 rather than 15 before leveling off as $\Delta t \to 0$. This is evidence of the quadrature convergence from choosing $j = 5$ Lobatto nodes in each substep where a convergence rate of $2j - 2$ limits the convergence rate. By choosing more nodes, one would expect this convergence rate to increase. This phenomenon is also visible in Figure 5.5 which shows the same data as Figure 5.4, except the spring constants are $k = k_c = 0$. Notice that for $n_{iter} = 4, 5, 15$, the convergence rate appears to be 8, rather than the anticipated 4, 5, or 15, respectively. The $n_{iter} = 15$ case is the same as discussed above, but the $n_{iter} = 4$ and $n_{iter} = 5$ cases are such that the convergence rate exceeds the expected rate. This is a case that since the springs have no added effect to the system, for many correction iterations the solution and provisional solution are close. Thus, the error is subdominant to the quadrature error in this case.

Now to discuss stability, consider the $n_{iter} = 5$ case, which as shown in Figure 5.4, should be 5th order. Consider sampling a variety of spring constants, k, allowing the spring constant of the center springs, k_c (which connect the center and each point on the sphere's surface), to vary proportionally to the spring constant among nearest neighbors on the surface: $k_c = 0.1k$. Consider the number of time steps $N_t = 2^n$, for $n = 2, 3, \ldots, 8$, and spring constants $k = 2^n$ for $n = 2, 3, \ldots, 6$. The $k = 0$ case will again be considered. A reference solution with $N_t = 512$ time steps per rod revolution is used to compute position errors. Figure 5.6 shows the position error versus time step for four chosen spring constants, $k = 0, 8, 16, 64$, using both SDC and MESDC. Notice that for larger Δt, as k increases, the system becomes unstable. However, for fixed k, the instability occurs at a smaller Δt for the SDC case than MESDC. This indicates an increase in stability when using MESDC over SDC. Also, notice that the MESDC error is consistently smaller than the SDC error.

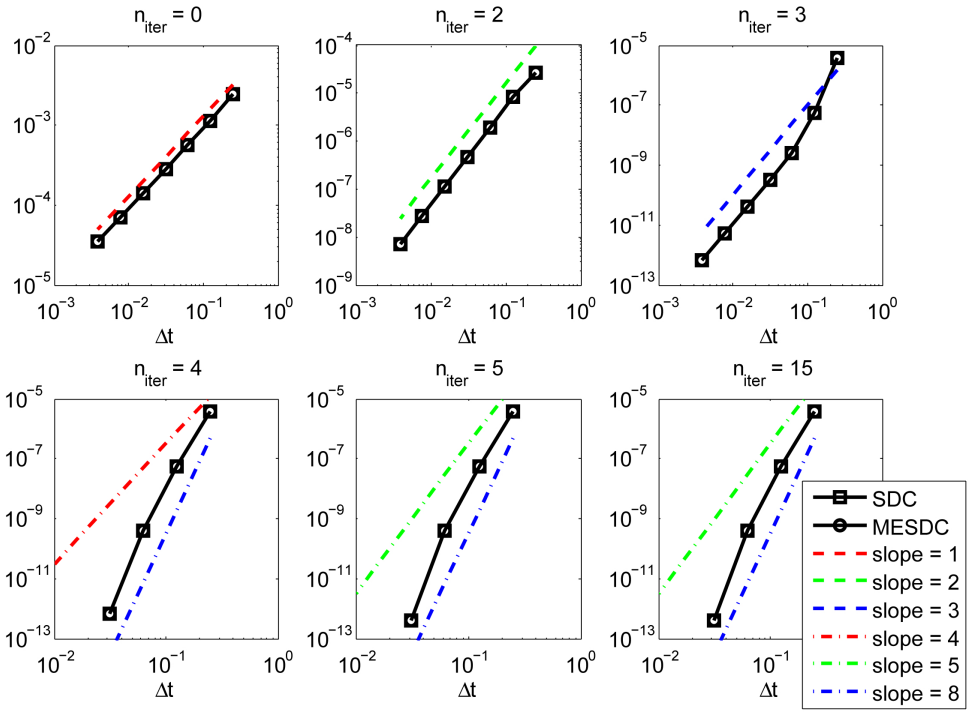

FIGURE 5.5. Error in position versus time step using SDC and MESDC for a variety of n_{iter} values (number of correction iterations). Notice that the convergence rate increases as n_{iter} increases. Here $k = k_c = 0$.

To view the same data in a slightly different context, consider plotting the error as a function of effective Δt rather than Δt, where the effective Δt takes into account the fact that MESDC adds another level of substeps. Referring to Figure 5.3, letting $N_m = 5$ and $N_p = 5$, then each time step is broken into five substeps and each of those substeps is divided into five smaller substeps. Then some portion of the calculation (the contribution from the sphere on the sphere) is computed 25 times each time step with MESDC, as opposed to the remaining contributions which are computed 5 times per time step. Looking at this same scenario in terms of SDC, all contributions are computed five times per substep. Thus, the effective Δt refers to comparing the time step of the finest level of calculation whereas just considering Δt compares the time step of the coarsest

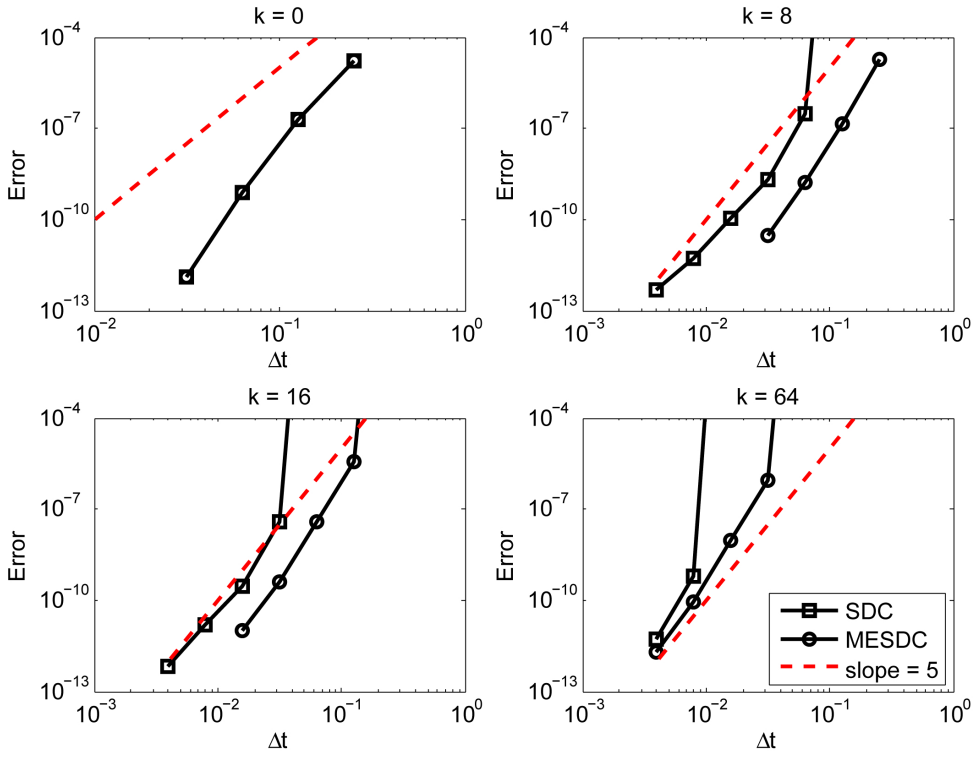

FIGURE 5.6. Error in position versus time step using SDC and MESDC for a variety of spring constants with $n_{iter} = 5$.

level of calculation (and consequently the first level of substeps which is the same size in both SDC and MESDC). In this example where $N_m = N_p = 5$, $\Delta t_{eff} = \frac{1}{5}\Delta t$ for MESDC while $\Delta t_{eff} = \Delta t$ for SDC. Figure 5.7 shows the same data as Figure 5.6, except the error is plotted against the effective time step. One noteworthy feature is that the instability occurs at approximately the same effective Δt value.

When shifting perspectives to consider effective Δt rather than Δt, the finest substeps are commensurate in size and the difference between SDC and MESDC is that the linear solves happen less frequently in the MESDC case than in the SDC case. Thus, this can either be viewed as a scenario where one might want to add a finer level of substeps for a particular portion of a calculation or, conversely, one might want to eliminate a part of a calculation on a coarser level.

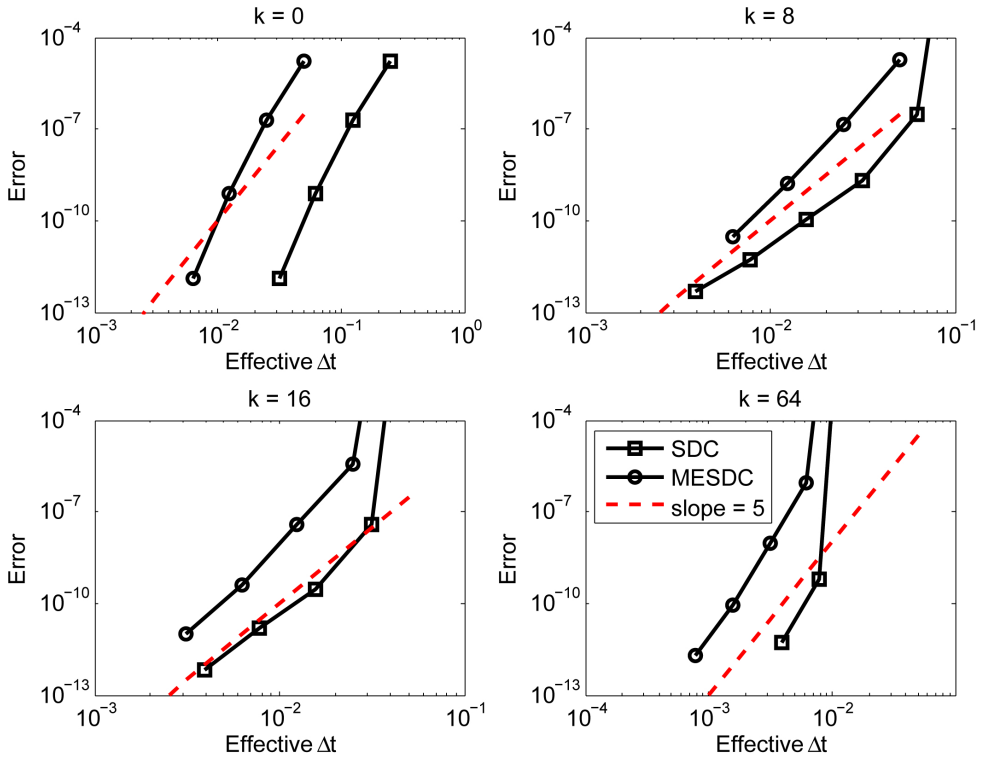

FIGURE 5.7. Error in position versus effective time step using SDC and MESDC for a variety of spring constants with $n_{iter} = 5$.

Another perspective to consider when studying the rigid sphere moving in a fluid is how spherical the points on the sphere remain throughout the course of the simulation. Initially, the regularized Stokeslets are distributed on the surface of the sphere using Centroidal Voronoi Tessellations (see Appendix G). There is also a regularized Stokeslet placed at the center of the sphere. This initial configuration determines the resting lengths of the springs. As time progresses, if the sphere were perfectly rigid, the springs connecting adjacent regularized Stokeslets (and the center) would have a constant length equal to the resting length. However, this would equate to an infinitely large spring constant and a very stiff system. As such, finite spring constants must be used to compromise. To clarify terminology, rigid will be used to describe a collection of points whose relative displacement to each other remains constant as a rigid body would. The term

soft will be used to describe a collection of points which are passive tracers in the flow (when $k = 0$). Let d_i^j represent the length of the jth spring at time t_i, then the resting length of the jth spring is denoted d_0^j. For a rigid sphere, $d_i^j = d_0^j$ for all i. For finite spring constants, the normalized displacement $\frac{|d^j - d_0^j|}{d_0^j}$ will be viewed as a measure of the sphere's rigidity. The mean normalized displacement at time t_i is represented by η_i:

$$\eta_i = \frac{1}{N_s} \sum_{j=1}^{N_s} \frac{|d_i^j - d_0^j|}{d_0^j},$$

where N_s is the number of springs used to construct the sphere. Figure 5.8 shows the mean normalized displacement, η, as a function of time for a variety of spring constants. The horizontal lines in Figure 5.8 represent the time average of the mean normalized displacement, $\bar{\eta}$:

$$\bar{\eta} = \frac{1}{N_T} \sum_{i=1}^{N_T} \eta_i,$$

where N_T is the total number of time steps[2]. Figure 5.9 displays $\bar{\eta}$ as a function of time step as well as spring constant. The magnitude of $\bar{\eta}$ is much larger than the magnitude of the error from the time integrator, so the rigidity remains relatively constant with respect to Δt. However, the rigidity varies linearly with spring constant, k.

5.4. Summary

The multi-explicit spectral deferred correction method is effective in the context of modeling the flow generated by a precessing rod with an additional rigid object in the flow. The MESDC method is a novel, accurate, stable, efficient explicit method which allows the non-stiff components of a system to be treated with a larger time step than the stiff components, reducing the number of necessary expensive linear solves. The time

[2]In Figure 5.8, the time average is over 5 rod revolutions, so $N_T = 5N_t$, where N_t is the number of time steps per rod revolution.

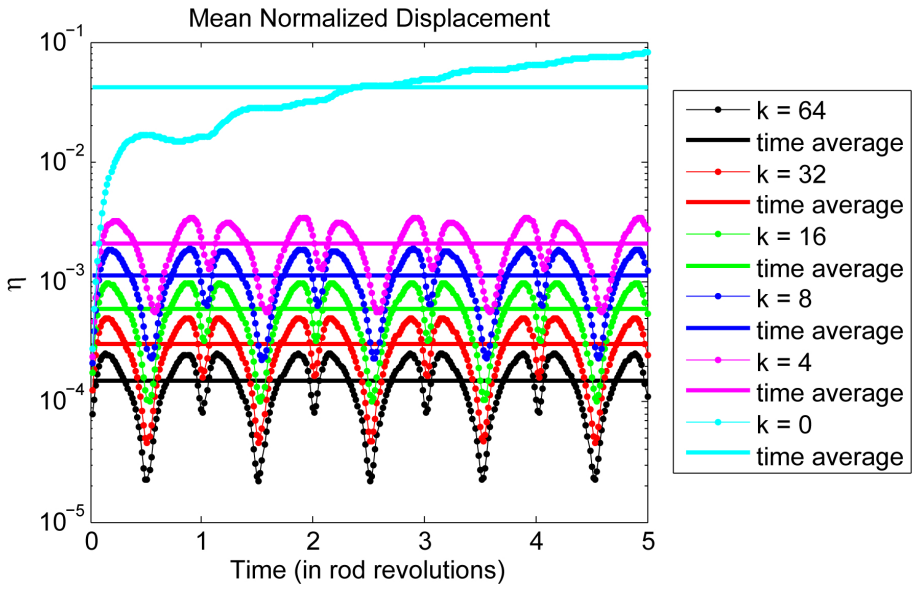

FIGURE 5.8. Mean normalized displacement (η) of points on the sphere as a function of time. The horizontal lines represent the time averaged mean normalized displacement ($\bar{\eta}$).

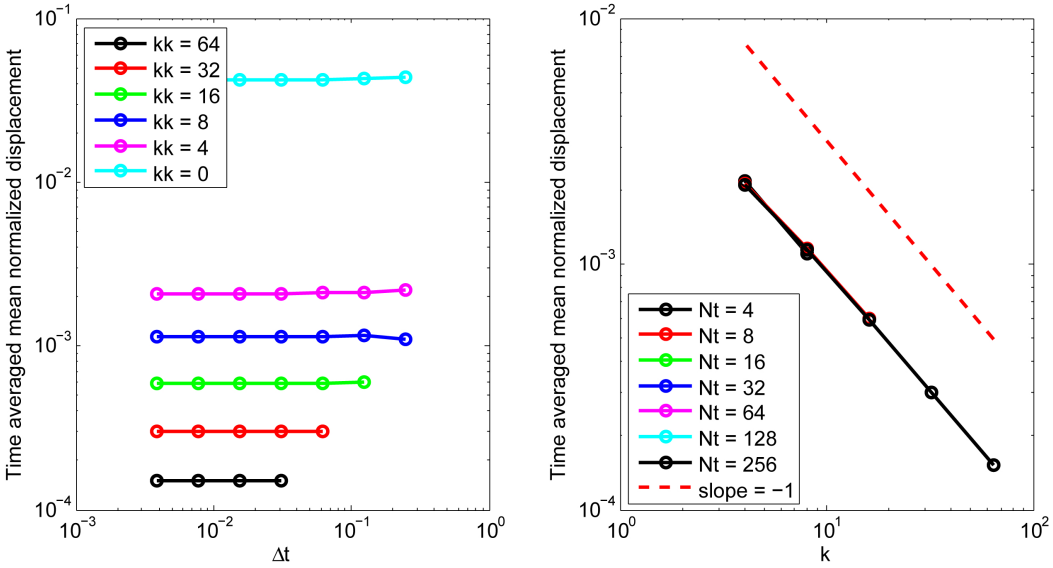

FIGURE 5.9. Time averaged mean normalized displacement versus time step and spring constant.

integration error can easily be made small with respect to the error components in the

system, such as regularization, slenderness, and quadrature error, that were discussed in Section 3.2.

CHAPTER 6

Rotational Mixing Experiments

This chapter focuses on using the numerical solution to model experimental results from the Rotational Mixing Experiment (RMX)[1]. Two cases will be considered. First, motivated by the primary nodal cilia introduced in Section 1.1, the hydrodynamics of a rod precessing about a tilted axis in a semi-infinite fluid will be discussed. Second, motivated by the micro-scale experiments of Jing [**37**] mentioned in Section 1.2, the hydrodynamics of a bent rod precessing about a vertical axis in a semi-infinite fluid will be presented [**8**]. Both of these discussions use the numerical solution to verify interesting hydrodynamic behavior present in the laboratory experiments.

As mentioned in Section 1.2, challenges of the experimental work of Jing on the micro-scale along with the mathematical theory of Camassa *et. al.* and Leiterman serve as motivation for the Rotational Mixing Experiment (RMX) [**7, 10, 42**]. The RMX experimental setup consists of a metal pin held to the bottom of a cubical tank of viscous fluid by a magnet mounted on a motor below the tank. When properly calibrated, the magnetic field causes the pin to precess about a vertical axis through its contact point with the bottom of the tank. The viscous fluid used in the RMX experiments is corn syrup. To visualize the fluid motion, small bubbles are inserted into the corn

[1]The discussion in this section often refers to the researchers involved with the RMX group. Please see the acknowledgements section at the beginning of this dissertation for a complete listing of the people involved in the various components of the RMX research effort.

syrup and then tracked during post-processing analysis. Bouzarth *et. al.* present more details of the experimental setup in [**7**]. For a straight rod sweeping an upright cone, the RMX trajectory results match fairly well with the predicted trajectories produced by the Blakeslet solution discussed in Section 1.3.3. However, there are some experimental questions which the asymptotic solution may not be able to describe or may lack validation to confidently use that solution as the only mathematical tool. A numerical solution can provide insight into the fluid dynamics and also serve as a guide for building new analytical solutions. The two cases beyond a straight pin sweeping out a vertical cone, a rod precessing about a tilted axis and a bent rod, will be discussed in Sections 6.1 and 6.2, respectively.

6.1. Tilted rod

Studying the hydrodynamics of a tilted rod is valuable because it more closely corresponds to the motion of primary nodal cilia than the vertical cone structures that have been examined thus far. Hirokawa *et. al.* suggest that each primary nodal cilium beats about a tilted axis. Figure 6.1 shows the tilted rod scenario discussed in this section, including τ, the tilt angle of the axis of rotation from vertical. While Cartwright has studied the hydrodynamics of this system using rotlets in free space [**15**] and full three dimensional Navier-Stokes equations [**14**], this is a question that the RMX group desires to study experimentally in conjunction with the numerical and asymptotic mathematical models of Bouzarth *et. al.* [**9**].

The hydrodynamics of a tiled rod are of interest to the RMX research group as a biologically relevant scenario to study in low Reynolds number macro-scale fluid dynamics experiments. As part of the RMX group's research effort, the fluid flow generated by a

tilted rod was studied using the regularized singularity numerical solution discussed in this dissertation. In addition, Bouzarth *et. al.* incorporated a tilted axis of precession into the Blakeslet solution of Camassa *et. al.* and Leiterman, discussed in Section 1.3.3 [**9, 10, 42**]. The results using both of the mathematical and numerical modeling techniques show qualitative agreement and interesting flow properties. The details of implementing a single macro-scale pin precessing about a tilted axis experimentally are not fully worked out yet, but the study of tilted rods experimentally is a future research plan for the RMX group, augmented by the findings of the work of Bouzarth *et. al.* [**9**]. Another experimental opportunity stemming from the RMX group comes from Evans *et. al.* and Carstens *et. al.* who create arrays of biomimetic cilia on the micro-scale. They can actuate these cilia so that each cilium's motion approximately precesses about a tilted axis. In this case, they observe directional flow, which is suggestive of the observed nodal flow [**13, 28, 29**]. Their preliminary findings are consistent with the numerical and mathematical observations of the RMX group thus far [**9**].

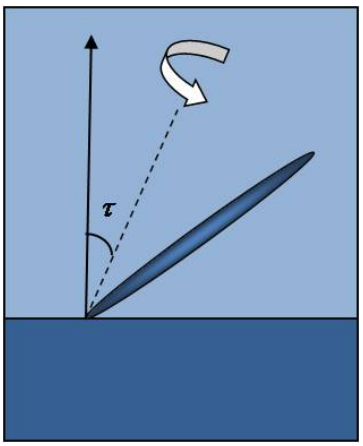

FIGURE 6.1. Sketch of a slender rod precessing about an axis tilted off vertical by a tilt angle, τ, above a no-slip plane.

The main question being considered here in conjunction with the aforementioned models and experiments is if one tilted rod can generate fluid transport. The idea being that if one rod can generate transport, then the hydrodynamics of a collection of rods (as in the nodal region) may be able to generate a directional flow, as happens in the nodal region. By studying this simplified case where experiment, mathematical models and numerical simulations overlap, one can learn of the hydrodynamic effects and use this information in conjunction with biological research to develop a fuller understanding of this system.

Figures 6.2 and 6.3 show side and top views of fluid particle trajectories resulting from modeling a tilted rod with regularized Stokeslets and the corresponding system of regularized image singularities discussed in Section 2.5. The results are for three different tilt angles are shown: $\tau = 0$, $\tau = \frac{\pi}{10}$, and $\tau = \frac{\pi}{5}$ in subplots (a), (b), and (c), respectively. Note that $\tau = 0$ corresponds to a standard vertical cone as discussed in previous chapters. The following parameters are used: cone angle $\kappa = \frac{\pi}{6}$, rod length $L = 1$, spreading parameter $\epsilon = 0.025$, and number of regularized Stokeslets $N = 100$. The computed data is shown for a time span of 1000 rod rotations. There are nine fluid locations sampled. The initial position of these locations stays fixed with respect to the rod as it tilts in each case. That is, for the upright cone, the markers are placed in a horizontal line and as the cone angle increases, the line of markers rotates so that the line of markers is parallel to the top of the cone structure. The initial tracer locations are marked by green circles in the side view images shown in Figure 6.2. The bottom of each plot coincides with the bottom of the fluid tank where the no-slip velocity boundary condition is imposed. For perspective of the rod position relative to the fluid markers, the rod position is superimposed for a variety of time steps, denoted by the blue lines.

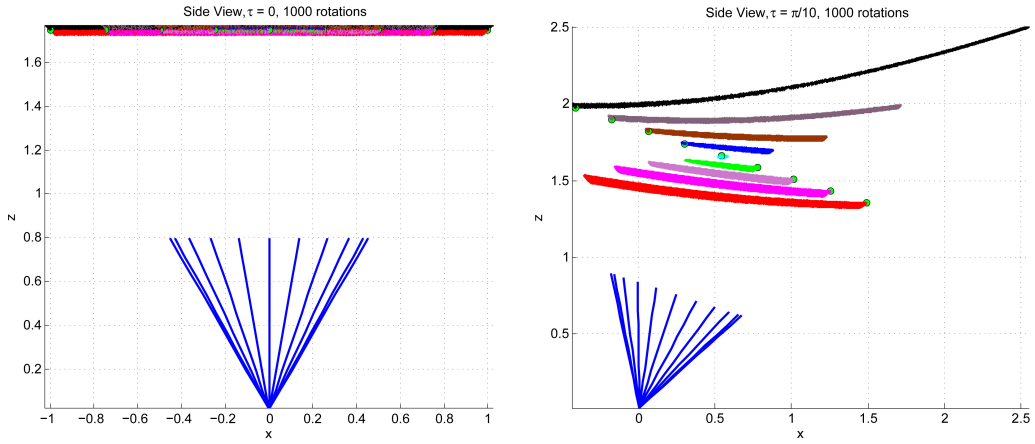

(a) (b)

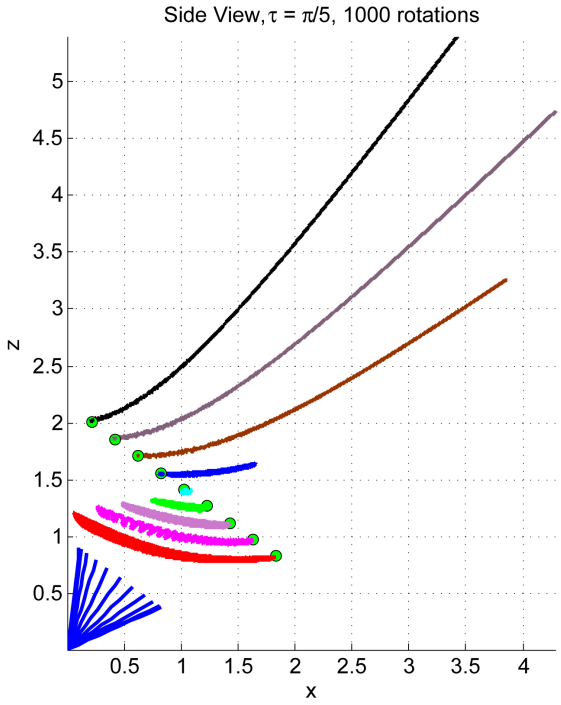

(c)

FIGURE 6.2. Side view of trajectories of nine initial conditions, fixed with respect to the cone that the rod sweeps through. The tilt angle varies from (a) $\tau = 0$ to (b) $\tau = \frac{\pi}{10}$ to (c) $\tau = \frac{\pi}{5}$. The initial positions are marked by green circles. Each trajectory is shown for 1000 rod rotations. Image produced in conjunction with Bouzarth *et. al.* (RMX group work in preparation) [**9**].

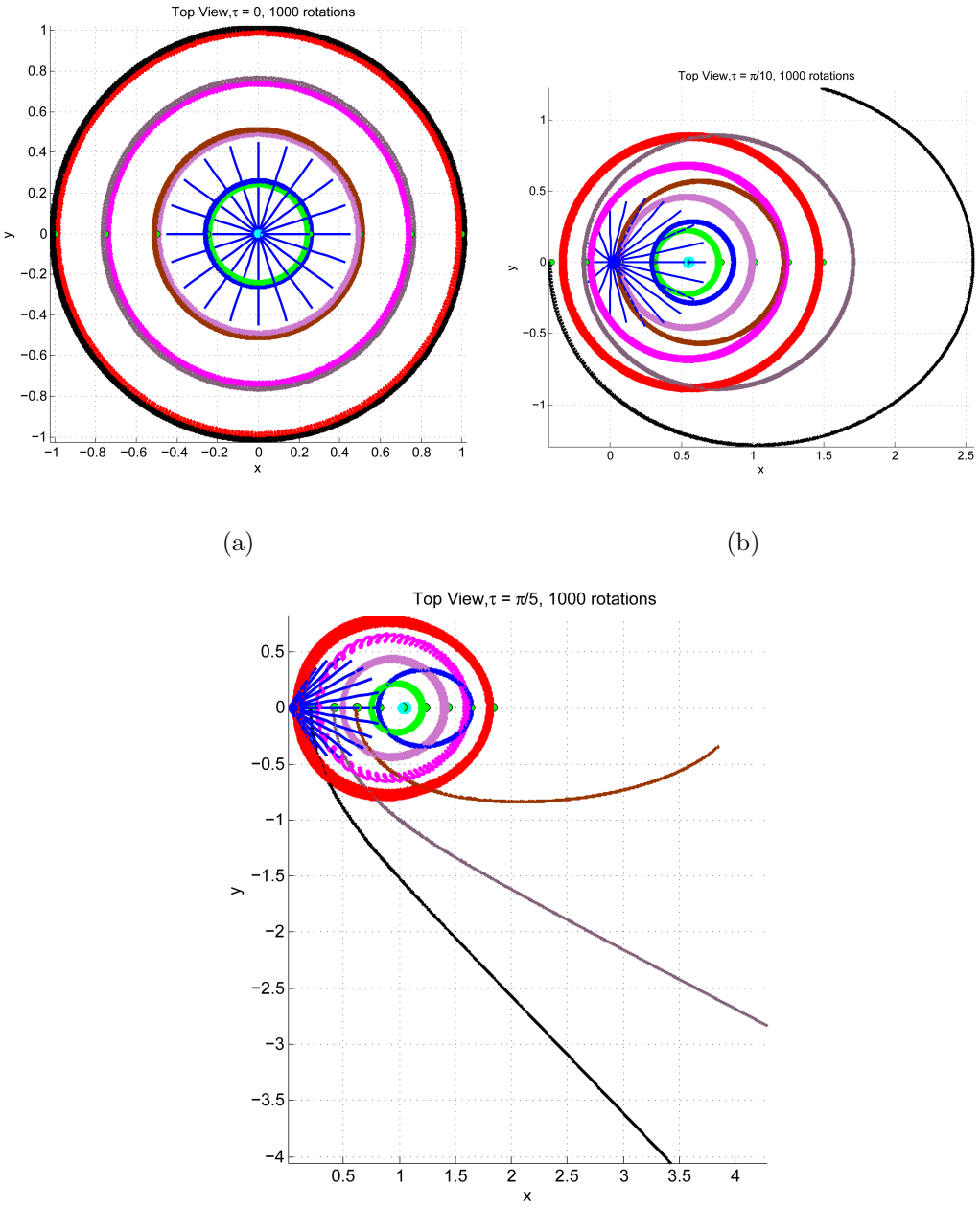

(a) (b)

(c)

FIGURE 6.3. Top view of trajectories of nine initial conditions, fixed with respect to the cone that the rod sweeps through. The tilt angle varies from (a) $\tau = 0$ to (b) $\tau = \frac{\pi}{10}$ to (c) $\tau = \frac{\pi}{5}$. The initial positions are marked by green circles. Each trajectory is shown for 1000 rod rotations. Image produced in conjunction with Bouzarth *et. al.* (RMX group work in preparation) [**9**].

Figure 6.3 shows the same data as Figure 6.2, but viewed from the top rather than the side. Notice as the tilt angle increases, the tracer trajectories change dramatically in both their horizontal and vertical motion. These figures only capture the general trends of the trajectories, but by zooming in, one can see that there is epicyclic structure on a smaller scale. Figure 6.4 shows a portion of two trajectories for $\tau = 0$ taken from Figure 6.3(a).

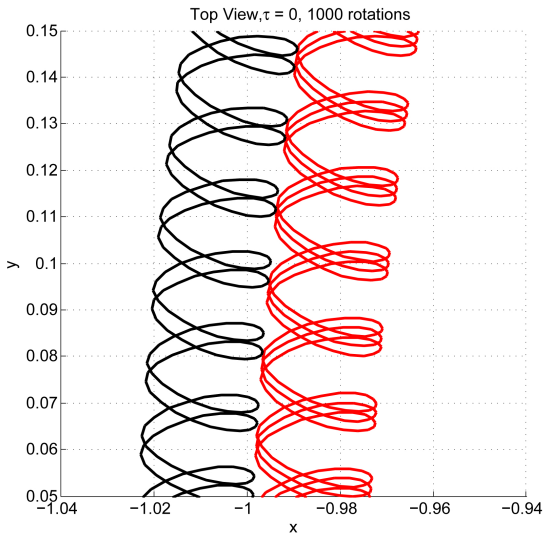

FIGURE 6.4. A zoomed in top view of a portion of two trajectories from the $\tau = 0$ top view shown in Figure 6.3(a). This demonstrates the fine scale structure that is lost in the way the data is displayed in Figures 6.2 and 6.3. Image produced in conjunction with Bouzarth *et. al.* (RMX group work in preparation) [**9**].

Another way to view the effect of a tilted cone is by looking at the radial and vertical components of each trajectory with respect to time. The radial and vertical positions are calculated in cylindrical coordinates with respect to the origin, defined as the contact point of the rod with the floor. Figures 6.5 and 6.6 show the radial and vertical positions as a function of time, respectively. Again, some structure is lost by viewing the data over

such a long time scale. As such, Figure 6.7 shows the same data as Figure 6.6, except over a shorter time interval.

Regardless of how one views this data, it is evident that tilting the axis of precession with respect to the no-slip plane has a dramatic effect on the fluid flow. The trajectories change in such a way that there are large vertical and horizontal departures from the trajectories generated by the $\tau = 0$ vertical case. As such, this supports the idea that a system of tilted rods can generate bulk transport of a fluid. While the trajectories change dramatically as the tilt angle increases, it appears that the trajectories eventually overlap with themselves in such a way to suggest that a single rod does not produce transport by itself. However, if one considers the case of primary nodal cilia where there are typically tens of somewhat rigid cilia precessing about tilted axes (that are all tilted the same direction), then one can imagine that the large vertical and horizontal excursions of fluid particles in motion due to a tilted precessing rod might cause a fluid parcel to travel into a neighboring cilium's hydrodynamic influence. As such, fluid may get passed from one tilted precessing rod to the next, to the next, etc., producing the net effect of fluid transport. Using regularized singularities to model a tilted rod as shown here can be adapted to model multiple tilted precessing rods. Exploring scenarios with multiple rods that are more closely related to the physical setup of primary nodal cilia is a topic of future work.

6.2. Bent rod

One of the questions resulting from studying Jing's micro-scale experimental results [**37**] is what effect a precessing bent rod would have on the resulting fluid particle trajectories. The RMX group implemented a precessing bent rigid rod in the macro-scale

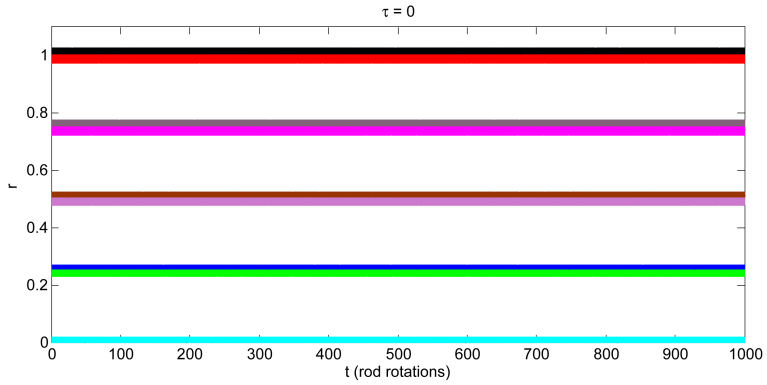

(a)

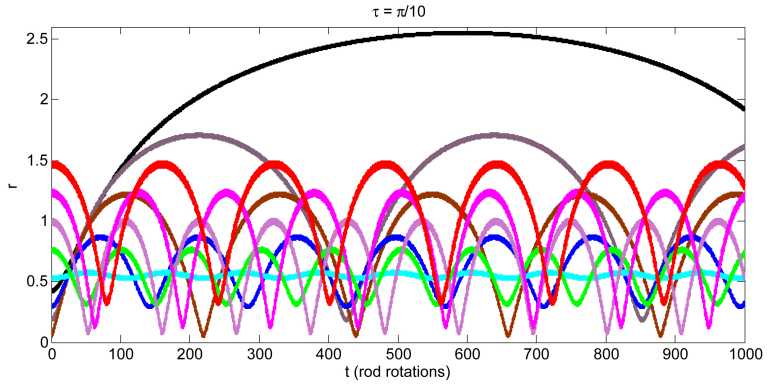

(b)

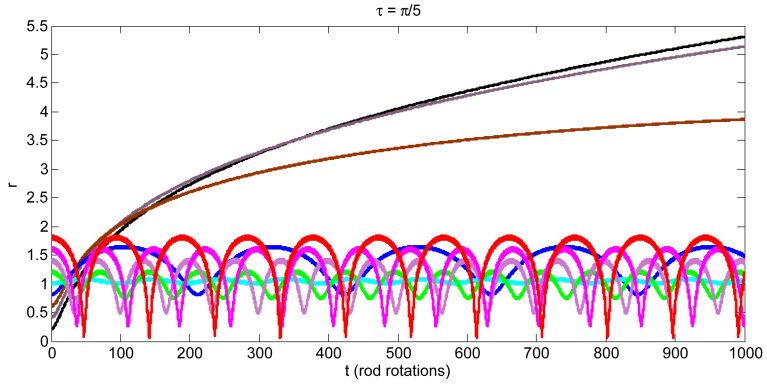

(c)

FIGURE 6.5. Radial position versus time measured in rod rotations for the nine markers depicted in Figures 6.2 and 6.3. The tilt angle varies from (a) $\tau = 0$ to (b) $\tau = \frac{\pi}{10}$ to (c) $\tau = \frac{\pi}{5}$. Image produced in conjunction with Bouzarth *et. al.* (RMX group work in preparation) [**9**].

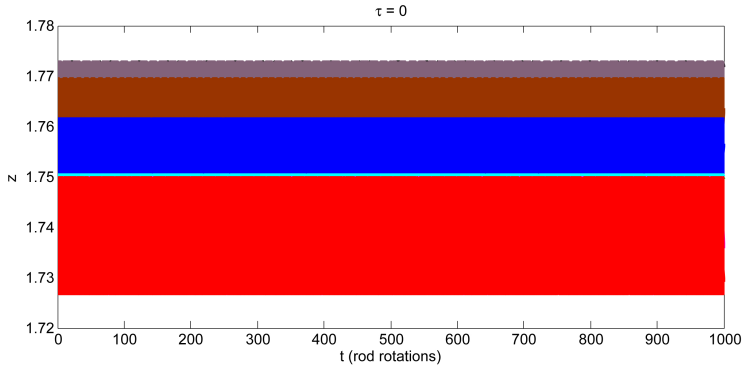

(a)

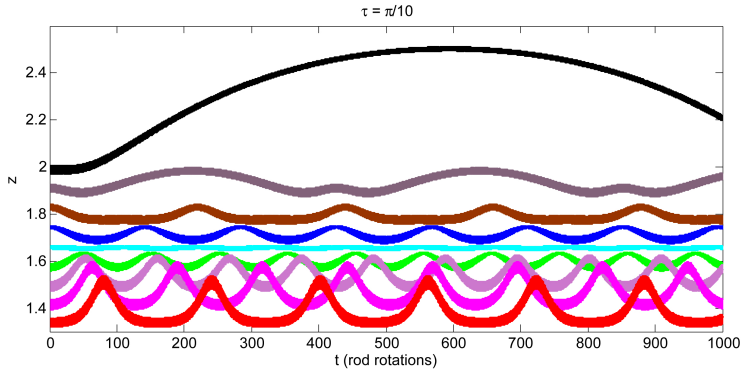

(b)

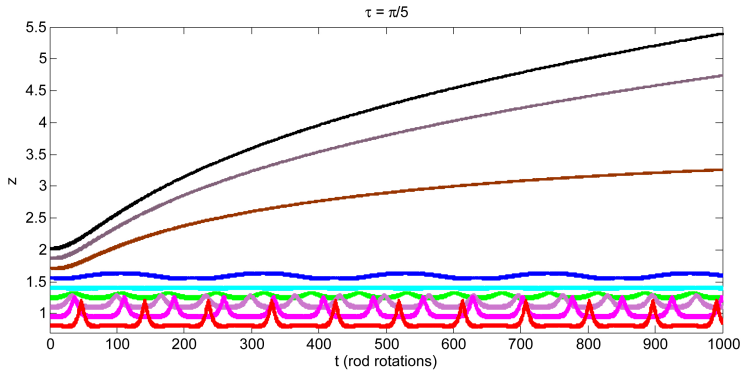

(c)

FIGURE 6.6. Vertical position versus time measured in rod rotations for the nine markers depicted in Figures 6.2 and 6.3. The tilt angle varies from (a) $\tau = 0$ to (b) $\tau = \frac{\pi}{10}$ to (c) $\tau = \frac{\pi}{5}$. Image produced in conjunction with Bouzarth *et. al.* (RMX group work in preparation) [**9**].

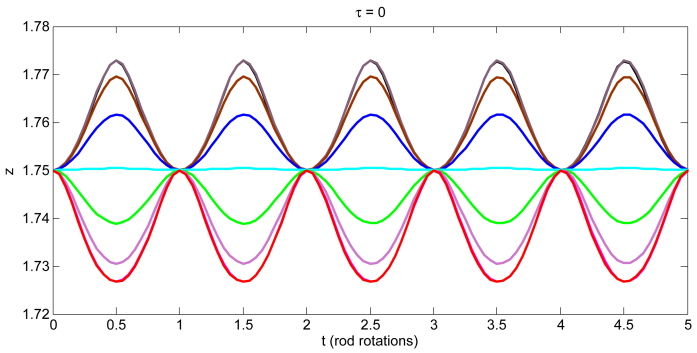

(a)

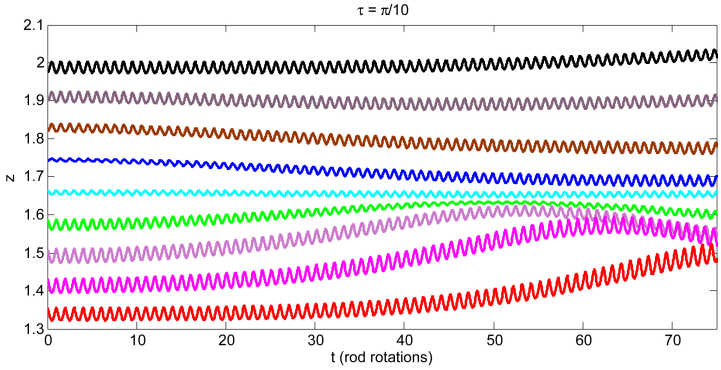

(b)

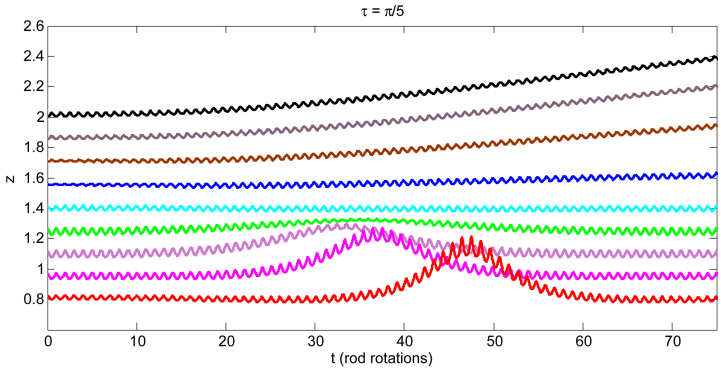

(c)

FIGURE 6.7. Vertical position versus time measured in rod rotations for the nine markers depicted in Figures 6.2 and 6.3 over shorter time scales to show the epicycle structure. The tilt angle varies from (a) $\tau = 0$ to (b) $\tau = \frac{\pi}{10}$ to (c) $\tau = \frac{\pi}{5}$. Image produced in conjunction with Bouzarth *et. al.* (RMX group work in preparation) [**9**].

fluid dynamics experiments to explore the resulting fluid flow. The initial trajectory results from the RMX experiments uncovered an interesting flow pattern. It appears that a fluid particle can travel on a more complicated orbit in the presence of a bent rod compared to a straight rod. The numerical model using regularized singularities verifies that the interesting experimental results discovered by the RMX group are indeed viable. In studying the bent rod scenario numerically, a more complete picture is obtained pertaining to the effect of the orientation of the bent rod and the resulting trajectories. The numerical model is also used to help develop and verify the asymptotic model of the bent rod scenario from the Blakeslet solution implemented by Camassa *et. al.* [**12**]. The nuances of the bent rod configurations and the resulting trajectories are discussed in the remainder of this section. The focus of the discussion is on using the numerical methods developed in this dissertation to explore the fluid flow generated by a precessing bent rod, a problem motivated by the results of the aforementioned macro-scale fluid experiments of the RMX group.

Figure 6.8 shows the initial bent pin used. Pins with constant curvature are currently being incorporated into the experimental design. Besides investigating the bent rod because of curiosities relating to the micro-scale experiments of Jing, bent rods may also have biological contexts. For instance, there are microorganisms that use fluid flow created by flagella for feeding purposes [**55**]. It may be applicable to model the motion of these flagella with a bent rod. Also, as one can conclude from the images of primary nodal cilia in the work of Hirokawa *et. al.*, it is likely that primary nodal cilia are not completely rigid and straight, as the mathematical and numerical models originally suppose; there might be some bending of the cilia during their conical beat.

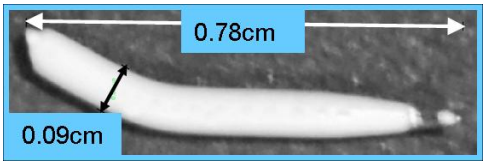

FIGURE 6.8. Profile view of a bent pin used in RMX experiments. Image courtesy of Bouzarth *et. al.* (RMX group work in preparation) [**9**].

When replacing the straight pin in the RMX experiments with a bent one, there are multiple configurations that could produce different results. Define $\rho \in [0, 2\pi)$ as the scooping angle, which gives a measure of the orientation of the curve of the pin. For this discussion, assume that when viewed from above, the pin precesses in a counterclockwise manner. A scooping angle of $\rho = 0$ corresponds to the case we will term *belly out*. The chord connecting the tips of the bent rod coincide with the location of a straight rod of the same cone angle, but the bend falls below the chord. This is shown for a rod with constant curvature of 1 in Figures 6.9(a) and 6.9(b) from the top and side, respectively. A scooping angle of $\rho = \frac{\pi}{2}$ corresponds to the *scooping* configuration. In this case, the tips of the bent rod lead the bend of the rod through the fluid, as shown in Figure 6.10 where the motion is counterclockwise in the top view. The $\rho = \pi$ case is termed *belly in*. In a similar fashion to belly out, when viewed from the top, the rod projects onto a straight line, but the bend is above the chord connecting the rod tips, as shown in Figure 6.11. The last named configuration is *slicing* with $\rho = \frac{3\pi}{2}$. This configuration can be viewed as the time reversal configuration of the scooping case. That is, the bend of the rod leads the tips through the fluid, as shown in Figure 6.12 where again the motion is counterclockwise in the top view. In Figures 6.9 - 6.12, the motion is counterclockwise when viewed from the top. As mentioned, the scooping picture in Figure 6.10 can also depict slicing if the motion of the rod is taken as clockwise in the top view.

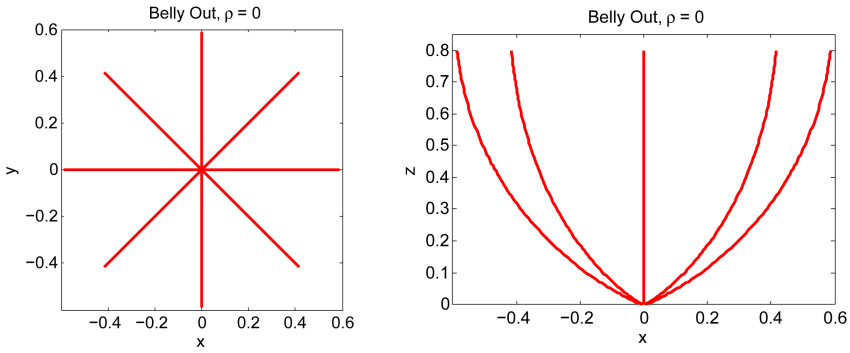

(a) Top View (b) Side View

FIGURE 6.9. Top and side views of representative time snapshots of a bent rod in the belly out configuration with scooping angle $\rho = 0$. Image produced in conjunction with Bouzarth *et. al.* (RMX group work in preparation) [**9**].

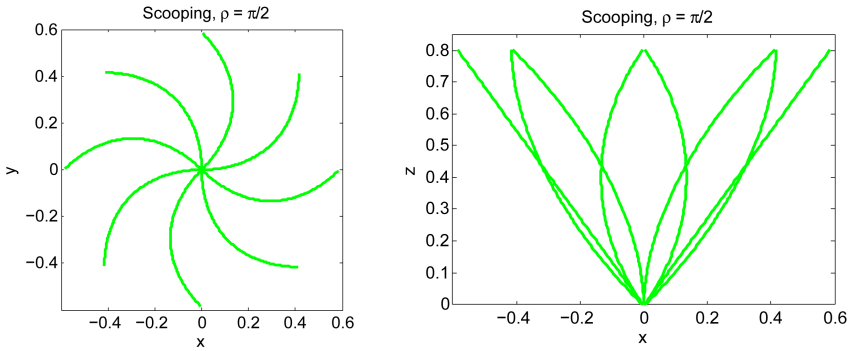

(a) Top View (b) Side View

FIGURE 6.10. Top and side views of representative time snapshots of a bent rod in the scooping configuration with scooping angle $\rho = \frac{\pi}{2}$. The rod moves counterclockwise in the top view. Image produced in conjunction with Bouzarth *et. al.* (RMX group work in preparation) [**9**].

When the RMX experiment initially used a bent rod in the scooping configuration, a curious trajectory resulted, as mentioned above. From the side view, the trajectory had a dramatic vertical descent, a feature not present in the previously studied straight rod

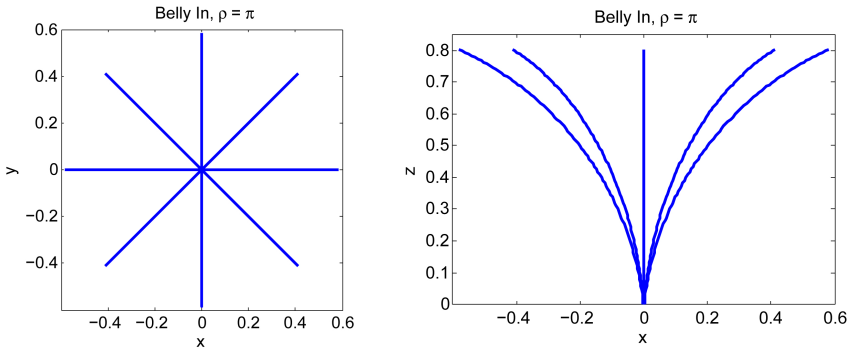

(a) Top View (b) Side View

FIGURE 6.11. Top and side views of representative time snapshots of a bent rod in the belly in configuration with scooping angle $\rho = \pi$. Image produced in conjunction with Bouzarth *et. al.* (RMX group work in preparation) [**9**].

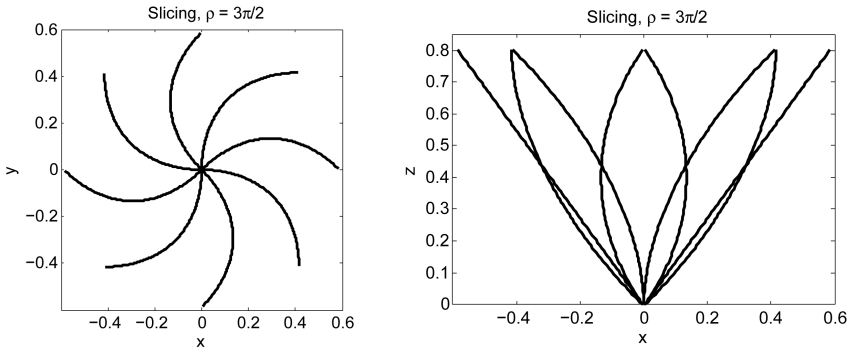

(a) Top View (b) Side View

FIGURE 6.12. Top and side views of representative time snapshots of a bent rod in the slicing configuration with scooping angle $\rho = \frac{3\pi}{2}$. The rod moves counterclockwise in the top view. Image produced in conjunction with Bouzarth *et. al.* (RMX group work in preparation) [**9**].

trajectories. Regularized singularities are used to model the bent rod experiments and the results reveal the same qualitative behavior, suggesting the fact that the experiment

reveals interesting fluid dynamics rather than a failed experiment. The side view experimental and numerical trajectories are shown in Figure 6.13. With the caveat that the

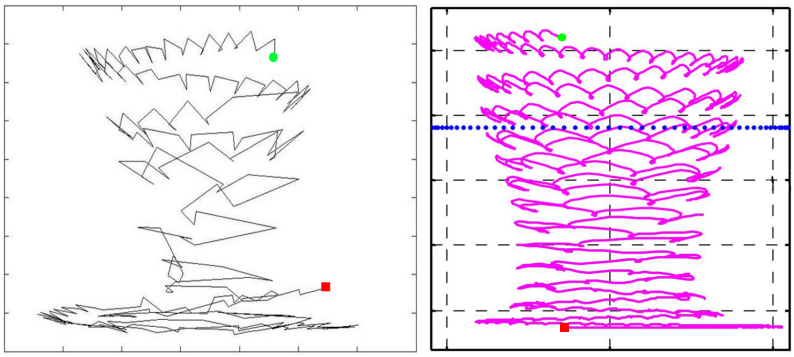

(a) Experiment (b) Simulation

FIGURE 6.13. Side views of trajectories resulting from a scooping rod in (a) an experiment and (b) a regularized singularity simulation. The green circle denotes the starting position of the fluid particle and the red square denotes its final position some time later. The parameters are not exactly matched, so slight discrepancies exist, but the general structure is the same. The bottom of the each figure coincides with the no-slip plane. The contact point of the pin with the fluid tank floor is in the center of the bottom edge of each plot. In the simulation plot, the blue dots denote locations of the tip of the rod at different instances in time. Notice the vertical descent and radial fluctuation trends in both cases, which are not present for an analogous straight rod. Image produced in conjunction with Bouzarth *et. al.* (RMX group work in preparation) [**9**].

model parameters were not specifically tuned to those of the experiment, this data with similar parameters shows the dramatic shift from the straight rod case capturing the qualitative motion. In both cases, the fluid particle starts above the cone structure and

descends as time progresses. Then as the particle nears the floor, its radial position and vertical position both increase as well. This experimental result supported by numerical simulation results led the RMX team of researchers to hypothesize that there is a long time scale structure induced by certain configurations of a bent rod that are not present in the case of a precessing straight rod. For a scooping rod, particles that begin near or above the cone structure tend to descend towards the floor, increase their radius and vertical position and recirculate up further away from the rod. Conversely, since Stokes flow is reversible, for a slicing rod, fluid should generally rise near the cone structure, travel radially outward, then vertically downward, and back radially inward near the base of the rod. This hypothesis will be further investigated numerically in the remainder of this section.

The new trajectory characteristics suggest that a fluid particle travels on a long time scale toroidal orbit in addition to the epicyclic precession exhibited in straight rod trajectories. To determine if all bent rod configurations or just some have the interesting long time scale toroidal behavior, consider looking at numerical simulation results for four different scooping angles, $\rho = 0, \frac{\pi}{2}, \pi, \frac{3\pi}{2}$. Figures 6.14 and 6.15 show the radial and vertical positions[2] versus time, respectively, for the four aforementioned scooping angles. Data is also shown for a straight rod with the same parameters. The bend has a constant curvature of 1. The parameters used are: rod length $L = 1$, spreading parameter $\epsilon = 0.05$, number of regularized Stokeslets $N = 100$, and initial position $(x, y, z) = (-0.75, 0, 1.25)$. This initial condition is above the cone structure, so from previous observations, one would expect the scooping case to spiral down and in, which

[2]As in Section 6.1, these are taken from cylindrical coordinates using the contact point of the rod with the floor as the origin.

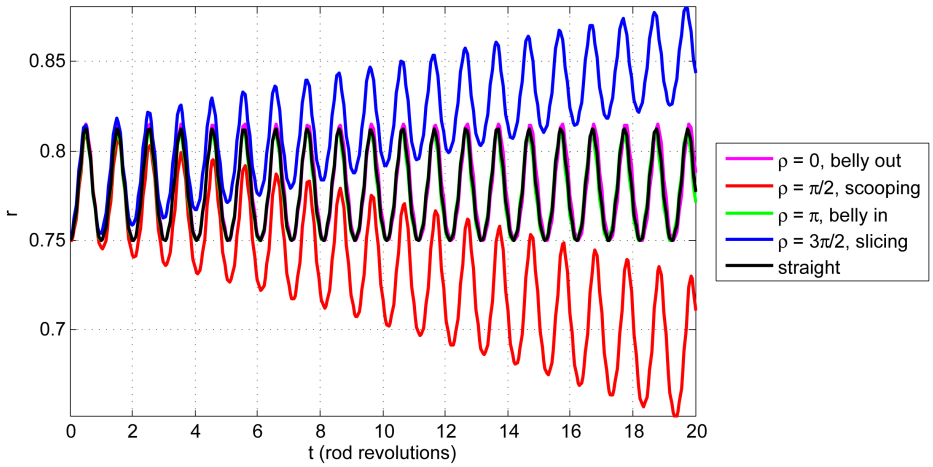

FIGURE 6.14. Radial position versus time for a variety of scooping angles and a straight rod. Image produced in conjunction with Bouzarth *et. al.* (RMX group work in preparation) [**9**].

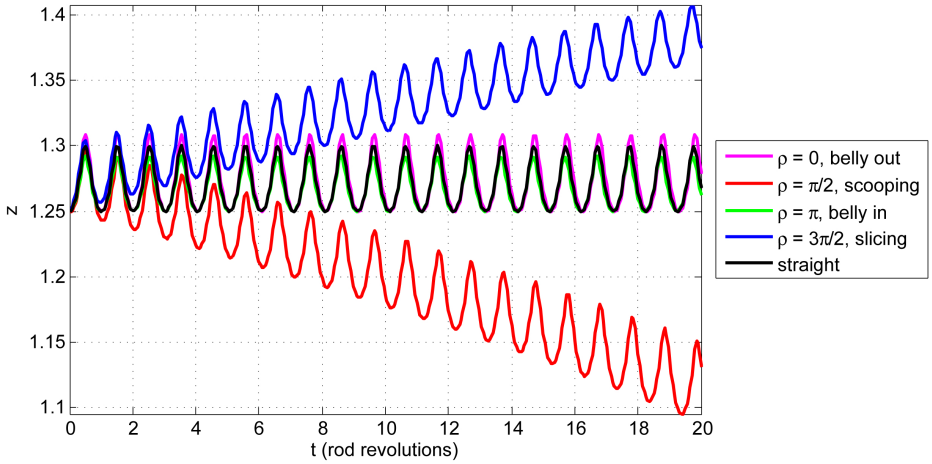

FIGURE 6.15. Vertical position versus time for a variety of scooping angles and a straight rod. Image produced in conjunction with Bouzarth *et. al.* (RMX group work in preparation) [**9**].

is reflected by the decreasing trend in the time series plots. In the slicing case, one would expect the opposite to occur as a sign of reversibility of Stokes flow. Indeed the figures reveal this behavior in the data. The initially less intuitive cases are the belly in and belly out scenarios. Notice that the radial and vertical positions both oscillate around a

fixed height, unlike in the scooping and slicing cases. This is characteristic of a straight rod trajectory. It is difficult to see in these figures, but the data is only slightly different for the straight, belly in, and belly out cases, but the behavior trend is the same. The belly in and belly out configurations produce trajectories that are similar to a straight rod of slightly geometric parameters, namely rod slenderness.

Figure 6.16 gives a specific example of the effect of a scooping rod compared to a straight rod on a fluid particle's trajectory. In this case, the initial tracer position, rod diameter, and cone angle are the same in both the bent and straight rod cases. The length of the rod in the straight case matches the length of the chord connecting the tips of the bent rod so that the tips of the bent rod and the straight rod coincide. One can notice that the introduction of a slight bend in the scooping configuration produces dramatically different trajectory results compared to the straight rod, as alluded to previously. Figures 6.16(a) and 6.16(b) show three dimensional views of the data in the lab frame for 100 rod rotations. Figure 6.16(c) shows the same data as Figure 6.16(b), except the time duration is extended to 1000 rod rotations. While the difference between the straight and scooping cases is evident from examining Figures 6.16(a) and 6.16(b) alone, extending the duration of the scooping case shows an example of how the tracers behave once they descend towards the floor and begin to recirculate. Figures 6.16(d) and 6.16(e) show the same data as Figures 6.16(a) and 6.16(c), respectively, but viewed from the side in the body frame. The body frame is the frame of reference where the rod is still and the fluid is rotating around it. In contrast, the lab frame is the reference frame that is the most intuitive, where the rod is precessing through the fluid that is at rest at infinity. The following parameters are used to generate these plots: rod length $L = 0.7879$, spreading parameter $\epsilon = 0.05$, number of regularized Stokeslets $N = 100$, cone angle $\theta = \frac{3\pi}{10}$, and

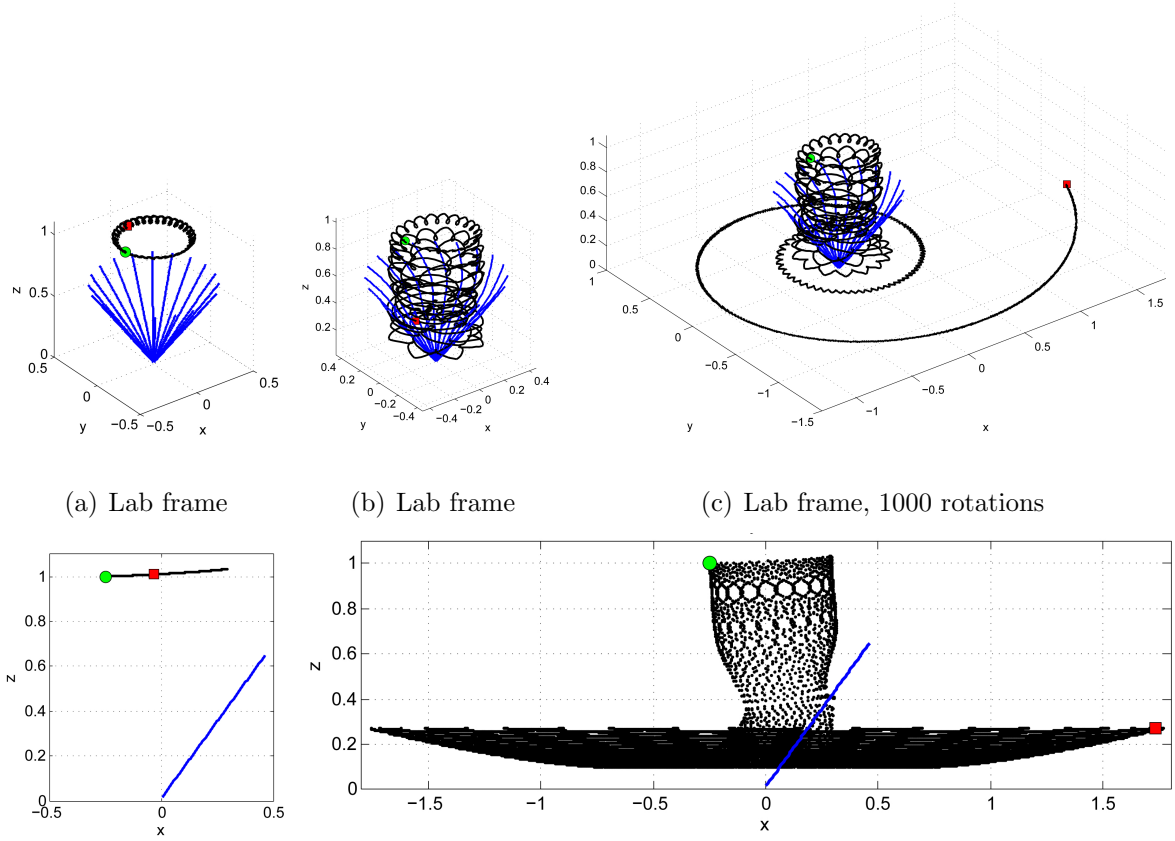

(a) Lab frame (b) Lab frame (c) Lab frame, 1000 rotations

(d) Body frame (e) Body frame, 1000 rotations

FIGURE 6.16. (a) A trajectory generated by a straight rod in 100 rotations. (b) A trajectory generated by a scooping bent rod in 100 rotations. (c) Same trajectory as (b) except for 1000 rod rotations. (d) Trajectory from (a) shown from the side in the body frame. (e) Trajectory from (c) shown from the side in the body frame. The initial and final positions are marked with a green circle and red square. In all plots, the initial positions are $(x, y, z) = (-0.25, 0, 1)$. Image produced in conjunction with Bouzarth *et. al.* (RMX group work in preparation) [**9**].

initial position $(x, y, z) = (-0.25, 0, 1)$. The curve of the bent rod matches that of the bent pin shown in Figure 6.8 used in the initial RMX macro-scale fluid experiments.

The straight rod case has rotation on two time scales. The first is a short time scale that is roughly commensurate with the period of a rod rotation, referred to as an epicycle. The second is the time scale it takes for a fluid particle to make an orbit around the cone structure. This time scale varies greatly depending on the proximity to the rod. In the scooping bent rod case, the third time scale is longer yet and also varies with respect to location. This is a toroidal excursion in addition to the epicycles and orbits discussed in the straight rod case.

To demonstrate the hypothesized long time toroidal structure present for scooping bent rods, but not straight rods, consider Figure 6.17. These trajectories have an initial position of $(x, y, z) = (-1, 0, 1)$ shown for 1000 rod rotations. The rest of the parameters are the same as in Figure 6.16. The trajectories in both the lab frame and the body frame shown in Figure 6.17 show evidence of the long time scale toroidal structure in addition to the epicyclic precession.

To further investigate the toroidal structure, consider taking a slice of the body frame through $y = 0$ and plotting the trajectories as they penetrate this plane for a variety of initial conditions. This result is shown in Figure 6.18. The plane is taken with a width tolerance of $tol = 0.01$ to account for the discrete nature of numerical data. From this view point, one can see a nested toroidal structure developing. Again, to compare with the straight rod case, Figure 6.19 shows the same type of plot for a straight rod of similar parameters. Notice there is no toroidal structure here. Figure 6.20 displays the data in the same way for a variety of scooping angles. There are four data sets displayed for $\rho = \frac{\pi}{2}$, $\rho = \frac{3\pi}{4}$, $\rho = \frac{11\pi}{12}$ and $\rho = \pi$. Notice as the scooping angle approaches the belly in case ($\rho = \pi$), the plot resembles that of a straight rod. This gives further evidence that bent rods in the belly in or belly out configuration produce trajectories that are

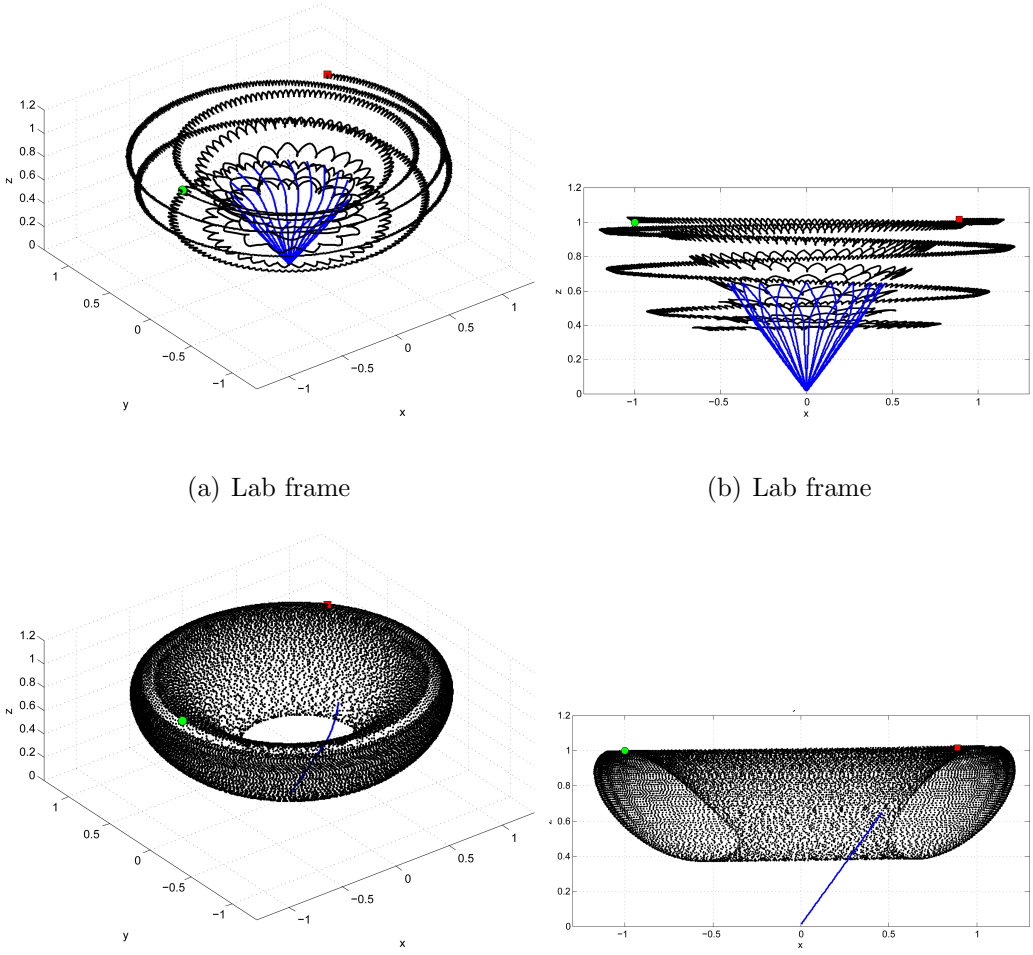

(a) Lab frame

(b) Lab frame

(c) Body frame

(d) Body frame

FIGURE 6.17. (a) Three dimensional and (b) side views of a trajectory generated by a bent rod in the lab frame. (c) Three dimensional and (d) side views of the same trajectory viewed in the body frame. The initial and final positions are marked with a green circle and red square, respectively. In all plots, the initial position is $(x, y, z) = (-1, 0, 1)$. Image produced in conjunction with Bouzarth *et. al.* (RMX group work in preparation) [**9**].

characteristic of a straight rod, whereas bent rods with any degree of scooping or slicing ($\rho \in (0, \pi) \cup (\pi, 2\pi)$) exhibit the aforementioned long time scale toroidal structure.

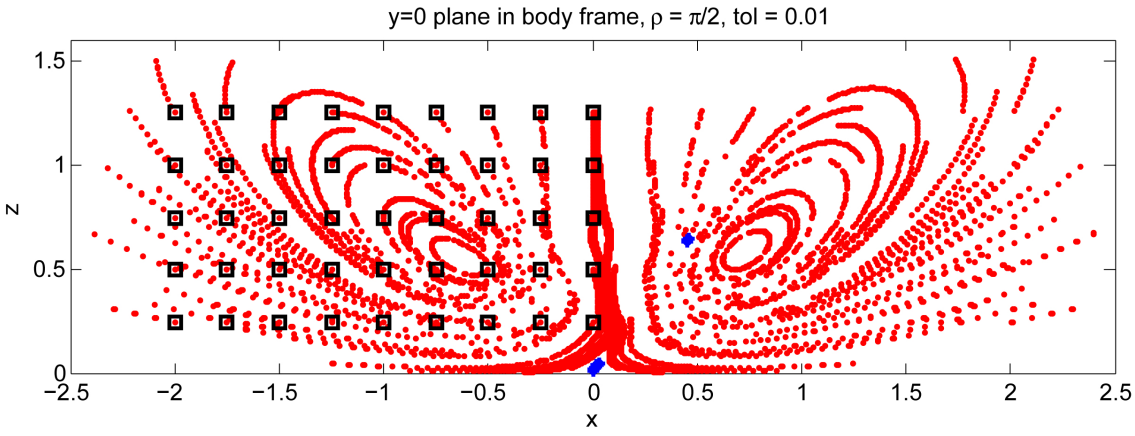

FIGURE 6.18. A slice through $y = 0$ in the body frame for 45 initial positions, marked by black squares. The blue regions of the plot denote where the tips of the bent rod penetrate the plane. In this scooping configuration, the bend of the rod comes out of the page. Image produced in conjunction with Bouzarth *et. al.* (RMX group work in preparation) [**9**].

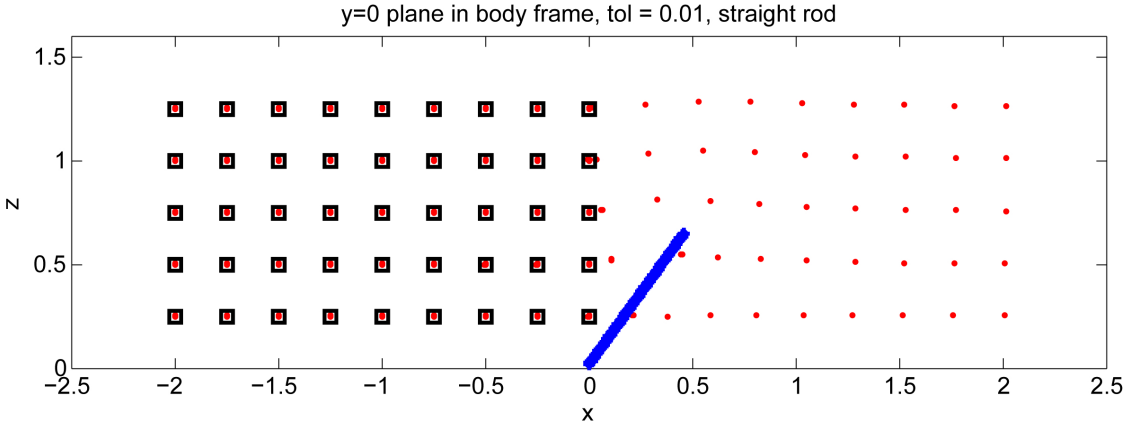

FIGURE 6.19. A slice through $y = 0$ in the body frame for 45 initial positions, marked by black squares. The blue region of the plot denotes where the straight lies in the plane. Image produced in conjunction with Bouzarth *et. al.* (RMX group work in preparation) [**9**].

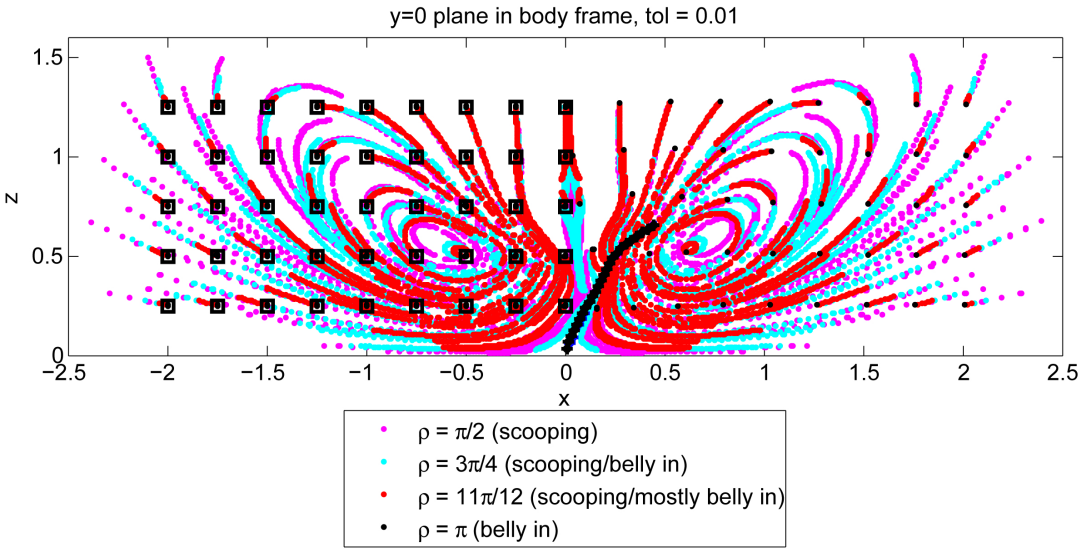

FIGURE 6.20. A slice through $y = 0$ in the body frame for 45 initial positions, marked by black squares. The black curve denotes where the belly in bent rod lies in the plane for the $\rho = \pi$ case. Data is shown for four scooping angles, $\rho = \frac{\pi}{2}$, $\rho = \frac{3\pi}{4}$, $\rho = \frac{11\pi}{12}$ and $\rho = \pi$. Image produced in conjunction with Bouzarth *et. al.* (RMX group work in preparation) [**9**].

The change in fluid flow structure for a belly in or belly out rod versus a bent rod that is scooping or slicing can be explained by the rod configuration. Consider the belly out case (the same argument holds for the belly in case as well). At each instance of time, the rod lies in a vertical plane that includes the axis of rotation. From the perspective of a fluid particle, the rod's structure appears the same when the rod moves towards the particle location as it does when it moves away from it. As such, the particle trajectory behaves like a straight rod seeing as this symmetry is also present in that case. However, when a bent rod is in a configuration that has any degree of slicing or scooping ($\rho \in (0, \pi) \cup (\pi, 2\pi)$), the plane of the rod is no longer vertical and a fluid particle does not see the same rod configuration when the rod is coming towards it as it does when the rod is moving away. For instance, when the rod is scooping and approaching a fluid

particle, the fluid near the tip of the rod will be pushed downward by the rod. However, when a rod is moving toward the same fluid particle in a slicing configuration, the fluid near the tip will be pushed upward. By contrast, in the straight rod case (and belly in and belly out cases), the rod exerts a horizontal force on the fluid with no vertical components.

When studying the fluid flow generated by a bent rod, the macro-scale fluid dynamic experiments of the RMX group first demonstrated the presence of an additional structure in a particle's trajectory, a long time scale toroidal structure. The numerical model developed in this dissertation provides a more complete understanding of the fluid dynamics that the experiments could not produce due to practical limitations (*e.g.* length of an experiment). Although it was not discussed in detail here, Camassa *et. al.* [**12**] are studying this behavior with their mathematical model derived from the Blakeslet solution of Camassa *et. al.* [**10**]. Understanding the intricacies of the hydrodynamics of a precessing bent rod is a topic of current research actively being pursued by the RMX research group with experimental, mathematical, and numerical approaches.

CHAPTER 7

Summary

With the study of cilia in the context of the Virtual Lung Project as initial motivation, this dissertation presents a collection of mathematical models, numerical solutions, and experimental results that have a common ground in modeling a physical scenario of a slender rigid rod precessing in a conical fashion that mimics the motion of primary nodal cilia. This common ground provides a valuable benchmarking opportunity where closed form solutions, numerical simulations, and experimental results support, predict, and verify each other. Developing numerical solutions that utilize regularized Stokeslets and multi-explicit spectral deferred correction methods in this environment provides the unique opportunity for careful error analysis and parameter studies for nontrivial fluid flows with an exact solution. The intuition and tools developed in the benchmarking process between the mathematical models, numerical solutions, and experiments aid in adapting these methods to study more complicated physical systems that incorporate increasingly more features of the motivating biological problems. The remainder of this chapter summarizes the discussion of the numerical solution in the body of this dissertation.

The exact solution of Camassa *et. al.* and Leiterman [**11, 42**] for a spheroid precessing about its center, as described in Section 1.3, provides the opportunity to perform detailed error analysis on the method of regularized Stokeslets. As such, error contributions due

to slenderness, regularization, and quadrature were identified and explored in Section 3.2. Time integration error was considered separately in Chapter 5. The dominant error contributions come from slenderness and regularization, as the quadrature and time integration errors are often negligible.

The exact solution of Camassa *et. al.* and Leiterman is also used in conjunction with the numerical solution to explore parameter and boundary condition choices that minimize the velocity error. Two cases are considered in Chapters 3 and 4, slender and non-slender spheroids, respectively. In the slender case, regularized Stokeslets are distributed along the centerline of the spheroid and in the non-slender case, they are distributed along the surface of a spheroid. In both cases, it is demonstrated that collections of regularized Stokeslets exhibit an effective geometry which minimizes a physical volume. In the slender case, a one dimensional line of regularized Stokeslets can model a three dimensional slender spheroid due the effects of regularization. In the non-slender case, it was found that by placing the regularized Stokeslets on the surface of a slightly smaller spheroid than the one being modeled incorporates the increased effective radius in such a way that the velocity error is reduced. In both cases, it was shown that the increase from actual radius to effective radius is approximately one quarter of the spreading parameter for the particular cutoff function used.

In the time domain, the multi-explicit spectral deferred correction (MESDC) method is introduced in Chapter 5 as a numerical integrator that lends itself well for use with the method of regularized Stokeslets. In particular, when modeling a stiff system, the MESDC method allows for the explicit treatment of different components with different time steps. In the case discussed in Section 5.2.1, there are two components, a rod and a sphere that is represented by a collection or regularized Stokeslets connected by stiff

springs. The rod is treated with a larger time step since it is not a stiff component of the system. This is beneficial because calculating the force on the rod necessary to satisfy the boundary conditions requires the solution of a dense linear system. Thus, decreasing the frequency of this calculation improves efficiency. The MESDC method is an accurate, stable, versatile, novel time integration method that is also applicable to immersed boundary problems using the Blob Projection Method [**20**].

The results of the aforementioned error analysis, parameter study, and numerical integration discussion are used in conjunction with the experimental results of the RMX research group to predict and verify experimental results. Two areas of current research are understanding the hydrodynamics of a rod precessing about a tilted axis and a bent rod precessing about a vertical axis. In both of these cases, numerical and asymptotic models are used to gain understanding of the hydrodynamics and to predict and verify experimental results. In the tilted rod case, the numerical results presented here show dramatic departures from the standard epicyclic orbits created by straight rods precessing about a vertical axis, as shown in Section 6.1 [**9**]. The results are for one tilted rod, but in the environment of primary nodal cilia which undergo this motion, there are multiple rods whose collective motion generates directional flow. The results discussed here are consistent with the idea that the hydrodynamics alone can create the observed transport in the nodal region. It is a topic of future work to expand the tilted rod study to incorporate multiple rods. This is feasible with the numerical solution discussed here. In addition, Carstens *et. al.* , Evans, and Evans *et. al.* (members of the RMX group) fabricate arrays of biomimetic cilia that are actuated in a motion similar to that of primary nodal cilia [**13, 28, 29**]. Carstens *et. al.* have experimental evidence of directed

fluid transport [**13**]. Hence, studying the hydrodynamics of fields of tilted precessing rods in both the laboratory and numerical setting is desirable.

In the bent rod case, the numerical solution is used to verify an interesting experimental discovery made by the RMX group [**8**], namely a precessing bent rod creates a dramatic change in behavior from that of a straight rod. Specifically, for certain configurations of the bent rod, a third time scale is introduced into the trajectory of a fluid particle. In addition to the epicyclic orbits generated by a straight rod, a fluid particle also travels on the surface of a torus over long time scales. Bouzarth *et. al.* have verified this phenomenon experimentally, numerically, and mathematically [**8**].

APPENDIX A: Nondimensionalization of the Navier-Stokes Equations

This appendix discusses the details of the nondimensionalization of the Navier-Stokes equations and the assumptions made to derive the Stokes equations. Start with the incompressible Navier-Stokes equations from (2.1) – (2.2):

$$\rho\frac{\partial \mathbf{u}}{\partial t} + \rho\mathbf{u}\cdot\nabla\mathbf{u} = -\nabla p + \mathbf{F} + \mu\nabla^2\mathbf{u} \tag{A.1}$$

$$\nabla\cdot\mathbf{u} = 0, \tag{A.2}$$

where ρ is the fluid density, $\mathbf{u}$ is the fluid velocity, p is the pressure, $\mathbf{F} = \rho\mathbf{g}$ is the body force due to gravity, and μ is the dynamic viscosity. It is assumed that both ρ and μ are constant and uniform throughout the fluid. Divide (A.1) by the fluid density to obtain

$$\frac{\partial \mathbf{u}}{\partial t} + \mathbf{u}\cdot\nabla\mathbf{u} = -\frac{1}{\rho}\nabla p + \mathbf{g} + \frac{\mu}{\rho}\nabla^2\mathbf{u}. \tag{A.3}$$

Use the variables defined in (2.3)

$$\hat{\mathbf{u}} = \frac{\mathbf{u}}{\mathcal{U}} \tag{A.4}$$

$$\hat{\mathbf{x}} = \frac{\mathbf{x}}{\mathcal{L}} \tag{A.5}$$

$$\hat{t} = \frac{t}{\mathcal{T}} \tag{A.6}$$

$$\hat{p} = \frac{p\mathcal{L}}{\mu\mathcal{U}} \tag{A.7}$$

$$\hat{\mathbf{g}} = \frac{\mathbf{g}}{g} \tag{A.8}$$

to find the following derivatives:

$$\frac{\partial}{\partial t} = \frac{1}{\mathcal{T}}\frac{\partial}{\partial \hat{t}} \tag{A.9}$$

$$\nabla = \frac{1}{\mathcal{L}}\hat{\nabla} \tag{A.10}$$

$$\nabla^2 = \frac{1}{\mathcal{L}^2}\hat{\nabla}^2. \tag{A.11}$$

Substitute the derivatives and nondimensional variables from (A.4) – (A.11) into (A.2) and (A.3) to obtain

$$\frac{1}{\mathcal{T}}\frac{\partial}{\partial \hat{t}}\left(\mathcal{U}\hat{\mathbf{u}}\right) + \left(\mathcal{U}\hat{\mathbf{u}}\right)\cdot\left(\frac{1}{\mathcal{L}}\hat{\nabla}\left(\mathcal{U}\hat{\mathbf{u}}\right)\right) = -\frac{1}{\rho}\left(\frac{1}{\mathcal{L}}\hat{\nabla}\left(\frac{\mu\mathcal{U}\hat{p}}{\mathcal{L}}\right)\right) + \frac{\mu}{\rho\mathcal{L}^2}\hat{\nabla}^2\left(\mathcal{U}\hat{\mathbf{u}}\right) + g\hat{\mathbf{g}} \tag{A.12}$$

$$\hat{\nabla}\cdot\hat{\mathbf{u}} = 0. \tag{A.13}$$

After multiplying by $\frac{\mathcal{L}^2}{\mathcal{U}\nu}$ and recognizing the kinematic viscosity $\nu = \frac{\mu}{\rho}$, (A.12) becomes

$$\frac{\mathcal{L}^2}{\nu\mathcal{T}}\frac{\partial\hat{\mathbf{u}}}{\partial\hat{t}} + \frac{\mathcal{U}\mathcal{L}}{\nu}\hat{\mathbf{u}}\cdot\hat{\nabla}\hat{\mathbf{u}} = -\hat{\nabla}\hat{p} + \hat{\nabla}^2\hat{\mathbf{u}} + \frac{g\mathcal{L}^2}{\nu\mathcal{U}}\mathbf{g}. \tag{A.14}$$

Recognizing the unsteadiness parameter, $\beta = \frac{\mathcal{L}^2}{\nu\mathcal{T}}$, the Reynolds number $Re = \frac{\mathcal{U}\mathcal{L}}{\nu}$, and the Froude number, $Fr = \frac{\mathcal{U}}{\sqrt{g\mathcal{L}}}$, (A.14) becomes the nondimensionalized Navier-Stokes equations [**57**]:

$$\beta\frac{\partial\hat{\mathbf{u}}}{\partial\hat{t}} + Re\hat{\mathbf{u}}\cdot\hat{\nabla}\hat{\mathbf{u}} = -\hat{\nabla}\hat{p} + \hat{\nabla}^2\hat{\mathbf{u}} + \frac{Re}{Fr^2}\hat{\mathbf{g}}. \tag{A.15}$$

After considering $\beta \ll 1$ and $Re \ll 1$, (A.15) reduces further to

$$0 = -\hat{\nabla}\hat{p} + \hat{\nabla}^2\hat{\mathbf{u}} + \frac{Re}{Fr^2}\hat{\mathbf{g}}. \tag{A.16}$$

Converting (A.16) and (A.13) back to the original variables $\mathbf{u}, \mathbf{x}, t$ and p, one arrives at the incompressible quasi-steady Stokes equations originally presented in (2.5):

$$\mu \nabla^2 \mathbf{u} = \nabla p - \mathbf{F} \tag{A.17}$$

$$\nabla \cdot \mathbf{u} = 0. \tag{A.18}$$

APPENDIX B: Derivation of Image Singularities for a Stokeslet

This appendix presents a derivation of the system of image singularities required to create a no-slip plane in the presence of one Stokeslet. This collection of singularities is termed a Blakeslet in the work of Camassa *et. al.* and Leiterman, which is derived from that of Blake [**4, 10, 42**]. Recall the notation from Section 2.3, specifically Figure 2.1, $\mathbf{x}_0$ is the location of the original Stokeslet and $\mathbf{y}_0$ is the location of the image singularities outside of the fluid domain. Without loss of generality, assume the location of the wall is at $x_3 = w$, then $\mathbf{x}_0 = (x_{0,1}, x_{0,2}, x_{0,3})$ and $\mathbf{y}_0 = (x_{0,1}, x_{0,2}, 2w - x_{0,3})$. Consider $\mathbf{x}$ on the wall, so $\mathbf{x} = (x_1, x_2, w)$. Define r as $r = |\mathbf{x} - \mathbf{x}_0| = |\mathbf{x} - \mathbf{y}_0|$.

The Stokeslet at $\mathbf{x}_0$ produces the following velocity:

$$\mathbf{u}^S = \frac{1}{8\pi\mu}\left[\frac{\mathbf{f}}{r} + \frac{[\mathbf{f}\cdot(\mathbf{x}-\mathbf{x}_0)](\mathbf{x}-\mathbf{x}_0)}{r^3}\right]. \tag{B.1}$$

First place a Stokeslet at $\mathbf{y}_0$, which produces the velocity field

$$\mathbf{u}^{S*} = \frac{1}{8\pi\mu}\left[\frac{\mathbf{f}}{r} + \frac{[\mathbf{f}\cdot(\mathbf{x}-\mathbf{y}_0)](\mathbf{x}-\mathbf{y}_0)}{r^3}\right]. \tag{B.2}$$

The asterisk denotes that the singularity is placed at the image location $\mathbf{y}_0$. Thus the net velocity so far due to the two Stokeslets is

$$\mathbf{u}^S - \mathbf{u}^{S*} = \frac{1}{8\pi\mu}\left[\frac{[\mathbf{f}\cdot(\mathbf{x}-\mathbf{x}_0)](\mathbf{x}-\mathbf{x}_0)}{r^3} - \frac{[\mathbf{f}\cdot(\mathbf{x}-\mathbf{y}_0)](\mathbf{x}-\mathbf{y}_0)}{r^3}\right]. \tag{B.3}$$

Notice that the Stokeslet at the image location $\mathbf{y}_0$ has opposite strength of the original Stokeslet at $\mathbf{x}_0$, implemented as $\mathbf{u}^S$ - $\mathbf{u}^{S*}$ in (B.3)[1]. Using the fact that $\mathbf{x}$ is on the wall,

[1] Alternatively, (B.2) could be expressed as $\mathbf{u}^{S*} = -\frac{1}{8\pi\mu}\left[\frac{\mathbf{f}}{r} + \frac{[\mathbf{f}\cdot(\mathbf{x}-\mathbf{y}_0)](\mathbf{x}-\mathbf{y}_0)}{r^3}\right]$ to denote the opposite strength. In that case, $\mathbf{u}^S + \mathbf{u}^{S*}$ would be considered throughout the text in place of $\mathbf{u}^S - \mathbf{u}^{S*}$.

and letting $h = x_{0,3} - w$, then $\mathbf{x}_0 = \mathbf{y}_0 + 2h\hat{e}_3$ and $\mathbf{u}^S - \mathbf{u}^{S*}$ becomes

$$\text{(B.4)} \quad \mathbf{u}^S - \mathbf{u}^{S*} = \frac{1}{8\pi\mu}\left[\frac{[\mathbf{f}\cdot(\mathbf{x}-\mathbf{y}_0-2h\hat{e}_3)](\mathbf{x}-\mathbf{y}_0-2h\hat{e}_3) - [\mathbf{f}\cdot(\mathbf{x}-\mathbf{y}_0)](\mathbf{x}-\mathbf{y}_0)}{r^3}\right]$$

$$\text{(B.5)} \quad = \frac{1}{8\pi\mu}\left[\frac{-2h[\mathbf{f}\cdot(\mathbf{x}-\mathbf{y}_0)]\hat{e}_3 - 2h[\mathbf{f}\cdot\hat{e}_3](\mathbf{x}-\mathbf{y}_0) + 4h^2[\mathbf{f}\cdot\hat{e}_3]\hat{e}_3}{r^3}\right].$$

Substituting $\hat{\mathbf{x}} = \mathbf{x} - \mathbf{y}_0$, (B.5) becomes

$$\text{(B.6)} \quad \mathbf{u}^S - \mathbf{u}^{S*} = \frac{1}{8\pi\mu}\left[\frac{-2h[\mathbf{f}\cdot\hat{\mathbf{x}}]\hat{e}_3 - 2h[\mathbf{f}\cdot\hat{e}_3]\hat{\mathbf{x}} + 4h^2[\mathbf{f}\cdot\hat{e}_3]\hat{e}_3}{r^3}\right].$$

Switching to summation notation, the net velocity at the wall due to the original Stokeslet and the image Stokeslet can be expressed as

$$\text{(B.7)} \quad u_i^S - u_i^{S*} = \frac{1}{8\pi\mu}\left[\frac{-2h\hat{x}_j\delta_{i3} - 2h\hat{x}_i\delta_{j3} + 4h^2\delta_{i3}\delta_{j3}}{r^3}\right] f_j.$$

Since this is a non-zero velocity on the wall, more image singularities are required to cancel the remaining velocity terms.

Consider the velocity due to an image point source dipole of strength $\mathbf{f}$, from (2.17):

$$\text{(B.8)} \quad u_i^{D*} = \frac{1}{8\pi\mu}\left[-\frac{2\delta_{ij}}{r^3} + \frac{6\hat{x}_i\hat{x}_j}{r^5}\right] f_j.$$

Also consider the velocity due to an image Stokes doublet of strength $\mathbf{f}$, from (2.25):

$$\text{(B.9)} \quad u_i^{SD*} = \frac{1}{8\pi\mu}\left[\frac{\hat{x}_k\delta_{ij}}{r^3} - \frac{\hat{x}_j\delta_{ik}}{r^3} - \frac{\hat{x}_i\delta_{jk}}{r^3} + \frac{3\hat{x}_i\hat{x}_j\hat{x}_k}{r^5}\right] f_k.$$

Now reindex (B.9), letting $j = 3$, $k = j$, and $\hat{x}_3 = h$ to obtain

$$\text{(B.10)} \quad u_i^{SD*} = \frac{1}{8\pi\mu}\left[\frac{\hat{x}_j\delta_{i3}}{r^3} - \frac{h\delta_{ij}}{r^3} - \frac{\hat{x}_i\delta_{3j}}{r^3} + \frac{3h\hat{x}_i\hat{x}_j}{r^5}\right] f_j.$$

From (B.8) and (B.10), one sees that

$$\text{(B.11)} \quad u_i^{SD*} - \frac{h}{2}u_i^{D*} = \frac{1}{8\pi\mu}\left[\frac{\hat{x}_j\delta_{i3}}{r^3} - \frac{\hat{x}_i\delta_{j3}}{r^3}\right] f_j.$$

Observe each component of (B.7) and (B.11):

$$u_1^S - u_1^{S*} = \frac{1}{8\pi\mu}\left[\frac{-2h\hat{x}_1\delta_{j3}}{r^3}\right] f_j \tag{B.12}$$

$$u_2^S - u_2^{S*} = \frac{1}{8\pi\mu}\left[\frac{-2h\hat{x}_2\delta_{j3}}{r^3}\right] f_j \tag{B.13}$$

$$u_3^S - u_3^{S*} = \frac{1}{8\pi\mu}\left[\frac{-2h\hat{x}_j + 2h^2\delta_{j3}}{r^3}\right] f_j \tag{B.14}$$

$$u_1^{SD*} - \frac{h}{2}u_1^{D*} = \frac{1}{8\pi\mu}\left[-\frac{\hat{x}_1\delta_{j3}}{r^3}\right] f_j \tag{B.15}$$

$$u_2^{SD*} - \frac{h}{2}u_2^{D*} = \frac{1}{8\pi\mu}\left[-\frac{\hat{x}_2\delta_{j3}}{r^3}\right] f_j \tag{B.16}$$

$$u_3^{SD*} - \frac{h}{2}u_3^{D*} = \frac{1}{8\pi\mu}\left[\frac{\hat{x}_j}{r^3} - \frac{h\delta_{j3}}{r^3}\right] f_j. \tag{B.17}$$

Now comparing (B.12) – (B.14) with (B.15) – (B.17), one can see the following combination of aforementioned velocities satisfies the no-slip boundary condition on the wall:

$$u_i = \frac{1}{8\pi\mu}\left[S_{ij} - S_{ij}^* + 2h\left[SD_{ij}^* - \frac{h}{2}D_{ij}^*\right](2\delta_{i3} - 1)\right] f_j \tag{B.18}$$

$$= u_i^S - u_i^{S*} + 2h(2\delta_{i3} - 1)\left[u_i^{SD*} - \frac{h}{2}u_i^{D*}\right], \tag{B.19}$$

which appears as (2.32).

APPENDIX C: Derivation of a Regularized Stokeslet

This appendix shows the derivation of a regularized Stokeslet, which was developed by Cortez [**18**]. To derive a regularized Stokeslet, $S_{ij}^{\phi_\epsilon}$, consider the incompressible Stokes equations with a regularized forcing term (from (2.38)):

$$\mu\nabla^2\mathbf{u} = \nabla p - \mathbf{f}\phi_\epsilon(r) \tag{C.1}$$

$$\nabla\cdot\mathbf{u} = 0, \tag{C.2}$$

where ϕ_ϵ is given by (2.35)

$$\phi_\epsilon(r) = \frac{15\epsilon^4}{8\pi(r^2+\epsilon^2)^{7/2}}. \tag{C.3}$$

As in (2.41), one can write the fluid velocity $\mathbf{u}$ in terms of the regularized Stokeslet $S_{ij}^{\phi_\epsilon}$

$$u_i = \frac{1}{8\pi\mu}S_{ij}^{\phi_\epsilon}f_j. \tag{C.4}$$

Similarly, express the pressure p as

$$p = \frac{1}{8\pi}P_j^{\phi_\epsilon}f_j. \tag{C.5}$$

Substitute (C.4) and (C.5) into (C.1) and (C.2) to obtain

$$\nabla^2 S_{ij}^{\phi_\epsilon} = \frac{\partial P_j^{\phi_\epsilon}}{\partial x_i} - 8\pi\delta_{ij}\phi_\epsilon \tag{C.6}$$

$$\frac{\partial S_{ij}^{\phi_\epsilon}}{\partial x_i} = 0. \tag{C.7}$$

Now differentiate (C.6) with respect to x_i and substitute (C.7), resulting in

$$\nabla^2 P_j^{\phi_\epsilon} = 8\pi\nabla\phi_\epsilon. \tag{C.8}$$

Define G^{ϕ_ϵ} and B^{ϕ_ϵ} as follows:

$$\nabla^2 G^{\phi_\epsilon} = \phi_\epsilon \tag{C.9}$$

$$\nabla^2 B^{\phi_\epsilon} = G^{\phi_\epsilon}. \tag{C.10}$$

Substitute (C.9) into (C.8) to obtain

$$P_j^{\phi_\epsilon} = 8\pi \frac{\partial G^{\phi_\epsilon}}{\partial x_j}. \tag{C.11}$$

Substituting this result into (C.6) produces

$$\nabla^2 S_{ij}^{\phi_\epsilon} = 8\pi \frac{\partial^2 G^{\phi_\epsilon}}{\partial x_i x_j} - 8\pi \delta_{ij} \phi_\epsilon. \tag{C.12}$$

Inserting (C.9) and (C.10) into (C.12) for ϕ_ϵ and G^{ϕ_ϵ}, respectively, produces

$$\nabla^2 S_{ij}^{\phi_\epsilon} = 8\pi \frac{\partial^2 \nabla^2 B^{\phi_\epsilon}}{\partial x_i x_j} - 8\pi \delta_{ij} \nabla^2 G^{\phi_\epsilon}. \tag{C.13}$$

Then

$$S_{ij}^{\phi_\epsilon} = 8\pi \left[\frac{\partial^2 B^{\phi_\epsilon}}{\partial x_i x_j} - \delta_{ij} G^{\phi_\epsilon} \right]. \tag{C.14}$$

Once B^{ϕ_ϵ} and G^{ϕ_ϵ} are derived for a particular cutoff function (in this case ϕ_ϵ), then the form of the regularized Stokeslet will result. Since the cutoff function ϕ_ϵ is only a function of r, we can consider the radial dependence of the three dimensional Laplacian in spherical coordinates:

$$\nabla^2 = \frac{1}{r^2} \frac{\partial}{\partial r} \left(r^2 \frac{\partial}{\partial r} \right). \tag{C.15}$$

Since $\nabla^2 G^{\phi_\epsilon} = \frac{1}{r^2}\frac{\partial}{\partial r}\left(r^2 \frac{\partial}{\partial r}\right) G^{\phi_\epsilon} = \phi_\epsilon$,

$$\frac{\partial G^{\phi_\epsilon}}{\partial r} = \frac{1}{r^2}\int_0^r s^2 \phi_\epsilon(s) ds \tag{C.16}$$

$$= \frac{15\epsilon^4}{8\pi r^2}\int_0^r \frac{s^2}{(s^2+\epsilon^2)^{7/2}} ds. \tag{C.17}$$

With the following trigonometric substitutions

$$s = \epsilon \tan\theta \tag{C.18}$$

$$ds = \epsilon \sec^2\theta d\theta \tag{C.19}$$

$$(s^2+\epsilon^2)^{1/2} = \epsilon \sec\theta \tag{C.20}$$

(C.17) becomes

$$\frac{\partial G^{\phi_\epsilon}}{\partial r} = \frac{15}{8\pi r^2}\int_{s=0}^{s=r} \sin^2\theta \cos^3\theta d\theta \tag{C.21}$$

$$= \frac{15}{8\pi r^2}\left[\frac{\sin^3\theta}{3} - \frac{\sin^5\theta}{5}\right]\Bigg|_{s=0}^{s=r} \tag{C.22}$$

$$= \frac{15}{8\pi r^2}\left[\frac{s^3}{3(s^2+\epsilon^2)^{3/2}} - \frac{s^5}{5(s^2+\epsilon^2)^{5/2}}\right]\Bigg|_{s=0}^{s=r} \tag{C.23}$$

$$= \frac{1}{8\pi}\left[\frac{5r}{(r^2+\epsilon^2)^{3/2}} - \frac{3r^3}{(r^2+\epsilon^2)^{5/2}}\right]. \tag{C.24}$$

Now integrate (C.24) to obtain

$$G^{\phi_\epsilon} = \frac{1}{8\pi}\int\left(\frac{5r}{(r^2+\epsilon^2)^{3/2}} - \frac{3r^3}{(s^2+\epsilon^2)^{5/2}}\right) dr. \tag{C.25}$$

Again, use the trigonometric substitutions from (C.18) – (C.20):

$$G^{\phi_\epsilon} = \frac{1}{8\pi\epsilon}\left[5\int \sin\theta d\theta - 3\int \sin^3\theta d\theta\right] \tag{C.26}$$

$$= \frac{-1}{8\pi\epsilon}\left[2\cos\theta + \cos^3\theta\right] \tag{C.27}$$

$$= \frac{-1}{8\pi}\left[\frac{2}{(r^2+\epsilon^2)^{1/2}} + \frac{\epsilon^2}{(r^2+\epsilon^2)^{3/2}}\right]. \tag{C.28}$$

Derive B^{ϕ_ϵ} in a similar fashion to G^{ϕ_ϵ}. Since $\nabla^2 B^{\phi_\epsilon} = G^{\phi_\epsilon}$, begin with

$$\frac{\partial B^{\phi_\epsilon}}{\partial r} = \frac{1}{r^2}\int_0^r s^2 G^{\phi_\epsilon}(s)ds \tag{C.29}$$

$$= \frac{-1}{8\pi r^2}\left[2\int_0^r \frac{s^2}{(s^2+\epsilon^2)^{1/2}}ds + \epsilon^2\int_0^r \frac{s^2}{(s^2+\epsilon^2)^{3/2}}ds\right]. \tag{C.30}$$

Substituting (C.18) – (C.20) produces:[2]

$$\frac{\partial B^{\phi_\epsilon}}{\partial r} = \frac{-\epsilon^2}{8\pi r^2}\left[2\int_{s=0}^{s=r}\frac{\sin^2\theta}{\cos^3\theta}d\theta + \int_{s=0}^{s=r}\frac{\sin^2\theta}{\cos\theta}d\theta\right] \tag{C.31}$$

$$= \frac{-\epsilon^2}{8\pi r^2}\left[\frac{\sin^3\theta}{\cos^2\theta}\Big|_{s=0}^{s=r} - \int_{s=0}^{s=r}\frac{\sin^2\theta}{\cos\theta}d\theta + \int_{s=0}^{s=r}\frac{\sin^2\theta}{\cos\theta}d\theta\right] \tag{C.32}$$

$$= \frac{-\epsilon^2}{8\pi r^2}\left[\frac{\sin^3\theta}{\cos^2\theta}\right]\Big|_{s=0}^{s=r} \tag{C.33}$$

$$= \frac{-1}{8\pi r^2}\left[\frac{s^3}{(s^2+\epsilon^2)^{1/2}}\right]\Big|_{s=0}^{s=r} \tag{C.34}$$

$$= \frac{-r}{8\pi(r^2+\epsilon^2)^{1/2}}. \tag{C.35}$$

Now integrate (C.35) to find B^{ϕ_ϵ}:

$$B^{\phi_\epsilon} = \frac{-1}{8\pi}\int \frac{r}{(r^2+\epsilon^2)^{1/2}}dr. \tag{C.36}$$

Again, substitute (C.18) – (C.20):

$$B^{\phi_\epsilon} = \frac{-\epsilon}{8\pi}\int \sec\theta\tan\theta d\theta \tag{C.37}$$

$$= \frac{-\epsilon\sec\theta}{8\pi} \tag{C.38}$$

$$= \frac{-(r^2+\epsilon^2)^{1/2}}{8\pi}. \tag{C.39}$$

[2]To progress from (C.31) to (C.32), the following integral identity was used:

$$\int \frac{\sin^n ax}{\cos^m ax}dx = \frac{\sin^{n+1} ax}{a(m-1)\cos^{m-1} ax} - \frac{n-m+2}{m-1}\int \frac{\sin^n ax}{\cos^{m-2} ax}dx,$$

for $m \neq 1$.

Now that expressions for G^{ϕ_ϵ} and B^{ϕ_ϵ} have been derived, substitute (C.28) and (C.39) into (C.14) to find the equation for a regularized Stokeslet associated with the cutoff function ϕ_ϵ:

$$
\begin{aligned}
S_{ij}^{\phi_\epsilon} &= -\frac{\partial^2}{\partial x_i x_j}\left((r^2+\epsilon^2)^{1/2}\right) + \delta_{ij}\left(\frac{2}{(r^2+\epsilon^2)^{1/2}} + \frac{\epsilon^2}{(r^2+\epsilon^2)^{3/2}}\right) && \text{(C.40)}\\
&= -\frac{\partial}{\partial x_i}\left(\frac{\hat{x}_j}{(r^2+\epsilon^2)^{1/2}}\right) + \delta_{ij}\left(\frac{2}{(r^2+\epsilon^2)^{1/2}} + \frac{\epsilon^2}{(r^2+\epsilon^2)^{3/2}}\right) && \text{(C.41)}\\
&= \frac{-\delta_{ij}}{(r^2+\epsilon^2)^{1/2}} + \frac{\hat{x}_i\hat{x}_j}{(r^2+\epsilon^2)^{3/2}} + \delta_{ij}\left(\frac{2}{(r^2+\epsilon^2)^{1/2}} + \frac{\epsilon^2}{(r^2+\epsilon^2)^{3/2}}\right) && \text{(C.42)}\\
&= \delta_{ij}\left(\frac{1}{(r^2+\epsilon^2)^{1/2}} + \frac{\epsilon^2}{(r^2+\epsilon^2)^{3/2}}\right) + \frac{\hat{x}_i\hat{x}_j}{(r^2+\epsilon^2)^{3/2}} && \text{(C.43)}\\
&= \delta_{ij}\frac{r^2+2\epsilon^2}{(r^2+\epsilon^2)^{3/2}} + \frac{\hat{x}_i\hat{x}_j}{(r^2+\epsilon^2)^{3/2}}, && \text{(C.44)}
\end{aligned}
$$

which matches (2.39).

APPENDIX D: Derivation of a Regularized Dipole

This appendix shows the derivation of a regularized dipole, which is a component of the image of regularized singularities introduced by Cortez that will be explored in Appendix F [**17**]. As with all of the regularized singularities, the form of the regularized dipole will depend on the chosen cutoff function. This derivation will use φ_ϵ from (2.36) because it will be useful in the derivation of the system of image singularities in Appendix F. To derive a regularized dipole, consider the following Hodge decomposition from which one wants to find $\mathbf{u}^{D,\varphi_\epsilon}$, the velocity induced by a regularized dipole:

$$\mathbf{u}^{D,\varphi_\epsilon} + \nabla\psi = \mathbf{f}\varphi_\epsilon(\mathbf{x} - \mathbf{x}_0), \tag{D.1}$$

assuming $\nabla \cdot \mathbf{u}^{D,\varphi_\epsilon} = 0$. First, take the divergence of (D.1). This implies

$$\nabla^2\psi = \mathbf{f} \cdot \nabla\varphi_\epsilon. \tag{D.2}$$

Combining (D.2) with the fact that $\nabla^2 G^{\varphi_\epsilon} = \varphi_\epsilon$ produces:

$$\psi = \mathbf{f} \cdot \nabla G^{\varphi_\epsilon} \tag{D.3}$$

and

$$\mathbf{u}^{D,\varphi_\epsilon} = \mathbf{f}\varphi_\epsilon - (\mathbf{f} \cdot \nabla)\nabla G^{\varphi_\epsilon}. \tag{D.4}$$

In summation notation, (D.4) becomes:

$$u_i^{D,\varphi_\epsilon} = \left[\delta_{ij}\varphi_\epsilon - \frac{\partial^2 G^{\varphi_\epsilon}}{\partial x_j \partial x_i}\right] f_j. \tag{D.5}$$

Recall that G^{φ_ϵ} can be expressed as a function of r only, so

$$\frac{\partial}{\partial x_k} G^{\varphi_\epsilon}(r(\hat{\mathbf{x}})) = \frac{\partial G^{\varphi_\epsilon}}{\partial r}\frac{\partial r}{\partial x_k} = \frac{\partial G^{\varphi_\epsilon}}{\partial r}\frac{\hat{x}_k}{r}. \tag{D.6}$$

Incorporating (D.6) into (D.5) produces:

$$u_i^{D,\varphi_\epsilon} = \left[\delta_{ij}\varphi_\epsilon - \frac{\delta_{ij}}{r}\frac{\partial G^{\varphi_\epsilon}}{\partial r} - \frac{\hat{x}_i\hat{x}_j}{r^2}\frac{\partial^2 G^{\varphi_\epsilon}}{\partial r^2} + \frac{\hat{x}_i\hat{x}_j}{r^3}\frac{\partial G^{\varphi_\epsilon}}{\partial r}\right] f_j. \tag{D.7}$$

To derive $\frac{\partial G^{\varphi_\epsilon}}{\partial r}$, start with $\nabla^2 G^{\varphi_\epsilon} = \varphi_\epsilon$ in spherical coordinates as in Appendix F:

$$\frac{\partial G^{\varphi_\epsilon}}{\partial r} = \frac{1}{r^2}\int_0^r s^2\varphi_\epsilon ds \tag{D.8}$$

$$= \frac{3\epsilon^2}{4\pi r^2}\int_0^r \frac{s^2}{(s^2+\epsilon^2)^{5/2}} ds. \tag{D.9}$$

Substituting the trigonometric expressions in (C.18) – (C.20) one finds:

$$\frac{\partial G^{\varphi_\epsilon}}{\partial r} = \frac{3}{4\pi r^2}\int_{s=0}^{s=r} \sin^2\theta\cos\theta d\theta \tag{D.10}$$

$$= \frac{1}{4\pi r^2}\sin^3\theta\Big|_{s=0}^{s=r} \tag{D.11}$$

$$= \frac{1}{4\pi r^2}\left.\frac{s^3}{(s^2+\epsilon^2)^{3/2}}\right|_0^r \tag{D.12}$$

$$= \frac{1}{4\pi}\frac{r}{(r^2+\epsilon^2)^{3/2}}. \tag{D.13}$$

Differentiating (D.13) with respect to r produces

$$\frac{\partial^2 G^{\varphi_\epsilon}}{\partial r^2} = \frac{1}{4\pi}\frac{-2r^2+\epsilon^2}{(r^2+\epsilon^2)^{5/2}}. \tag{D.14}$$

Substituting (D.13) and (D.14) into (D.7) results in the velocity resulting from a regularized dipole:

$$u_i^{D,\varphi_\epsilon *} = \frac{1}{8\pi\mu}\left[\frac{6\delta_{ij}\epsilon^2}{(r^2+\epsilon^2)^{5/2}} - \frac{2\delta_{ij}}{(r^2+\epsilon^2)^{3/2}} + \frac{6\hat{x}_i\hat{x}_j}{(r^2+\epsilon^2)^{5/2}}\right] f_j, \tag{D.15}$$

as shown in (2.45).

APPENDIX E: Derivation of a Regularized Rotlet

This appendix shows the derivation of a regularized rotlet, which will be utilized in the system of regularized image singularities introduced by Cortez and discussed in Appendix F [**17**]. A rotlet describes the resulting fluid flow due to a point torque (as opposed to the flow due to a point force in the case of a Stokeslet). There are two ways one can derive a rotlet. First, as discussed in Chapter 2, the rotlet is the anti-symmetric component of a Stokes doublet. This is useful in deriving $R_{ij}^{\phi_\epsilon}$, but not as useful with $R_{ij}^{\varphi_\epsilon}$ because it requires beginning with a regularized Stokeslet derived from the corresponding cutoff function. Since the only regularized Stokeslet derived here is with ϕ_ϵ, we will consider an alternative way of deriving a rotlet that does not explicitly depend on a regularized Stokeslet. As a consistency check, it will be shown that both methods produce the same results for $R_{ij}^{\phi_\epsilon}$. For the sake of generality, let Φ_ϵ represent any cutoff function. The velocity due to a regularized rotlet can be expressed as

$$\mathbf{u}^{R,\Phi_\epsilon} = \mathbf{L} \times \nabla G^{\Phi_\epsilon} \tag{E.1}$$

$$= \frac{1}{r}\frac{\partial G^{\Phi_\epsilon}}{\partial r}(\mathbf{L} \times \hat{\mathbf{x}}), \tag{E.2}$$

where $\mathbf{L}$ denotes the rotlet strength coefficient. Then the components of the rotlet become

$$u_1^{R,\Phi_\epsilon} = \frac{1}{r}\frac{\partial G^{\Phi_\epsilon}}{\partial r}(L_2\hat{x}_3 - L_3\hat{x}_2) \tag{E.3}$$

$$u_2^{R,\Phi_\epsilon} = \frac{1}{r}\frac{\partial G^{\Phi_\epsilon}}{\partial r}(L_3\hat{x}_1 - L_1\hat{x}_3) \tag{E.4}$$

$$u_3^{R,\Phi_\epsilon} = \frac{1}{r}\frac{\partial G^{\Phi_\epsilon}}{\partial r}(L_1\hat{x}_2 - L_2\hat{x}_1). \tag{E.5}$$

First consider building a rotlet from ϕ_ϵ using a form of $\frac{\partial G^{\phi_\epsilon}}{\partial r}$ that is equivalent to (C.24):

$$u_1^{R,\phi_\epsilon} = \frac{1}{8\pi}\left[\frac{2}{(r^2+\epsilon^2)^{3/2}} + \frac{3\epsilon^2}{(r^2+\epsilon^2)^{5/2}}\right](L_2\hat{x}_3 - L_3\hat{x}_2) \tag{E.6}$$

$$u_1^{R,\phi_\epsilon} = \frac{1}{8\pi}\left[\frac{2}{(r^2+\epsilon^2)^{3/2}} + \frac{3\epsilon^2}{(r^2+\epsilon^2)^{5/2}}\right](L_3\hat{x}_1 - L_1\hat{x}_3) \tag{E.7}$$

$$u_1^{R,\phi_\epsilon} = \frac{1}{8\pi}\left[\frac{2}{(r^2+\epsilon^2)^{3/2}} + \frac{3\epsilon^2}{(r^2+\epsilon^2)^{5/2}}\right](L_1\hat{x}_2 - L_2\hat{x}_1) \tag{E.8}$$

By choosing

$$\mathbf{L} = \frac{1}{2\mu}(\alpha_3\beta_2 - \alpha_2\beta_3, \alpha_1\beta_3 - \alpha_3\beta_1, \alpha_2\beta_1 - \alpha_1\beta_2), \tag{E.9}$$

one can verify that the velocity produced by the rotlets in (E.6) – (E.8) is equivalent to (2.59).

To derive the regularized rotlet from φ_ϵ, begin again with (E.3) – (E.5). Using $\frac{\partial G^{\varphi_\epsilon}}{\partial r}$ given by (D.13) produces

$$u_1^{R,\varphi_\epsilon} = \frac{1}{4\pi}\frac{L_2\hat{x}_3 - L_3\hat{x}_2}{(r^2+\epsilon^2)^{3/2}} \tag{E.10}$$

$$u_2^{R,\varphi_\epsilon} = \frac{1}{4\pi}\frac{L_3\hat{x}_1 - L_1\hat{x}_3}{(r^2+\epsilon^2)^{3/2}} \tag{E.11}$$

$$u_3^{R,\varphi_\epsilon} = \frac{1}{4\pi}\frac{L_1\hat{x}_2 - L_2\hat{x}_1}{(r^2+\epsilon^2)^{3/2}}. \tag{E.12}$$

Both u^{R,ϕ_ϵ} and u^{R,φ_ϵ} are used in the derivation of the system of regularized image singularities in Appendix F.

APPENDIX F: Derivation of Regularized Image Singularities for a Regularized Stokeslet

This appendix shows a derivation of the system of regularized image singularities required to create a no-slip plane in the presence of one regularized Stokeslet. This collection of regularized singularities was developed by Cortez [**17**]. Recall the notation from Section 2.3, specifically Figure 2.1, where $\mathbf{x}_0$ is the location of the original regularized Stokeslet and $\mathbf{y}_0$ is the location of the regularized image singularities outside of the fluid domain. If the location of the wall is at $x_3 = w$, then $\mathbf{x}_0 = (x_{0,1}, x_{0,2}, x_{0,3})$ and $\mathbf{y}_0 = (x_{0,1}, x_{0,2}, 2w - x_{0,3})$. Consider $\mathbf{x}$ on the wall, so $\mathbf{x} = (x_1, x_2, w)$. Define r as $r = |\mathbf{x} - \mathbf{x}_0| = |\mathbf{x} - \mathbf{y}_0|$.

As derived in Appendix C, the velocity due to the initial regularized Stokeslet located at $\mathbf{x}_0$ is

$$u_i^{S,\phi_\epsilon} = \frac{1}{8\pi\mu}\left[\delta_{ij}\frac{r^2+2\epsilon^2}{(r^2+\epsilon^2)^{3/2}} + \frac{(x_i - x_{0i})(x_j - x_{0j})}{(r^2+\epsilon^2)^{3/2}}\right] f_j. \tag{F.1}$$

To construct the system of regularized image singularities, again start by subtracting a regularized Stokeslet at the image location, $\mathbf{y}_0$, and express the resulting net velocity field[3]

$$u_i^{S,\phi_\epsilon *} = \frac{1}{8\pi\mu}\left[\delta_{ij}\frac{r^2+2\epsilon^2}{(r^2+\epsilon^2)^{3/2}} + \frac{(x_i - y_{0i})(x_j - y_{0j})}{(r^2+\epsilon^2)^{3/2}}\right] f_j \tag{F.2}$$

$$u_i^{S,\phi_\epsilon} - u_i^{S,\phi_\epsilon *} = \frac{1}{8\pi\mu}\left[\frac{(x_i - x_{0i})(x_j - x_{0j})}{(r^2+\epsilon^2)^{3/2}} - \frac{(x_i - y_{0i})(x_j - y_{0j})}{(r^2+\epsilon^2)^{3/2}}\right] f_j. \tag{F.3}$$

[3] As mentioned in Appendix B, (F.2) could be expressed as $u_i^{S,\phi_\epsilon *} = -\frac{1}{8\pi\mu}\left[\delta_{ij}\frac{r^2+2\epsilon^2}{(r^2+\epsilon^2)^{3/2}} + \frac{(x_i-y_{0i})(x_j-y_{0j})}{(r^2+\epsilon^2)^{3/2}}\right] f_j$ to denote the opposite strength. In that case, $u_i^{S,\phi_\epsilon} + u_i^{S,\phi_\epsilon *}$ would be considered throughout the text in place of $u_i^{S,\phi_\epsilon} - u_i^{S,\phi_\epsilon *}$.

Recognizing that $\mathbf{x}_0 = \mathbf{y}_0 + 2h\hat{e}_3$, letting $\hat{\mathbf{x}} = \mathbf{x} - \mathbf{y}_0$, and restricting $\mathbf{x}$ to be on the wall so that $\hat{x}_3 = h$ produces

$$u_i^{S,\phi_\epsilon} - u_i^{S,\phi_\epsilon *} = \left[-\frac{2h\hat{x}_i\delta_{j3}}{(r^2+\epsilon^2)^{3/2}} - \frac{2h\hat{x}_j\delta_{i3}}{(r^2+\epsilon^2)^{3/2}} + \frac{4h^2\delta_{i3}\delta_{j3}}{(r^2+\epsilon^2)^{3/2}} \right] f_j. \tag{F.4}$$

At this point of the derivation in the singular case discussed in Appendix B, a point-source dipole and a Stokes doublet were included to complete the system of image singularities. In an analogous fashion, consider the velocity contribution from a regularized dipole as derived in Appendix D and a regularized doublet.

(D.15) describes the velocity due to a regularized dipole at $\mathbf{y}_0$:

$$u_i^{D,\varphi_\epsilon *} = \frac{1}{8\pi\mu} \left[\frac{6\delta_{ij}\epsilon^2}{(r^2+\epsilon^2)^{5/2}} - \frac{2\delta_{ij}}{(r^2+\epsilon^2)^{3/2}} + \frac{6\hat{x}_i\hat{x}_j}{(r^2+\epsilon^2)^{5/2}} \right] f_j. \tag{F.5}$$

The velocity induced by a regularized Stokes doublet at the image location, given in (2.53), is

$$\begin{aligned} u_i^{SD,\phi_\epsilon *} &= \frac{1}{8\pi\mu} \left[\frac{\hat{x}_k\delta_{ij}}{(r^2+\epsilon^2)^{3/2}} - \frac{\hat{x}_i\delta_{jk}}{(r^2+\epsilon^2)^{3/2}} - \frac{\hat{x}_j\delta_{ik}}{(r^2+\epsilon^2)^{3/2}} + \frac{3\epsilon^2\hat{x}_k\delta_{ij}}{(r^2+\epsilon^2)^{5/2}} \right. \\ &\quad \left. + \frac{3\hat{x}_i\hat{x}_j\hat{x}_k}{(r^2+\epsilon^2)^{5/2}} \right] f_j. \end{aligned} \tag{F.6}$$

As in Appendix B, let $j = 3$, $k = j$, and $h = \hat{x}_3$:

$$\begin{aligned} u_i^{SD,\phi_\epsilon *} &= \frac{1}{8\pi\mu} \left[\frac{\hat{x}_j\delta_{i3}}{(r^2+\epsilon^2)^{3/2}} - \frac{\hat{x}_i\delta_{3j}}{(r^2+\epsilon^2)^{3/2}} - \frac{h\delta_{ij}}{(r^2+\epsilon^2)^{3/2}} + \frac{3\epsilon^2\hat{x}_j\delta_{i3}}{(r^2+\epsilon^2)^{5/2}} \right. \\ &\quad \left. + \frac{3h\hat{x}_i\hat{x}_j}{(r^2+\epsilon^2)^{5/2}} \right] f_j. \end{aligned} \tag{F.7}$$

As in the singular case, examine $u_i^{SD,\phi_\epsilon *} - \frac{h}{2}u_i^{D,\varphi_\epsilon *}$ from (F.5) and (F.7):

$$\begin{aligned} u_i^{SD,\phi_\epsilon *} - \frac{h}{2}u_i^{D,\varphi_\epsilon *} &= \frac{1}{8\pi\mu} \left[\frac{\hat{x}_j\delta_{i3}}{(r^2+\epsilon^2)^{3/2}} + \frac{\hat{x}_i\delta_{3j}}{(r^2+\epsilon^2)^{3/2}} + \frac{3\epsilon^2\hat{x}_j\delta_{i3}}{(r^2+\epsilon^2)^{5/2}} \right. \\ &\quad \left. - \frac{3h\epsilon^2\delta_{ij}}{(r^2+\epsilon^2)^{5/2}} \right] f_j. \end{aligned} \tag{F.8}$$

At this point in the singular calculation, the collection of Stokeslets, dipoles, and doublets are sufficient to satisfy the no-slip boundary condition on the plane, but this is not the case with the regularized singularities:

$$u_1^{S,\phi_\epsilon} - u_1^{S,\phi_\epsilon *} - 2h\left(u_1^{SD,\phi_\epsilon *} - \frac{h}{2}u_1^{D,\varphi_\epsilon *}\right) = \frac{1}{8\pi\mu}\left[\frac{6h\epsilon^2\delta_{1j}}{(r^2+\epsilon^2)^{5/2}}\right] f_j \tag{F.9}$$

$$u_2^{S,\phi_\epsilon} - u_2^{S,\phi_\epsilon *} - 2h\left(u_2^{SD,\phi_\epsilon *} - \frac{h}{2}u_2^{D,\varphi_\epsilon *}\right) = \frac{1}{8\pi\mu}\left[\frac{6h\epsilon^2\delta_{2j}}{(r^2+\epsilon^2)^{5/2}}\right] f_j \tag{F.10}$$

$$\begin{aligned} u_3^{S,\phi_\epsilon} - u_3^{S,\phi_\epsilon *} + 2h\left(u_3^{SD,\phi_\epsilon *} - \frac{h}{2}u_3^{D,\varphi_\epsilon *}\right) &= \frac{1}{8\pi\mu}\left[\frac{6h\epsilon^2 x_j}{(r^2+\epsilon^2)^{5/2}}\right. \\ &\left. -\frac{6h^2\epsilon^2\delta_{3j}}{(r^2+\epsilon^2)^{5/2}}\right] f_j. \end{aligned} \tag{F.11}$$

A combination of the two rotlets derived from ϕ_ϵ and φ_ϵ in Appendix E will provide the right form to cancel the remaining velocity terms. Let $\mathbf{L} = (L_1, L_2, 0)$. Then the difference of regularized rotlets from (E.6) – (E.8) and (E.10) – (E.12) is

$$u_1^{R,\phi_\epsilon *} - u_1^{R,\varphi_\epsilon *} = \frac{1}{8\pi}\left[\frac{3\epsilon^2}{(r^2+\epsilon^2)^{5/2}}\right] L_2 h \tag{F.12}$$

$$u_2^{R,\phi_\epsilon *} - u_2^{R,\varphi_\epsilon *} = -\frac{1}{8\pi}\left[\frac{3\epsilon^2}{(r^2+\epsilon^2)^{5/2}}\right] L_1 h \tag{F.13}$$

$$u_3^{R,\phi_\epsilon *} - u_3^{R,\varphi_\epsilon *} = \frac{1}{8\pi}\left[\frac{3\epsilon^2}{(r^2+\epsilon^2)^{5/2}}\right] (L_1 x_2 - L_2 x_1). \tag{F.14}$$

Letting $\mathbf{L} = \frac{f_j}{\mu}(2h\delta_{2j}, -2h\delta_{1j}, 0)$, (F.12) – (F.14) become

$$u_1^{R,\phi_\epsilon *} - u_1^{R,\varphi_\epsilon *} = -\frac{1}{8\pi\mu}\left[\frac{6h^2\epsilon^2\delta_{1j}}{(r^2+\epsilon^2)^{5/2}}\right] f_j \tag{F.15}$$

$$u_2^{R,\phi_\epsilon *} - u_2^{R,\varphi_\epsilon *} = -\frac{1}{8\pi\mu}\left[\frac{6h^2\epsilon^2\delta_{2j}}{(r^2+\epsilon^2)^{5/2}}\right] f_j \tag{F.16}$$

$$u_3^{R,\phi_\epsilon *} - u_3^{R,\varphi_\epsilon *} = \frac{1}{8\pi\mu}\left[\frac{6h\epsilon^2(\delta_{2j}x_2 + \delta_{1j}x_1)}{(r^2+\epsilon^2)^{5/2}}\right] f_j. \tag{F.17}$$

Comparing (F.9) – (F.11) with (F.15) – (F.17), one might notice that adding the respective first and second velocity components eliminates the first two velocity components,

but the third component is not as obvious. Consider taking the difference of the third velocity components and expanding the implied sum over j:

$$u_3 = u_3^{S,\phi_\epsilon} - u_3^{S,\phi_\epsilon *} + 2h\left(u_3^{SD,\phi_\epsilon *} - \frac{h}{2}u_3^{D,\varphi_\epsilon *}\right) - (u_3^{R,\phi_\epsilon *} - u_3^{R,\varphi_\epsilon *}) \tag{F.18}$$

$$= \frac{1}{8\pi\mu}\left[\frac{6h\epsilon^2 x_j}{(r^2+\epsilon^2)^{5/2}} - \frac{6h^2\epsilon^2\delta_{3j}}{(r^2+\epsilon^2)^{5/2}} - \frac{6h\epsilon^2\delta_{2j}x_2}{(r^2+\epsilon^2)^{5/2}} - \frac{6h\epsilon^2\delta_{1j}x_1}{(r^2+\epsilon^2)^{5/2}}\right] f_j \tag{F.19}$$

$$= \frac{1}{8\pi\mu}\left[\left(\frac{6h\epsilon^2 x_1}{(r^2+\epsilon^2)^{5/2}} - \frac{6h\epsilon^2 x_1}{(r^2+\epsilon^2)^{5/2}}\right) f_1 + \left(\frac{6h\epsilon^2 x_2}{(r^2+\epsilon^2)^{5/2}} - \frac{6h\epsilon^2 x_2}{(r^2+\epsilon^2)^{5/2}}\right) f_2 + \left(\frac{6h^2\epsilon^2}{(r^2+\epsilon^2)^{5/2}} - \frac{6h^2\epsilon^2}{(r^2+\epsilon^2)^{5/2}}\right) f_3\right] \tag{F.20}$$

$$= 0. \tag{F.21}$$

Thus, the following combination of regularized singularities satisfies the no-slip boundary condition on a plane at $x_3 = w$:

$$u_i = u_i^{S,\phi_\epsilon} - u_i^{S,\phi_\epsilon *} - 2h\,(1-2\delta_{i3})\left(u_i^{SD,\phi_\epsilon *} - \frac{h}{2}u_i^{D,\varphi_\epsilon *}\right) + (1-2\delta_{i3})\left(u_i^{R,\phi_\epsilon *} - u_i^{R,\varphi_\epsilon *}\right), \tag{F.22}$$

which matches (2.62).

APPENDIX G: Centroidal Voronoi Tessellations

Centroidal Voronoi tessellations (CVT) are used in this discussion to determine well separated locations of regularized Stokeslets on a sphere, but there are many other applications of this technique. The potential applications are far-reaching, including numerical meshing schemes, image compression, cellular biology, statistics, and animal behavior, to name a few [**25**].

The following discussion follows closely from the work of Du *et. al.* [**25, 26**]. For an open set $\Omega \in \mathbb{R}^n$, the collection of sets $\{V_i\}_{i=1}^k$ is a *tessellation* of Ω if $\cup_{i=1}^k \bar{V}_i = \bar{\Omega}$ and $V_i \cap V_j = \emptyset$ for $i \neq j$. For a collection of points $\{z_i\}_{i=1}^k \in \bar{\Omega}$, the *Voronoi region* $\hat{V}_i$ corresponding to z_i is

$$\hat{V}_i = \{x \in \Omega : \ |x - z_i| < |x - z_j|, \text{ for } j = 1, \ldots, k, \ i \neq j\} . \tag{G.1}$$

The set $\{z_i\}_{i=1}^k$ are *generators*. A *Voronoi tessellation* or *Voronoi diagram* refers to $\{\hat{V}_i\}_{i=1}^k$. For $V_i \in \mathbb{R}^n$ and density function ρ,

$$z^* = \frac{\int_{V_i} \mathbf{y}\rho(\mathbf{y})d\mathbf{y}}{\int_{V=i} \rho(\mathbf{y})d\mathbf{y}} \tag{G.2}$$

is the *mass centroid* of V_i.

A *centroidal Voronoi tessellation* is a Voronoi tessellation whose generators coincide with mass centroids ($z_i = z_i^*$). From a set of generators, it is natural to find the associated Voronoi region. Alternatively, from a Voronoi region, it is natural to compute its mass centroid. The goal of centroidal Voronoi tessellations is to mesh these two processes to find the set of generators that are also mass centroids.

In addition to using CVTs to find tessellations of a plane, a modification of centroidal Voronoi tessellations, known as constrained centroidal Voronoi tessellations (CCVT),

allows the same idea to be used to find well separated points on a surface. The regularized Stokeslet locations for non-slender spheroids are produced with CCVT on a sphere. The idea behind CCVT is similar to CVT except it is possible that the mass centroids do not lie on the surface in question. As such, consider the *constrained mass centroid*

$$z_i^c = \min_{\mathbf{z}\in S} \int_{V_i} \rho(\mathbf{x})|\mathbf{x}-\mathbf{z}|^2 d\mathbf{x}|, \tag{G.3}$$

where $|\cdot|$ represents the Euclidean norm. A Voronoi tessellation is a constrained centroidal Voronoi tessellation if and only if the generators of the Voronoi tessellation are the constrained mass centroids [**26**].

The CCVT algorithm used to place regularized Stokeslets on a sphere in the numerical model presented in this dissertation is the SCVT (spherical CVT) routine written by Burkhardt as a probabilistic CCVT routine [**35**]. Figures 0.1(a) and 0.1(b) show the results of using Burkhardt's code to generate 200 regularized Stokeslet locations on a sphere and projected onto a spheroid, respectively.

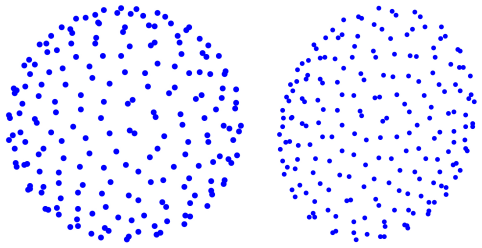

(a) (b)

FIGURE 0.1. Results of using Burkhardt's CCVT routine [**35**] to distribute 200 regularized Stokeslets on the surface of (a) a sphere and (b) a non-slender spheroid.

BIBLIOGRAPHY

1. B.A. Afzelius, *A human syndrome caused by immotile cilia*, Science **193** (1976), no. 4250, 317–319.

2. P.J. Atzberger, P.R. Kramer, and C.S. Peskin, *A stochastic immersed boundary method for fluid-structure dynamics at microscopic length scales*, J. Comput. Phys. **224** (2007), no. 2, 1255–1292.

3. J.R. Blake, *Infinite models for ciliary propulsion*, Journal of Fluid Mechanics **49** (1971), 209–222.

4. _____, *A note on the image system for a Stokeslet in a no-slip boundary*, Proceeding of the Cambridge Philosophical Society **70** (1971), 303–310.

5. R.C. Boucher, *New concepts of the pathogenesis of cystic fibrosis lung disease*, European Respiratory Journal **23** (2004), 146–158.

6. A. Bourlioux, A.T. Layton, and M.L. Minion, *High-order multi-implicit spectral deferred correction methods for problems of reactive flow*, Journal of Computational Physics **198** (2003), 351–376.

7. E.L. Bouzarth, A. Brooks, R. Camassa, H. Jing, T.J. Leiterman, R.M. McLaughlin, R. Superfine, J. Toledo, and L. Vicci, *Epicyclic orbits in a viscous fluid about a precessing rod: Theory and experiments at the micro and macro scales*, Physical Review E **76** (2007), 016313.

8. E.L. Bouzarth, R. Camassa, P. Chtcheprov, B. LaRoque, D. Marron, R.M. McLaughlin, J. Toledo, L. Vicci, and L. Zhao, *Epicyclic toroidal orbits generated by a precessing bent rod in a viscous fluid: Theory, simulation, and experiment*, (in preparation).

9. E.L. Bouzarth, R. Camassa, R.M. McLaughlin, and L. Zhao, *Asymptotic and numerical solutions for a tilted precessing rod*, (in preparation).

10. R. Camassa, T.J. Leiterman, and R.M. McLaughlin, *Trajectory and flow properties for a rod spinning in a viscous fluid. Part 2: An asymptotic solution with a no-slip plane*, (in preparation).

11. _____, *Trajectory and flow properties for a rod spinning in a viscous fluid. Part 1: An exact solution*, Journal of Fluid Mechanics (to appear, 2008).

12. R. Camassa, R.M. McLaughlin, and L. Zhao, *An asymptotic solution for a bent precessing rod*, (unpublished).

13. B. Carstens, B.A. Evans, M.R. Falvo, A.R. Shields, R. Superfine, and S. Washburn, *Directed fluid transport with biomimetic cilia arrays* (in preparation).

14. J.H.E. Cartwright, N. Piro, O. Piro, and I. Tuval, *Embryonic nodal flow and the dynamics of nodal vesicular parcels*, Journal of the Royal Society Interface **4** (2007), no. 12, 49–55.

15. J.H.E. Cartwright, O. Piro, I. Tuval, and L. Kadanoff, *Fluid-dynamical basis of the embryonic development of left-right asymmetry in vertebrates*, Proceedings of the National Academy of Sciences of the United States of America **101** (2004), no. 19, 7234–7239.

16. A.T. Chwang and T.Y. Wu, *Hydromechanics of low-Reynolds-number flow. part 2. singularity method for Stokes flows*, Journal of Fluid Mechanics **67** (1975), 787–815.

17. R. Cortez, Notes on a system of regularized image singularities (unpublished).

18. _____, *The method of regularized Stokeslets*, SIAM Journal of Scientific Computation **23** (2001), no. 4, 1204–1225.

19. R. Cortez, L. Fauci, and A. Medovikov, *The method of regularized Stokeslets in three dimensions: Analysis, validation, and application to helical swimming*, Physics of Fluids **17** (2005), no. 3, 031504.1–031504.14.

20. R. Cortez and M. Minion, *The blob projection method for immersed boundary problems*, Journal of Computational Physics **161** (2000), 428–453.

21. J.W. Demmel, *Applied numerical linear algebra*, SIAM, 1997.

22. R.H. Dillon and L.J. Fauci, *An integrative model of internal axoneme mechanics and external fluid dynamics in ciliary beating*, Journal of Theoretical Biology **207** (2000), 415–430.

23. R.H. Dillon, L.J. Fauci, C. Omoto, and X. Yang, *Fluid dynamic models of flagellar and ciliary beating*, Annals of the New York Academy of Sciences **1101** (2007), 494–505.

24. R.H. Dillon, L.J. Fauci, and X. Yang, *Sperm motility and multiciliary beating: An integrative mechanical model*, Computers and Mathematics with Applications **52** (2006), 749–758.

25. Q. Du, V. Faber, and M. Gunzburger, *Centroidal Voronoi tessellations: Applications and algorithms*, SIAM Review **41** (1999), no. 4, 637–676.

26. Q. Du, M. Gunzburger, and L. Ju, *Constrained centroidal Voronoi tessellations for surfaces*, SIAM Journal of Scientific Computation **24** (2003), no. 5, 1488–1506.

27. A. Dutt, L. Greengard, and V. Rokhlin, *Spectral deferred correction methods for ordinary differential equations*, BIT **40** (2000), no. 2, 241–266.

28. B.A. Evans, *Design, fabrication, and actuation of biomimetic cilia*, Ph.D. thesis, The Univeristy of North Carolina at Chapel Hill, 2008.

29. B.A. Evans, A.R. Shields, R.L. Carroll, S. Washburn, M.R. Falvo, and R. Superfine, *Magnetically actuated nanorod arrays as biomimetic cilia*, Nano Letters **7** (2007), no. 5, 1428 – 1434.

30. L.J. Fauci and R. Dillon, *Biofluidmechanics of reproduction*, Annual Review of Fluid Mechanics **38** (2006), 371–394.

31. J.K. Fisher, J. Cribb, K.V. Desai, L. Vicci, B. Wilde, K. Keller, R.M. Taylor II, J. Haase, K. Bloom, E. Timothy O'Brien, and R. Superfine, *Thin-foil magnetic force system for high-numerical-aperture microscopy*, Review of Scientific Instruments **77** (2006), 023702.

32. G.R. Fulford and J.R. Blake, *Muco-ciliary transport in the lung*, Journal of Theoretical Biology **121** (1986), 381–402.

33. L. Greengard and V. Rokhlin, *A fast algorithm for particle simulations*, Journal of Computational Physics **73** (1987), 325–348.

34. N. Hirokawa, Y. Tanaka, Y. Okada, and S. Takeda, *Nodal flow and the generation of left-right asymmetry*, Cell **125** (2006), 33–24.

35. `http://people.scs.fsu.edu/~burkardt/f_src/scvt/scvt.html`.

36. `http://www.cs.unc.edu/Research/nano/vl/vlindex.html`.

37. H. Jing, *Nano scale devices: Fabrication, actuation, and related fluidic dynamics*, Ph.D. thesis, The Univeristy of North Carolina at Chapel Hill, 2006.

38. Y. Kim and C.S. Peskin, *2-D parachute simulation by the immersed boundary method*, SIAM J. Sci. Comput. **28** (2006), no. 6, 2294–2312.

39. A.T. Layton and M.L. Minion, *Conservative multi-implicit spectral deferred correction methods for reacting gas dynamics*, Journal of Computational Physics **194** (2004), 697–715.

40. _____, *Implications of the choice of quadrature nodes for picard integral deferred corrections methods for ordinary differential equations*, BIT Numerical Mathematics **45** (2005), no. 2, 341–373.

41. L. Lee and R.J. LeVeque, *An immersed interface method for incompressible Navier-Stokes equations*, SIAM Journal of Scientific Computation **25** (2003), no. 3, 832–856.

42. T.J. Leiterman, *Exact and asymptotic low reynolds, time-varying solutions for spinning rods with a comparison to experiments on the micro and macroscale*, Ph.D. thesis, The Univeristy of North Carolina at Chapel Hill, 2006.

43. R.L. LeVeque and Z. Li, *The immersed interface method for elliptic equations with discontinuous coefficients and singular sources*, SIAM Journal of Numerical Analysis **31** (1994), no. 4, 1019–1044.

44. H. Matsui, S.H. Randell, S.W. Peretti, C.W. Davis, and R.C. Boucher, *Coordinated clearance of periciliary liquid and mucus from airway surfaces*, Journal of Clinical Investigation **102** (1998), no. 6, 1125–1131.

45. A.A. Mayo and C.S. Peskin, *An implicit numerical method for fluid dynamics problems with immersed elastic boundaries*, Contemp. Math. **141** (1993), 261–277.

46. M.L. Minion, *Semi-implicit spectral deferred correction methods for ordinary differential equations*, Communincations in Mathematical Sciences **1** (2003), no. 2, 471–500.

47. S.M. Mitran, *Metachronal wave formation in a model of pulmonary cilia*, Computers and Structures **85** (2007), no. 11–14, 763–774.

48. E.P. Newren, A.L. Fogelson, R.D. Guy, and R.M. Kirby, *Unconditionally stable discretizations of the immersed boundary equations*, J. Comput. Phys. **222** (2007), no. 2, 702–719.

49. S. Nonaka, Y. Tanaka, Y. Okada, S. Takeda, M. Kido, and N. Hirokawa, *Randomization of left-right asymmetry due to loss of nodal cilia generating leftward flow of extraembryonic fluid in mice lacking KIF3B motor protein*, Cell **95** (1998), 829–837.

50. Y. Okada, S. Takeda, Y. Tanaka, J-C.I. Belmonte, and N. Hirokawa, *Mechanism of nodal flow: A conserved symmetry breaking event in left-right axis determination*, Cell **121** (2005), 633–644.

51. C.S. Peskin, *Flow patterns around heart valves: A numerical method*, Journal of Computational Physics **10** (1972), 252–271.

52. _____, *Mathematical aspects of heart physiology*, Courant Institute Lecture Notes, 1975.

53. C.S. Peskin and D.M. McQueen, *A three-dimensional computational method for blood flow in the heart i. immersed elastic fibers in a viscous incompressible fluid*, J. Comput. Phys. **81** (1989), 372–405.

54. _____, *A general method for the computer simulation of biological systems interacting with fluids*, Biological Fluid Dynamics: Proceedings of a meeting held at the University of Leeds, UK, July 4-8, 1994 (C. P. Ellington and T.J. Pedley, eds.), Cambridge, 1994.

55. M.E. Pettitt, B.A.A. Orme, J.R. Blake, and B.S.C. Leadbeater, *The hydrodynamics of filter feeding in choanoflagellates*, European Journal of Protistology **38** (2002), 313–332.

56. C. Pozrikidis, *Boundary integral and singularity methods for linearized viscous flow*, Cambridge University Press, 1992.

57. ———, *Introduction to theoretical and computational fluid dynamics*, Oxford University Press, 1997.

58. Y. Saad and M.H. Schultz, *GMRES: A generalized minimal residual algorithm for solving nonsymmetric linear systems*, SIAM Journal on Scientific and Statistical Computing **7** (1986), no. 3, 856–869.

59. J.M. Stockie and B.R. Wetton, *Analysis of stiffness in the immersed boundary method and implications for time-stepping schemes*, J. Comput. Phys. **154** (1999), no. 1, 41–64.

60. T. Yokoyama, *Motor or sensor: A new aspect of primary cilia function*, Anatomical Science International **79** (2004), 47–54.